Technische Universität München
Institut für Photogrammetrie und Karthographie
Lehrstuhl für Methodik der Fernerkundung

Monitoring of volcanic sulfur dioxide emissions and estimation of the plume height using GOME-2 measurements

Meike Rix

Vollständiger Abdruck der von der Fakultät für Bauingenieur- und Vermessungswesen der Technischen Universität München zur Erlangung des akademischen Grades eines Doktors (Dr. rer. nat.) genehmigten Dissertation.

Vorsitzender: Univ.-Prof. Dr.-Ing. Uwe Stilla

Prüfer der Dissertation:
1. Univ.-Prof. Dr.-Ing. habil. Richard Bamler
2. Apl. Prof. Dr. rer. nat. habil. Thomas Trautmann, Universität Leipzig
3. Univ.-Prof. Dr. rer. nat. habil., Dr. h.c. Donald Bruce Dingwell, Ludwig-Maximilians-Universität München

Die Dissertation wurde am 16.06.2011 bei der Technischen Universität München eingereicht und durch die Fakultät für Bauingenieur- und Vermessungswesen am 23.03.2012 angenommen.

Abstract

Satellite observations of volcanic sulfur dioxide emissions can provide critical information for reducing volcanic hazards, as they allow global monitoring of volcanic emissions, while ground-based monitoring is only carried out for a limited number of volcanoes. The work presented in this thesis addresses the determination of volcanic SO_2 emissions using the GOME-2 satellite instrument and the development of a new method to estimate the SO_2 plume height in near-real time, which is of particular importance for aviation safety.

The SO_2 total columns are retrieved from the GOME-2 measurements of backscattered solar radiance in the ultraviolet range of the spectrum using the well established differential optical absorption spectroscopy (DOAS). The DOAS method uses the highly structured absorption patterns of trace gases, i.e. SO_2, to determine the slant columns. The SO_2 slant column retrieval, the applied slant column corrections and the determination of the vertical SO_2 columns through application of a suitable air mass factor are explained in detail. The SO_2 total columns are operationally retrieved at the German Aerospace Center (DLR) in the framework of EUMETSAT's Satellite Application Facility on Ozone and Atmospheric Chemistry Monitoring (O3M-SAF).

The standard DOAS technique assumes optically thin atmospheric conditions, which can lead to significant underestimation for the retrieval of high total SO_2 columns when using a single wavelength air mass factor. By applying the DOAS method to synthetic GOME-2 spectra the errors induced by the use of a single wavelength air mass factor, as well as additional errors due to ozone interference and insufficient treatment of the Ring effect are quantified. The strengths and limitations of the standard DOAS retrieval of volcanic SO_2 are assessed, showing good retrieval results up to total SO_2 columns of ~ 20 DU. Further, a modified DOAS method and a direct fitting algorithm are applied to the synthetic GOME-2 spectra and the improvements, which can be achieved by using these retrieval techniques are evaluated for different atmospheric conditions. Especially for the retrieval of high total SO_2 columns, major improvements can be achieved, reducing the underestimation from ~ 40 % to ~ 10 %. The different retrieval techniques are then applied to GOME-2 observations of volcanic SO_2 plumes from eruptions of Kilauea, Kasatochi and Etna and the results are discussed. Further, the GOME-2 total SO_2 columns from the operational retrieval algorithm are compared with measurement data from the SCIAMACHY satellite instrument. The comparison shows a good agreement between the two satellite instruments, with differences typically below 25 %. In addition the GOME-2 SO_2 data is validated against ground-based SO_2 observations. For the validation, comparisons with Max-DOAS measurements of anthropogenic pollution in Beijing, FLYSPEC observations of emissions from Kilauea and Brewer measurements of the Kasatochi eruption plume are conducted. The comparison with the Brewer observations of SO_2 in the stratosphere shows a good agreement for individual observations, the correlation between the two observations being > 0.65 for most stations, while for the observations in the lower troposphere a good agreement can be achieved for monthly averaged values.

As information on the SO_2 plume height is very important for aviation safety after volcanic eruptions and it is also a major source of error in the retrieval of the SO_2 columns, a new method to retrieve the plume height in near-real time from GOME-2

observations is developed. The retrieval matches GOME-2 measurement spectra with simulated GOME-2 radiance spectra for various plume heights. To allow near-real time plume height estimation the simulated spectra are stored in a look-up table. The accuracy of the new method is estimated through application to synthetic GOME-2 spectra to better than 2 km in most cases. In addition, the near-real time plume height retrieval is used to analyze the volcanic eruption clouds of Kilauea, Kasatochi and Eyjafjallajökull and the results are compared with height estimates from other sources.

Finally, the use of the GOME-2 data of volcanic SO_2 emissions in early warning of volcanic hazard is discussed. The near-real time GOME-2 SO_2 columns are used for aviation safety after volcanic eruptions and also for early warning of volcanic unrest. Case studies of volcanic eruptions that caused disruption to air traffic (Kasatochi, Eyjafjallajökull) are presented and the degassing at Nyiragongo volcano is shown as an example where changes in the volcanic SO_2 emissions could be related to upcoming eruptions.

Zusammenfassung

Satellitenbeobachtungen von vulkanischen Schwefeldioxidemissionen liefern wichtige Informationen zur Reduktion der von Vulkanen ausgehenden Gefahren. Während bodenbasierte Messungen nur an wenigen Vulkanen weltweit durchgeführt werden, ermöglichen Satellitendaten eine globale Überwachung vulkanischer Aktivität. Diese Arbeit beschäftigt sich mit der Bestimmung von vulkanischen SO_2-Emissionen mit Hilfe des GOME-2-Satelliteninstruments, sowie mit der Entwicklung eines Verfahrens zur zeitnahen Bestimmung der SO_2-Höhe, was von besonderer Bedeutung für die Sicherheit des Flugverkehrs ist.

Die Bestimmung der SO_2-Gesamtsäulen aus den GOME-2-Messungen der rückgestreuten Sonnenstrahlung erfolgt im ultravioletten Bereich des Spektrums mit Hilfe der Differentiellen Optischen Absorptionsspektroskopie (DOAS). Das DOAS-Verfahren nutzt die stark strukturierten Absorptionsmuster der Spurengase, in diesem Fall SO_2, um die schrägen Säulengehalte der Gase zu bestimmen. Die Bestimmung der schrägen SO_2-Säulen, sowie erforderliche Korrekturen der schrägen SO_2-Säulen und die Umwandlung in vertikale Säulen mit Hilfe von entsprechenden „Air Mass“ Faktoren (AMF) wird im Detail erläutert. Die operationelle Bestimmung der SO_2-Gesamtsäulen erfolgt am Deutschen Zentrum für Luft- und Raumfahrt (DLR) im Rahmen des „EUMETSAT’s Satellite Application Facility on Ozone and Atmospheric Chemistry Monitoring“ (O3M-SAF).

Das Standard-DOAS Verfahren geht von einer optisch dünnen Atmosphäre aus, was, im Falle der Verwendung eines bei einer einzelnen Wellenlänge berechneten Air Mass Faktors, zu einer erheblichen Unterschätzung von großen SO_2-Gesamtsäulen führen kann. Durch Anwendung der DOAS-Methode auf synthetische GOME-2-Spektren, werden die entstehenden Fehler quantifiziert. Des Weiteren werden zusätzliche Fehler, die durch Interferenz mit der Ozon-Absorption und durch unzureichende Berücksichtigung des Ring-Effekts entstehen, untersucht. Die Stärken und Schwächen des Standard-DOAS-Verfahrens werden untersucht und es wird gezeigt, dass dieses bis zu einer Gesamtsäule von etwa 20 DU gute Ergebnisse liefert. Außerdem werden ein erweitertes DOAS- und ein „Direct Fitting“-Verfahren

auf die synthetischen GOME-2-Spektren angewandt und die Verbesserungen, die mit Hilfe dieser Verfahren erzielt werden, für verschiedene Atmosphärenbedingungen bewertet. Insbesondere bei der Bestimmung von großen SO_2-Gesamtsäulen kann der Fehler von ~ 40 % auf ~ 10 % reduziert werden. Die unterschiedlichen Verfahren werden außerdem auf GOME-2-Messungen der Eruptionswolken des Kilauea, des Kasatochi und des Etna angewandt und die Ergebnisse der einzelnen Verfahren verglichen. Des Weiteren erfolgt ein Vergleich der GOME-2-SO_2-Gesamtsäulen der operationellen Prozesskette mit Messdaten des SCIAMACHY-Satelliteninstruments. Der Vergleich zeigt eine gute Übereinstimmung der beiden Satelliteninstrumente mit Abweichungen, welche typischerweise kleiner als 25 % sind. Zusätzlich werden die GOME-2-Daten mit bodengebundenen SO_2-Messungen validiert. Für die Validierung werden Vergleiche mit Max-DOAS-Messungen anthropogener Verschmutzung in Beijing, mit FLYSPEC-Messungen nicht-eruptiver SO_2-Emissionen des Kilauea, sowie mit Brewer-Messungen der Eruptionswolke des Kasatochi durchgeführt. Der Vergleich mit den Brewer-Messungen der stratosphärischen SO_2-Wolke zeigt eine gute Übereinstimmung der einzelnen Messwerte, mit einer Korrelation > 0.65 für die meisten Stationen. Für die Messungen von SO_2 in der unteren Troposphäre wird eine gute Übereinstimmung für die Monatsmittel erzielt.

Informationen über die Höhe der SO_2-Wolke sind für die Sicherheit des Flugverkehrs nach Vulkanausbrüchen von großer Bedeutung, außerdem stellt die SO_2-Höhe eine der Hauptfehlerquellen bei der Bestimmung der SO_2-Gesamtsäulen dar. Daher wird eine Methode entwickelt, um die SO_2-Höhe in naher Echtzeit aus den GOME-2-Messungen zu bestimmen. Das Verfahren vergleicht das gemessene GOME-2-Spektrum mit simulierten GOME-2-Spektren für verschiedene SO_2-Höhen. Um eine zeitnahe Bestimmung der SO_2-Höhe zu ermöglichen, werden die simulierten Spektren in einer „Look-up“ Tabelle gespeichert. Eine Abschätzung der Genauigkeit des neuen Verfahrens anhand der Anwendung auf synthetischen Spektren zeigt, dass in den meisten Fällen eine Genauigkeit besser als 2 km erreicht wird. Das Verfahren wird auf die Eruptionswolken des Kilauea, des Kasatochi und des Eyjafjallajökull angewandt und die Resultate wurden mit Höheninformationen aus anderen Quellen verglichen.

Abschließend wird die Verwendung der GOME-2-Messungen von vulkanischem SO_2 zur Gefahrenreduzierung im Zusammenhang mit Vulkanausbrüchen erläutert. Die in naher Echtzeit bereitgestellten GOME-2-SO_2-Säulen werden zur Verbesserung der Flugsicherheit nach Vulkanausbrüchen sowie in Frühwarnsystemen genutzt. In diesem Zusammenhang werden Fallstudien zu Ausbrüchen, die Beeinträchtigungen im Luftverkehr (Kasatochi, Eyjafjallajökull) verursachten, durchgeführt. Außerdem werden Messungen der nicht-eruptiven SO_2-Emissionen des Vulkans Nyiragongo analysiert und ein Zusammenhang zwischen Veränderungen der SO_2-Emissionen und dem Beginn von Eruptionen hergestellt.

Contents

1. Introduction

Volcanic eruptions pose a major danger to people living in the vicinity of volcanoes. Due to the fast growing population more people live close to active volcanoes, and the growing developments in infrastructure and transportation systems make societies more vulnerable (Schmincke, 2004). The region surrounding the volcano is directly affected by the eruption, e.g. due to lava flows, pyroclastic flows, and lahars. Besides being a direct danger to the local population, volcanic ash has proven to be a major hazard to aviation. The difficulty to correctly predict the time and location of volcanic eruption events, especially in remotely located areas, has caused many disasters.

Volcanic eruptions and passive degassing of volcanoes are the most important natural source of SO_2 (Graf et al., 1997). During an eruption, SO_2 is the third most abundant gas found in volcanic plumes after H_2O and CO_2. Changes in SO_2 flux can be a precursor for the onset of volcanic activity. In addition, SO_2 is also produced by anthropogenic activities like power plants, refineries, metal smelting and burning of fossil fuels, but its atmospheric background level is usually very low, which makes it an excellent indicator for volcanic activity. The lifetime of atmospheric SO_2 varies from approximately 1–2 days in the troposphere to several weeks in the stratosphere. In the troposphere it is transformed into sulfuric acid and is responsible for acid rain. If SO_2 is directly brought into the stratosphere by volcanic eruptions, it can remain there for several weeks and travel over long distances (e.g. Kasatochi eruption, Aug. 2008), and as sulfuric aerosols it can also have a cooling effect on the atmosphere (e.g. Pinatubo eruption, 1991) (McCormick et al., 1995).

Ground-based measurements of volcanic gases in combination with other observations, e.g. seismicity, have proven to be a valuable tool for gaining insight into magmatic processes occurring at depth (Stevenson and Blake 1998). However, only very few of the active volcanoes worldwide are monitored on a regular basis. During the last 30 years satellite instruments have contributed global information on volcanic gas emissions. The Total Ozone Monitoring Spectrometer (TOMS) was the first satellite instrument to detect volcanic SO_2 from the eruption of El Chichon in 1982 (Krueger, 1983). Due to its limited sensitivity for SO_2, the detection was confined to large SO_2 amounts after volcanic eruptions (e.g. Krueger et al., 1989). With the launch of the Global Ozone Monitoring Experiment (GOME) onboard ERS-2 in 1995 the detection limit for SO_2 has been greatly improved (Eisinger and Burrows, 1998). However, this instrument has a fairly poor spatial coverage and needs several days for the acquisition of a contiguous global map. The successor of the GOME instrument (GOME-2) on MetOp-A since 2006 and OMI (Ozone Monitoring Instrument) on EOS-Aura since 2004 make it possible to monitor volcanic SO_2 emissions on a global scale and daily basis. Both sensors have also proven their ability to detect passive degassing of volcanoes (Carn et al., 2008, Rix et al, 2009).

The contiguous wavelength coverage of the recent satellite instruments made it possible to use the differential optical absorption spectroscopy method (DOAS) (Platt, 1994) from space. The DOAS technique uses the highly structured absorption patterns of trace gases, therefore a detailed quantification of effects with fairly broad extinction features, e.g. Rayleigh and Mie scattering, is not necessary. The method

allows fast retrieval of SO_2 columns, i.e. SO_2 data from GOME-2 are made available to users less than two hours after sensing.

A limitation of the DOAS method is the assumption of an optically thin atmosphere that is not strictly fulfilled for the SO_2 retrieval in the UV wavelength range. Retrieval techniques, such as modified DOAS (Richter, 1997) or direct fitting (Spurr et al, 2009), can provide improvements, especially for large SO_2 columns. The disadvantage of these techniques is that they are computationally expensive, therefore they are currently not applicable for near-real time data processing. The near-real time availability of GOME-2 SO_2 data is of great advantage when using the information for early warning of volcanic hazards, especially for aviation warning. In addition, information on the altitude of the volcanic emissions is important for aviation safety. It is also necessary for the correct quantitative SO_2 column retrieval. Plume height information has up to date mainly be obtained from reports of volcanoclogical observatories and from inverse trajectory modeling (Eckhardt et al., 2008). Recently the direct retrieval of the SO_2 plume height from spectral information from space has been demonstrated (Yang et al., 2009).

In this work the focus is on the retrieval of volcanic SO_2 total columns and the SO_2 plume height using GOME-2 observations. The daily global coverage and the operational retrieval of SO_2 makes GOME-2 a valuable tool for monitoring volcanic SO_2 emissions. The operational GOME-2 SO_2 data, provided by the German Aerospace Center (DLR) in the framework of EUMETSAT's Satellite Application Facility on Ozone and Atmospheric Chemistry Monitoring (O3M-SAF), are available in near-real time allowing the use of GOME-2 SO2 data for early warning of volcanic hazards.

The main objectives of this thesis are:

- Assessment of the quality of the GOME-2 SO_2 retrieval using the DOAS method.

  The DOAS method is widely applied in the retrieval of SO_2 from satellites, as it provides the possibility of near-real time processing. However, the DOAS approach includes several limitations, which lead to difficulties when retrieving volcanic SO_2. Here, the strengths and limitations of the method are systematically evaluated and compared with other retrieval techniques such as modified DOAS and direct fitting.

- Development of a near-real time SO_2 plume height retrieval algorithm

  A method is developed to retrieve the SO_2 plume altitude in near-real time directly from GOME-2 measurements. The plume height information is important for a correct quantitative retrieval of the SO2 total columns and for aviation safety.

- Validation of the operational GOME-2 SO_2 data and plume height

  The GOME-2 SO2 data are compared with other satellite observations of volcanic eruptions and with ground-based measurements of volcanic SO_2 emissions and anthropogenic SO_2 pollution. Further, the results of the near-real time plume height estimation are validated against other observations.

- Application of the GOME-2 SO_2 data in volcanic early warning services

  The use of near-real time GOME-2 SO_2 data in several early warning services has proven valuable in terms of aircraft safety and pre-eruptive warning of volcanic activity.

1.1 State of the art

The work presented in this thesis is mainly based on the differential optical absorption spectroscopy (DOAS) (Platt, 1994). The DOAS technique utilizes the highly structured absorption patterns of trace gases. Its main advantage is the exclusion of fairly broad extinction features, e.g. due to Rayleigh and Mie scattering, making a detailed quantification of these effects unnecessary. With the DOAS method trace gas columns are retrieved using a two step approach, first the slant column of the trace gas through the atmosphere is obtained, which is then converted to vertical columns using a suitable air mass factor. Since the development of the DOAS technique it has been widely applied in remote sensing of atmospheric trace gases (Platt and Stutz, 2008). One important application of DOAS instruments is the monitoring of volcanic gas emissions (e.g. Brobowski et al., 2003, Galle et al., 2003, Brobowski and Platt, 2007). With the launch of the Global Ozone Monitoring Experiment (GOME) onboard ERS-2 (Burrows et al., 1999) in 1995, the contiguous wavelength coverage of the satellite instruments made it possible to use the DOAS method from space. Since then volcanic SO_2 has been retrieved from satellite UV measurements using the DOAS method very successfully (Eisinger and Burrows, 1998, Thomas et al., 2005, Khokar et al., 2005, Loyola et al, 2008).

When using the DOAS method for the retrieval of volcanic SO_2 several limitations arise, which are specific to SO_2. The DOAS method assumes an optically thin atmosphere. In the UV wavelength range used for the SO_2 retrieval, this assumption is not strictly fulfilled. Further the air mass factor for SO_2 strongly depends on the vertical SO_2 profile, which, especially for volcanic eruptions, is unknown at the time of measurement. Due to the typically low SO_2 concentration in the atmosphere, insufficient treatment of the Ring effect and interference of ozone absorption can have a high influence on the retrieval. Despite these known issues the DOAS method is widely applied in retrieving SO_2 from satellite observations, as it allows a near-real time retrieval with reasonable accuracy. At this stage only rough estimates of the errors introduced by these effects exist. The slant column errors are estimated to ~ 30 %, the errors introduced by the air mass factor are approximated to ~ 40 % (Thomas et al., 2005, Valks et al., 2009).

Several improved retrieval methods that are based on the DOAS principle have been developed in recent years. A modified DOAS method for the retrieval of ozone total columns has been introduced (Richter, 1997, Bovensmann et al., 1999), which fits a trace gas optical density instead of a slant column. A different approach, which is also based on the DOAS method, is the Weighting Function DOAS (WF-DOAS) (Coldewey-Egbers et al., 2005), that has mainly been developed and used for the retrieval of ozone total columns (Weber et al., 2005, Bracher et al., 2005). Lee et al. (2008) applied this approach successfully to the SO_2 retrieval from the SCIAMACHY instrument (Bovensmann et al., 1999). The method fits the vertically integrated total column weighting function. The modified and WF-DOAS avoid the two step

separation of slant column fitting and air mass factor computation, allowing the use at higher optical densities in the UV wavelength region. Recently a direct fitting approach has been developed for an improved retrieval of total ozone columns (Spurr et al., 2009). With the direct fitting method the total column is retrieved from direct least squares inversion of radiances using radiative transfer simulations of the radiances and total column weighting functions. A similar algorithm is used for the retrieval of volcanic SO2 columns from the OMI instrument (Yang et al., 2007). However, compared to the standard DOAS technique these advanced methods are of complex nature and computationally expensive.

The validation of satellite SO_2 retrieval results has proven difficult. The satellite data are fairly noisy, e.g. noise levels (expressed as the standard deviation, σ) for individual observations of the OMI instrument are ~ 0.2 DU for a plume height of 7.5 km (Pinardi et al., 2010) and ~ 1.5 DU for the planetary boundary layer (Krotkov et al., 2008), while the SO_2 loadings in the atmosphere are often < 2 DU. Earlier comparisons between different satellite sensors show differences in total SO_2 loading and in the total SO_2 columns of up to > 100 % (Thomas et al., 2009), as differences in the retrieval, the measurement time and uncertainties in the plume height strongly influence the results. Comparing satellite SO_2 data with ground based observations, especially of volcanic origin, is complicated by the highly variable nature of volcanic SO_2 fluxes. As ground-based observations are point measurements, which are compared with satellite observations averaged over the pixel area, spatial gradients in the SO_2 concentrations can lead to large differences between the two observations. Comparisons of GOME-2 and OMI SO_2 data with Max-DOAS observations at different volcanoes show a reasonable qualitative agreement for most volcanoes, however, with definite differences in the individual observations, which are often > 100% (Pinardi et al., 2010). Similar differences can be observed in the comparisons of OMI, GOME-2 and SCIAMACHY data with ground-based Max-DOAS and Brewer observations shown in Van Geffen et al., 2008. Also a validation of the OMI SO_2 data using aircraft observations shows a good qualitative agreement, but again quantitatively the differences are large, as the OMI values are approximately twice the aircraft values (Krotkov et al., 2008).

Vertical profile information is required for the correct quantitative retrieval of the SO_2 total columns, as the DOAS methods and the direct fitting technique all use a priori assumptions on the vertical SO_2 distribution. Unlike other trace gases, SO_2 can be present in the atmosphere at very different altitudes, from the planetary boundary layer in case of anthropogenic pollution to the stratospheric heights for explosive volcanic eruptions. Therefore it is not possible to use a climatology to obtain a reasonable a priori profile. In case of volcanic eruptions the plume height is also extremely important for aviation safety. Apart from eruption height information provided by volcanological observatories, recently various techniques have been developed to retrieve the volcanic plume height. The inverse trajectory modeling uses a trajectory model to simulate the SO_2 transport for several assumed injection heights and matches the results with satellite observations to determine the most probable plume height (Eckhardt et al., 2008). The technique has successfully been applied to the eruption of Kasatochi (Kristiansen et al., 2010). A second approach retrieves the plume height directly from satellite spectral observations and is based on an extension of the Iterative Spectral Fitting (ISF) algorithm for the OMI instrument (Yang et al., 2007). It retrieves ozone column, SO_2 column and SO_2 altitude simultaneously (Yang et al., 2009) through a direct fitting technique. A direct fitting

algorithm to determine the SO_2 plume height has also been applied by Nowlan et al. (2010). However, these techniques are computationally time consuming and especially for aviation safety the plume height information is required in near-real time (NRT).

1.2 Outline of the thesis

Chapter 2 gives a general introduction into atmospheric sulfur chemistry with the focus on sulfur dioxide emissions from volcanoes and their impact on climate and atmospheric chemistry. Further, different measurement techniques used for volcanic SO_2 emissions are introduced.
In Chapter 3 the operational retrieval of SO_2 total columns is presented in detail. An introduction of the differential optical absorption spectroscopy (DOAS) is given. Further, the algorithm settings for the slant column retrieval of SO_2 from GOME-2 data and the corrections applied to the SO_2 slant columns are explained and the computation of the vertical SO_2 columns is discussed.
Chapter 4 addresses limitations that arise when applying the standard DOAS technique to the retrieval of SO_2. Using synthetic GOME-2 irradiance spectra the resulting errors are estimated. Further, a modified DOAS method and a direct fitting algorithm are applied to the synthetic spectra and the improvements that can be achieved are analyzed. The three retrieval methods are then applied to GOME-2 measurements of volcanic eruptions and the results are compared.
A validation of the operational GOME-2 SO_2 data is presented in Chapter 5. The GOME-2 SO_2 data is compared with the satellite instrument SCIAMACHY and several ground-based instruments, e.g. Max-DOAS and FLYSPEC. For validation, volcanic SO_2 emissions as well as measurements of SO_2 pollution in China are used.
In Chapter 6 the direct retrieval of the SO_2 plume height from GOME-2 measurements is discussed. An algorithm to retrieve the plume height in near-real time through matching simulated spectra with GOME-2 measurements is presented. The plume height retrieval is applied to synthetic GOME-2 spectra and the accuracy of the retrieval is estimated. The near-real time height estimation is then applied to GOME-2 observations of volcanic eruptions and the results are compared with plume heights retrieved using other techniques. A paper has been submitted published in a special issue on the Eyjafjallajökull eruption in *Journal of Geophysical Research* (Rix et al., 2012) based on parts of Chapter 6 and 7.
The use of satellite monitoring of volcanic SO_2 in early warning of volcanic hazards is presented in Chapter 7. Two applications of GOME-2 data concerned with early warning of volcanic hazards are presented, one focusing on volcanic hazards to aviation, the other dealing with pre-eruptive warning of volcanic unrest. This chapter is based on a publication in *IEEE Journal of Selected Topics in Applied Earth Observations and Remote Sensing* (Rix et al., 2009).
In Chapter 8 concluding remarks and an outlook into future perspectives are given.

2. Impact of volcanic sulfur emissions on atmospheric processes and climate

Sulfur compounds are present in the atmosphere as gas and aerosols. They originate mainly from biological processes, volcanoes and anthropogenic activities. Despite the low atmospheric concentration, with volume mixing ratios of typically less than 1 ppmv (Seinfeld and Pandis, 2006), sulfur compounds are part of various chemical reactions. Their impact on particle formation is considered to be high and emissions of sulfur dioxide are responsible for acid rain. If sulfur is brought into the stratosphere, e.g. by volcanic eruptions, it can influence the climate, leading to a reduction in surface temperature, and enhance the destruction of stratospheric ozone.

In the first section sources and sinks of atmospheric sulfur compounds will be discussed and the importance of atmospheric SO_2 is described. The next section focuses on volcanic SO_2 emissions and their impact on atmospheric processes and climate. Further the use of volcanic SO_2 measurements in volcanic risk assessment will be introduced. In the last session a short overview of ground-based and satellite measurements of atmospheric SO_2 is given and their use in monitoring pollution and volcanic gas emissions is discussed.

2.1 Atmospheric sulfur compounds

Most sulfur compounds are naturally released to the atmosphere by biological processes as hydrogen sulfide (H_2S), carbon disulfide (CS_2), dimethyl sulfide/ DMS (CH_3SCH_3), carbonyl sulfide (COS) and through sea spray as SO_4^{-2} in the liquid phase. Table 2.1 lists the main atmospheric sulfur sources and sinks together with their estimated annual sulfur flux. Volcanism contributes to the global sulfur budget by the release of sulfur dioxide (SO_2) and H_2S. However, most SO_2 emissions stem from anthropogenic activities, e.g. combustion processes.

Anthropogenic sulfur emissions contribute heavily to the tropospheric sulfur budget. They mainly originate from industrial activities. The major component from anthropogenic activities is SO_2 originating from fossil fuel combustion, oil refineries, copper smelting and biomass burning which contribute around 90 % of the total SO_2 burden (Seinfeld and Pandis, 2006). Further anthropogenic contributions of sulfur stem from vehicle and industrial gas exhaust. Although anthropogenic sulfur emissions contribute more than 80 % of the total sulfur emissions they play only a minor role for stratospheric sulfur processes. Most emissions take place in the lower troposphere and the short lifetime of SO_2 does not allow transport into the stratosphere.
The main natural sources of sulfur are biogenic sources (DMS, H_2S, COS), sea spray (SO_4^{-2}) and volcanoes (SO_2) (Table 2.1). The dominant source of stratospheric sulfur is COS, which mainly originates from the sea. Due to its long lifetime it can be transported from the lower troposphere into the stratosphere, where it is converted to SO_2 and to sulfur aerosol (Brasseur et al., 1999). Volcanoes contribute to

stratospheric sulfur irregularly, as only explosive eruptions (VEI > 3*) reach stratospheric heights.
Most sulfur compounds are removed from the troposphere by oxidation to SO_2 and SO_4^{-2} which are then deposited by wet- and dry-deposition. SO_2 can be removed from the troposphere by formation of sulfuric acid which acts as condensation nuclei for clouds and aerosols. Further SO_2 sinks in the troposphere are the direct uptake on aerosols and clouds which are then removed by dry and wet deposition. The main sink for stratospheric sulfur is the exchange with the troposphere. This mechanism has been studied following big volcanic eruptions (Weisenstein et al., 1997, Pitari et al., 2002). The time to reduce the sulfur compounds in the stratosphere to levels that are similar to those before the eruption is 1 – 2 years and is on the same time scale as that for mixing of stratospheric constituents into the troposphere.

	Compound	Flux
Sources		
Volcanoes	SO_2, H_2S,COS	7-10
Vegetation and soils	H_2S, DMS, COS, CS_2, DMDS	0.4-1.2
Biomass burning	SO_2, COS, H_2S	2-4
Ocean	DMS, COS, CS_2, H_2S	10-40
Anthropogenic	SO_2, sulfates	88-92
Sinks		
Dry deposition	SO_2, sulfates	50-75
Wet deposition	SO_2, sulfates	50-75

Table 2.1: Global sulfur fluxes in Tg yr^{-1} (Brasseur et al., 1999)

Sulfur compounds can affect the atmospheric radiation budget directly by cooling through sulfate particles and indirectly by serving as cloud condensation nuclei (CCN). SO_2, SO_3 and sulfuric acid (H_2SO_4) are aerosol precursors and lead to cloud formation. This indirect effect also has a cooling effect as the sulfur particles enhance the number of aerosols which leads to the formation of more and smaller cloud droplets and therefore increases the reflectivity. As a result the incoming solar radiation is decreased. The influence of SO_2 on the earth's albedo will be discussed in more detail in Section 2.3.1. Sulfur is further responsible for acid rain and as SO_2 or sulfate aerosol it is one of the major causes of air pollution, as described in the next section.

2.2 Atmospheric sulfur dioxide

Sulfur dioxide is a poisonous, colorless gas with a sharp smell. It takes part in a variety of chemical reactions and reacts to atmospheric sulfuric acid, H_2SO_4, which is an important aerosol nucleation precursor. SO_2 can be dangerous to human health especially the respiratory system.

* The volcanic eruption index (VEI) is a scale developed to classify the size of explosive volcanic eruption (1 – 10). It is based on the volume of erupted material and the height of the eruption column. (Newhall and Self, 1982)

The main natural source of SO_2 are volcanoes, but in total they only account for roughly 10 % of the global SO_2 emissions. The biggest source, around 90 % of the total SO_2 burden, are anthropogenic emissions mainly fossil fuel combustion, metal smelters and biomass burning (Seinfeld and Pandis, 2006). The highest pollution originates from industrialized regions like Europe, the USA, China and India. Between 1960 and 1980 the emission rate of SO_2 has been constantly increasing worldwide. A reduction in sulfur emissions has been observed for Europe and the US since 1980, due to stringent precautions that have been taken to minimize the negative environmental effects of industrial emissions, whereas in Asia SO_2 emissions continued to increase (Streets et al., 2000). Recently satellite observations show a decrease in SO_2 emissions in some of the highly industrialized regions in China, that are most probably due to new measures taken by the Chinese Government to increase the air quality (Gielen and Changhong, 2001, Li et al., 2010). Figure 2.1 shows the development of global SO_2 emissions until today and an estimate of the future development (Andreae et al., 2005).
SO_2 is removed from the atmosphere via gas and aqueous-phase reactions to form sulfuric acid, leading to a lifetime of several days in the troposphere and up to several weeks in the stratosphere.

$$SO_2 + OH \longrightarrow HSO_3 \quad (2.1)$$

$$HSO_3 + O_2 \longrightarrow HO_2 + SO_3 \quad (2.2)$$

$$SO_3 + H_2O \longrightarrow H_2SO_4 \quad (2.3)$$

Alternatively the following aqueous-phase reaction takes part in clouds

$$SO_2 + H_2O \longrightarrow H_2SO_3 \quad (2.4)$$

$$H_2SO_3 + H_2O_2 \longrightarrow H_2SO_4 + H_2O \quad (2.5)$$

Sulfuric acid condenses and forms aerosols and is removed from the troposphere via wet and dry deposition. In the stratosphere it can stay for several years.

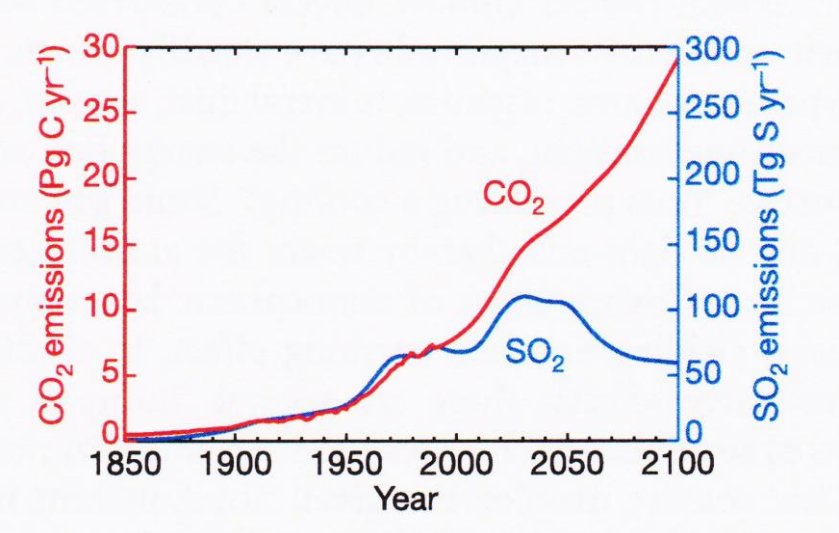

Figure 2.1: Historical global SO_2 and CO_2 emissions and estimated emissions until 2100 from the SRES[251] emission scenario used in the IPCC. (Andreae et al., 2005)

[1] SRES (Special Report On Emission Scenarios) published in IPCC, 2001

2.3 Volcanic sulfur dioxide emissions

Around 160 volcanoes are active per decade, with ~ 60 volcanoes being active per year. Volcanic activity is closely linked to the active zones of plate tectonics with most active volcanoes being located around the pacific ocean along what is called the “ring of fire” (Figure 2.2). The volcanic gas emissions depend strongly on the magma composition and the thermodynamic conditions (temperature and pressure) in the conduit. Most of the global magma erupted is of basaltic composition, with basaltic volcanoes typically located along mid-oceanic ridges at depth in the oceans. Exceptions are Iceland and the Azores where the eruption rate is so large that volcanic islands have formed. Basaltic magma is typically of low viscosity and gas content and poor in silicate. Basaltic magmas are also typical for intra-plate volcanoes that are often referred to as hot-spot volcanoes. An example of this type of volcano is the island chain of Hawaii. The contribution of basaltic magma to volcanic sulfur emissions into the atmosphere is only minor.

Figure 2.2: Plate tectonics and worldwide distribution of active volcanoes. Most active volcanoes are located around the Pacific along the “Ring of Fire” (USGS, 1997)

In comparison felsic magmas are rich in silicate and contain more dissolved gases, mainly water. They are highly viscous which leads to generally more explosive eruptions. Magmas of this type are called rhyolite. Typical for volcanoes at subduction zones are andesitic magmas with intermediate silicate content. Eruptions of rhyolitic and andesitic volcanoes occur less frequently but more explosively. They can emit high amounts of magma and gas, sometimes injecting them directly into the stratosphere. Many volcanoes also continuously emit gases during non-eruptive periods in what is called passive degassing. Subduction zone volcanoes contribute the largest part to the global volcanic sulfur emissions (Textor et al., 2004).
Studies of volcanic gas emissions are mainly motivated by two issues. Volcanic gases can significantly influence atmospheric chemistry, both in the troposphere (passive degassing and small eruptions) and stratosphere (major eruptions). The second important aspect is that volcanic gas emissions and their changes can

provide insight into the volcanic processes occurring at depth. In combination with other volcanic parameters (e.g. seismicity, deformation) measurements of volcanic gas fluxes are a useful parameter for hazard assessment and eruption forecasting.
The main gas compounds emitted are water vapor, CO_2, SO_2, H_2S, HCl, HF, H_2, CO and HBr (in order of descending magnitude, Table 2.2). The gas composition is dependent on the magma composition and the volcanic processes at depth and can therefore provide valuable insight in terms of risk evaluation (Aiuppa et al., 2007).
SO_2 is typically the third most abundant gas in volcanic plumes, and is often used as an indicator for volcanic activity and as a tracer for volcanic plumes for two reasons. The atmospheric background level of SO_2 is relatively low, compared to the more abundant gases H_2O and CO_2. The other major source apart from volcanoes are anthropogenic activities which can normally be distinguished easily as they are locally restricted. The volcanic input of CO_2 into the atmosphere with approximately $2.4x10^{13}$ g(C)/a (Kerrick, 2001) is orders of magnitude below the current anthropogenic emissions of about $7x10^{15}$ g(C)/a (IPCC, 2007) making it difficult to distinguish volcanic emissions from other emission sources. Apart from being not very abundant in the atmosphere, SO_2 is also a fairly stable species compared to some of the other volcanic gases. With a lifetime on the order of days in the troposphere and weeks in the stratosphere, SO_2 can be used as a tracer for tracking volcanic plumes.

Species	H_2O	CO_2	SO_2	H_2S	HCl	HF	HBr	COS	CS_2
Composition [%/vol]	50-90	1-40	1-25	1-10	1-10	$< 10^{-3}$	?	10^{-4}-10^{-2}	10^{-4}-10^{-2}
Global Flux [Tg/a]	?	75	1.5-20	1-2.8	0.4-11	0.06-6	0.00.78-0.1	0.006-0.1	0.007-0.096

Table 2.2: Volcanic gas composition and estimated global annual flux (Textor et al., 2004)

2.3.1 Climate effect of volcanic gas emissions

Volcanism is assumed to be one of the driving factors in the development of the Earth's atmosphere, as massive volcanic eruptions emitted large amounts of the greenhouse gases carbon dioxide and methane during the early Archaean (~ 3 billion years ago).
Apart from being an important factor in the historical development of the Earth's atmosphere, volcanic gas emissions also have a significant influence on today's atmosphere and climate. Volcanic sulfate aerosol brought into the stratosphere by large eruptions causes tropospheric cooling (Robock, 2000) and emissions of halogens can lead to destruction of ozone. Major volcanic eruptions lead to considerable climatic perturbations, when large amounts of ash and SO_2 are emitted into the stratosphere. The resulting H_2SO_4 aerosols are responsible for the dominant radiative effect after large volcanic eruptions. Figure 2.3 shows the major radiative processes that result from stratospheric aerosol input after large volcanic eruptions. Best-known is the direct effect on solar radiation. The sulfate aerosols are of similar size as the wavelength of visible light, with a typical effective radius of 0.5 µm and a single scattering albedo of 1, therefore they strongly interact with the solar radiation by scattering. Some of the solar radiation is backscattered and reflected back to space, increasing the planetary albedo and reducing the solar radiation at the Earth's surface. The second effect is heating of the stratosphere, as the top of the aerosol cloud is warmed by absorption of solar radiation in the near infrared and the lower stratosphere is heated by absorption of upward long-wave radiation from the surface

and the troposphere. At the surface the large reduction in shortwave radiation dominates the additional downward flux of long-wave radiation, resulting in a net cooling. This cooling at the surface is a well known effect after volcanic eruptions (McCormick et al., 1995). Because sulfate aerosols in the stratosphere are advected around the globe fast, single eruptions can produce global or hemispheric cooling for 2-3 years (Robock and Mao, 1995).

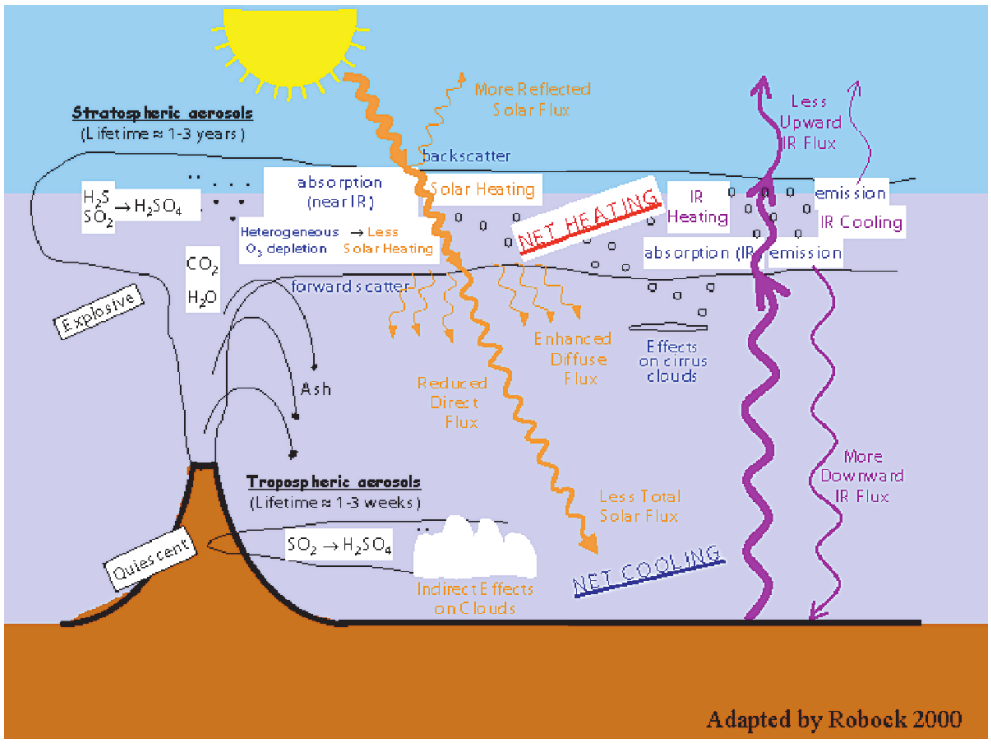

Figure 2.3: Volcanic influence on the atmospheric radiation budget (Robock, 2000)

A recent example of global cooling due to volcanic activity is the eruption of Mt. Pinatubo (Philippines) in 1991 (McCormick et al., 1995), during which approximately 20 Tg of SO_2 were emitted into the stratosphere (Bluth et al., 1992). The eruption led to a reduction in Earth global surface temperature of 0.4 °C in the year following the eruption and 0.25°C the next year. As a result of the absorption of volcanic aerosol the lower stratosphere showed a positive temperature anomaly of 1.5 °C at the same time.

Besides the described direct cooling effect of large volcanic eruptions, there is also an indirect climatic effect. Volcanic eruptions in tropical regions result in a rise in stratospheric temperature at low latitudes compared to high latitudes, leading to a stronger temperature gradient from pole to equator, especially during winter. This causes a more stable polar vortex in the Northern Hemisphere, resulting in stronger jet streams and a characteristic stationary wave pattern of the tropospheric circulation. This indirect effect on the global circulation is stronger than the direct radiative effects. This results in cooler summers and warmer winters at higher latitudes after large tropical volcanic eruptions, which have been observed in several cases (Robock and Mao, 1992, Graf et al., 1993, Kirchner et al., 1999).

Further, volcanic aerosols in the stratosphere serve as surfaces for heterogeneous chemical reactions that destroy ozone. Observations after the Pinatubo eruption showed mid-latitude ozone depletion related to this eruption (Solomon et al., 1996, Solomon et al., 1999). This effect opposes the stratospheric warming, because it lowers the ultraviolet absorption, but the net effect of volcanic aerosol in the lower

stratosphere is warming. The destruction of stratospheric ozone after large volcanic eruptions depends on the presence of anthropogenic chlorine, therefore it has only become important in recent decades (Hofmann and Solomon, 1989, Brasseur and Granier, 1992). Due to the measures having been taken against CFC (chlorofluorocarbon) production in several international agreements, chlorine concentration in the stratosphere is decreasing and the effect of eruptions on O_3 is likely to decrease in the future. Further, volcanic eruptions can directly lead to the destruction of stratospheric ozone through the input of halogens into the stratosphere.
Besides the total amount of sulfur emitted into the stratosphere, several parameters determine the climatic influence of a volcanic eruption. The total amount of sulfur, mainly SO_2, which is brought into the stratosphere plays a key role. There are however several other important parameters, especially the latitude of the volcano.

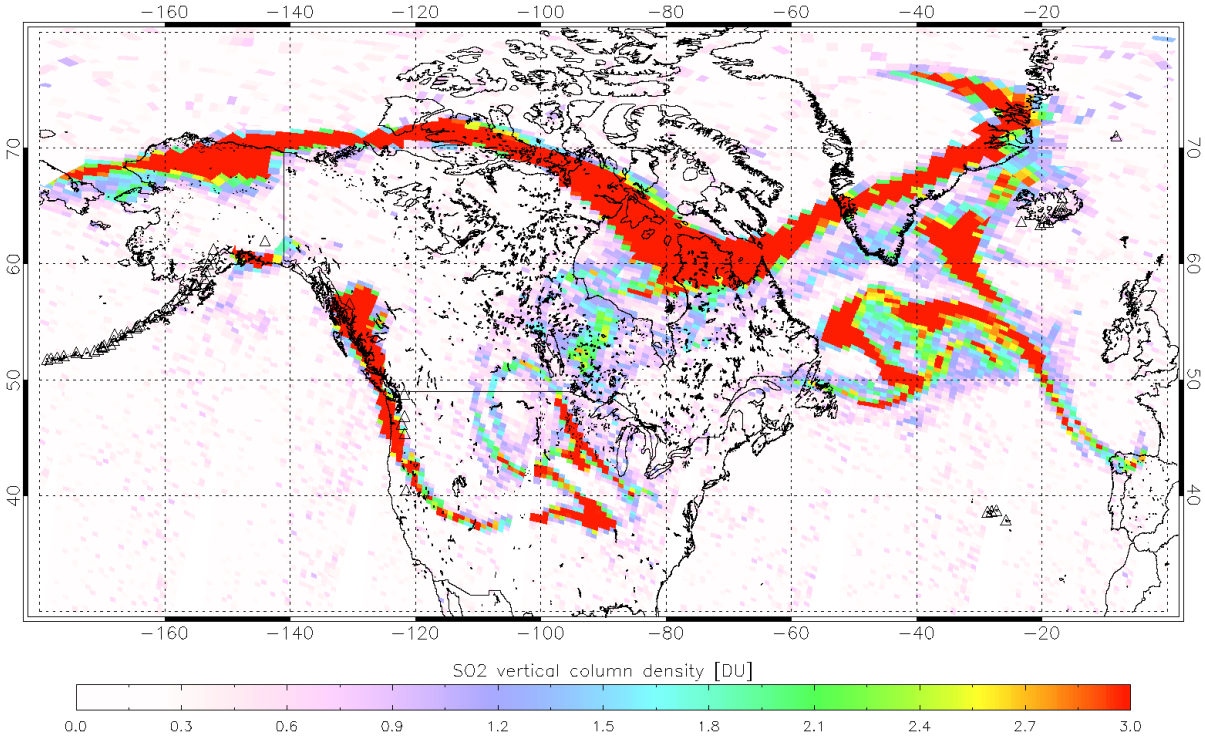

Figure 2.4: Volcanic SO_2 cloud on 14 August 2008 one week after the eruption of Kasatochi volcano, Alaska, measured by GOME-2. The eruption emitted > 1.5 Tg of SO_2.

Volcanic eruptions in the tropics have a much higher impact on climate than those at higher latitudes. Due to the global circulation patterns, aerosol from tropic eruptions can cause global or at least hemispheric effects, whereas aerosol from high latitude eruption is rarely distributed south of 30° N (Stothers, 1996). Also the residence time of volcanic aerosol is much shorter for high latitude eruptions compared to tropical eruptions due to large scale subsidence in polar winter that removes the volcanic sulfate aerosol from the stratosphere (Hamill et al., 1997). Model calculations have shown, that the e-folding lifetime of sulfate aerosols at high latitudes is approximately 4 months in summer and 2 months in winter (Robock et al., 2008) compared to an average of 1 year in the tropics (Gao et al, 2007). A further important parameter in estimating the climate impact of volcanic eruptions, especially for high latitude eruptions, is the time of the year when the eruption occurs (Kravitz and Robock, 2010). As most of the effects are due to radiative processes, eruptions occurring in spring have a much higher impact on global temperatures than eruptions occurring

during other seasons, as the maximum aerosol loading can be detected several months after the eruption and the reduction of radiation has a much higher impact during the summer. Due to these effects, the recent high latitude eruptions of Okmok and Kasatochi (Figure 2.4) in July and August 2008 had no measurable impact on temperature even though together they injected significant amounts of SO_2, estimates range from around 1 Tg to over 3 Tg, into the stratosphere (Kravitz et al., 2010).

2.3.2 Volcanic SO_2 emissions in the troposphere

The effect of volcanic emissions from non-eruptive degassing or minor eruptions with gas input only in the troposphere is different from the major eruptions that can have a significant effect on climate. The influence of SO_2 emitted at lower altitudes on the atmospheric composition is confined to a more local area, due to the much shorter lifetime of SO_2 and other sulfur species in the troposphere. In the oxidizing environment all emitted sulfur species are converted to sulfate eventually. The oxidation of SO_2 in the gaseous phase with OH via H_2SO_4 (2.1-2.3) is however occurring on the timescale of several weeks (Blitz et al., 2003). If taken up by particles SO_2 is oxidized much more efficiently through reactions with e.g. O_3, H_2O_2, HOC or HOBr (Seinfeld and Pandis, 2006) which results in a reduction of the atmospheric lifetime from weeks to days. Most sulfur of volcanic origin is emitted as SO_2. Other sulfur species emitted by volcanoes such as H_2S and CS_2 are eventually oxidized to SO_2 through reactions with OH. As the number of volcanic eruptions as well as their strength varies considerably from year to year, total estimates of the annual sulfur fluxes show a high variability. Although volcanoes are only responsible for 10 % of the total sulfur flux, its contribution to the total atmospheric SO_2 burden and their radiative effect could be much higher than the total amount compared with anthropogenic sources suggest (Graf et al., 1997). Most anthropogenic emissions take place in the PBL, whereas most volcanoes emit the SO_2 in the free troposphere, where the lifetime of sulfur species is considerably longer and can therefore have a stronger influence on climate.

When emitted in the troposphere, SO_2 has two major effects influencing the local environment, one is the conversion of SO_2 to sulfuric acid and the later deposition as acid rain, the other is that sulfate aerosol acts as cloud condensation nuclei (CCN). Acid rain is a very common phenomenon in the vicinity of active volcanoes. At Kilauea volcano (Hawaii) pH of 3 was measured in rain water 800 meters downwind of the volcano due to passive degassing (Harding and Miller, 1982). This acid rain can cause immediate health risks to humans and animals and damages the vegetation (Delmelle et al., 2002).

When the SO_2 is emitted into the troposphere and converted to sulfate an indirect effect dominates the climatic influence. Sulfate acts as CCN, therefore volcanic eruptions can enhance the number of CCN in a certain area. The number and size of the CCN determine its scattering parameters, especially the single scattering albedo. Sulfate aerosols from volcanic eruptions provide additional CCN, that reduce the average particle size, which enhances the single scattering albedo and more radiation is backscattered. At the same time, the lifetime of the cloud is increased, as it also depends on the particle size. An example of this effect has been observed during the eruption of Mt. Michaels in the South Atlantic Ocean 2006 (Gasso, 2008), where inside the volcanic eruption plume a reduced size of the cloud droplets has been observed.

2.3.3 Risk assessment for volcanic activity

As described above, SO_2 is often used as an indicator for volcanic activity. Volcanic gas emission rates are closely related to magmatic supply and transport processes, therefore gas fluxes vary over time and can provide information on dynamic processes responsible for volcanic degassing (Stevenson and Blake, 1998). It has been shown that variations on the order of months or years are often related to magma intrusion and volatile depletion by degassing (Ripepe et al., 2002, Badalamenti et al., 2004). Higher frequency variations are typically caused by processes occurring near the surface (Lautze et al., 2004).
SO_2 emissions fluxes can also be an indicator for lava effusion rates (Delgado Granados et al., 2001, Sutton et al., 2001), but degassing often occurs without lava reaching the surface. Volatiles are released from magma whenever the concentration exceeds solubility, which is a function mainly of pressure and temperature. Therefore gas emissions can indicate magma being displaced to shallower levels and lower pressure, which causes a decrease in solubility. The composition of the degassed magma can provide insight into the depth at which the processes are occurring as the different gases have typical pressures at which they become oversaturated. For example, sulfur exsolves earlier than chlorine (Métrich et al., 2004) during magma ascend.
Volcanic degassing in some cases has been shown to have a periodic character (Watson et al., 2000, Fischer et al., 2002, Sweeney et al., 2008) making it possible to use the SO_2 gas flux measurements in attempting to forecast possible eruptions. There are some cases in which the SO_2 fluxes have indicated the onset of a volcanic crisis. Increases in SO_2 emissions have been reported before eruptions of Mount Etna (Malinconico, 1979) and at Santa Anna volcano in El Salvador. SO_2 fluxes increased from several hundred to several thousand tons per day before the eruption in 2005 (Olmos et al., 2007). This simple relationship only holds true in case of an open vent system, most volcanic systems are more complex. When gas passes through fractures in the volcanic edifice, many other reactions can influence the gas emissions. Here increasing SO_2 emissions rates can indicate magma supply from depth (Edmonds et al., 2003) as well as formation of cracks in the ceiling of the magma chamber (Stoiber et al., 1983).
The complexity of most volcanic systems makes it almost impossible to understand the ongoing processes by using just a single monitoring technique. Therefore a multi-disciplinary approach has to be used, which is coupled with numerical modeling to infer from the observations the processes occurring at depth. Measurements of gas fluxes at volcanoes however, contribute greatly to improving the prediction of future eruptions.

2.4 Atmospheric sulfur dioxide measurements

It has long been recognized that atmospheric SO_2 is one of the dominant precursors of acid rain and that industrial emissions of SO_2 are responsible for acidic “London Type” smog. First reports of this type of smog that contains mainly soot particles and aerosols consisting of sulfuric acid date back to the 19th century (Brimblecombe and Heymann, 1998). At the beginning of the 1970s, first air quality standards for SO_2 were set in the United States and a monitoring network for air quality was established. For continuous air quality monitoring, mainly in situ measurements have been used that analyze the air composition directly at the instrument.

Besides in situ measurements of SO_2, a variety of remote sensing instruments is being used to measure atmospheric SO_2. These remote observations have proven extremely useful for situations where the direct sampling of air is difficult or even dangerous, e.g. during volcanic emissions. Volcanic gas emissions have been collected and analyzed as far back as 1790 (Morello, 1998), but only since the development of remote sensing instruments continuous monitoring of volcanic gas emissions became possible.
In this section, the most common instruments for monitoring atmospheric SO_2 are introduced. First in situ observations are explained followed by an introduction of ground-based remote sensing methods focusing on the application in volcanic gas monitoring. In the second part satellite observations of SO_2 are discussed.

2.4.1 Ground-based measurements

In situ measurements
In situ measurements of atmospheric trace gases, where the air is analyzed directly inside the measurement device, have a long tradition (Brasseur et al., 1999). For in situ measurements two different techniques can be used. One possibility is to have the instrument at the place of interest and directly analyze the ambient air. In this case, the air is typically advected into the instrument by a vacuum and the composition is determined. The main advantage of this method is that chemical reactions that may change the composition after a certain time do not play an important role. Furthermore, this method provides the possibility for continuous sampling and long term monitoring of atmospheric composition. The second possibility is to sample the air at the place of interest and analyze it later in a laboratory. As this implies several difficulties, e.g. chemical reactions within the sample can change the composition, this method is mainly used if continuous sampling is difficult, e.g. at volcanoes, or if only a limited number of samples is necessary. The principles for analyzing the sampled air are described below.

Resonance fluorescence
For resonance fluorescence measurements, the gas molecules are excited using electromagnetic radiation. For that purpose, a beam of photons is produced that corresponds in wavelength to an electronic transition from the ground state of the gas to be observed. The molecules absorb photons and reemit them in all directions. Photons can be scattered elastically by all molecules (Rayleigh scattering) and resonantly. The Rayleigh signal can be removed by measuring a sample not containing the gas of interest. The fluorescence intensity is linearly proportional to the gas mixing ratio. This measurement technique has for example been used for aircraft measurements of SO_2 in volcanic plumes (Schumann et al., 2010).

Chemiluminescence
During chemiluminescent reactions a molecule emits light during the transition from an excited electronic or vibrational state. A fairly simple example is the chemiluminescent detection of nitric oxide through the reaction with ozone.

$$O_3 + NO \longrightarrow NO_2^* + O_2 \tag{2.6}$$

$$NO_2^* \longrightarrow NO_2 + h\nu \tag{2.7}$$

The * denotes the molecule in an electronically excited state. During the transition to the ground state, the molecule emits a photon that can be detected. Chemiluminescence is also used for the detection of SO_2, but the chemical reactions during the detection of SO_2 are fairly complex (e.g. Zhang et al., 1985). The main advantage of this technique is the high sensitivity to SO_2, the detection limit has been shown to be around 10 pptv SO_2 (Meixner and Jaeschke, 1981).

Spectroscopic measurements

Spectroscopic measurements are widely applied in determining atmospheric constituents. They are based on the fact that different chemical components absorb electromagnetic radiation at specific wavelengths. The absorption pattern is unique for the chemical component and the absorption intensity depends on the absorber amount. The technique is used for in situ as well as remote sensing measurements. Spectroscopic instruments work at a wide range of different wavelength, from UV to radio waves. Spectroscopic measurements are commonly used for SO_2 observations. SO_2 measurements can be carried out in the UV, as SO_2 shows distinct absorption structures below 320 nm and in the IR, where SO_2 has absorption bands at 1360 cm^{-1}, 1150 cm^{-1} and 517 cm^{-1}. Examples of spectroscopic instruments for SO_2 detection are DOAS instruments for measurements in the UV wavelength range or Fourier Transform Infrared (FTIR) spectrometers measuring in the IR. As both instruments are also used for remote sensing measurements they are introduced in more detail in the next section.

Remote sensing measurements

The characteristic property of remote sensing is that the measurement location is different from the location of the instrument. Remote sensing instruments measure radiation and from these measurements the atmospheric characteristics can be inferred. Remote sensing of atmospheric trace gases has been applied since the development of the Dobson spectrophotometer in the 1920s (Dobson, 1968). The main advantage of remote sensing measurements is that the instrument can be located at a distance from the area that is observed, allowing for example measurements of the gas composition in volcanic eruption plumes or of stratospheric ozone. However, compared to in situ measurements they often provide a limited sensitivity to trace gases and the atmospheric conditions can influence the measurement significantly.

Dobson/Brewer

The Dobson spectrometer was developed in the 1920s to measure ozone. A global network of Dobson instruments was established in the 1960s. The measurement principle is based on the differential absorption of solar light by ozone. The intensity of the solar light arriving at the Earth's surface is measured at two wavelengths in the UV that are strongly and weakly absorbed by ozone and compared. Through the ozone absorption spectrum and the instrument calibration, the ozone content of the atmosphere can be determined. The Brewer spectrometer is the successor of the Dobson spectrometer and was developed in the 1970s. It uses the same principle but measures the radiation intensity at a number of different wavelengths. The inclusion of more wavelengths made it possible to use the Brewer spectrometer for the determination of atmospheric SO_2 (Bais et al., 1993, Fioletov et al., 1998) which also shows strong absorption features in the UV wavelength range. Measurements using a Brewer spectrometer are described in more detail in Chapter 5.3.3.

COSPEC/ FLYSPEC

The correlation spectrometer (COSPEC) was originally designed in the late 1960s to monitor industrial SO_2 and NO_2 emissions (Millan et al., 1969, Davies, 1970). It was first used to monitor volcanic SO_2 emissions in 1971 (Okita, 1971). Since then, COSPEC SO_2 measurements have been applied at more than 70 volcanoes worldwide (Andres and Kasgnoc, 1998) and it has been the primary method for monitoring volcanic SO_2 emissions for about three decades. The COSPEC instrument scans the volcanic plume while it allows specific wavelengths of solar UV light between 300 nm and 316 nm to pass to the signal processing electronics. The instrument measures wavelengths that are located on and off the SO_2 absorption features. The difference in signal is related to the amount of SO_2 in the volcanic plume through internal instrument calibration standards. Through the scanning process, the cross-sectional concentration of SO_2 in the plume is determined. Through multiplication with the plume velocity the SO_2 flux is determined.

Recently, COSPEC instruments have been started to be replaced by smaller, lightweight and low-cost UV spectrometers. The UV correlation spectrometer FLYSPEC is the successor of the COSPEC instrument (Horton et al., 2005). It operates in a similar way with an in situ correlation spectroscopy calibration system. Two SO_2 cells of known concentration can be inserted into the light path of the instrument for calibration. The instrument was named FLYSPEC for its small size which is very convenient for monitoring volcanic plumes. A more detailed description of the FLYSPEC instrument will be provided in Chapter 5.3.2.

FTIR

The Fourier Transform Infrared (FTIR) spectrometer uses measurements with infrared light and has been used in ground-based remote sensing of the atmosphere for several decades (Delbouille, 1993). The measurement principle is the absorption of radiation at different wavelengths by the gases to be analyzed. The FTIR is capable of analyzing several gases simultaneously. It can either be used as a remote sensing instrument (open path) or as an in situ instrument (closed path). The open path method uses an optical telescope to aim the FTIR at a target gas in the distance. The infrared light source can be natural solar radiation or radiation from a heated object behind the target gas. For the closed path method, the gas is delivered to a gas cell within the FTIR. As SO_2 shows strong absorption in the infrared, FTIR instruments can be used for measurements of atmospheric SO_2. They are frequently used to monitor volcanic SO_2 emissions, e.g. at Kilauea, Hawaii.

DOAS instruments

The DOAS principle (Platt, 1979) is applied in a wide range of measurement setups and instruments. The main classification of DOAS instruments is according to their light source; techniques using artificial light are named active DOAS, those relying on natural light sources such as solar or lunar light are termed passive DOAS. Both instrument types are based on the principle that the light detected at the instrument has traversed the atmosphere and shows trace gas absorption structures. A detailed description of the DOAS principle is given in Chapter 3.

Active DOAS instruments are mainly used where a high sensitivity (low detection limit) is required. They offer a high flexibility concerning light path length and spectral range. Active DOAS systems have the advantage of being independent of daylight and they can operate at a wide spectral range, but they require a very sophisticated optical system and regular maintenance. Therefore, they are not suitable for

observations in remote locations, e.g. observations of volcanic plumes. Active DOAS is often used for monitoring air pollution, especially for long-term observations.
The original design for an active DOAS system consists of a receiving telescope pointing at a light source. The alignment of the optical elements at either end of the light path and the necessity for power supply at both locations can be challenging. An advanced version of this basic design uses a reflector to return light from a source located next to the spectrometer. The total light path is enhanced to twice the distance between light source/detector and reflector.

Passive DOAS measurements are widely used where automated operation and a simple measurement setup are required, e.g. in remote locations, where instrument maintenance and power supply are difficult. The most common light sources used with passive DOAS measurements are the sun and the moon, in principle it is also possible to use starlight. When using the moon or stars as a light source only direct light can be used due to the low intensity of the radiation. In case of sunlight scattered light can be used additionally. The different techniques are termed direct and scattered light measurements. Scattered light DOAS measurements where first applied by Sanders et al. (1993) for observations of OClO over Antarctica.
Scattered sunlight measurements offer a wider variety of applications compared to direct light measurements. The “Off-Axis” geometry enhances the sensitivity for lower atmospheric trace gas layers, as the tropospheric absorption is increased for the off-axis measurements while the stratospheric absorption is comparable to the zenith observation. Multi-axis DOAS (Max-DOAS) uses multiple telescope angles to derive vertical profiles of atmospheric trace gases. A high sensitivity for absorbers close to the ground can be achieved by a low telescope elevation, for this measurement setup the light has a significantly longer path through the lower atmosphere compared to higher telescope elevations.
In recent years, Max-DOAS instruments have started to replace the COSPEC instruments for observations of volcanic plumes (Galle et al., 2010). The first flux observations of volcanic gas emissions using a mini Max-DOAS were made in Nicaragua in 2001 (Galle et al., 2003). Observations using a Max-DOAS instrument will be described in Chapter 5.3.1.
Another DOAS instrument that has been used for volcanic plume observations is the Imaging DOAS (Borowski, 2005). This instrument measures at several elevation angles simultaneously and allows a 2-dimensional observation of volcanic plumes.
DOAS instruments have been deployed on a variety of platforms including airplanes, balloons and satellites.

2.4.2 Satellite measurements

Satellite-based instruments operating in the ultraviolet (UV) spectral region have played an important role in monitoring and quantifying global SO_2 emissions. The Total Ozone Mapping Spectrometer (TOMS) was the first satellite instrument to detect volcanic SO_2 released during the El Chichon eruption in 1982 (Krueger, 1983). The detection sensitivity for SO_2 was limited to large SO_2 amounts due to the discrete wavelengths that were designed for ozone measurements (Gurevich and Krueger, 1997). The detection limit to measure volcanic and anthropogenic SO_2 greatly improved with the Global Ozone Monitoring Experiment (GOME) (Burrows et al., 1999), launched in 1995 onboard the ERS-2 satellite and the Scanning Imaging Spectrometer for Atmospheric Cartography (SCIAMACHY) (Bovensmann et al.,

1999), launched in 2002 onboard the ENVISAT satellite. These instruments provide contiguous wavelength coverage but have a fairly poor spatial coverage. They need several days for the acquisition of a contiguous global map and may, therefore, miss smaller short-lived volcanic events. The contiguous wavelength coverage of these instruments made it possible to use the differential optical absorption spectroscopy method (DOAS) (Platt, 1994) from space. The newest UV satellite sensors OMI (Ozone Monitoring Instrument) (Levelt et al., 2006) on EOS-AURA since 2004 and GOME-2 (see Section 3.5.1) on MetOp-A since 2006 make it possible to monitor volcanic activity and eruptions as well as anthropogenic SO_2 pollution on a global scale and daily basis. MetOp-A, unlike the research satellites ENVISAT or AURA, is an operational satellite. Therefore, GOME-2 will provide a long and contiguous time series of atmospheric trace gas measurements as two identical instruments are to follow on future satellites. MetOp-B and MetOp-C are planned to be launched in 2012 and 2016.
Volcanic SO_2 has been retrieved from satellite UV measurements using the DOAS method (and other multi spectral techniques) very successfully (Eisinger and Burrows, 1998, Thomas et al., 2005, Khokar et al., 2005, Loyola et al, 2008).

Thermal infrared sounders, such as the Atmospheric Infrared Sounder (AIRS) (Aumann et al., 2003) on EOS-AQUA (launched in 2002) and the Tropospheric Emission Spectrometer (TES), onboard EOS-AURA, have demonstrated their ability to provide an alternative in monitoring volcanic plumes from space (Carn et al, 2005, Clerbaux et al, 2008). The Infrared Atmospheric Sounding Interferometer (IASI) (Clerbaux et al., 2009) on MetOp-A is also able to detect SO_2 with an excellent global coverage in combination with small footprints (Clarisse et al., 2008). These infrared sounders provide additional nightly measurements, as well as plume altitude estimation. However, they provide a limited sensitivity to SO_2 in the lower troposphere.

The main advantage that satellite measurements provide over ground-based observations is their global coverage. They provide a daily picture of the global SO_2 emissions and make it possible to trace volcanic eruption clouds that can be hazardous to aircraft or locate areas of high pollution. Global coverage is of great advantage for monitoring volcanic activity as only very few volcanoes worldwide have an extensive ground based monitoring network. Especially for remotely located volcanoes, satellites are often the only source that provides regular information on volcanic gas emissions. With their contiguous time series, satellites also make it possible to detect trends in SO_2 pollution or changes in volcanic degassing behavior, which can be an indicator for the onset of volcanic unrest.
However, a limitation of satellite observations is the relatively coarse spatial resolution. This can make it difficult to attribute the measured emissions to a specific source, e.g. a certain volcano, if several emission sources are located close to each other. Furthermore, satellite instruments provide only one, or in case of the infrared sensors, two measurements a day. They can only provide a daily snapshot and can sometimes miss short-lived volcanic events or short-term changes in SO_2 emissions. A combination of several different instruments can improve the spatial coverage.
Both the UV-VIS and infrared satellite instruments show a reduced sensitivity for SO_2 in the lower troposphere. In the case of the UV instruments the sensitivity is a function of optical depth, that depends for example on parameters like ozone and SO_2 absorption, Rayleigh scattering and albedo, for infrared sensors the water vapor absorption limits the ability to detect SO_2 at low altitudes. In the presence of clouds,

the SO_2 below the clouds is shielded from view and cannot be detected. Generally the SO_2 detection limit for satellite instruments is higher than for ground-based instruments, especially in the lower troposphere.

2.5 Summary

In this chapter atmospheric sulfur dioxide and its relevance for atmospheric and climatic processes has been discussed. First sulfur compounds and the atmospheric sulfur cycle have been presented and the sinks and sources of SO_2 have been discussed with special focus on volcanoes as the most important natural source of SO_2. The climatic influence of volcanic SO_2 emitted in the stratosphere is explained followed by the influence on atmospheric processes of volcanic SO_2 emitted at tropospheric heights. Further the use of volcanic SO_2 emission measurements in risk assessment of volcanic activity has been described.
In the last section different in-situ and remote sensing measurement techniques that are used for monitoring volcanic SO_2 measurements have been presented and a short overview of SO_2 measurements using satellite instruments has been given explaining advantages and disadvantages of satellite observations.

3. Atmospheric sulfur dioxide retrieval for GOME-2 using the DOAS method

This chapter addresses the retrieval of atmospheric sulfur dioxide (SO_2) from the GOME-2 satellite instrument using the differential optical absorption spectroscopy (DOAS) method. First the GOME-2 instrument and the operational data processing are introduced. Then a comprehensive description of the SO_2 retrieval algorithm for the GOME-2 instrument is given, where the DOAS retrieval of SO_2, with specific settings, slant column corrections and determination of the vertical column densities is discussed in detail.

3.1 The GOME-2 instrument

The Second Global Ozone Monitoring Experiment (GOME-2) on MetOp-A is an improved version of the GOME instrument on the ERS-2 satellite (Callies et al., 2000, Munro et al., 2006). The satellite MetOp-A has been launched in October 2006 and is part of the EUMETSAT polar system (EPS). The calibrated and geolocated level-1 irradiances (Figure 3.1) and trace gas level-2 data from the GOME-2 instrument are available since January 2007. MetOp-A is in a sun-synchronous orbit with an equator crossing time in the descending node of 09:30 local time and a repeat cycle of 29 days. GOME-2 continues the long term data record of atmospheric trace gases, e.g. ozone and SO_2, that has been started by GOME on ESA ERS-2 launched in 1995 and SCIAMACHY on ESA ENVISAT launched in 2002. The MetOp-A satellite is the first in a series of three identical satellites that will extend the long-term data series until 2020. GOME-2 is an across-track nadir-scanning UV-VIS spectrometer with four main optical channels, covering a spectral range from 240 – 790 nm with a spectral (FWHM) resolution between 0.26 nm and 0.51 nm. To provide a good spectral resolution for the complete wavelength range and to ensure a proper stray light level in channel 1 and 2, the instrument is set up as a double spectrometer. GOME-2 measures the back-scattered radiation from the earth-atmosphere system. In addition, a direct sun spectrum is recorded once a day via a diffuser plate. Further, two polarization components are measured at 30 broad-band channels covering the complete spectral range with Polarization Measurement Devices (PMDs). The light is directed into the telescope by a scan mirror, which can also be pointed at two internal calibration light sources and at the Sun diffuser. An off-axis parabolic mirror collimates the light onto the Double Brewster/pre-disperser prism configuration for generating the s- and p-polarized light beam for the PMD and to produce the pre-dispersion for the main spectrometer. The beam is focused onto the channel separator prism. The band separator is a quartz prism, the first surface is partially coated with a transmission coating for channel 1 and with a reflective coating for channel 2. The light for channel 3 and 4 passes the prism edge and is separated into the two channels by a diachronic filter. The four channels consist of a collimating off-axis parabolic mirror, a grating and a focusing objective that images the spectrum on the detector.

The default swath width of 1920 km allows global coverage at the equator in 1.5 days and results in several observations a day at higher latitudes. While the along-track dimension of the ground pixel size is constant (~ 40 km), the across-track dimension depends on the integration time. The size of the instantaneous field of view is 80 km

x 40 km (across-track x along-track), for the 1920 km swath and default integration time of 187.5 ms.

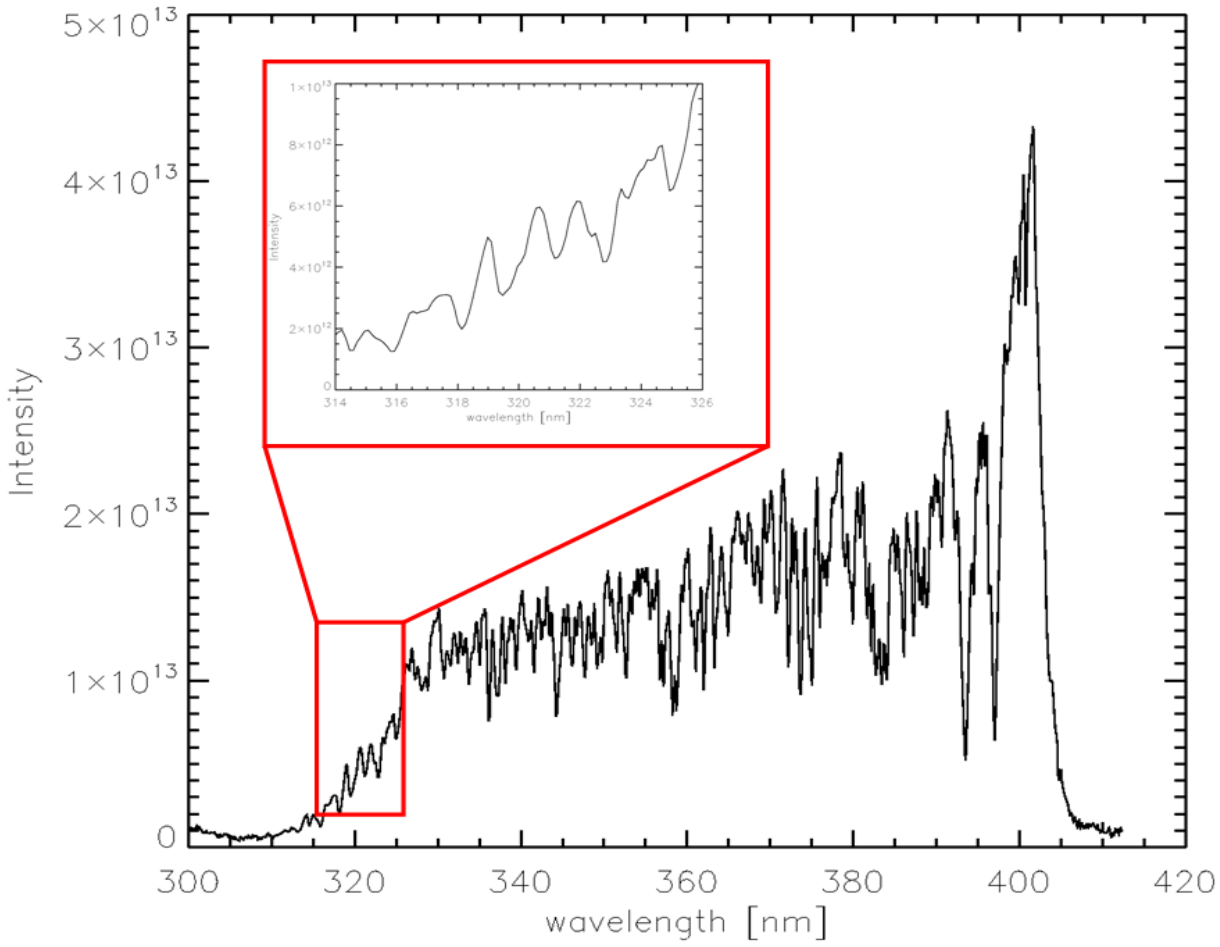

Figure 3.1: GOME-2 channel 2 Level-1 radiance spectrum from Kasatochi eruption 8 August 2008, the enlargement shows the wavelength region used for the SO_2 retrieval (315-326 nm).

3.2 Operational SO_2 processing

The operational GOME-2 total column SO_2 product is provided by the German Aerospace Center (DLR) in the framework of EUMETSAT's Satellite Application Facility on Ozone and Atmospheric Chemistry Monitoring (O3M-SAF). The focus of the O3M-SAF is to process, archive, validate and disseminate atmospheric data products of ozone, various trace gases, aerosols and surface ultraviolet radiation. The first step in the processing chain is the production of calibrated and geolocated level 1 radiances (Level 0-to-1 processing), which is performed at EUMETSAT in the Core Ground Segment (CGS). The level 1 products are delivered to DLR and other users via the EUMETCast broadcast system approximately 1:45 h after sensing in data chunks containing 3 minutes of measurements (PDUs). The DLR multi-mission payload ground segment system (Heinen et al., 2009) controls the reception, processing, archiving, ordering and dissemination of the GOME-2 trace gas products. The operational level 1-to-2 processing of the PDUs is then performed at DLR with UPAS (Universal Processor for Atmospheric Spectrometers), a new generation system for the processing of operational trace gas and cloud property products in near-real time and off-line (Livschitz and Loyola, 2003). UPAS takes level 1 irradiances from different sensors as input. The SO_2 total column information is

derived using a DOAS approach, which is easily applicable in operational processing and allows near-real time retrieval of SO_2 information. The ground-segment at DLR needs less than 15 min for acquiring the input data, retrieving the trace gas total columns and disseminating the resulting products, which means the level 2 near-real time SO_2 products are delivered via EUMETCast, WMO/GTS and the Internet to the end-users approximately 2:00 hours after sensing. In addition, DLR provides offline and reprocessed GOME-2 Level-2 products on an orbital basis. The German National Remote Sensing Data Library stores the GOME-2 SO_2 data for enabling the long-term monitoring of global change, and data reprocessing (http://wdc.dlr.de/sensors/gome2) (Loyola et al., 2008).

3.3 DOAS slant column retrieval of SO_2

The SO_2 slant column retrieval for GOME-2 is based on the Differential Optical Absorption Spectroscopy (DOAS) method (Platt, 1994). With this approach, atmospheric trace gas columns are determined using their absorption in the UV (and visible) wavelength range.

3.3.1 The DOAS principle

Absorption of electromagnetic radiation by matter is expressed by the Lambert-Beer law, the intensity I of the radiation in case of homogeneous absorption decreases exponentially with the light path L

$$I(\lambda) = I_0(\lambda) e^{-L\rho\sigma(\lambda)} \tag{3.1}$$

where $I_0(\lambda)$ denotes the initial intensity of the light beam, λ the wavelength, ρ the particle density of the absorber and σ(λ) its absorption cross-section. The absorption cross-section is unique for all absorbers. The absorption cross-sections are dependent on temperature and pressure, which results in a variation of the cross-sections along the light path. For atmospheric absorption more than one absorber has to be taken into account, with the number of absorbers being J the Lambert-Beer law can be rewritten as follows:

$$I(\lambda) = I_0(\lambda) \exp\left\{ -\int \sum_{j=1}^{J} \rho_j(l)\sigma_j(\lambda,l) + \varepsilon_M(\lambda,l) + \varepsilon_R(\lambda,l) dl \right\} \tag{3.2}$$

For each gas j, σ_j denotes the absorption cross-section and ρ_j is the particle concentration at the position l along the light path. The integral is taken along the light path through the atmosphere and is dependent on wavelength, solar zenith angle and viewing geometry. Rayleigh- and Mie-scattering are described by the extinction coefficients ε_R and ε_M, respectively.

When determining trace gases in atmospheric measurements the Rayleigh scattering on air molecules and Mie scattering of aerosols is treated analogously to the absorption as a weakening of the light beam. This can be expressed by the Lambert-Beer law by using scattering cross-sections (σ_{Ray} and σ_{Mie}) instead of the absorption cross-sections.

$$I(\lambda) = I_0(\lambda)\exp\left\{-\int\sum_{j=1}^{J}\rho_j(l)\sigma_j(\lambda,l) + \rho_{Ray}(l)\sigma_{Ray}(\lambda,l) + \rho_{Mie}(l)\sigma_{Mie}(\lambda,l)dl\right\} \quad (3.3)$$

If the pressure and temperature dependence of the absorption cross-sections is neglected, the equation can be simplified further. The cross-sections are then independent of the light path and can be drawn in front of the integral. The line integral over the particle density can be replaced by the slant column density S_j of the absorber.

$$S_j = \int_{l=0}^{L}\rho_j(l)dl \quad (3.4)$$

Equation 3.3 can then be rewritten as follows

$$I(\lambda) = I_0(\lambda)\exp\left\{-\sum_j \sigma_j(\lambda)S_j - \sigma_{Ray}(\lambda)S_{Ray} - \sigma_{Mie}(\lambda)S_{Mie}\right\} \quad (3.5)$$

The equation cannot be used to determine the slant columns directly as the contributions from the different processes cannot be separated in this form. Therefore the basic idea of DOAS is to separate the narrow band absorption of the trace gases σ' from the other broad band contributions σ_B (Figure 3.2).

$$\sigma(\lambda) := \sigma'(\lambda) + \sigma_B(\lambda) \quad (3.6)$$

where σ' is called the differential absorption cross-section. The separation of the differential and broadband features can be achieved by subtraction of a low order polynomial. The broad band contributions can be combined with Rayleigh- and Mie-scattering as these can both be approximately represented by a Polynomial ($\sigma_{Ray} \sim \lambda^4$, $\sigma_{Mie} \sim \lambda^{-\kappa}$, with κ=0,...,2).

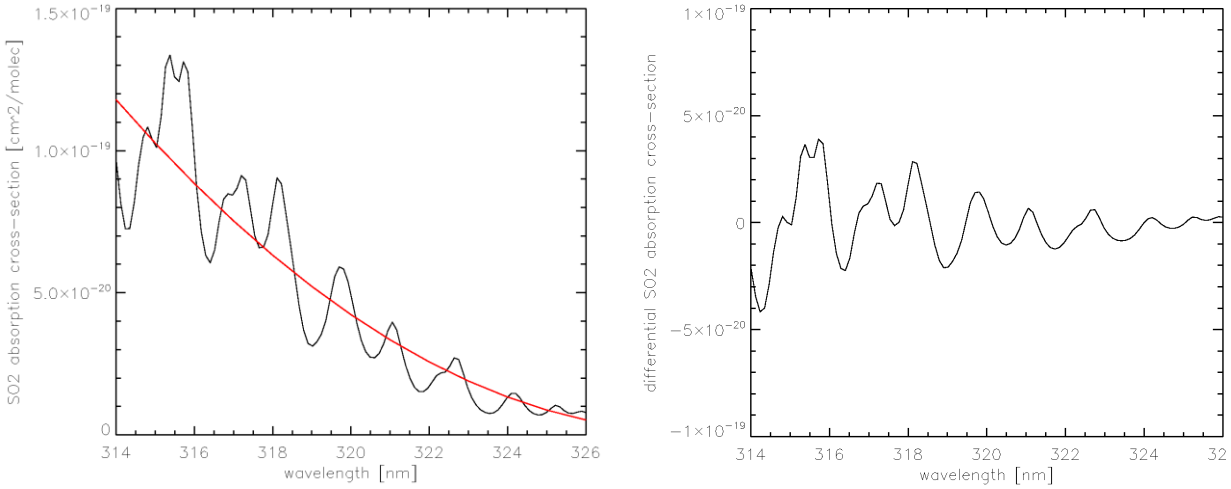

Figure 3.2: The SO_2 absorption cross-section (left) is converted to the differential SO_2 absorption cross-section (right) by subtraction of a low order polynomial.

$$I(\lambda) = I_0(\lambda)\exp\left\{-\sum_j \sigma'_j(\lambda)S_j + \sum_p a_p\lambda^p\right\} \quad (3.7)$$

The separation into differential and broad band absorption features is only possible if the absorption cross-section has highly structured features in the wavelength region used for the retrieval, otherwise the absorption cannot be separated from contributions by scattering.

For data evaluation, the logarithm of the measured spectrum is used

$$\ln I(\lambda) = \ln I_0(\lambda) - \sum_j \sigma'_j(\lambda)S_j - \sum_p a_p\lambda^p \quad (3.8)$$

The slant column densities of the trace gases can now be determined together with the coefficients of the polynomial by using a linear least squares fit (Figure 3.3). For the retrieval of SO_2 columns from GOME-2 the UV wavelength region around 320 nm is used.

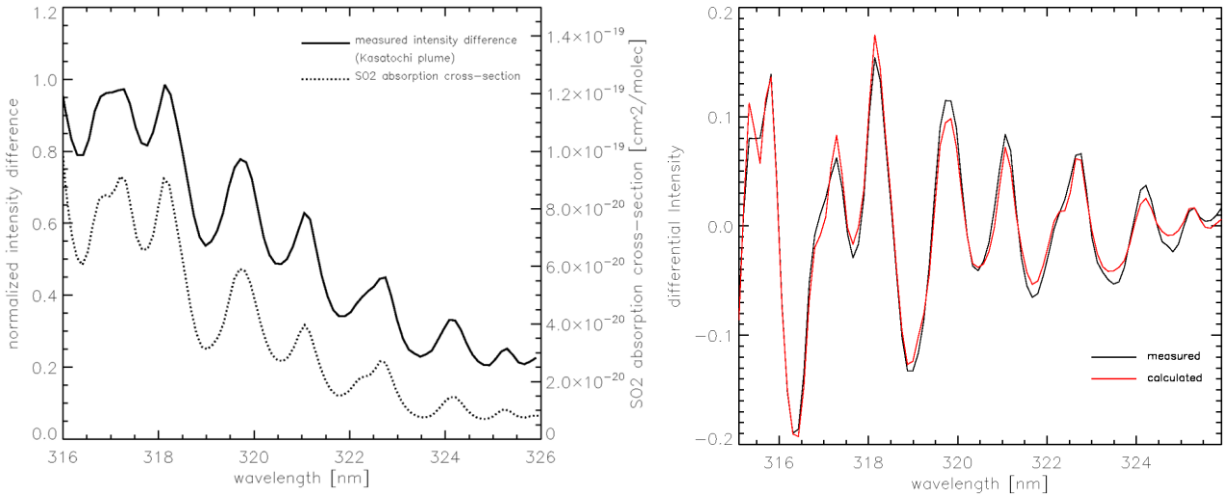

Figure 3.3: Normalized intensity difference $(\ln(I/I_0)_{\text{inside plume}}-\ln(I/I_0)_{\text{outside plume}})$ for the Kasatochi eruption on 8 August 2008, as measured by GOME-2 (solid line) illustrating the strong SO_2 absorption features used by the DOAS retrieval method (left) and DOAS SO_2 fit for the same measurement (right).

3.3.2 Spectra corrections

When applying the DOAS method to atmospheric radiation measurements, a suitable reference spectrum has to be chosen and the measurement spectra have to be corrected for effects due to wavelength calibration errors, instrument resolution and atmospheric processes. First the choice of a suitable reference spectrum I_0 is discussed followed by the corrections applied to correct for wavelength shift, I_0-effect and Ring effect.

Reference spectra

When using the DOAS technique for in situ measurements a reference spectrum I_0 can be obtained easily by removing the trace gas from the light path. For atmospheric remote sensing measurements this is not possible, making the choice of a suitable reference spectrum I_0 more difficult. For satellite measurements of SO_2 there are two commonly used possibilities.

Direct sun spectrum:
As opposed to ground based instruments, satellites offer the possibility to measure a sun spectrum directly. This spectrum is completely free of atmospheric absorption structures and contains only the Fraunhofer lines. As it is measured with the same spectral resolution as the backscattered radiances no convolution with the instrument slit function is necessary.

Equatorial earthshine spectrum:
The second option is to use a backscatter radiance spectrum as reference. In this case, a measurement will be selected where it is assumed that the absorber of interest, e.g. SO_2, is not present. For determination of SO_2, usually a spectrum from a measurement over an unpolluted area away from possibly degassing volcanoes is chosen, typically over the equatorial region of the Pacific. The advantage of this type of reference spectrum is that atmospheric effects, for example ozone that can obstruct the retrieval of SO_2 may cancel out at least to some extent. However it can also cause additional problems if for some reason (e.g. volcanic eruption cloud), SO_2 is present in the reference measurement or if the atmospheric conditions in the case of the reference measurement differ significantly from those in the retrieval.

For the DOAS retrieval of SO_2 from GOME-2, a direct sun spectrum is used as reference. The direct sun spectrum is recorded by the GOME-2 instrument once a day.

Correction of Fraunhofer lines (wavelength shift)

As the solar spectrum is highly structured due to the absorption of the solar atmosphere resulting in the Fraunhofer lines, wavelength calibration issues in measured spectra and laboratory cross-sections can be a major source of error in DOAS retrievals (Aliwell et al, 2002). Ideally the solar structures would cancel between I_0 and I, but Doppler shift and calibration issues cause wavelength differences between measured spectra and cross-section that have to be accounted for. The important parameter for satellite DOAS applications is the relative alignment of the absorption cross-sections with respect to the measured spectra. This relative alignment can be derived from the DOAS fit itself with enough accuracy.

For the retrieval of SO_2 from GOME-2 the solar spectrum is used as wavelength reference. Shift and squeeze parameters are applied to each Earthshine wavelength grid in order to resample the Earthshine spectrum. Further, shift parameters are required for the cross-section wavelength grids to improve the wavelength registration against Level-1 spectra and to compensate for inaccuracies in the wavelength calibration of the cross-section data. It has been shown, that the fitting of such non-linear parameters on a pixel-by-pixel basis can lead to numerical instabilities, therefore an optimized pre-shift needs to be applied (Lambert et al., 2002).

Solar I_0 Effect

The GOME-2 spectrometer has a resolution of ~ 0.26 nm in the UV wavelength region. This spectral resolution is coarse compared to the very narrow absorption structures in the solar radiation. This leads to the fact that the Fraunhofer lines would

not be fully resolved even in the case of an ideal measurement. Absorption structures of trace gases can overlap with strong Fraunhofer lines. Because of the low resolution of the instrument a simple convolution of high resolution reference spectra with the instrument slit function leads to the so-called I_0-effect. It was named solar I_0-effect because it is caused by the narrow structures of the solar spectrum. A correction has to be implemented for the spectra and cross-sections that have been convolved with the instrument function. For satellite measurements only the absorption cross-sections have to be corrected. As the reference spectra are taken using the same instrument, they automatically have the same resolution as the measurements.

The correction for the GOME-2 SO_2 retrieved is calculated as follows (Aliwell et al., 2002):
A high resolution Fraunhofer spectrum I_0 (Kurucz et al., 1984) is convolved with the GOME-2 instrument slit function H (Siddans et al., 2006).

$$I_0^*(\lambda) = I_0(\lambda) * H \tag{3.9}$$

In a second step a synthetic spectrum is calculated using a high resolution absorption cross-section and a concentration typical for the trace gas of interest. The resulting absorption spectrum is also convolved with the instrument function.

$$I^*(\lambda) = \left(I_0(\lambda) \cdot e^{-\sigma \cdot S_0}\right) * H \tag{3.10}$$

with S_0 being a typical SO_2 slant column.
The I_0-corrected cross section σ* is then calculated as:

$$\sigma^* = \frac{1}{S_0} \cdot \ln\left(\frac{I_0^*(\lambda)}{I^*(\lambda)}\right) \tag{3.11}$$

For the retrieval of SO_2 only the ozone cross-section has been corrected for the I_0-effect, as tests have shown that the uncorrected SO_2 cross-section is no major source of error.

3.3.3 Ring effect

In 1962 Grainger and Ring (1962) discovered that the depth of the Fraunhofer structures decreases in scattered sunlight compared to direct sunlight. They observed a “filling in” of the lines, that is stronger for large solar zenith angles. This effect, which became known as “Ring Effect”, cannot be explained by Rayleigh- or Mie-scattering, as these result in a simple scaling of the spectrum but not in a change in line shape. The Ring effect is a result of inelastic scattering, during which the photons not only change direction but also wavelength through absorption or release of energy. The scattering processes responsible for this phenomenon have to cause a wavelength shift large enough to explain the filling broad line features of approximately 1 nm and a filling by several percent. Several studies (e.g. Fish and Jones, 1995; Joiner et al., 1995; Vountas et al., 1998, Sioris and Evans, 1999) have demonstrated that Rotational Raman scattering (RRS) by molecular O_2 and NO_2 is the process mainly responsible for the observed filling-in of absorption lines. A

photon reacting inelasticly with an air molecule excites a higher/lower rotational and/or vibrational level of the molecule.
The inelastic scattering of radiation does not only result in a filling in of the Fraunhofer lines, the same process is also responsible for a filling in of the trace gas absorption structures. This process is known as the molecular or telluric ring effect.

In DOAS applications a correct treatment of the Ring effect is important as the optical density changes caused by the Ring effect are on the order of a few percent. The atmospheric absorption structures used in DOAS evaluations can be more than an order of magnitude smaller than changes due to the Ring effect, therefore the Ring effect can seriously influence the fitting accuracy (Sioris and Evans, 1999)

The Ring effect in DOAS analysis is treated as a "pseudo absorber" by adding a Ring reference spectrum, R(λ), to Eq. (3.8) that is defined as the change in optical depth between intensities calculated with and without Raman scattering. A scaling parameter α_{Ring} to adjust the amplitude of the Ring spectrum is included in the fit.

$$\ln I(\lambda) = \ln I_0(\lambda) - \sum_j \sigma'_j(\lambda) S_j - \sum_p a_p \lambda^p - \alpha_{Ring} R(\lambda) \tag{3.12}$$

Ideally the calculated Ring spectrum relies on radiative transfer simulations of nadir radiances including and excluding Raman scattering. The Ring spectrum is calculated using realistic atmospheric parameters (ozone and SO_2 profile, clouds, satellite geometry, etc.) as

$$R(\lambda) = \ln\left(\frac{I_{total}(\lambda)}{I_{elastic}(\lambda)}\right) \tag{3.13}$$

However, due to the complexity of this approach in the operational GOME-2 SO_2 retrieval a simpler approximation for the Ring spectrum is used which can be obtained by convolution of the solar spectrum with Raman cross-sections (Chance and Spurr, 1997). For the GOME-2 SO_2 retrieval a second Ring spectrum is included to account for the molecular Ring effect which can be a major source of error when fitting minor trace gas species (van Roozendael et al., 2002).

3.3.4 DOAS settings for SO_2 slant column retrieval

The settings for the operational retrieval algorithm of GOME-2 SO_2 were tested using several combinations of SO_2 and ozone cross-sections and fitting windows. The settings listed here have been found to return good fitting results when retrieving SO_2 from GOME-2 measurements. The DOAS slant column fit of SO_2 is performed in the UV wavelength range between 315-326 nm (Thomas et al., 2005). A single SO_2 cross-section is included in the fit, the SO_2 cross-sections are the SCIAMACHY Flight Model (SCIA FM) cross-sections from Bogumil et al. (1999) reconvolved with the GOME-2 slit function data. For the DOAS fit the 203K cross-section is used and the retrieved slant columns are corrected a posteriori for the temperature dependence of the cross-sections (Section 3.3.5). Further cross-sections of the interfering trace gases ozone and NO_2 are included in the fit. Good results in this wavelength region are obtained using the Malicet et al. (1995) ozone cross-sections at two temperatures

(218 K and 243 K) with a pre-shift of -0.01 nm and corrected for the I_0-effect (see Section 3.3.2). For NO_2, the GOME-2 Flight Model/CATGAS cross-section is used at 241 K (Gür et al., 2005) with a pre-shift of -0.022 nm.
As described above, to account for Raman scattering two Ring reference spectra are included as additive fitting parameters to also account for the molecular Ring effect. As intensity offset effects, that may be induced by residual stray-light or imperfect Level 0-1 processing, are known to be sources of bias in DOAS retrievals of minor trace gas species, the inverse of the sun spectrum is fitted as another effective cross-section to correct for any offset. The polynomial used for broadband filtering is cubic. A solar spectrum that is recorded by GOME-2 once a day is used as reference spectrum as described in Section 3.3.2.

3.3.5 SO_2 slant column corrections

The retrieved SO_2 slant columns show a dependency on the ozone slant columns, due to interference of SO_2 and O_3 absorption structures. Further the SO_2 cross-sections are dependent on temperature, which needs to be accounted for according to the altitude of the SO_2. In the following section the corrections applied to the SO_2 slant columns are discussed.

Equatorial offset correction
To account for any systematical bias in the SO_2 slant column, that can arise for example due to instrumental or calibration problems, an equatorial offset is calculated. Further, the equatorial offset corrects the influence of the instrument degradation (Chapter 5.1) on the SO_2 slant columns to a large extent. This offset is calculated on a daily basis from the GOME-2 measurements in the equatorial region, where no continuous sources of SO_2 are present and the average SO_2 amount is assumed to be zero. First, all GOME-2 measurements within the equatorial region are used to calculate the standard deviation as an estimate of the instrumental noise. Then all measurements with SO_2 total columns greater than twice the standard deviation are excluded from the correction to avoid including measurements showing "real" SO_2 that can appear in the equatorial region due to volcanic eruptions. The remaining measurements are averaged to obtain the equatorial offset and the result is subtracted from the original slant column values:

$$S_{corr} = S - offset \tag{3.14}$$

Typical offset values are on the order of ~ 0.6 DU.

Temperature correction of the SO_2 Cross-Sections
The SO_2 absorption cross-sections show a dependence on temperature. In the atmosphere the temperature is mainly a function of height, therefore cross-sections at different temperatures should be used for the different plume heights assumed in the GOME-2 retrieval (Section 3.4.3). The simplest approach to correct for the temperature dependence is to calculate a scaling factor α_T for the dependence using a linear least-squares fit. As can be seen in Figure 3.4 the scaling coefficients with respect to the 203 K cross-section show a linear dependency which allows the application of the scaling factor. With the help of the scaling factor the SO_2 cross-section at 203 K can be scaled to the atmospheric temperature necessary.

$$\sigma_T = \alpha_T (T_0 - T) * \sigma_{T_0} \qquad \text{with } \sigma_{T_0} \text{ being the } SO_2 \text{ cross-section at 203K} \qquad (3.15)$$

As the scaling factor is constant it is possible to change the order of T-correction and slant column retrieval, which means that the slant column retrieval has to be performed only once at a certain temperature and can then be corrected to whatever temperature necessary. The slant column density for the correct temperature can then be calculated as

$$S_T = \frac{S_{T_0}}{1 - \alpha (T_{T_0} - T)} \qquad (3.16)$$

with $\alpha = 0.0030$ for the reconvolved SCIA FM SO_2 cross-sections when using 203 K as reference temperature T_0.
The SO_2 from volcanic eruptions is assumed to be constrained in an atmospheric layer of small vertical extension; therefore a single temperature cross-section has been assumed for the DOAS retrieval. The cross-section temperature, T_1, for the retrieval has been selected from the US Standard Atmosphere temperature profile as a function of assumed central plume height. This simple approach yields sufficient accuracy.

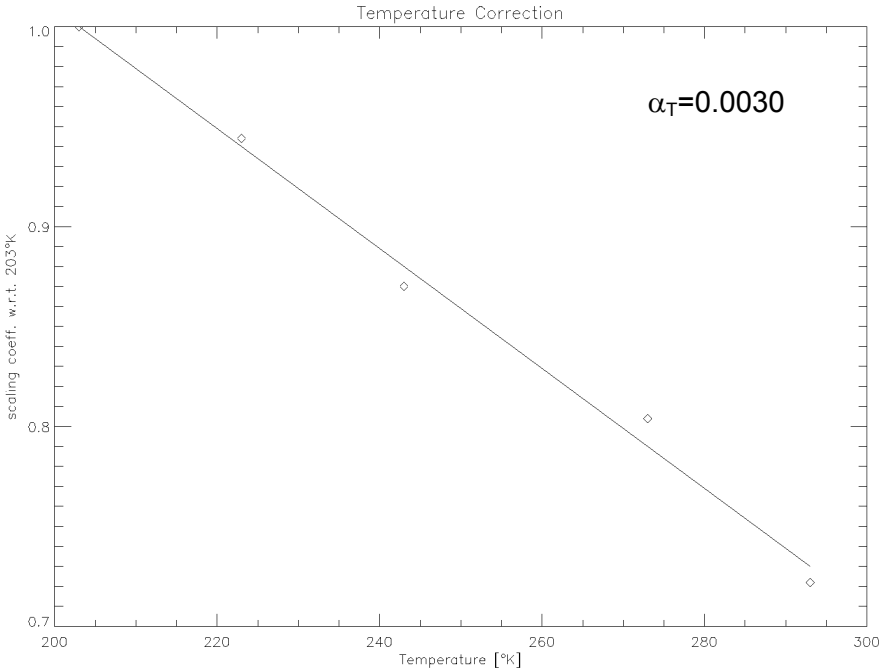

Figure 3.4: Scaling coefficients for temperature dependence of SO_2 cross-sections with respect to the 203 K cross-section and a linear regression through the data.

Correction for Ozone interference

In the wavelength range 315 – 326 nm used for the retrieval of SO_2 there is a strong interference of the SO_2 and ozone absorption signals, because the absorption cross-sections of the two gases show a similar structure (Figure 3.5). As the ozone columns are typically much larger than the SO_2 columns this results in “negative” SO_2 slant column values for high ozone amounts. The opposite effect can be observed for extremely high SO_2 columns after large volcanic eruptions, where reduced ozone values are retrieved in the area covered by the SO_2 plume (Yang et al., 2007).

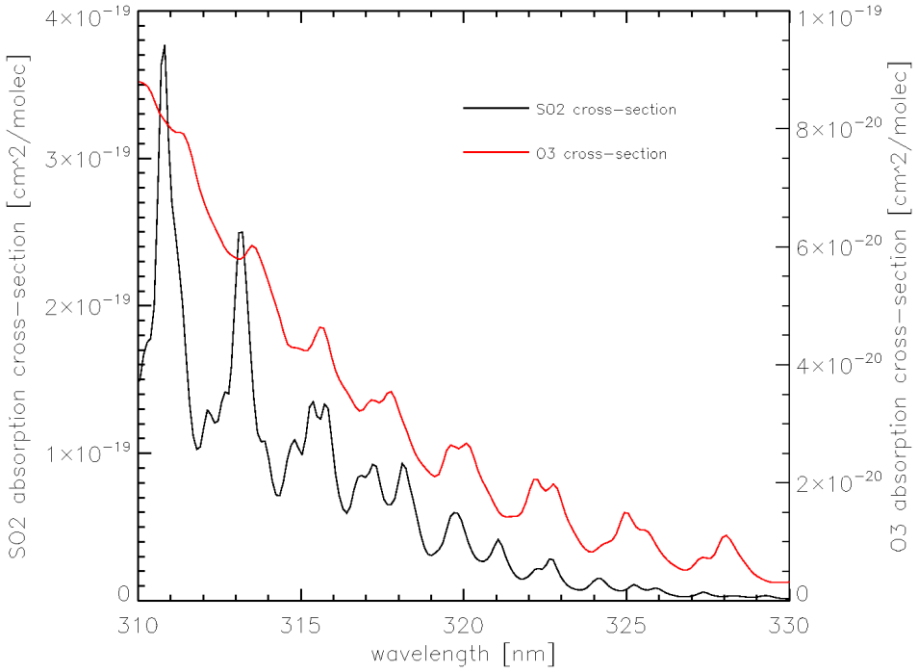

Figure 3.5: SO_2 and ozone absorption cross-section, the similar structure of the two cross-sections leads to interference of the absorption signal.

The dependency of the SO_2 slant column on the O_3 slant column amount can be approximated by a third order polynomial (Figure 3.6). The ozone correction factors c_i, which is the polynomial coefficients, are determined from two years of GOME-2 ozone and SO_2 data and applied to each individual SO_2 slant column as

$$S_{SO2,corrected} = S_{SO2} - \sum_{i=0}^{3} c_i S_{O3}^{i} \tag{3.17}$$

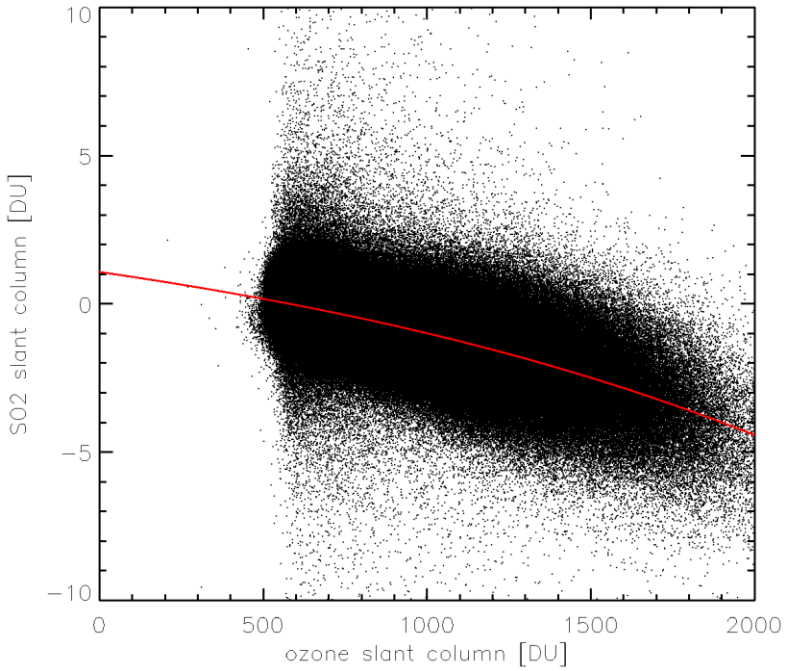

Figure 3.6: Dependence of SO_2 slant column on ozone slant column. The fitted polynomial is used as an additive correction to the slant column SO_2 values.

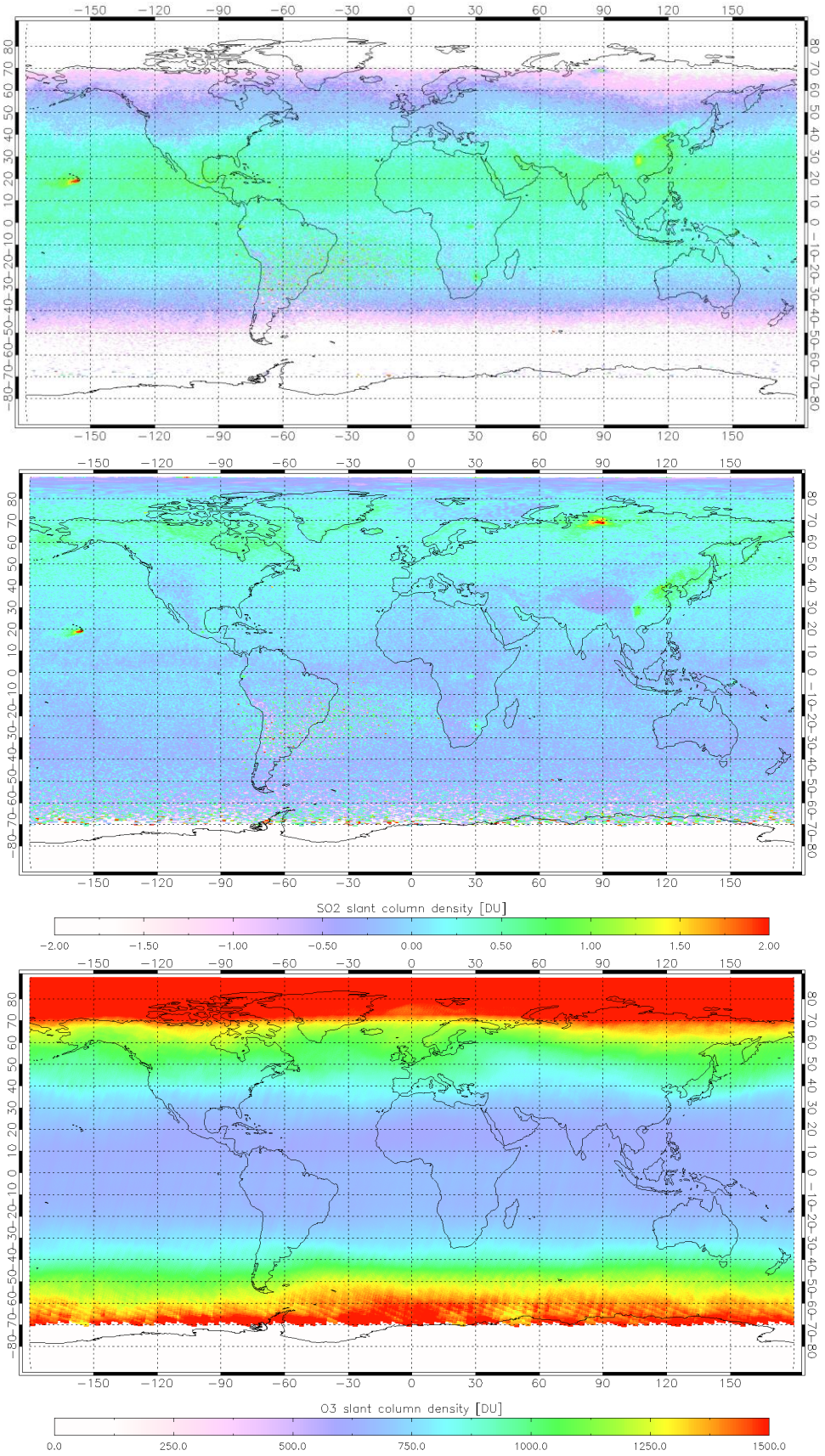

Figure 3.7: Averaged uncorrected SO_2 slant columns (top), equatorial offset and ozone corrected SO_2 slant columns (middle) and ozone slant columns for April 2008

Figure 3.7 demonstrates the effect of equatorial offset and ozone interference corrections for April 2008. The top panel shows the uncorrected SO_2 slant column values. The structure of the atmospheric ozone distribution (Figure 3.7, bottom) is clearly visible in the uncorrected SO_2 values. High O_3 columns lead to SO_2 slant columns smaller than – 2 DU. The slant column values that have been corrected for ozone interference are shown in the middle panel of Figure 3.7, in this case the average SO_2 value is around zero as one would expect for unpolluted areas. The correction allows the detection of SO_2 sources that are located at higher latitudes, e.g. the metal smelters at Norilsk, northern Russia; before the correction the SO_2 emissions are barely detectable, after the SO_2 values have been corrected for ozone interference they become clearly visible.

3.4 Total SO_2 column computation

3.4.1 Air mass factor

Using the DOAS technique the fitted trace gas quantity is the slant column of the absorbing gases, which is the amount of absorber along the line of sight. The quantity of interest is however the vertical column. The conversion between slant column (S) and vertical column (V) is achieved by division with an appropriate air mass factor (AMF) which is defined as follows:

$$M = \frac{S}{V} \tag{3.18}$$

The easiest assumption is to use a geometrical air mass factor where the length of the light path in the atmosphere is determined only by the solar zenith angle θ_0 and viewing angle θ (Figure 3.8). M_{geo} is defined as:

$$M_{geo} = \frac{1}{\cos(\theta_0)} + \frac{1}{\cos(\theta)} \tag{3.19}$$

In reality the AMF is not only dependent on satellite viewing geometry but also on albedo, clouds, wavelength as well as absorber amount and profile. The AMF is a measure for the instrument's sensitivity to SO_2, e.g. the AMF for SO_2 at high altitudes is generally high (close to M_{geo}) and low for SO_2 in the boundary layer (much smaller M_{geo}), indicating a reduced sensitivity in the PBL. The calculation of the air mass factors using a radiative transfer model will be discussed in the following section.

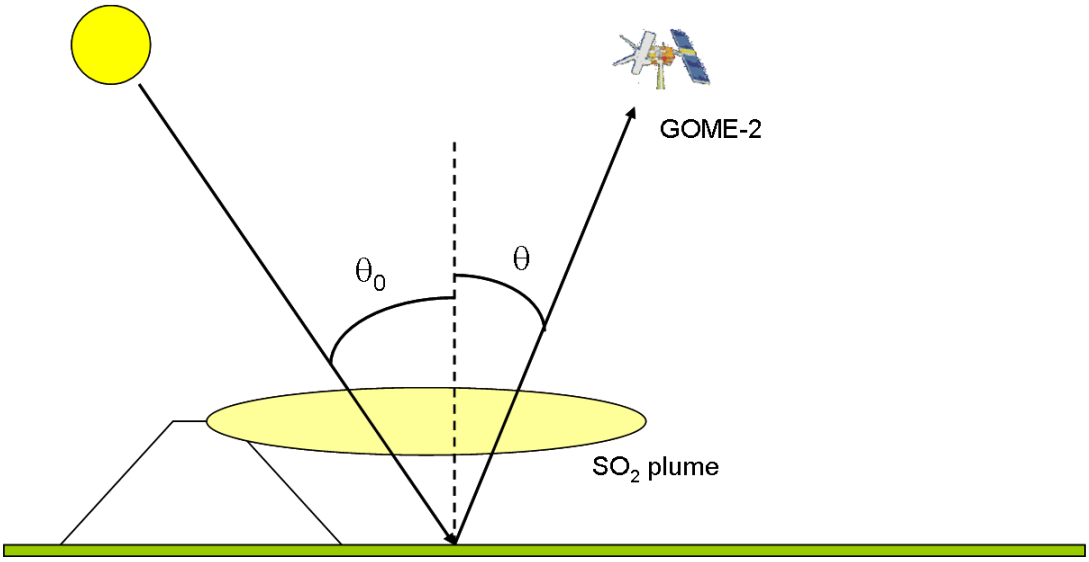

Figure 3.8: Schematic illustration of the light path through the atmosphere.

3.4.2 The radiative transfer model LIDORT

The air mass factors are calculated using the radiative transfer model LIDORT (Spurr et al., 2001). LIDORT is a pseudo spherical, multi-layer, multiple scattering model. It is a linearized discrete ordinate radiative transfer code. The atmosphere is assumed to consist of a number of uniform sub-layers. The total phase function is assumed to have a Legendre polynomial expansion in the cosine of the scattering angle and the phase function is normalized to 4π.

As input parameters LIDORT requires a set of optical properties of the atmosphere for each layer n. The inputs are the total extinction optical thickness Δ_n, the total single scattering albedo ω_n, and the set of Legendre expansion coefficients β_{ln} for the total phase function. The optical input parameters are inferred from pre-defined atmospheric profiles of temperature, pressure, air density and trace gas distributions together with Rayleigh scattering parameters, ground albedo and trace gas absorption cross-sections. Aerosols are not taken into account.

LIDORT solves the radiative transfer equation (RTE) through the discrete ordinate method (Chandrasekhar, 1989, Stamnes et al. 1988). For unpolarized light the RTE for a single layer n is

$$\mu\frac{\partial I(\Omega,x)}{\partial x} = I(\Omega,x) - \frac{\omega}{4\pi}\int P(\Omega,\Omega')I(\Omega',x)d\Omega' - \frac{\omega}{4\pi}P(\Omega,\Omega_0)FTe^{-\eta x} \qquad (3.20)$$

Where x is the optical thickness measured downward from the top of the layer, $\Omega = \{\mu,\phi\}$ is the directional variable where μ is the cosine of the polar angle and ϕ is the azimuth angle between plane containing incident and scattering beams. P is the phase function for scattering from direction Ω' to Ω. The integral represents the multiple scattering contribution. The primary scattering of direct sunlight is represented by the second term and proportional to the flux F. $\Omega_0 = \{-\mu_0,\phi_0\}$ is the solar direction with angles defined at the bottom of the atmosphere and T is the solar beam transmittance to the top of the atmosphere. The factor η in the primary scatter

attenuation is an average secant through a spherical-shell atmosphere (pseudo-spherical approximation) and is determined by ray tracing.

To solve Eq. (3.20) I and P are expanded into a Fourier series in the cosine of the relative azimuth ϕ- ϕ_0. In the resulting equation for the Fourier component $I_m(x, \mu)$ the multiple scattering integral is replaced by a summation using a double Gauss-Legendre quadrature scheme. The result is a set of 2N coupled linear differential equations for the discrete ordinate intensities $I_m(\pm\mu_j)$,

$$\mu_j \frac{\partial I_m(\mu_j)}{\partial x} = I_m(\mu_j) - \frac{\omega}{2}\sum_{k=\pm 1}^{\pm N} a_k \Pi(\mu_j, \mu_k) I_m(\mu_k) - \frac{\omega F}{4\pi}\Pi(\mu_j, -\mu_0) FTe^{-\eta x} \tag{3.21}$$

where N is the number of quadrature streams in the half space and $\pm\mu_j$, j = 1…N are the discrete ordinate polar directional cosines with quadrature weights a_j, j = 1…N. The homogenous equations in Eq. (4.2) are solved by standard eigenvalue methods (Stamnes et al. 1988).

Three boundary conditions are applied for the different layers:

- No downwelling diffuse radiation at TOA
- A surface reflection condition at the lower boundary linking upwelling and downwelling intensities
- Continuity of the radiation field at all intermediate boundary layers

This results in a matrix algebra problem **AX=B** where **X** is the unknown vector of integration constants.

The solutions are post processed using the source function integration technique (Chandrasekhar, 1960). The discrete ordinate solution is substituted into the RTE and integrated over layer optical thickness values. For TOA radiances

$$I(0,\Omega) = I_{surface}(\Psi_n, \Omega) e^{-\Psi_n/\mu} + \sum_{p=1}^{n} \Lambda_p(\Omega) e^{-\Psi_p/\mu} \tag{3.22}$$

Where Λ_p are the integrated layer source terms for layer p, $\exp(-\Psi_p/\mu)$ is the line of sight attenuation factor for cumulative optical depth Ψ_p, and $I_{surface}$ is the upwelling radiation at the bottom of the atmosphere which follows from the surface boundary conditions. Summing the Fourier azimuth cosines completes the solution.

The AMF has been calculated using LIDORT Version 3.3, which possesses corrections for beam attenuation along curved line of sight paths, necessary for GOME-2 due to the wide swaths (1920 km) and the therefore wide viewing angles (scan angles: 40° – 50°) (Spurr, 2008).

3.4.3 Air mass factor calculation

For the calculation of the AMF the radiative transfer through the atmosphere is simulated twice, once including the absorbing gas of interest (SO_2) and once without the absorber, the atmospheric settings are kept the same for both simulations. By dividing the simulated intensities at the top of the atmosphere, atmospheric

contributions not originating from the absorber cancel and result in the slant optical thickness of the absorber.

$$\ln\left(\frac{I_{+gas}(\lambda)}{I_{-gas}(\lambda)}\right) = \tau_{slant,gas} \tag{3.23}$$

with

$$\tau_{slant,gas}(\lambda) = \int \rho_{gas}(l)\sigma_{gas}(\lambda,l)dl \tag{3.24}$$

where I_{+gas} and I_{-gas} are the intensities at the top of the atmosphere with and without absorber respectively.
Division by the vertical optical density of the relevant absorber

$$\tau_{vert,gas}(\lambda) = \int_{o}^{z_0} \rho_{gas}(z)\sigma_{gas}(\lambda,z)dz \tag{3.18}$$

yields the air mass factor

$$M(\lambda) = \frac{\ln\left(I_{+gas}(\lambda)/I_{-gas}(\lambda)\right)}{\tau_{vert,gas}(\lambda)} \tag{3.25}$$

The gas vertical column density can now be calculated according to Eq. (3.18).

For standard DOAS a fixed AMF at a single wavelength is calculated for easy use of Eq. (3.18). An important assumption for the use of a single wavelength air mass factor is an optically thin atmosphere, as in that case the AMF is wavelength independent. This assumption leads to problems in wavelength regions with strong absorption. For the SO_2 retrieval in the UV wavelengths range this assumption in not strictly fulfilled due to Rayleigh scattering and the strong absorption of ozone in the UV. Further, for large SO_2 columns also strong SO_2 absorption leads to higher optical thickness. These effects result in a change of light path with wavelength and therefore in a wavelength dependency of the AMF. However, despite not strictly fulfilling the assumption of low optical thickness, the use of a single wavelength AMF calculated at 315 nm still yields good results, especially for low and medium SO_2 total columns. For high SO_2 total columns the method can lead to significant underestimation of the total column. Issues due to the use of a single wavelength AMF are discussed in more detail in Chapter 4.

For SO_2, the conversion from the slant column to a vertical column is complicated further by the strong dependence of the AMF on the a priori vertical profile of SO_2 in the atmosphere. Especially the different emission sources of SO_2, i.e. volcanic emissions and anthropogenic pollution, should be taken into account in the air mass factor calculations.
A volcanic SO_2 profile is used for the calculation of the AMF with a predefined central plume height and a Gaussian SO_2 distribution around that central height. The SO_2 column for volcanic eruptions is computed for three different assumed SO_2 plume heights: 2.5 km above ground level, 6 km and 15 km. The first height represents

passive degassing of low volcanoes, the second one effusive volcanic eruptions or passive degassing of high volcanoes and the third one explosive eruptions.
Apart from the plume height the AMF depends on the total column amount of SO_2, two different a priori total columns are assumed, 3 DU for cases with presumably low SO_2 amounts, e.g. passive volcanic degassing, and 30 DU for explosive volcanic eruptions.
The sensitivity of the retrieval to the assumed SO_2 profile is discussed in Chapter 4.

Further the AMF is influenced by the atmospheric boundary conditions that are used for the radiative transfer calculations such as albedo. The surface albedo for the AMF calculation is the same that has been used for ozone retrieval (Van Roozendael et al., 2004) and based on a combination of the GOME Lambertian equivalent reflectivity (LER) data set of albedos (Koelmeijer et al., 2003) and the Nimbus 7 TOMS LER data set (Herman and Celarier, 1997).

3.4.4 Influence of clouds

Clouds influence satellite measurements of SO_2 in two very different ways depending on their relative position. If the SO_2 plume is below the clouds, it is shielded from the view of the satellite (Figure 3.9, left) and cannot be detected. However, in cases where the SO_2 plume is above the clouds (Figure 3.9, right), the measurement sensitivity to the SO_2 is enhanced, due to the high albedo, which increases the intensity of the backscattered radiation. The effect of clouds is accounted for through the AMF.

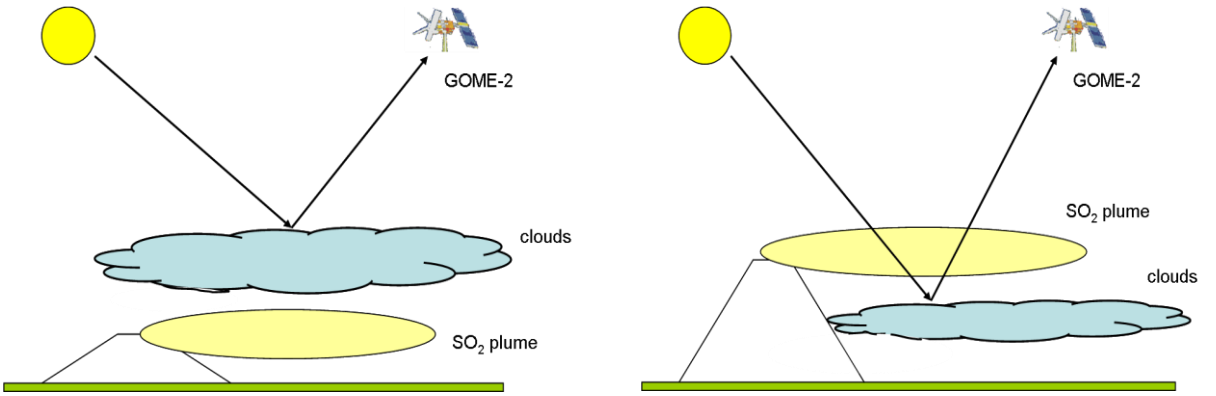

Figure 3.9: Effect of clouds on the GOME-2 measurement of SO_2. SO_2 below the clouds is shielded from the view of the satellite (left). The sensitivity to SO_2 above clouds is enhanced due to higher albedo (right).

For cloudy condition Eq. (3.18) can be extended using the independent pixel approximation for clouds and a Lambertian reflecting boundary cloud model. Using the cloud radiance fraction Φ which is defined as

$$\Phi = \frac{c_f I_{cloud}}{(1-c_f) I_{clear} + c_f I_{cloud}} \tag{3.26}$$

where c_f is the cloud fraction, I_{clear} and I_{cloud} are the backscattered radiances for a cloud-free and cloudy atmosphere, respectively. I_{clear} and I_{cloud} are dependent mainly on the surface and cloud albedo, as well as the satellite viewing geometry. They are calculated using the LIDORT model. The cloud information is obtained from the

OCRA and ROCINN algorithms (Loyola et al, 2007). OCRA provides the cloud fraction from the GOME-2 broad-band polarization measurements and ROCINN retrieves the cloud-top height and albedo from GOME-2 measurements in and adjacent to the oxygen A-band around 760 nm.

Equation (3.18) can now be rewritten as follows to account for clouds.

$$V = \frac{S}{(1-\Phi)M_{clear} + \Phi M_{cloud}} \tag{3.27}$$

where M_{clear} is the clear sky air mass factor and M_{cloud} the air mass factor for the atmosphere down to the top of the clouds. For the retrieval of SO_2 only the "visible" column is retrieved and no "ghost column" is added.

3.5 Summary

In this chapter the operational SO_2 retrieval from GOME-2 observations using the DOAS method has been described. An overview of the instrument and the operational processing has been given. The operational GOME-2 total column SO_2 product is provided in the framework of EUMETSAT's Satellite Application Facility on Ozone and Atmospheric Chemistry Monitoring (O3M-SAF). The SO_2 columns are available approximately two hours after measurement.
Further a description of the DOAS method is given and the adaptation of DOAS retrieval to the GOME-2 measurements is discussed. The settings for the SO_2 slant column retrieval and the slant column corrections, that account for equatorial offset, temperature dependence of the SO_2 cross-sections and ozone interference, are explained. In the last section the total column computation through the use of appropriate air mass factors, that are calculated using the radiative transfer model LIDORT, is described. As the AMF depends strongly on the vertical distribution of the SO_2 in the atmosphere, which in typically unknown at the time of the measurements, the AMF is calculated for three assumed plume heights. The assumed plume heights of 2.5 km, 6 km and 15 km represent typical heights of volcanic eruptions and degassing.

4. Analysis of GOME-2 SO_2 retrieval: Standard DOAS, modified DOAS and direct fitting

When using standard DOAS analysis for the retrieval of sulfur dioxide several limitations arise, as discussed in Chapter 3. In this chapter the limitations with standard DOAS fitting of atmospheric SO_2 are discussed and the systematic errors introduced by using a standard DOAS approach are estimated by applying the standard DOAS method to synthetic GOME-2 radiance spectra. The errors due to ozone interference, imperfect treatment of the Ring effect and the use of a single wavelength AMF are estimated. The synthetic spectra have been simulated with RRS-LIDORT. Improved methods for retrieving atmospheric SO_2, modified DOAS and direct fitting, are introduced and applied to the synthetic GOME-2 spectra. The improvements that can be achieved by these techniques are discussed. Finally all retrieval methods are applied to GOME-2 measurements of different volcanic eruptions and the results are compared.

4.1 Computation of synthetic GOME-2 spectra

GOME-2 spectra have been simulated, for estimating the systematic errors that can be introduced by using a standard DOAS approach and the improvements that can be achieved with more advanced retrieval methods. The great advantage of using synthetic spectra is that the atmospheric conditions can be controlled. For example, simulations have been conducted with O_3 removed from the atmosphere to estimate the influence on the retrieval of SO_2 or Raman scattering has been neglected in the simulations to infer the influence of the Ring effect on the SO_2 retrieval. Further the SO_2 profile shape and total column amount can be varied to simulate different eruptive scenarios and investigate the performance and limitations of the different retrieval methods.

The simulations of the GOME-2 radiance spectra were done using the radiative transfer model LIDORT (Spurr et al., 2001), which has been introduced in Section 3.4.2. The RRS-LIDORT version used for the simulations allows the inclusion of Rotational Raman scattering (RRS) (Spurr et al., 2008). A brief introduction to RRS-LIDORT is given below.

LIDORT-RSS

The LIDORT-RRS discrete-ordinate algorithm is based on the methods developed for the scalar LIDORT. The model considers RRS as a first order perturbation, all orders of elastic scattering are considered but only one order of RRS. This means that photons are considered, which are Raman scattered only once into and out of a given wavelength λ. For multiply scattered light it is assumed that the diffuse fields at λ and all Raman-shifted redistribution wavelengths have been determined by using a zero-order elastic radiative transfer calculation before being Raman scattered for the first time. The RTE then contains a number of additional source terms due to first-order RRS. The RTE including first-order RRS is

$$\mu\frac{dI(x,\Omega,\lambda)}{dx}=I(x,\Omega,\lambda)-\frac{\omega_E(\lambda)}{4\pi}\int P_E(\Omega,\Omega',\lambda)I(x,\Omega',\lambda)d\Omega'-\frac{F(\lambda)}{4}\omega_E(\lambda)P_E(\Omega,\Omega_0,\lambda)\exp^{-T(x)}$$
$$-\sum_{s=1}^{NS}\frac{\omega_R(\lambda_s)}{4\pi}\int P_R(\Omega,\Omega',\lambda)I(x,\Omega',\lambda)d\Omega'-\sum_{s=1}^{NS}\frac{F(\lambda_s)}{4}\omega_R(\lambda_s)P_R(\Omega,\Omega_0,\lambda)\exp^{-T(x_s)} \quad (4.1)$$

The last term represents the light scattered inelastically from Raman-shifted wavelength. ω_E is the single scattering albedo from purely elastic scattering and P_E is the normalized elastic-scattering phase function. ω_R and P_R are the Raman gain single-scattering albedo and the Raman gain scattering phase function, respectively. The RTE containing the Raman gain term can now be solved using the discrete ordinate method.

The simulations of the GOME-2 measurement spectra have been conducted in the wavelength range between 310 nm – 330 nm, this covers the wavelength range used for the operational SO_2 retrieval (315 nm – 326 nm) and allows the inclusion of Raman scattering in the simulations, where radiation can be scattered inelastically from wavelengths outside the retrieval interval. The synthetic spectra have been calculated at the resolution of the GOME-2 instrument. The parameters that have been varied during the simulations are the total SO_2 column, the SO_2 plume height, the O_3 total column and the solar zenith angle. All simulations have been conducted twice, once including Raman scattering and once without.

4.2 Limitations of standard DOAS retrieval of SO_2

Standard DOAS retrieval of SO_2 has several limitations that are unique to this specific gas. The main problems are the dependence of the AMF on the vertical distribution and total column of SO_2 and also the interference of the absorption features of SO_2 and ozone. SO_2 retrieval is complicated by the fact that the SO_2 distribution in the atmosphere differs very much over time and location. Standard background levels are very close to zero. SO_2 from anthropogenic pollution is distributed in the boundary layer with total column values of up to ~ 10 DU. SO_2 from volcanic activity is mostly found in the free troposphere but can also reach altitudes of 15 km – 20 km and total column values range from around 1 DU up to 500 DU. Further issues arise from the treatment of the Ring effect and for measurements at large solar zenith angles.
In the following sections the different issues will be discussed and an estimation of the induced errors on the total columns will be given. For the error estimation the standard DOAS retrieval is applied to synthetic GOME-2 radiance spectra.
To allow comparison with the operational retrieval results, the same settings in terms of fitting window and cross-section choice have been applied to the simulated spectra (Chapter 3.3.4). The only change introduced compared to the operational SO_2 retrieval is that NO_2 has been included neither in the simulation nor in the fit, as the inclusion has no significant effect on the results.
The simulated spectra were analyzed using the software WinDOAS 2.1 (Roozendael and Fayt, 2001) which derives the slant columns from the simulated spectra using a DOAS fit.

4.2.1 Ozone interference

In the UV wavelength range (315 – 326 nm) used for the retrieval of SO_2 the absorption of ozone is also strong. As both absorption cross-sections have similar structures (Figure 3.5), they interfere in the DOAS fit, especially for high ozone values. The ozone optical depth is typically an order of magnitude higher than the SO_2 optical depth, which results in a reduction of the fitted SO_2 column for high ozone values by several Dobson Units. To analyze the ozone interference simulations with and without ozone have been done and the fit results have been compared. Different combinations of SO_2 total column (0, 1, 3, 10, 20, 60, 100, 200, 500 DU), O_3 total column (0, 200, 300, 400, 500 DU) and solar zenith angle (35°, 45°, 55°, 65°, 75°, 85°) have been used for the simulations. An ozone profile from the U.S. Standard Atmosphere (U.S. Standard Atmosphere, 1976) has been used in the simulations and scaled to the different total column amounts. No Raman scattering has been included in the simulations. The reduction of the SO_2 slant columns was calculated as the difference between the fitted SO_2 slant columns for simulations including ozone and those without ozone. The different fits show that the effect is a function of ozone slant column and total SO_2 amount (Figure 4.1). The absolute reduction of the fitted SO_2 slant column is strongest for high SO_2 and ozone total columns, with negative offsets as high as - 50 DU for a total SO_2 column of 500 DU. For simulated ozone slant columns > 1500 DU, the negative offset increases rapidly.
In GOME-2 measurements high ozone total columns around 500 DU and high solar zenith angles, from 65° to 75°, typically occur in the northern hemisphere in the spring months, the offset in SO_2 total vertical column can be up to -15 DU for cases where no SO_2 is present in the atmosphere. For moderate ozone slant columns the observed offset is typically between -1 to -3 DU.

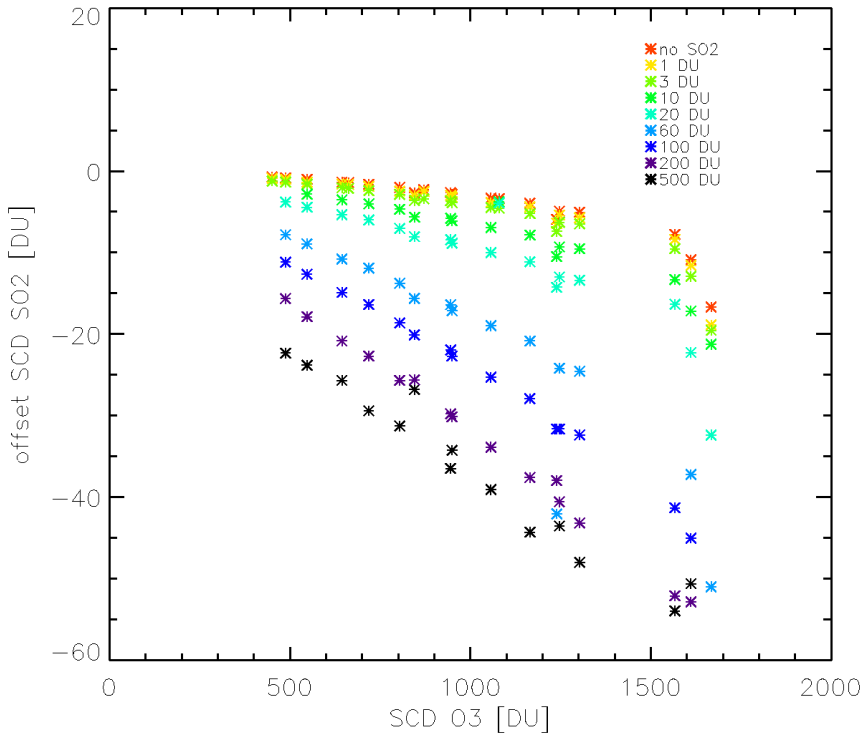

Figure 4.1: Dependence of SO_2 slant column on ozone slant column for different total SO_2 column amounts. The SO_2 offset is calculated as the difference of SO_2 SCD with ozone included in the simulations and SO_2 SCD without ozone ($SCD_{SO2withO3}$- $SCD_{SO2noO3}$).

4.2.2 Treatment of the ring effect

The Ring effect (Grainer and Ring, 1962) caused by Raman scattering leads to reduction of the depth of the Fraunhofer structures in scattered light compared to direct sunlight. In DOAS applications the Ring effect has to be accounted for as it can lead to severe errors in the retrieval. Typically that is done by adding a Ring cross-section (Chapter 3.3.3) to the DOAS equation. In the DOAS retrieval of SO_2 the molecular Ring effect, which leads to a filling in of the SO_2 absorption structures, is also treated by an additional Ring cross-section. The cross-sections have been calculated as explained in Chapter 3.3.3. This does not account for the Ring effect in an optimal way, as the atmospheric conditions vary throughout the measurements, while the Ring cross-sections are kept constant.
To estimate the effect of this simple treatment of Raman scattering, DOAS retrievals for synthetic spectra calculated with and without Raman scattering have been compared for various settings as shown in Table 4.1.
Compared to simulations without Raman scattering, it can be observed that the Ring effect causes a positive offset of the fitted SO_2 total column. The absolute offset varies between ~ 1.9 DU for SO_2 columns of 1 DU to ~ 85 DU for SO_2 columns of 500 DU, the relative offset is between around 190 % and 17 % respectively. The decrease that can be observed for high total SO_2 columns with respect to the input SO_2 is due to the use of a single wavelength AMF and will be discussed in Section 4.2.4.
The offset values also show a dependence on the total ozone. For low SO_2 values high ozone total columns lead to a decrease in total column SO_2 as would be expected from the investigations of the ozone interference. However, for high SO_2 total columns, enhanced ozone total columns result in an increase of SO_2 total column. Here O_3 interference and Raman scattering do not behave as additive effects, as the quality of the standard DOAS retrieval is limited due to the high optical thickness at high SO_2 total columns. This results in further issues when applying a single wavelength AMF, which will be explained in Section 4.2.4.
For SO_2 columns up to 20 DU the errors induced by an imperfect Ring correction and ozone interference cancel to a great extent, which allows using the standard DOAS technique for SO_2 retrieval without introducing large errors (Table 4.1).

Input SO_2 [DU]	Elastic scattering No O_3	Including RRS No O_3	Including RRS 200 DU O_3	Including RRS 300 DU O_3	Including RRS 400 DU O_3	Including RRS 500 DU O_3
1	1	2.89	1.41	1.25	1.06	0.8
3	3.01	4.7	3.24	3.13	2.95	2.71
10	8.23	10.9	9.6	9.57	9.48	9.34
20	16.1	19.5	18.5	18.6	18.6	18.6
60	44.9	51.8	52	52.6	53	53.6
100	70.9	81	82.5	83.7	84.7	85.8
200	125	143	149	151	154	156
500	227	312	283	288	293	298

Table 4.1: Effect of Raman Scattering on the retrieved vertical SO_2 columns for different O_3 total columns.

It is interesting to note that high SO_2 total columns lead to a significant reduction in the fitted total ozone column of up to ~ 30 % for a total SO_2 column of 500 DU. Further for high ozone columns (> 100 DU) an increase in the fitted SO_2 column can

be observed with increasing ozone (Table 4.1). As explained in Chapter 3.4, this effect can also be observed in satellite observations.

4.2.3 Measurements at large SZAs

For large solar zenith angles the light path through the atmosphere increases and therefore Rayleigh scattering, SO_2 and ozone absorption are increased, leading to a reduced sensitivity for SO_2 in the low and middle troposphere, which can be seen in the SZA dependence of the AMF (Figure 4.2). Further the total radiation received at the satellite decreases as a result of increased extinction resulting in an increased noise level and limiting the quality of the data. The DOAS retrievals on the simulated spectra indicate that solar zenith angles larger than 70° are highly problematic and lead to significant errors. As the retrievals on simulated spectra not including any ozone show good results up to SZAs of 85°, it can be assumed that the problems are mainly due to ozone interference and absorption. However, for SZA's of 75° the detection of SO_2 total columns > 10 DU is still possible, even though the correct quantification is difficult. Opposed to that, retrievals at solar zenith angles > 80° do not produce useful results, as even SO_2 columns > 60 DU are not detectable for higher ozone values.

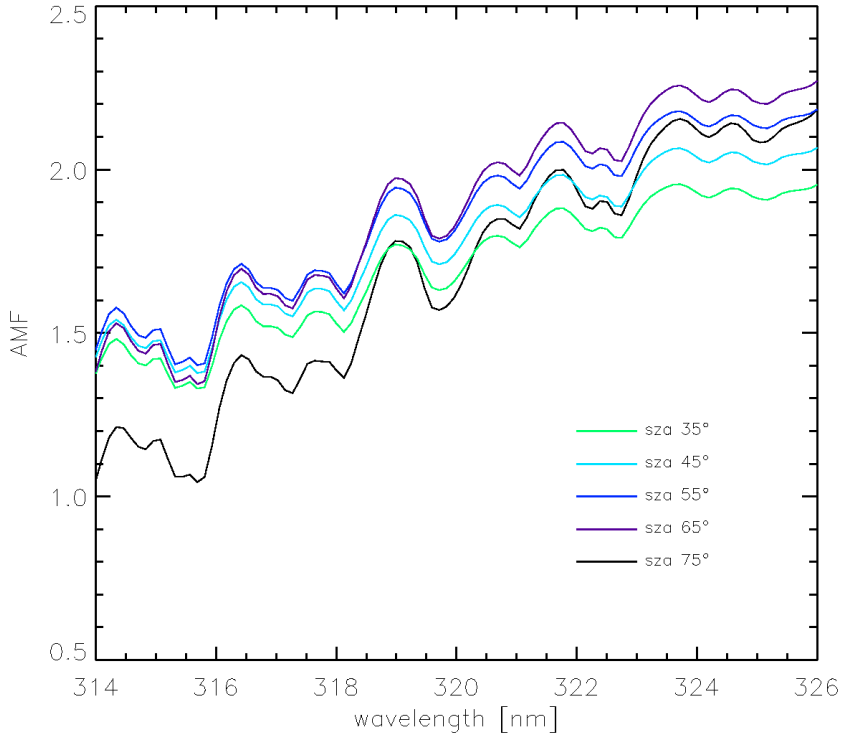

Figure 4.2: SZA dependence for SO_2 air mass factor for 60 DU SO_2 at 7km height with a total ozone column of 367 DU. The albedo was set to 0.03.

4.2.4 AMF calculation

As explained in Chapter 3, one of the central assumptions for using a standard DOAS retrieval is that the light path through the atmosphere is independent of wavelength. In most cases, also in the current SO_2 retrieval, it is assumed that this requirement is fulfilled and a single wavelength AMF at 315 nm is used for all calculations. However, at the shorter wavelengths used for the retrieval of SO_2 issues

arise when applying the standard DOAS concept. Due to the strong absorption of ozone and for larger SO_2 columns also due to SO_2 absorption, the assumption of an optically thin atmosphere does not hold true and the absorption structures of the two gases become apparent in the AMF. Rayleigh scattering is also strong at lower wavelength. These effects result in a change of light path with wavelength and lead errors when using a single wavelength AMF.

An a priori profile of the absorber is needed as input for the calculation of the AMF. For SO_2 the AMF depends not only on the profile shape, mainly the assumed plume height (Figure 4.3), but for large SO_2 columns also on the total amount (Figure 4.4). As explained in Chapter 3.4.3, in the operational SO_2 retrieval 3 different plume heights and 2 total column amounts are used. The simulations allow an estimation of the errors induced by deviations from these assumed profiles.

For the tests different SO_2 profiles, defined via a central plume height and a total column amount, were used for the simulations of the GOME-2 radiance spectra. Further settings include that no Raman scattering and ozone absorption was included. The solar zenith angle was set to 35° and the albedo to 0.03.

Dependence on SO_2 altitude

The measured signal at the satellite is comprised of backscattered radiation. Depending on the atmospheric situation these photons can be scattered by clouds, aerosols, the earth's surface or air molecules. Only radiation that is scattered below the SO_2 layer will show the characteristic absorption features. Mainly due to Rayleigh scattering and ozone absorption measurements are less sensitive for SO_2 in the lower atmosphere. This is represented by the AMF, which is a measure for the instrument sensitivity, which shows a strong dependence on the assumed height of the SO_2 profile. Whereas the AMF dependence is small for plume heights above ~ 10 km, AMF values are decreasing fast below that height (Figure 4.3).
This causes problems that are specific for SO_2 as the height of the SO_2 can be very different from case to case. While SO_2 from anthropogenic pollution is confined mostly within the planetary boundary layer, SO_2 from volcanic eruptions can reach very different heights in the atmosphere. Degassing volcanoes emit SO_2 at their summit level which is between 1 – 6 km, moderate eruptions reach mid- to high-tropospheric levels between 3 – 10 km and explosive eruptions can bring SO_2 well into the stratosphere. In most cases of volcanic eruptions the height of the SO_2 emission is not known at the time of measurement, therefore the uncertainty in the plume height can introduce significant errors in the AMF.

SO_2 profiles with a central plume height of 2 km, 7 km and 15 km were used for the simulation of the GOME-2 radiance spectra, which are similar to the assumed plume heights for the operational retrieval. Then the vertical columns were calculated using AMFs for different assumed plume heights from 1 to 15 km and the induced errors were estimated, assuming that typical plume height deviations are within $\pm$ 4 km of the height assumed for the AMF calculation.

The result shows that for an assumed plume height of 2 km for the AMF calculation the errors vary from about - 70 % for SO_2 in the planetary boundary layer (0 – 1 km) to + 40 % for SO_2 at an altitude of 5 km. When the plume height assumed for the AMF is 7 km, for SO_2 at 3 km height the total columns are decreased by ~ 50 %,

whereas they are enhanced by ~ 15 % for plume altitudes of 11 km. For an assumed plume height of 15 km in the AMF calculation, the error introduced for an SO_2 plume at 11 km is around -5 %.

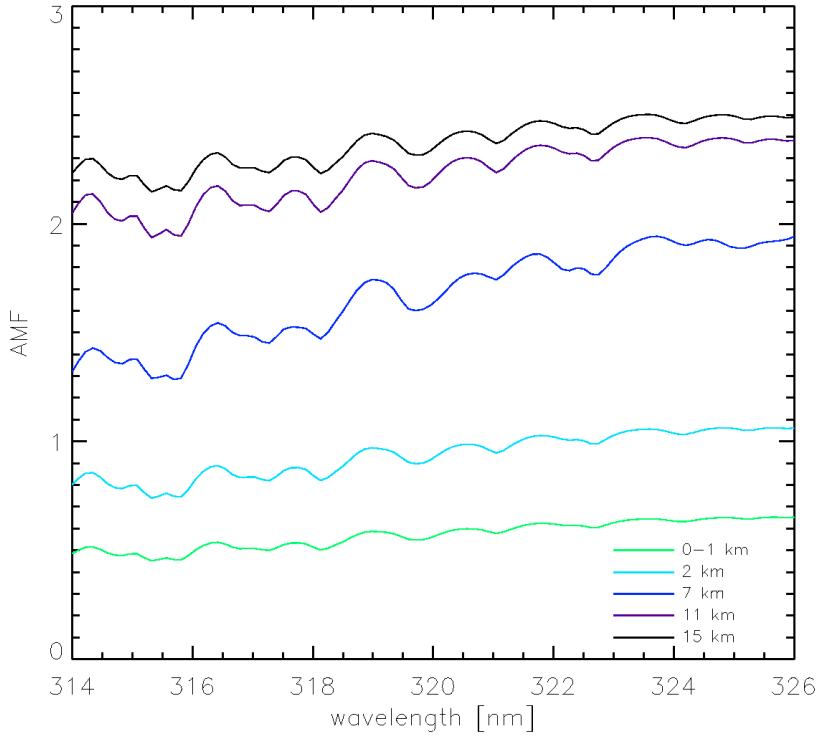

Figure 4.3: Dependence of SO_2 air mass factor for various plume heights. A total SO_2 column of 60 DU and a total ozone column of 367 DU have been assumed. The albedo was set to 0.03 and the SZA to 35°.

The tests also show that the influence of the AMF is higher for assumed plume heights < 7 km, as in this case the radiative transfer effects like scattering become more important, whereas the AMF shows little variation from 15 to 11 km (Figure 4.3).

As the errors induced by the assumption of a wrong plume height are significant especially for low heights, this emphasizes the importance of plume height information to correctly quantify the SO_2 total column. The plume height is typically inferred from observations or can be estimated to some extent if the emission source and, in case of volcanic emissions, the peak height and eruption style is known. Further options to get information on the plume height are trajectory modeling or the direct retrieval of the SO_2 plume height from the spectral information (Chapter 6).

Dependence on SO_2 total column

Figure 4.4 shows the dependence of the AMF on the total SO_2 column. At lower wavelength where the SO_2 absorption is stronger, the AMF shows clear structures of the SO_2 absorption cross-section.
The dependence of the AMF on total SO_2 column is small for low total SO_2 column, therefore the introduced errors are small, < 20 % for total SO_2 columns < 20 DU. For large total SO_2 columns the assumption of a lower SO_2 column for the AMF calculation will lead to a significant overestimation of the AMF and therefore an underestimation of the total column. If for an atmosphere with total column SO_2 > 200

DU an AMF for total columns < 10 DU is assumed, it results in a significant underestimation of the total column of ~ 70 %.
This error can be reduced by using an iterative approach when calculating the vertical column by adjusting the AMF according to the calculated vertical column. The best results are obtained when using an AMF for a high SO_2 total column as a starting value, in which case the iteration converges to the correct total column in most cases. Usually the iteration converges within 2 or 3 steps.

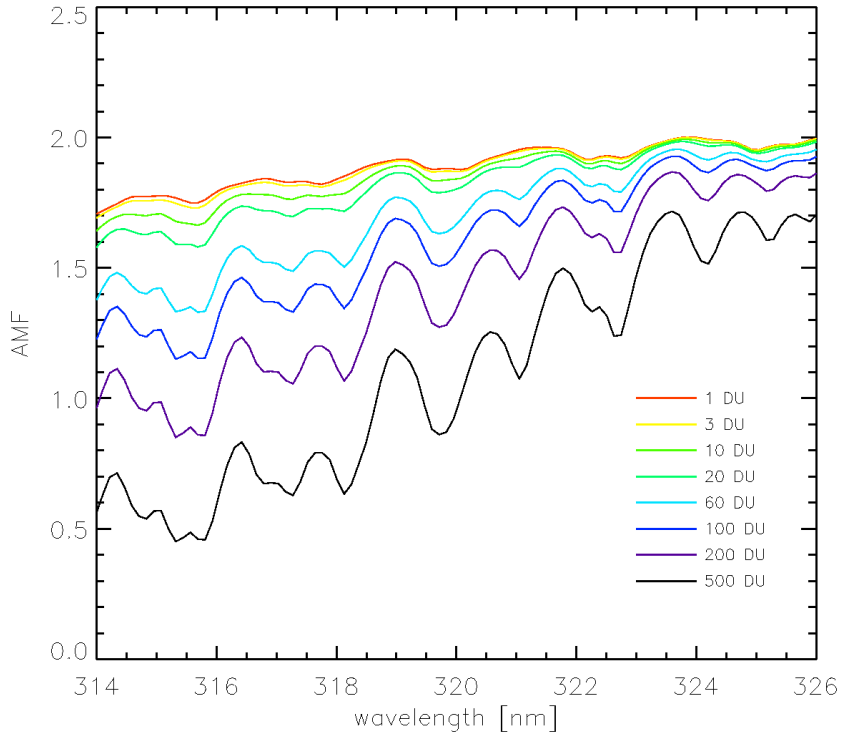

Figure 4.4: Dependence of SO_2 air mass factor on total SO_2 column and wavelength. The SO_2 plume height was assumed to be 7 km. The total ozone column was 367 DU, the albedo was set to 0.03 and the SZA to 35°.

Dependence on wavelength

As is clearly visible in Figure 4.4, the AMF strongly depends on the wavelength, especially for large total columns. Ideally the AMF should only show a weak dependence on wavelength, which allows the use of a single wavelength AMF for the computation of the vertical column. The SO_2 AMF decreases towards shorter wavelengths as a result of increased absorption of SO_2, ozone and Rayleigh scattering. This effect is moderate for small total columns, but becomes much larger for high SO_2 total columns.
The wavelength dependency of the light path at high SO_2 total columns results in a significant underestimation of the total SO_2 amount for high SO_2 total columns. For SO_2 values of up to 3 DU this effect does not influence the fit results. For SO_2 total columns > 10 DU the effect becomes important and leads to an underestimation of the total SO_2 columns from ~ 15 % for a total column of 10 DU up to ~ 55 % for a total column of 500 DU (Table 4.1). Further strongly increased fit residuals indicate a reduced fit quality for large total columns.
The issue will be further investigated in Section 4.3 where the use of a modified DOAS algorithm is discussed, that takes the wavelength dependency into account.

Dependence on surface albedo

The surface reflectivity influences the sensitivity of the measurement significantly, over bright surfaces more radiation is scattered back to the satellite which first of all leads to a reduction in noise. The sensitivity of the measurement increases especially for large surface albedos, mostly snow and ice. The effect is especially important in the presence of clouds, where the sensitivity to SO_2 above the clouds will be increased, whereas SO_2 below the clouds will be shielded and cannot be detected by the satellite. The treatment of clouds and albedo in the AMF is discussed in Chapter 3.4.4.

Summary

For low SO_2 total columns the relative errors can be very high, especially for high ozone total column and high solar zenith angles they can be up to – 90 %. However, the absolute errors are still moderate, especially if the total O_3 columns are not extremely high, the deviation from the simulated columns is typically < 1 DU, due to cancellation effects with errors induced by the Ring effect (Table 4.1). For low SO_2 amounts the dominant error source is the ozone interference. In operational retrieval this is reduced by applying a correction to the slant column as explained in Chapter 3.3.5. No error is induced by the use of a single wavelength AMF. When taking into account that ozone interference can be corrected after the fit, the standard DOAS method yields good results for low SO_2 total columns.
For high SO_2 total columns the relative errors are much smaller (- 40 %), but their absolute values can be quite large (- 200 DU). The major error source is the use of a single wavelength AMF, leading to a significant underestimation of the total SO_2 columns.

4.3 Modified DOAS

As explained in Section 4.2 the standard DOAS method is limited by several assumptions that are not exactly fulfilled for SO_2. Especially the assumption that the light path through the atmosphere is independent of wavelength and of the absorber itself is not valid. The atmosphere becomes optically thick in the wavelength region used for the retrieval, the use of a single wavelength AMF is not justified any more. For high SO_2 amounts the structure of the absorption cross-section is apparent in the AMF. The strong correlation of AMF and SO_2 absorption structures leads to errors when applying the standard DOAS method. Therefore a modified DOAS method (Burrows et al., 1999, Bovensmann et al, 1999) is introduced that allows treatment of these effects.

To account for the wavelength dependency of the light path at large SO_2 columns the DOAS equation (Eq. (3.8)) is modified. Instead of fitting the slant column densities of SO_2 and converting them to vertical columns through an AMF, the slant optical densities (τ_{slant}) are fitted (Richter, 1997). The slant optical densities are defined as the integral along the light path over the product of the absorption cross-section and the absorber concentration.

$$\tau_{slant} = \int_{l=0}^{L} \sigma(\lambda)\rho(l)dl \tag{4.2}$$

The DOAS equation now becomes

$$I(\lambda) = I_0(\lambda)\exp\left\{-\sum_j \tau_{slant,j}(\lambda) + \sum_p a_p \lambda^p\right\} \tag{4.3}$$

This reverses the order of integration and summation and unlike in Eq. (3.2) it is not necessary to assume that the cross-section is independent of the path l to draw it in front of the integral. The slant optical densities are computed according to Eq. (3.16) using the radiative transfer model LIDORT. τ_{slant} replaces the absorption cross-sections in the fit, the further procedure is analogous to the standard DOAS fit. The fit is performed using the following equation.

$$I(\lambda) = I_0(\lambda)\exp\left\{-\sum_j r_j \frac{\tau^0_{slant,j}(\lambda)}{V^0_j} + \sum_p a_p \lambda^p\right\} \tag{4.4}$$

The fitted linear quantities r_j represent no longer the slant column densities but are scaling factors that indicate the deviation of the real SO_2 column (V^0_j) from the one assumed for the calculation of the τ_{slant} ($\tau^0_{slant,j}$). The vertical column can be obtained by multiplying the scaling factor with the τ_{slant} divided by the assumed vertical column. Tests on simulated spectra show that interfering gases have to be included in the simulation of τ_{slant}, as otherwise no reliable results were obtained. When applying the modified DOAS technique to SO_2, not including the ozone absorption in

the simulation of $\tau_{slant,SO2}$ leads to SO_2 values that are 10 – 15% lower than those assumed in the simulations. Including a realistic ozone column in the simulations of $\tau_{slant,SO2}$ will yield very good results for the SO_2 and ozone total column and the fit residuals are lower indicating a better quality of the fit. For all results presented in the following sections a realistic ozone columns has been included in the simulation of τ_{slant}.

A different way of applying this method making it easier to implement the modified DOAS method into existing retrieval algorithms, is to multiply the absorption cross-section by a wavelength dependent AMF, that has been calculated according to Eq. (3.25). The modified DOAS equation for this case is as follows

$$I(\lambda) = I_0(\lambda)\exp\left\{-\sum_j V_j \sigma_j(\lambda) M_j(\lambda) + \sum_p a_p \lambda^p\right\} \tag{4.5}$$

Here the fitted quantities V_j are directly the vertical trace gas column. The major difference of this modified DOAS version is that a single temperature SO_2 cross-section is used in Eq. (4.5). The temperature was selected according to the assumed central plume height, as in practical applications the atmospheric temperature profile is normally not known at the time of measurement.

4.3.1 Improvements by using modified DOAS

To estimate the improvements that are possible using the modified DOAS technique, the two modified DOAS methods have been applied to simulated GOME-2 spectra. For the simulations different SO_2 total columns were used, the total vertical column varied from 0 to 500 DU. For all simulations a volcanic SO_2 profile was used with an assumed central plume height of 7 km. The ozone profile was taken from the U.S. Standard Atmosphere (U.S. Standard Atmosphere, 1976), which has a total ozone column of 369 DU. The ground albedo was set to 0.03 and the solar zenith angle was 55°. First tests were done without Raman scattering.

The retrievals without Raman scattering show that the SO_2 fitting can be significantly improved using a modified DOAS method (Table 4.2). For the standard DOAS method the issues that have been discussed in Section 4.2 can be observed. The ozone interference leads to a negative offset, which results in negative SO_2 values for low SO_2 total columns and for high SO_2 total columns the DOAS fit underestimates the SO_2 amount significantly.

By fitting the cross-sections multiplied by the AMF, major improvements of in the SO_2 retrieval can be achieved. The effect of the ozone interference is reduced significantly, the offset at low SO_2 amounts is reduced from around – 2 DU to about – 0.4 DU and for high SO_2 columns only a very slight enhancement of the ozone total columns can be observed. Further the underestimation of the total SO_2 column for high SO_2 amounts is improved. When applying the standard DOAS method to a simulated spectrum with an assumed total SO_2 column of 500 DU, the SO_2 amount is underestimated by ~ 60 %. Through fitting $\sigma_j(\lambda)M(\lambda)$ the underestimation can be reduced to ~ 8 % (Figure 4.5). The remaining difference is mainly due to the

difference between atmospheric temperature used in the simulation and the temperature assumed for the cross-section used in the fit.

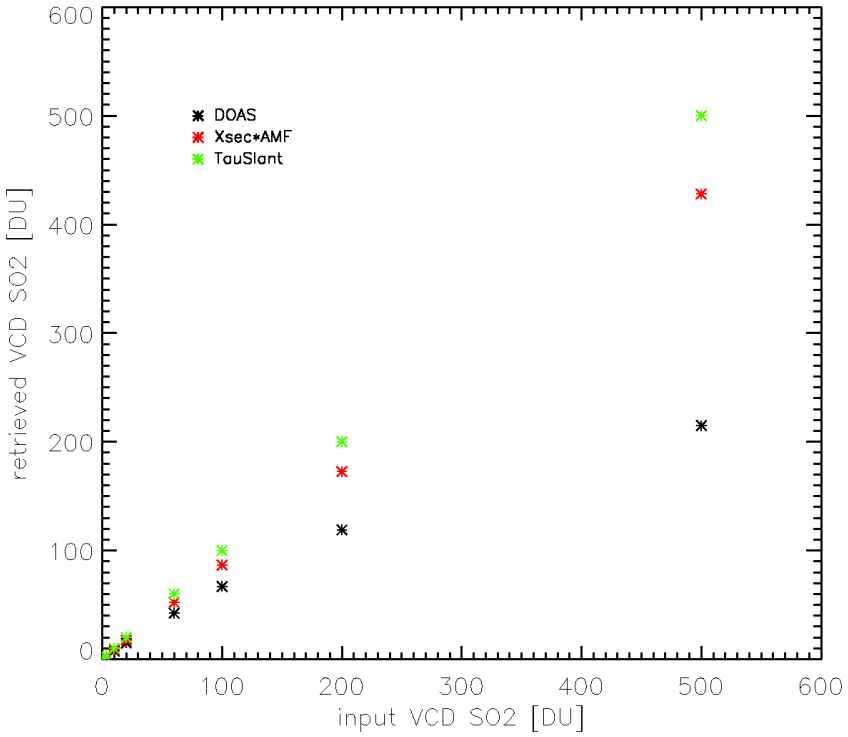

Figure 4.5: Retrieved total SO_2 column for standard DOAS and modified DOAS methods.

If fitting τ_{slant} both the retrieved SO_2 total column and the ozone total column are exactly the same as the column assumed for the simulations. These results show that under ideal conditions where the same trace gas profiles and atmospheric settings were used for the simulations and for the calculation of τ_{slant}, the retrieval works very well, e.g. no underestimation for high SO_2 values can be observed (Figure 4.5). Also the fit residuals are small. They are between 7.6 x 10^{-5} and 1.12 x 10^{-4}. Compared to the standard DOAS method it is also apparent that the fit residuals do not increase significantly when fitting high SO_2 values. Besides the retrieval of high SO_2 values, the fitting with no SO_2 included in the simulation has proven problematic in standard DOAS due to issues with the ozone interference. For this case a τ_{slant}, that has been calculated for 1 DU, has been used. The retrieved SO_2 total column of 6.13 x 10^{-4} is very low and an excellent result. The results show that fitting τ_{slant} instead of the slant column density does solve two of the major issues that occur in the standard DOAS retrieval of SO_2. It allows correct fitting of high SO_2 column values, not showing the significant underestimation that is apparent in the results retrieved using standard DOAS. Further it solves the issues due to the ozone interference, which is of major importance especially for low total SO_2 columns and therefore allows the correct retrieval of SO_2 total columns < 1 DU without the need for an external ozone correction.

Figure 4.6 shows SO_2 fits for all DOAS methods for different SO_2 total column amounts and it can be seen that the use of the modified DOAS retrievals strongly improves the fit for all total SO_2 columns, especially for very high and very low SO_2 total columns.

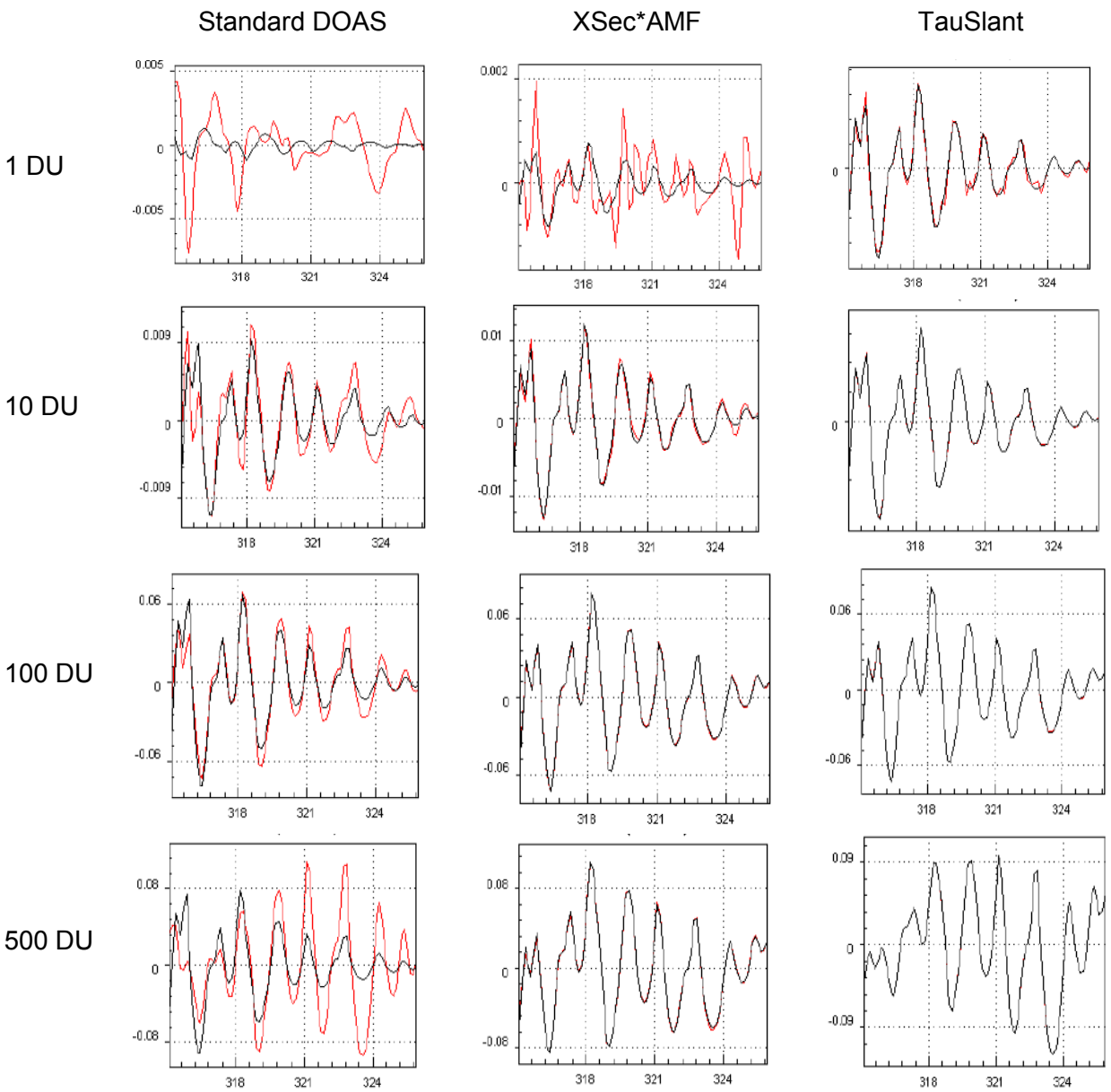

Figure 4.6: SO_2 fits for different SO_2 total columns for standard DOAS and modified DOAS methods.

Effect of Raman scattering

To estimate the influence of the Ring effect and different methods to account for it, the simulations were performed twice, once with Raman scattering included and once for elastic scattering only. Besides the two Ring cross-sections used in the operational DOAS fitting, a Ring spectrum for the specific atmospheric parameters was calculated according to Eq. (3.13) and the results for standard Ring cross-sections and the specific Ring spectrum were compared.

For all three DOAS methods the inclusion of Raman scattering in the simulations is almost negligible when using a specific Ring spectrum in the fit. For standard DOAS the fitted SO_2 total columns are almost the same for no Raman scattering and Raman scattering accounted for by a specific Ring spectrum, only for an assumed total column of 500 DU the inclusion of Raman scattering in the simulation leads to a further reduction of the SO_2 total column, so here the underestimation is even stronger when Raman scattering is included.

If fitting $\sigma_j(\lambda)M(\lambda)$ the effect of the inclusion of a specific Ring spectrum in the fit is negligible, the fitted SO_2 and ozone columns and the fit residuals do not change significantly. For the fitting of τ_{slant} the changes are very small for the total columns, for SO_2 a slight change can be observed for simulation with SO_2 total columns < 3 DU, here the results are enhanced a little, but they are still very accurate. A distinct effect can be seen in the fit residuals, they increase significantly if Raman scattering is included in the simulation.

In a second step the fits were repeated using two Ring cross-sections to account for Raman scattering. The effect for the standard DOAS fit is as explained in Section 4.1, a cancellation between the offsets induced by ozone interference and Ring effect occurs for low SO_2 total columns and for high SO_2 total columns the ozone total column is decreased.
For the modified DOAS fit using $\sigma_j(\lambda)M(\lambda)$ the effect is also significant, but here the insufficient treatment of Raman scattering affects mainly the higher SO_2 columns (Table 4.2). For total columns up to 3 DU the effect is a small positive offset as it is for standard DOAS. For higher SO_2 total columns the effect of Raman scattering is a negative offset, of up to ~ 6 % for an SO_2 column of 500 DU.
The simulations show that the error due to the insufficient treatment of the Ring effect is significant for all DOAS methods.

	Standard DOAS	τ_{slant}	$\sigma_j(\lambda)M(\lambda)$	$\sigma_j(\lambda)M(\lambda)$
Input SO_2 [DU]	**Elastic scattering**			**Including RRS**
1	-0.68	1.0	0.56	0.8
3	0.99	3.0	2.50	2.5
10	6.69	10.0	9.2	8.6
20	14.54	20.0	18.8	17.3
60	43.16	60.0	56.6	52.1
100	69.03	100.0	93.8	86.7
200	110.2	200.0	186.1	172.7
500	192.65	500.0	457.8	428

Table 4.2: Retrieval results for SO_2 total columns for standard DOAS and modified DOAS. The total ozone column was 369 DU, the solar zenith angle was set 55° and the albedo was 0.03.

4.4 Application and comparison of the standard and modified DOAS methods using GOME-2 measurement spectra

The standard and modified DOAS methods have been applied to GOME-2 data for two different volcanic eruptions. First, one measurement from each eruption, with significant SO_2 enhancement, has been selected. For this measurement according to the atmospheric conditions and trace gas concentrations inferred from the operational product a GOME-2 radiance spectrum has been simulated, to estimate how well the DOAS techniques perform under the specific conditions, when applying them to measurement data compared to the simulated GOME-2 spectra. No additional slant column corrections were applied for the tests.
In a second step the whole eruption cloud has been analyzed using standard DOAS and modified DOAS methods. The results are compared and the differences are discussed.

The eruptions of Kasatochi, Alaska (2008) and Kilauea, Hawaii (2008) were selected as they represent typical volcanic events. Kasatochi was an explosive eruption that brought large amounts of SO_2 to high altitudes, whereas the Kilauea eruption is an effusive eruption that releases only moderate SO_2 amounts at lower atmospheric levels.

4.4.1 Kilauea, Hawaii

The eruption of Kilauea, Hawaii, is a continuous eruption. The current highly active phase started in March 2008 and is still ongoing. For the tests 9 July 2008 has been selected, as the SO_2 emissions were relatively high on that day and the conditions were mainly cloud-free.
First, a single cloud-free measurement has been selected to compare the results from the different DOAS methods for real Hawaii measurements with a simulated Hawaii measurement. For the simulation, the measurement solar zenith angle (34°) was used, the ozone column was taken from the operational GOME-2 product (274 DU). For the total SO_2 column a value of 3 DU was assumed, as this is a typical value for the eruption of Kilauea. The plume height was assumed to be 2 km, as the eruption is effusive and the plume will not be much higher than the volcano summit (1222 m). The wavelength dependent AMF and the slant optical thickness required for the modified DOAS have been calculated according to these a priori settings. In addition, a Ring spectrum was calculated for the modified DOAS application using the specific settings for the measurement. The results from the modified DOAS methods were compared with the standard DOAS method using the same settings as for the operational retrieval (Chapter 3.3.4) with two Ring cross-sections, the AMF was adapted to the assumed plume height and total column.
When applying the DOAS methods to the measurement all three yield SO_2 values between 8.5 to 8.9 DU (Table 4.3), showing that the first guess of SO_2 total column (3 DU) was too low. Therefore the SO_2 total column was adapted to 10 DU and the calculations of AMF and slant optical thickness were repeated.

	Total SO_2 column of 3 DU assumed			**Total SO_2 column of 10 DU assumed**		
	Standard DOAS	$\sigma_j(\lambda)M(\lambda)$	τ_{slant}	**Standard DOAS**	$\sigma_j(\lambda)M(\lambda)$	τ_{slant}
Simulation	3.1	2.5	3.0	9.1	9.8	10.1
Measurement	8.5	8.9	8.9	9.8	9.4	9.8

Table 4.3: SO_2 total column obtained for one measurement during the Hawaii eruption with standard and modified DOAS for simulation and measurement. Assumed total SO_2 columns of 3 DU and 10 DU were used for the simulation and the calculation of the AMF and τ_{slant}.

For the standard DOAS method there are no differences in the fit (Figure 4.7), as only the AMF changes, this enhances the retrieved SO_2 total column to 9.8 DU. When comparing the measurement with the simulation assuming a total column of 10 DU, the retrieval from the measurement shows higher SO_2 values. The total column retrieved from the simulation of the measurement is 9.1 DU.
The initial fit of $\sigma_j(\lambda)M(\lambda)$ yields a total column of 8.9 DU if a total column of 3 DU is assumed for the AMF calculation. Repeating the calculation with an assumed total column of 10 DU enhances the retrieved SO_2 column to 9.4 DU. An improvement in the fit residuals can be observed, when assuming a total column of 10 DU. The retrieval on the simulated measurement shows a total SO_2 column of 9.8 DU.

Initially the fit of τ_{slant} results in a total retrieved SO_2 column of 8.9 DU. When assuming a total column of 10 DU for the calculation of τ_{slant}, the SO_2 total column is enhanced to 9.8 DU and also the fit residuals improve significantly. Comparison with the simulated measurement shows that the retrieved values match very well, the simulation yields a total SO_2 column of 10.1 DU.

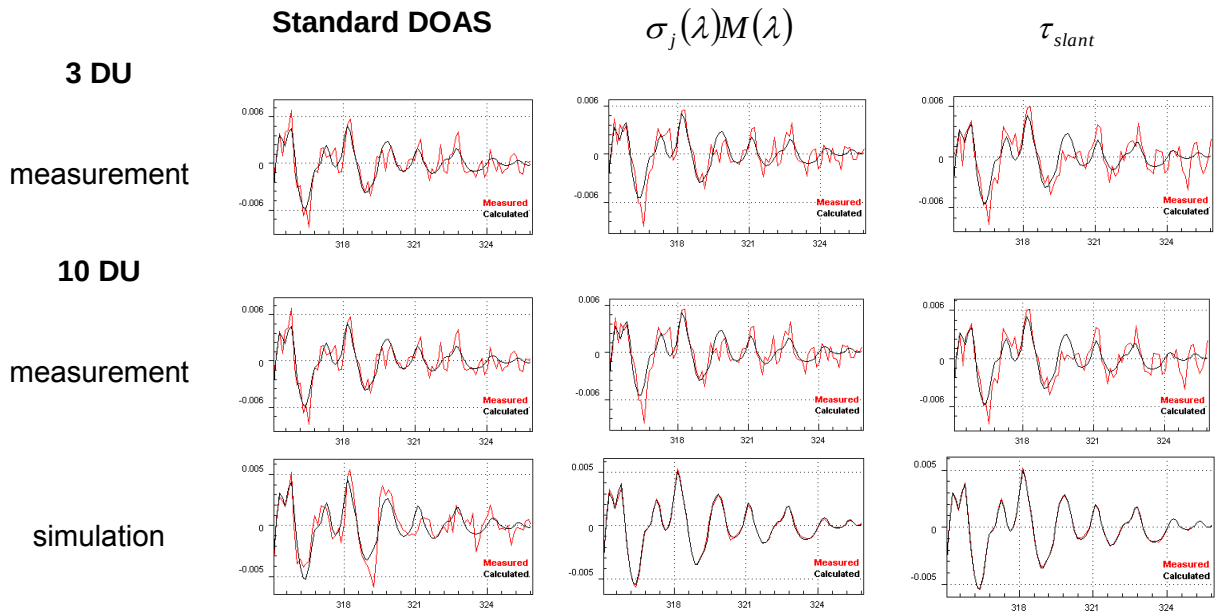

Figure 4.7: DOAS fits for measurement and simulation of Kilauea eruption, with different assumed total SO_2 columns.

Overall the results show that the "wrong" initial guess of SO_2 column did not have a high influence of the retrieved total column, using a corrected SO_2 column did enhance the retrieved column by ~ 1 DU in all cases. The fitted slant columns are very similar for all applied DOAS methods, for this moderate amount of SO_2 no significant improvement can be achieved using a modified DOAS method as here the standard DOAS fit also seems to perform very well and produces reliable results. This can also be seen in Figure 4.7 showing that the fits look similar for all three DOAS methods and that the difference between the two assumed total SO_2 columns is small.

The comparisons with the simulated measurements show, that the results do not differ significantly from the real measurement. Figure 4.7 shows that the fits are better for the simulations, especially for the modified DOAS methods. Difference between simulation and measurement can be due to the assumptions concerning SO_2 plume height, resulting in uncertainties in the AMF and also in the SO_2 cross-section, as the correct atmospheric temperature is unknown. However, using a correct temperature profile, taken from the ECMWF data for 9 July 2008, for the calculation of τ_{slant} does not improve the fit quality significantly. Also by varying the assumed plume height between 1 km and 4 km no significant improvement could be achieved. Therefore it can be concluded that the unknown atmospheric temperature is not the major source of uncertainty in this case. Aerosols can play an important role as they are not included in the simulation. Further, there is an uncertainty in the assumed ozone total column and profile. An imperfect treatment of the Ring effect also introduces additional errors compared to the simulations. A major difference when applying the DOAS methods to measurement spectra are additional errors

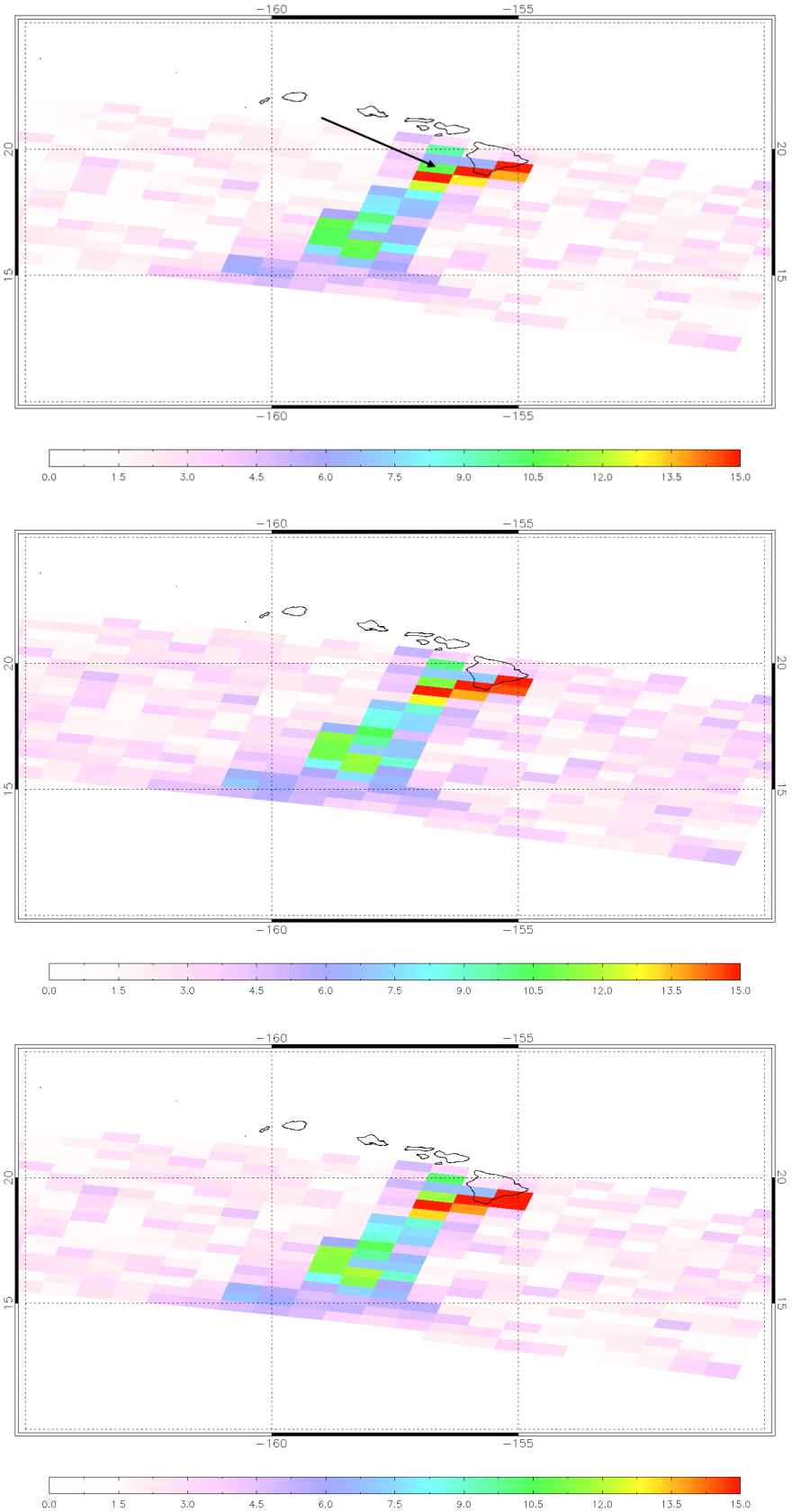

Figure 4.8: SO_2 plume from Hawaii eruption on 9 July 2008, retrieved from GOME-2 data using the standard DOAS (top) and modified DOAS approaches, $\sigma_j(\lambda)M(\lambda)$ (middle) and τ_{slant}(bottom). The arrow denotes the measurement used for the detailed comparison.

introduced by uncertainties in the GOME-2 irradiance spectra, e.g. due to instrument calibration issues, slit function inaccuracies, etalon structures and imperfect polarization corrections. Also uncertainties in the SO_2 cross-section are a possible error source. The instrument noise results in further fit errors. Instrument noise leads to deviations in the total SO_2 columns of up to ± 0.8 DU depending on the plume height (Chapter 5.1). Therefore these issues play an important role for moderate SO_2 amounts as observed for the Kilauea eruption.

When applying the different DOAS retrievals to the complete eruption on 9 July 2008 only small differences can be detected between the retrieval methods. In Figure 4.8 it can be seen that the modified DOAS methods retrieve slightly higher values close to the volcano. Figure 4.9 shows this effect in more detail, it can be seen that the modified DOAS methods always retrieve slightly higher results compared to standard DOAS, most probably due to the fact, that modified DOAS is more capable of dealing with the interference of ozone, as has been seen in the theoretical tests. However, as has already been determined from the tests using simulated spectra, the differences for all methods for low and moderate SO_2 total columns are small, typically below 10 %. When estimating the total SO_2 mass emitted by Kilauea volcano, the results are similar for all DOAS retrievals; estimates from standard DOAS yield a total emitted mass of 0.13 Tg for that day, modified DOAS results in 0.15-0.16 Tg SO_2.

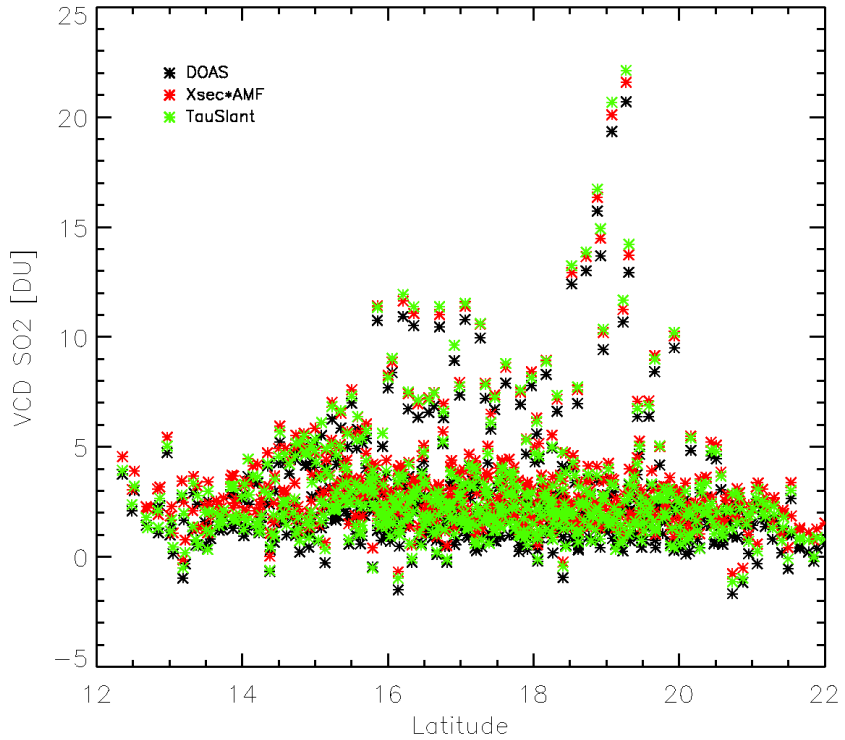

Figure 4.9: Total SO_2 columns for the Kilauea eruption on 9 July 2008 for standard DOAS and modified DOAS methods

4.4.2 Kasatochi, Alaska

The eruption of Kasatochi, Alaska, on 7 August 2008 brought large amounts of SO_2 high into the atmosphere. The measurement with the highest SO_2 amount for the first day after the eruption was selected from the operational DOAS fit. As for the Hawaii measurements the GOME-2 radiance has been simulated additionally to allow a

comparison of measured and simulated results. For the simulation and the calculation of the wavelength dependent AMF and τ_{slant} the SO_2 column from the operational DOAS fit has been used as first guess. The total SO_2 column was 120 DU. The plume height was chosen according to trajectory matching for the Kasatochi eruption that indicated 11 km to be the most probable height (Seidenberger, 2009). The ozone total column taken from the operational GOME-2 product was 340 DU and the measurement SZA was 41°. As for the Kasatochi eruption the scene was partly cloudy the TOA radiance was calculated using an independent pixel approximation as a linear combination of radiance from clear and fully cloudy scenes, weighted by the cloud fraction c_f. As for the Kilauea eruption a specific Ring spectrum was calculated for the modified DOAS methods and the results are compared with the standard DOAS method using the settings from the operational retrieval with the AMF being adjusted according to SO_2 plume height and total column.

	Total SO_2 column of 120 DU assumed			**Total SO_2 column of 150 DU assumed**		
	Standard DOAS	$\sigma_j(\lambda)M(\lambda)$	τ_{slant}	**Standard DOAS**	$\sigma_j(\lambda)M(\lambda)$	τ_{slant}
Simulation	114.3	128.0	120.0	140.4	160.0	150.0
Measurement	135.3	157.4	148.8	141.0	167.5	157.5

Table 4.4: SO_2 total column obtained for one measurement during the Kasatochi eruption with standard and modified DOAS for simulation and measurement. Assumed total SO_2 columns of 120 DU and 150 DU were used for the simulation and the calculation of the AMF and τ_{slant}.

The standard DOAS fit yields a total SO_2 column of 135.3 DU. When applying the modified DOAS methods, the values are significantly higher, 148.8 DU for fitting τ_{slant} and 157.4 DU for fitting $\sigma_j(\lambda)M(\lambda)$ (Table 4.4).

As the modified DOAS techniques indicate a much higher SO_2 column than the assumed initial column of 120 DU, the calculations were repeated assuming a total SO_2 column of 150 DU. For the standard DOAS approach simply the AMF changes and brings the value up to 141 DU. This matches the results for the simulated GOME-2 spectrum nicely, where a total SO_2 column of 140 DU is obtained for an assumed column of 150 DU.

Applying the modified DOAS techniques to the measurement, when assuming a total SO_2 column of 150 DU for the calculation of the AMF and τ_{slant}, enhances the results by about 10 DU. Fitting $\sigma_j(\lambda)M(\lambda)$ now yields a total SO_2 column of 167.5 DU. The simulation indicates total SO_2 columns very close to the assumed value of 150 DU. The fitting of τ_{slant} results in total SO_2 column values of 157.5 DU. The fit residuals are similar for both modified DOAS versions and about half of those for the standard DOAS fit.

The results show that for high SO_2 the improvement achieved by the use of modified DOAS is significant. While the standard DOAS technique retrieves total SO_2 columns of about 140 DU the results are around 160 DU for modified DOAS. It can also be seen, that the iterative adaptation of the first guess SO_2 total column leads to significant changes in the results and reduces the fit residuals indicating a better fit quality. Figure 4.10 shows that for these high SO_2 total columns the modified DOAS methods perform better, further it can be seen that the fits are better when assuming 150 DU for the total SO_2 column.

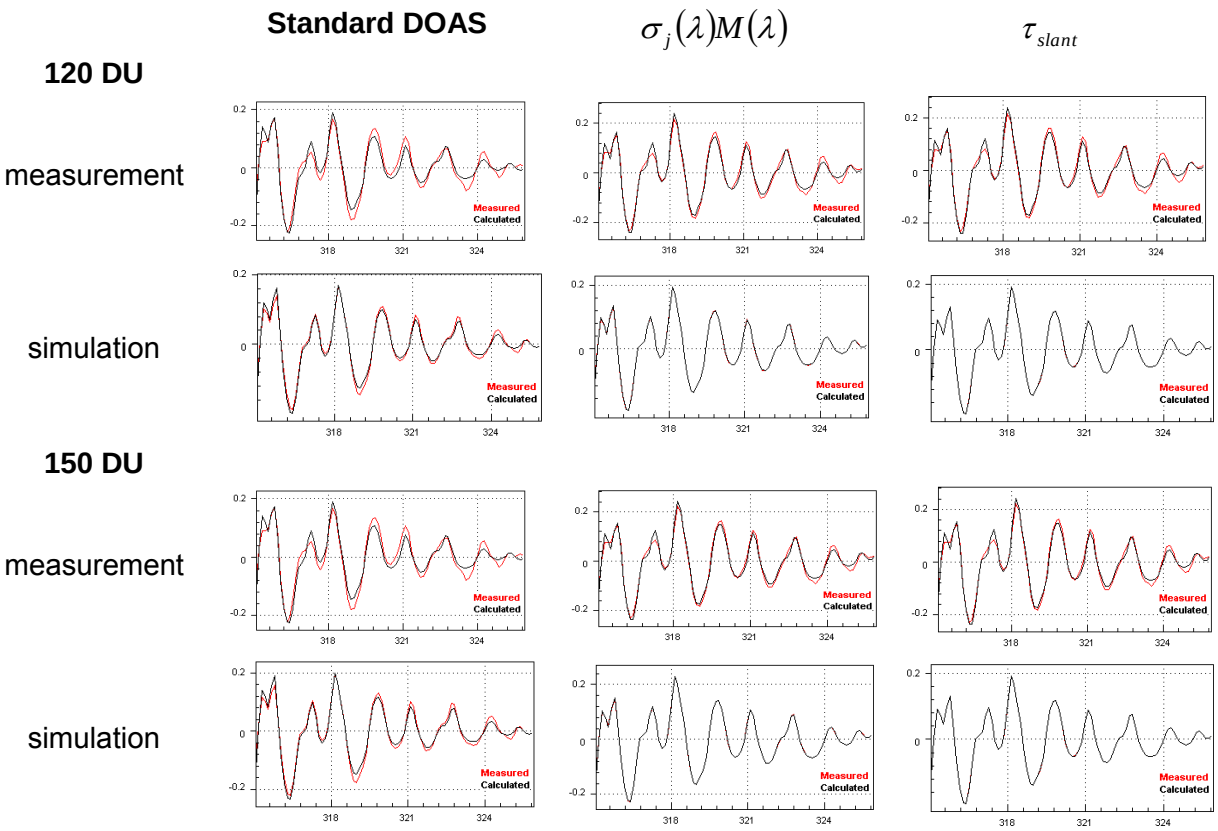

Figure 4.10: Standard and modified DOAS fits for measurement and simulation of Kilauea eruption, with different assumed total SO_2 columns.

For the Kasatochi eruption the results from measurements and simulations do not match as well as for the case of Hawaii, from the simulations a larger difference between the standard DOAS results and those from modified DOAS would be expected. Figure 4.10 shows a much better quality of the fits for the simulations, especially for the modified DOAS methods. For the eruption of Kasatochi a moderate improvement of the modified DOAS fit could be achieved by using an ECMWF temperature profile for the calculation of τ_{slant}, while the variation of the assumed SO_2 plume height had no significant effect. However, as for the eruption of Kilauea, the atmospheric temperature is not the major source of uncertainty. Besides the temperature, uncertainties in the total column can play an important role, as can uncertainties in the ozone profile or absorption cross-sections and an imperfect treatment of the Ring effect. GOME-2 irradiance issues should not have a significant effect in this case, as they introduce uncertainties on the order of 1 DU, which are negligible compared to the total column. Major differences compared to the Kilauea eruption are the presence of clouds and aerosols. The observation at Kilauea was cloud free and the plume from the effusive eruption typically contains little ash. Opposed to that the scene at Kasatochi was cloudy and a high amount of aerosol is very likely as the eruption was explosive and therefore the eruption plume most probably contained large amounts of ash.

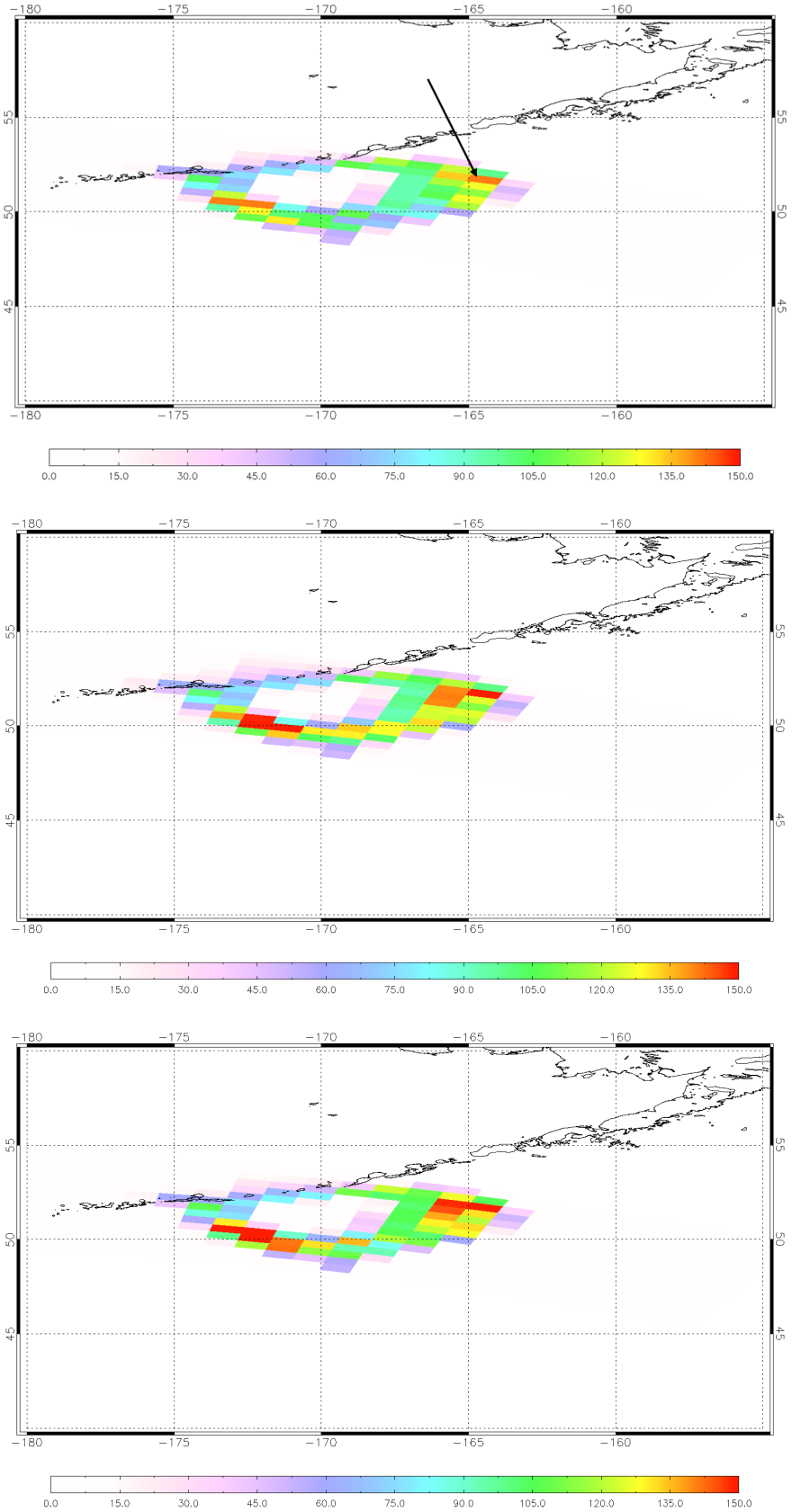

Figure 4.11: SO_2 plume from Kasatochi eruption on 8 August 2008, retrieved from GOME-2 data using the standard DOAS (top) and modified DOAS methods, $\sigma_j(\lambda)M(\lambda)$ (middle) and τ_{slant} (bottom). The measurement marked with the arrow, was used for the detailed comparison.

Applying the different DOAS methods to the complete eruption of Kasatochi shows major differences in the results (Figure 4.11). The total columns retrieved using modified DOAS are up to 25 % larger than those using standard DOAS, especially for high total SO_2 columns (Figure 4.12). The total SO_2 mass emitted during the Kasatochi eruption could be estimated to ~ 0.6 Tg using the Standard DOAS retrieval and to ~ 0.7 Tg using modified DOAS.

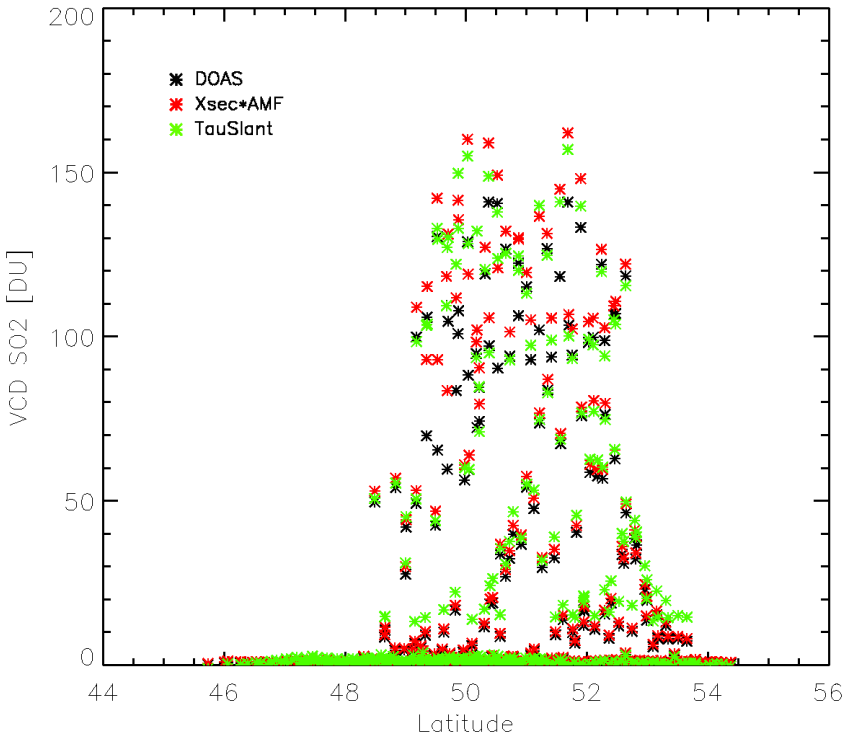

Figure 4.12: Total SO_2 columns for the Kasatochi eruption on 8 August 2008 for Standard DOAS and modified DOAS methods.

4.5 Direct fitting of SO_2

With the direct fitting method the total column is retrieved from direct least squares inversion of radiances using radiative transfer simulations of the radiances and total column weighting functions.

$$I_m - I = \Delta V_{O3} \left.\frac{\partial I}{\partial V_{O3}}\right|_{V_{O3}=V_{O3,0}} + \Delta V_{SO2} \left.\frac{\partial I}{\partial V_{SO2}}\right|_{V_{SO2}=V_{SO2,0}} + \left(\Delta R + \sum_{i=1}^{n} a_i (\lambda - \lambda_0)\right) \left.\frac{\partial I}{\partial R}\right|_{R=R_0} \quad (4.6)$$

where I_m is the measured radiance. Through a radiative transfer model the TOA radiance I is calculated as a function of the vertical columns of ozone (V_{O3}), SO_2 (V_{SO2}) and the surface albedo (R). For the retrieval the parameters V_{O3}, V_{SO2} and R are adjusted until the simulated radiances from the model match the measurements. An initial state vector is chosen as a reference point {$V_{O3,0}$, $V_{SO2,0}$, R_0, a_1=0, a_2=0} and changes in the parameters are expressed as deviations from this reference ($\Delta V_{O3} = V_{O3} - V_{O3,0}$, $\Delta V_{SO2} = V_{SO2} - V_{SO2,0}$, $\Delta R = R - R_0$).

The direct fitting method solves issues that arise in the standard DOAS retrieval due to the separation of slant column fitting and radiative transfer processes in the AMF

calculation. The direct fitting algorithm used was the GODFIT (**GO**ME **D**irect **Fit**ting) algorithm (Spurr et al., 2009) originally developed for ozone retrieval. It was used to retrieve SO_2 from simulated GOME-2 spectra. In this section first a short description of the GODFIT algorithm will be given followed by a discussion of the results and a comparison of the results with those obtained using standard DOAS and modified DOAS methods.

4.5.1 The GODFIT algorithm

The GODFIT algorithm uses a classical inverse method of iterative least squares merit-function minimization to solve Eq. (4.6). It is based on a linearized forward model (LIDORT) that allows on-the-fly multiple scatter radiative transfer simulation of GOME-2 earthshine radiances and weighting functions with respect to state vector elements. The state vector elements for fitting SO_2 are the total columns of SO_2 and ozone, albedo closure coefficients, a Ring correction amplitude, a wavelength registration shift and other ancillary parameters.

Figure 4.13 shows an overview of the GODFIT algorithm. After reading the GOME-2 radiance and irradiance data and the auxiliary data, e.g. cloud information or optional ECMWF profiles, an initial guess is made for the state vector. The cloud information is derived from OCRA (fractional cover) and ROCINN (cloud-top height and albedo) (Loyola et al., 2007).
Then unique ozone profiles are constructed from the total column estimate based on a column classified ozone profile climatology (TOMS Version 8) (Wellemeyer, et al., 2004). Further profiles of pressure and temperature are constructed and spectral reference data is created for the fitting window.
After the set-up the LIDORT model is called to deliver TOA radiances I(n) together with the associated trace gas columns and albedo weighting functions at each iteration step n. The simulated quantities are corrected for the Ring effect. In the next step the inversion module yields a new guess for the state vector parameters until suitable convergence criteria are satisfied.

The core of the system is the radiative transfer calculation using the LIDORT model, which has been described in Section 3.4.1. One major difference to the set-up explained before, is that for the GODFIT algorithm the albedo is not set as an external parameter but determined internally through an albedo closure term. This term includes surface reflectivity and aerosol scattering and absorption. It is assumed that the surface albedo R(λ) is a 3-parameter function of the wavelength λ

$$R(\lambda) = \gamma_0 + \gamma_1\left(1 - \lambda/\lambda_0\right) + \gamma_2\left(1 - \lambda/\lambda_0\right)^2 \tag{4.7}$$

The Jacobians are defined with respect to the fitted parameters ($\gamma_0, \gamma_1, \gamma_2$).

$$K_{\gamma_0}(\lambda) = K_R(\lambda) \tag{4.8}$$

$$K_{\gamma_1}(\lambda) = \left(1 - \lambda/\lambda_0\right) K_R(\lambda) \tag{4.9}$$

$$K_{\gamma_2}(\lambda) = \left(1 - \lambda / \lambda_0\right)^2 K_R(\lambda) \tag{4.10}$$

Where $K_R(\lambda)$ is the albedo weighting function. The initial value for γ_0 is taken from a suitable database, first guess values for γ_1, γ_2 are $\gamma_1 = \gamma_2 = 0$.

Furthermore, clouds are included in the radiative transfer simulations. GODFIT uses an independent pixel approximation (IPA). The TOA radiances for partly cloudy scenes are simulated as a linear combination of backscatter from clear and fully cloudy scenes, weighted by the effective cloud fractional cover ϕ. Cloud optical properties are obtained from the OCRA/ROCINN algorithm (Loyola et al., 2007). OCRA provides the cloud fractions and ROCINN the cloud-top height and albedo. Clouds are treated as Lambertian reflectors.

The GODFIT version used in this work uses the Optimal Estimation method as an inverse function, with loose a priori constraints on the state vector elements. For the operational use in the GDP5 project, a faster inversion method has been implemented, a variant of the Levenberg-Marquardt least squares algorithm with line searching.

The optimal estimation method involves minimizing of a chi-square merit (or cost) function, representing the difference between the observation and the simulated spectra from the forward model. As the retrieval problem is ill conditioned, that is the number of fitting parameters exceeds the pieces of independent information, a regularization term is added to the cost function.

$$\chi^2 = (\mathbf{Y}_m - F(\mathbf{X}))^{\mathrm{T}} \mathbf{S}_y^{-1} (\mathbf{Y}_m - F(\mathbf{X})) + (\mathbf{X} - \mathbf{X}_\mathrm{a})^{\mathrm{T}} \mathbf{S}_\mathrm{a}^{-1} (\mathbf{X} - \mathbf{X}_\mathrm{a}) \tag{4.11}$$

where $\mathbf{Y}_m$ is the measurement vector of TOA radiances, $\mathbf{X}$ is the state vector, $F(\mathbf{X})$ are the simulated radiances from the forward model and $\mathbf{S}_y$ is the error covariance matrix. $\mathbf{X}_\mathrm{a}$ is the a priori state vector with the corresponding covariance matrix $\mathbf{S}_\mathrm{a}$. The non-linear least squares fitting proceeds iteratively via a series of linearizations about the atmospheric state at each iteration step n:

$$\mathbf{X}_{i+1} = \mathbf{X}_\mathrm{a} + \mathbf{D}_y \left[\mathbf{Y}_m - F(\mathbf{X}_i) - \mathbf{K}_i (\mathbf{X}_i - \mathbf{X}_\mathrm{a})\right] \tag{4.12}$$

with

$$\mathbf{D}_y = \mathbf{S}_{i+1} \mathbf{K}_i^{\mathrm{T}} \mathbf{S}_y^{-1} \quad \text{and} \quad \mathbf{S}_{i+1} = \left(\mathbf{K}_i^{\mathrm{T}} \mathbf{S}_y^{-1} \mathbf{K}_i + \mathbf{S}_\mathrm{a}^{-1}\right)^{-1} \tag{4.13}$$

$\mathbf{K}_i = \dfrac{dF(\mathbf{X}_i)}{d\mathbf{X}_i}$ is the matrix of Jacobians which are also referred to as weighting functions, $\mathbf{D}_y$ is the matrix of contribution functions and $\mathbf{S}_{i+1}$ is the solution covariance matrix. The iteration stops when the convergence criteria are met.

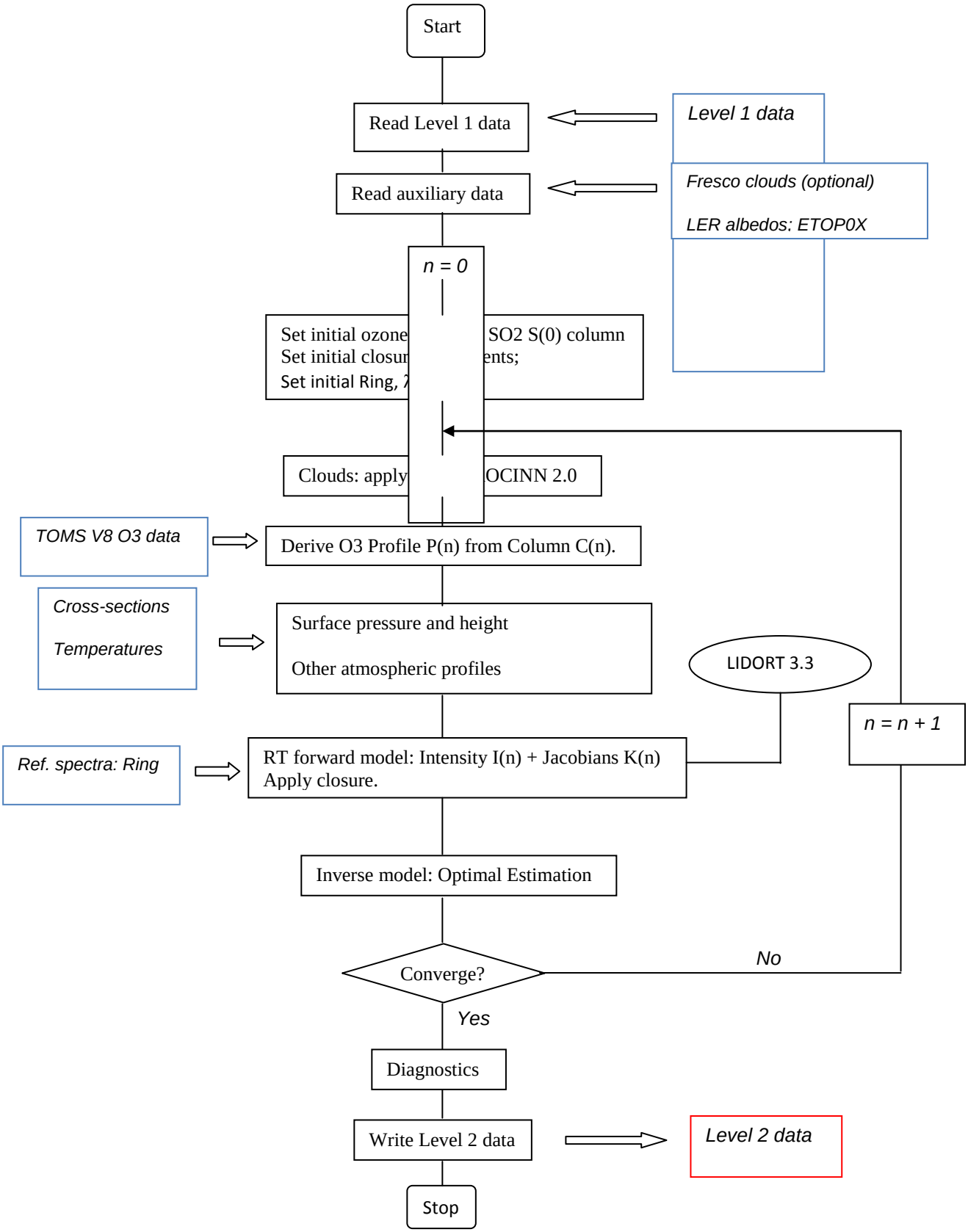

Figure 4.13: Flow Diagram of the GODFIT direct fitting retrieval algorithm (adapted from Spurr et al., 2009).

4.5.2 Improvements by using Direct Fitting

The direct fitting of SO_2 has first been applied to synthetic GOME-2 radiance spectra. To allow a comparison of the results the same set of retrieval settings concerning fitting window and cross-sections has been applied. Similar settings for the SO_2 total column and plume height, ozone total column and satellite viewing geometry were chosen (Total SO_2 column: 0.1 – 500 DU, SO_2 plume height: 7 km, total O_3 amount: 365 DU, SZA: 50°). Currently only a single temperature SO_2 cross-section can be used for the retrieval. The cross-section temperature has been chosen according to the assumed SO_2 plume height. All results discussed here have been conducted including Raman scattering. Then additional simulations have been performed for settings that have proven to be problematic in standard DOAS applications, e.g. high O_3 total columns or high SZAs. Further the sensitivity to the choice of input SO_2 profile has been tested.

Input SO_2 [DU]	Standard DOAS	$\sigma_j(\lambda)M(\lambda)$	Direct Fitting
1	-0.68	0.56	0.65
3	0.99	2.50	2.65
10	6.69	9.2	10.0
20	14.54	18.8	19.6
60	43.16	56.6	60.0
100	69.03	93.8	100.8
200	110.2	186.1	201.4
500	192.65	457.8	510.2

Table 4.5: Retrieval results for SO_2 total columns for standard DOAS, modified DOAS and direct fitting. The total ozone column was 369 DU, the solar zenith angle was set 55° and the albedo was 0.03.

The direct fitting results for SO_2 using the standard settings can overall be considered very accurate, especially for high SO_2 total columns (Table 4.5). For SO_2 total column amounts > 10 DU the deviation from the input SO_2 amount is less than 2 %. For lower SO_2 columns a slight negative offset of ~ 0.35 DU can be observed. Further simulations with different O_3 total columns show that this is due to ozone (Table 4.6). Unlike in the tests with modified DOAS, ozone can cause issues in the direct fitting tests. For the tests with modified DOAS the same ozone profile was used in the simulation of the spectra and for the calculation of the AMF and τ_{slant}, allowing an optimal treatment of ozone. For direct fitting a different ozone profile than for the spectra simulations is used as first guess in the fitting procedure and then adapted iteratively. For higher O_3 columns the negative offset at small SO_2 columns is ~ 0.8 DU for a total O_3 column of 450 DU. For high SO_2 columns the opposite effect can be observed, for O_3 columns of 365 DU and 450 DU the total SO_2 columns are enhanced by ~ 2 % and ~ 4 % respectively. For low O_3 total columns (200 DU) the effect changes, here the low SO_2 total columns are enhanced by ~ 0.65 – 1 DU, while higher SO_2 columns show almost no deviation from the input total SO_2. Increasing the SZA enhances the ozone interference slightly, for an SZA 70° and a total O_3 column of 365 DU, the offset increases to – 0.6 DU, which is still moderate compared to standard DOAS retrieval.

Input SO_2 [DU]	O_3 200 DU	O_3 365 DU	O_3 450 DU
1	1.57	0.65	0.23
3	3.65	2.65	2.21
10	11.3	10.0	9.53
20	21.2	19.6	19.0
60	62.3	60.0	59.4
100	102.8	100.8	100.7
200	199.9	201.4	204.1
500	497.5	510.2	519.3

Table 4.6: Retrieval results for SO_2 total columns with direct fitting using different total ozone columns, the solar zenith angle was set 55° and the albedo was 0.03.

Further it can be observed that direct fitting retrieval at high SZAs of up to 80° still yields fairly good results for the SO_2 total columns > 10 DU; the induced errors are ~ 4 % for SZA 70° and ~ 10 % for SZA 80°. For lower SO_2 total columns the errors are higher, but even values of 3 DU can still be detected for SZA=80°, whereas the standard DOAS retrieval at these solar zenith angles does not yield any useful results.

To test the sensitivity to the SO_2 input parameters, the retrieval has been repeated with a fixed a priori SO_2 profile containing 1 DU SO_2. For simulated total SO_2 columns up to 100 DU the choice of SO_2 profile does not influence the retrieval results. When retrieving 200 and 500 DU SO_2, the choice of an a priori SO_2 profile of 1 DU leads to an underestimation of the total columns of ~ 11 % and ~ 15 %, respectively. Overall the retrieval is mainly independent of the a priori choice of total SO_2 column, which is a major advantage compared to both DOAS methods, where in principle knowledge of the total SO_2 and ozone column is required to calculate a suitable AMF or τ_{slant}. However, as with DOAS retrieval, the choice of plume height influences the retrieval results significantly. The fitted total SO_2 columns increase for lower assumed plume heights.

Compared to standard DOAS the use of a direct fitting algorithm provides major improvements concerning the issues due to ozone interference, high solar zenith angles and high SO_2 total column amounts. Compared to modified DOAS the direct fitting results for low total SO_2 columns are within 5 % of those when fitting $\sigma_j(\lambda)M(\lambda)$, for higher SO_2 columns (> 10 DU) the direct fitting is more accurate. Fitting of τ_{slant} yields the most accurate results for the simulations carried out in this study. This is due to the fact, that for the simulation of the spectra and the calculation of τ_{slant} the exact same trace gas profiles and atmospheric settings have been used, while for the direct fitting the a priori ozone and SO_2 profiles in the fit are different from those used in the simulations. However, for SO_2 total columns > 10 DU, the direct fitting results are within 2 % of the correct value providing the advantage that no a priori knowledge of the SO_2 and O_3 total columns is needed, which is usually not available when applying the different retrieval methods to real GOME-2 measurement data.

4.6 Application of direct fitting to GOME-2 measurement spectra

The direct fitting method has been applied to GOME-2 measurements of two different volcanic eruptions. The eruption of Mount Etna in May 2008 is used as an example with low to moderate SO_2 total columns in the mid-troposphere and the Kasatochi eruption in August 2008 is chosen as an eruption that brought high amounts of SO_2 to the stratosphere. The results are compared with the standard DOAS method used for the operational GOME-2 SO_2 product.

Etna, Italy

The eruption of Mount Etna started on 11 May 2008 and lasted for 4 days. For the analysis 14 May 2008 has been selected. As the eruption brought moderate amounts of SO_2 to mid-tropospheric heights, a volcanic SO_2 profile with a central plume height of 6 km has been used for the direct fitting. For comparison the operational SO_2 product also with an assumed plume height of 6 km is used. Figure 4.14 shows the direct fitting results (left) and the standard DOAS results (right). It can be seen that the retrieved SO_2 total columns are very similar in both cases. The maximum SO_2 total column is 9.5 DU for both methods and also the estimated total SO_2 mass is very similar, the standard DOAS approach yields a total SO_2 mass of 0.023 Tg and with direct fitting the total mass yields 0.021 Tg.

From the theoretical fits (Table 4.5) slightly higher SO_2 values would have been expected for the direct fitting. However, when evaluating the simulated GOME-2 spectra no slant column corrections were applied to account for ozone interference. For this comparison the operational GOME-2 product was used, which includes SO_2 slant column corrections (Chapter 3.3.5). The good agreement between the two methods suggests that for this eruption the applied slant column corrections are suitable to limit the effects of ozone interference in the standard DOAS.

Overall it can be seen, that the direct fitting method does not improve the results from the standard DOAS approach significantly for low and moderate SO_2 total columns, as has already been seen in the tests using the synthetic GOME-2 spectra.

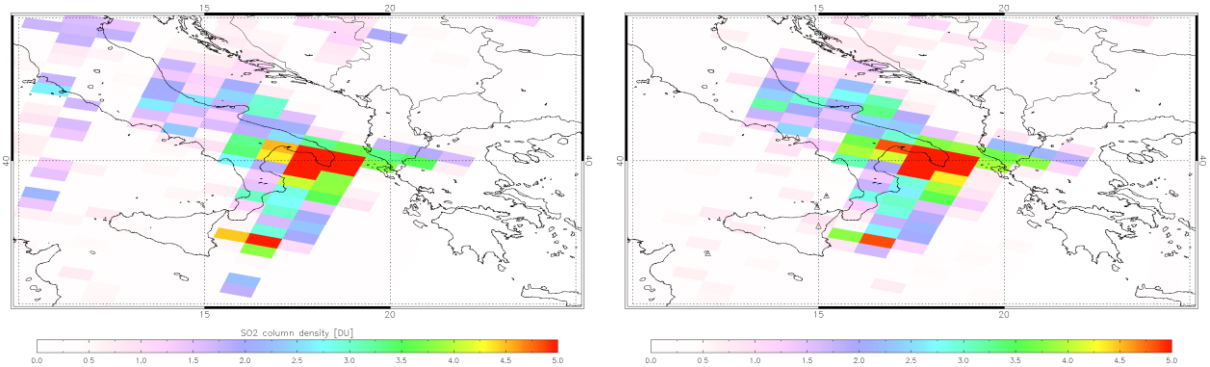

Figure 4.14: SO_2 plume from Etna eruption on 14 May 2008 retrieved with direct fitting (left) and standard DOAS (right).

Kasatochi, Alaska

The GODFIT algorithm has also been applied to GOME-2 measurement data of the Kasatochi eruption. For the retrieval an a priori SO_2 profile containing 100 DU SO_2 with a central plume height of 11 km is assumed. The results of the direct fitting method are compared with the results obtained in Section 4.4.2 using the standard and modified DOAS method, in this case no slant column corrections are applied.

For the Kasatochi eruption cloud, the direct fitting yields much higher SO_2 values (Figure 4.15, left) compared to all DOAS methods (Figure 4.11) in large parts of the plume. The estimated total SO_2 mass erupted for this day is 0.8 Tg, compared to ~ 0.6 Tg using the standard DOAS retrieval and to ~ 0.7 Tg using modified DOAS. Interesting is that the maximum SO_2 amount observed is with 302 DU not only much higher than for the DOAS methods (~ 140 -170 DU) but also in a different location (Figure 4.15, right).

Apparently the direct fitting algorithm is able to deal with very high SO_2 amounts released during the Kasatochi eruption better than the DOAS methods. From the theoretical tests the large difference compared to the standard DOAS approach could be expected, however the modified DOAS methods should yield similar results as the direct fitting (Table 4.5). As has been explained in Section 4.4 errors in the level-1 spectra and uncertainties in the trace gas total columns and profiles lead to additional errors when applying the retrieval methods to measurement spectra. However, besides these common issues there are two major differences between the two approaches. First a simple treatment of clouds was used in the modified DOAS approach, where only the change in albedo is taken into account. The GODFIT algorithm also uses the information on cloud-top height for the radiative transfer simulations. Additionally, in the direct fitting any aerosols that might be present are accounted for in the albedo closure directly, whereas in the DOAS methods aerosols are not taken into account. This could also explain why the maximum SO_2 amount was detected in a different area of the volcanic cloud.

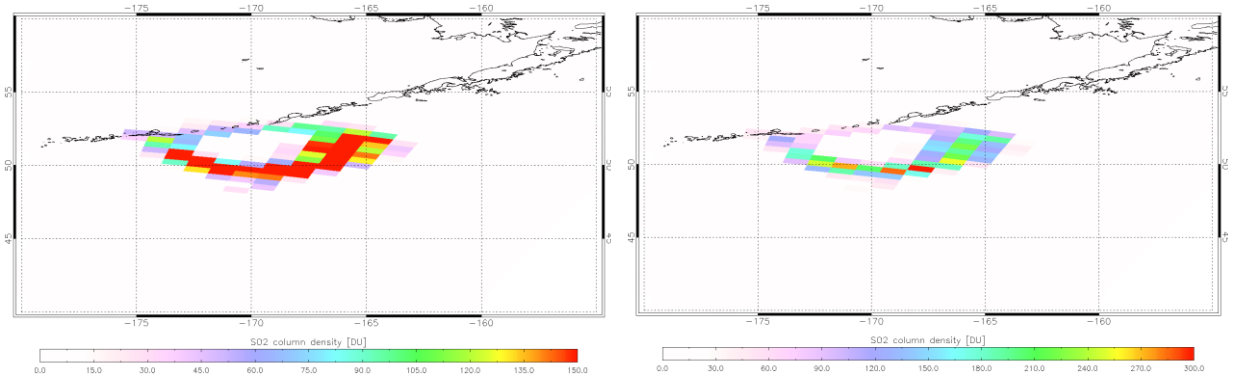

Figure 4.15: SO_2 plume from Kasatochi eruption on 8 August 2008, retrieved from GOME-2 data using direct fitting. The right panel shows the location of the maximum SO_2 amount (302 DU) observed. Note that the color scale is different in the right image to show the location of the maximum SO_2 amount.

4.7 Conclusions

Overall the application of the standard DOAS method to the simulated radiances shows that the retrieval yields good results for low and moderate SO_2 column amounts < 20 DU. Here the improvements that can be achieved using modified DOAS or direct fitting are small, especially when taking into account that the ozone dependence of the SO_2 slant column can be accounted for to a large extent with an external slant column correction. For higher SO_2 columns the improvements using modified DOAS or direct fitting become quite large, here the use of standard DOAS results in a significant underestimation of the total SO_2 columns (- 40 %). The best results for high SO_2 columns, with errors typically below 10 %, are obtained by fitting τ_{slant} or by using a direct fitting algorithm. Direct fitting has the major advantage, that the fit results are mainly independent of the a priori choice of SO_2 total column amount. This is of great importance when applying the different retrieval techniques to real measurement data, where the total column amount of SO_2 is not known beforehand.

Application of the retrieval methods to GOME-2 measurement data shows that for low SO_2 columns (Kilauea, Etna) the differences between the retrievals are small, as was expected from the simulations. For high SO_2 total columns (Kasatochi, Alaska) the differences become more apparent, here the use of the standard DOAS approach yields lower total column amounts than the other retrieval techniques. However, the difference between standard and modified DOAS (~ 15 %) is not as large as would be expected from the simulations. Likely reasons are calibration errors in the GOME-2 irradiance data and uncertainties in the SO_2 cross-sections, unknown SO_2 plume height and atmospheric temperature profile lead to additional uncertainties. The highest total column amounts, which are with maximum columns ~ 300 DU about twice the amount retrieved with the DOAS methods, are obtained using direct fitting. Further this retrieval method detects the maximum SO_2 amount in a different location than the DOAS techniques. Most likely this is due to the more sophisticated treatment of clouds and aerosol in the direct fitting algorithm, whereas aerosols can have a large effect on the AMF calculation for the DOAS retrievals.

However, the major advantage of the SO_2 retrieval using standard DOAS is that this approach allows the detection of SO_2 in near-real time (NRT), whereas the other methods, especially the direct fitting, are computationally expensive and therefore time consuming. This is of high importance in cases where the information on atmospheric SO_2 is needed in NRT, as for volcanic eruptions. In the case of volcanic emissions, SO_2 is often used for aviation hazard mitigation or for early warning of volcanic activity (Chapter 7). For these issues the NRT supply of information is a crucial requirement. Further in these cases the presence and location of SO_2 is the central piece of information, whereas the correct determination of the total column amount plays a minor role. It can therefore be concluded that currently the standard DOAS approach is a good choice for NRT operations, as it allows fast detection of atmospheric SO_2. Modified DOAS could also be an option when storing $\sigma_j(\lambda)M(\lambda)$ or τ_{slant} in a look-up table. Direct fitting is currently not suitable for NRT retrieval of SO_2, but is the state of the art method to reanalyze volcanic eruption in terms of maximum SO_2 column and total SO_2 amount emitted, as it is independent of a priori choice of total column SO_2 and O_3 and accounts for aerosols.

5. Validation of the operational GOME-2 SO_2 data

In this chapter a validation of the operational GOME-2 SO_2 product is presented. First an analysis of GOME-2 SO_2 data quality and detection limit is presented and the effect of instrument degradation on SO_2 is discussed. Then a comparison with the SCIAMACHY instrument for different volcanic eruptions is presented. Additionally, the GOME-2 SO_2 data are validated against ground-based measurements of volcanic SO_2 and anthropogenic pollution. The comparisons for volcanic SO_2 are made for the effusive SO_2 emissions at Kilauea, Hawaii and during the overpass of the Kasatochi eruption cloud in Europe and North America. The pollution measurements were conducted in Beijing.

5.1 GOME-2 SO_2 error and detection limit

In the following section the random noise and the detection limit for GOME-2 SO_2 is discussed for the different assumed plume heights (Chapter 3.4.3). The random error in the SO_2 total vertical column (σ_V) is mainly a function of errors in the slant column density S, which are to a large extent due to instrument noise.

$$\sigma_S^2 = \left(\frac{\partial V}{\partial S}\right)^2 \sigma_S^2 \tag{5.1}$$

Scaling σ_S with the air mass factor M yields the vertical column density error.

$$\sigma_V = \frac{\sigma_S}{M} \tag{5.2}$$

As M is smaller for lower plume heights the error increases with decreasing altitude of the SO_2 (Figure 5.1).

To estimate the noise of the GOME-2 SO_2 vertical columns the retrieval statistics over a pristine ocean region have been examined. In this region the SO_2 is only of background concentration which is typically close to zero (Seinfeld and Pandis, 2006). In this region the GOME-2 SO_2 values have a statistical distribution with a Gaussian shape around zero due to measurement errors. The detection limit is typically considered twice the standard deviation (2σ), which can be derived from the distribution of the SO_2 columns in this region.
Here, we use the equatorial Pacific from 10° N – 10° S and 170° E – 120° W. Typically no SO_2 is present in this region. However, as SO_2 clouds can occasionally occur in this area, due to volcanic eruptions in South America or Hawaii, after the first calculation of the standard deviation all measurements containing SO_2 values > 2σ are identified and excluded from the final analysis. The equatorial region is used to estimate the SO_2 detection limit as the measurement conditions are favorable in this region, the solar zenith angles are low and the ozone total columns do not show high variations. The average standard deviation of the SO_2 total columns is 0.18 DU for a plume height of 15 km, 0.26 DU for 6 km and 0.48 DU for 2.5 km.

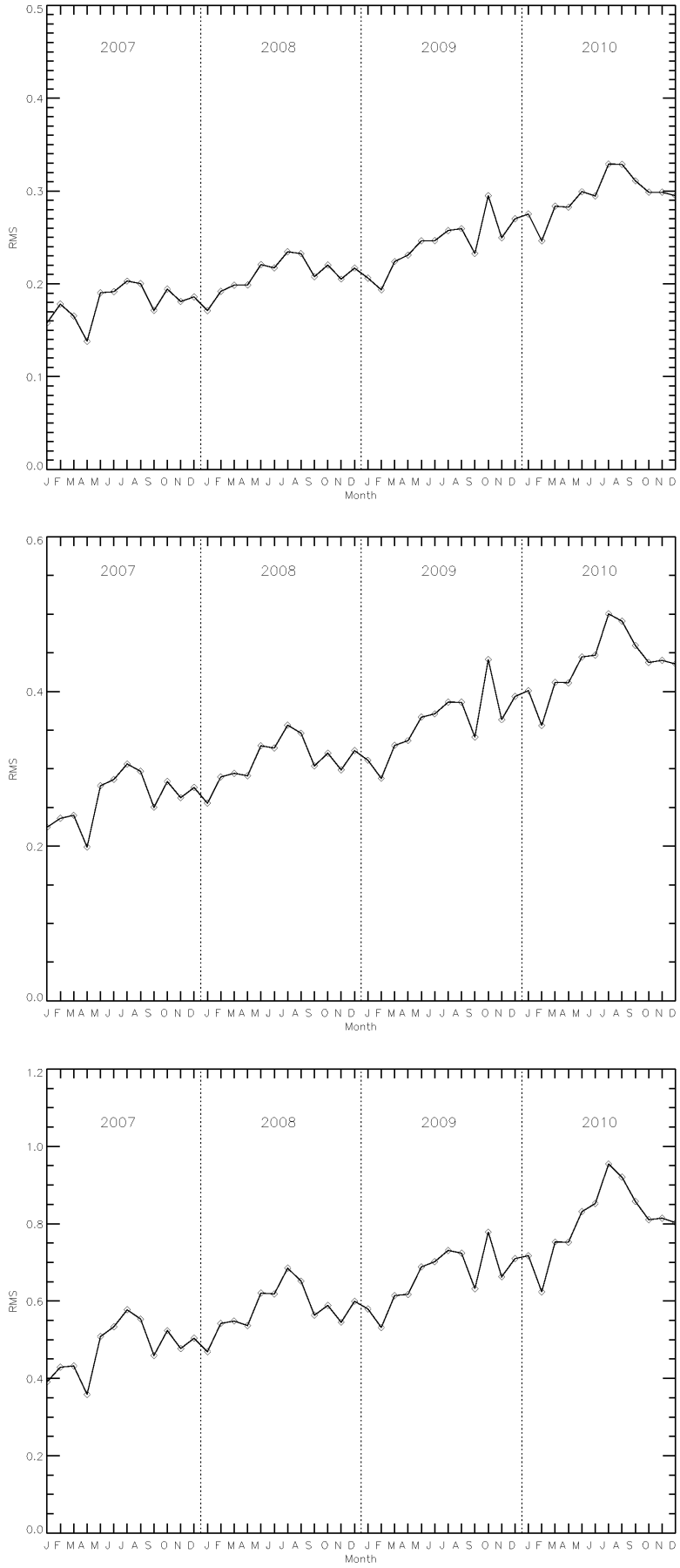

Figure 5.1: Standard deviation for GOME-2 SO_2 total columns for equatorial Pacific from 2007 to 2010, for plume heights of 15 km (top), 6 km (middle) and 2.5 km (bottom).

A long term degradation of the GOME-2 instrument has been observed. Instrument throughput tests have shown a significant change of instrument throughput with time. The tests have shown that the throughput degradation varies significantly with wavelength. A notable loss of throughput has occurred especially towards the UV, which is used for the SO_2 retrieval. The combined optical components show a degradation of 30 % around 311 nm for the first 18 months, resulting in a decreased signal to noise ratio as signal levels drop (EUMETSAT, 2009). A strong increase in the fit residual and therefore in uncertainty can be observed. Compared to the precursor instruments (GOME-1 and SCIAMACHY), the instrument degradation is proceeding at a much faster pace.

Figure 5.1 shows the monthly averages of σ in the SO_2 vertical column density for different plume heights in the time range from 2007 to 2010. Due to the instrument degradation a significant increase in the measurement noise can be detected, the σ values for 15 km plume height increases by ~ 60 % from ~ 0.18 DU at the beginning of GOME-2 operations in 2007 to ~ 0.3 DU at the end of 2010. For the lower heights an increase of ~ 100 % can be observed. This indicates that the GOME-2 detection limit for SO_2 at 15 km height varies between 0.4 DU for beginning of 2007 to currently 0.6 DU. For 2.5 km plume height the detection limit has increased from 0.9 DU to 1.6 DU over the time span of GOME-2 operations.

The degradation of the instrument does not only result in an increase in noise, it can also be seen in the uncorrected SO_2 slant column values (Figure 5.2). A continuous decrease can be observed over the time span of observations. However, this effect is less problematic as it is corrected to a large extent by the equatorial offset correction (Chapter 3.3.5).

Figure 5.2: Uncorrected GOME-2 SO_2 slant columns for equatorial Pacific from 2007 to 2010

Averaging the data over area can improve the results significantly as the random errors are reduced. Table 5.1 shows the effect of averaging over an area of 1°x1° (3 – 5 pixels) and 2°x2° (15 – 17 pixels). The scatter is reduced, improving the detection limit for SO_2. Further, it can be observed that the increase in noise in the SO_2 data is not as strong as it is for single measurements. For a plume height of 15 km the increase in the standard deviation is reduced to 32 %, when averaged over an area

of 1°x1° and is reduced even further to 13 % for an averaging area of 2°x2°. For the 2°x2° area no increase in measurement noise can be observed for the first 3 years of GOME-2 operations, indicating that averaging the data can help dealing with the decrease in data quality.

	15 km			**6 km**			**2.5 km**		
	1 pixel	1°x1°	2°x2°	1 pixel	1°x1°	2°x2°	1 pixel	1°x1°	2°x2°
2007	0.180	0.121	0.084	0.262	0.173	0.121	0.479	0.321	0.223
2008	0.210	0.138	0.084	0.311	0.197	0.125	0.581	0.372	0.243
2009	0.243	0.140	0.082	0.360	0.205	0.122	0.664	0.348	0.228
2010	0.295	0.160	0.095	0.436	0.240	0.142	0.804	0.444	0.265

Table 5.1: Standard deviation of SO_2 total columns [DU] in the equatorial region of the Pacific (10° N – 10° S, 170° E – 120° W) for a single measurements and averaged over area.

5.2 Comparison of GOME-2 SO_2 data with SCIAMACHY

This section presents a comparison of SO_2 total columns derived from GOME-2 measurements with SO_2 total columns derived from SCIAMACHY measurements (van Geffen et al., 2008). For the comparison two volcanic eruptions that represent typical eruptive cases have been selected. GOME-2 and SCIAMACHY measure within 40 minutes of each other and have a similar pixel size (GOME-2: 40 x 80 km, SCIAMACHY: 60 x 30 km) allowing a direct comparison of the measured SO_2 total columns. The comparison presented here is based on the analysis conducted for the initial GOME-2 SO_2 validation of the operational product (van Geffen et al., 2008).

5.2.1 Assumed elevation of the SO_2 plume in the atmosphere

Both satellite SO_2 products provide 3 vertical column densities based on different SO_2 plume heights, as shown in Table 5.2.

Instrument	SO_2 vertical distribution
GOME-2	The SO_2 is assumed to be in a layer with a Gaussian distribution around: ▪ 2.5 km above sea level ▪ 6 km above sea level ▪ 15 km above sea level
SCIAMACHY	The SO_2 is assumed to be in a 1 km thick layer centered around: ▪ 1 km above ground level ▪ 6 km above sea level, or 1 km above ground level if that is higher ▪ 14 km above sea level

Table 5.2: Assumed vertical SO_2 distribution for retrieval for different satellite instruments

The difference in time of the GOME-2 and SCIAMACHY measurements is about 40 minutes and the two are in approximately the same orbit. The SO_2 will have moved a little during that time and the cloud situation can be different, but a direct comparison of respective measurements is still reasonable.

5.2.2 Comparison of stratospheric SO_2 plume

On 7 August 2008 Kasatochi volcano on the Aleutian Islands (52.17°N, 175.51°W; summit height: 314 m) erupted after a period of inactivity of more than 200 years. The eruption took place in three phases between about 20:00 UTC on 7 August and 04:30 UTC on 8 August and emitted large amounts of SO_2 into the atmosphere, reaching altitudes of 10 – 15 km (Kristiansen et al, 2010). Figure 5.3 shows the SO_2 distribution as observed by GOME-2 and SCIAMACHY on 8 August.

The detected SO_2 cloud occurs in overlapping GOME-2 and SCIAMACHY orbits, allowing a direct comparison on a pixel-to-pixel basis. Therefore along-track and along-scan lines through the GOME-2 orbit are defined and the corresponding track and scan of SCIAMACHY are determined (Figure 5.3).

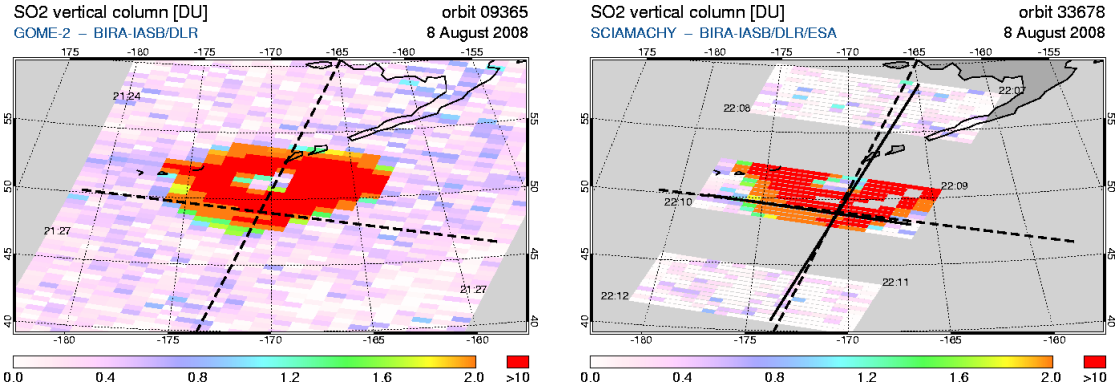

Figure 5.3: Along-track and along-scan lines in the GOME-2 (dashed) and SCIAMACHY (solid) orbit used for a direct pixel-to-pixel comparison of data on 8 August 2008.

Along-track and along-scan match only in cases where GOME-2 and SCIAMACHY orbits fully overlap. At higher latitudes the angle between the comparison lines is larger. The analysis was conducted only for the central part of the three SCIAMACHY nadir states, which includes the SO_2 eruption cloud.

The results of the pixel-to-pixel comparison along the lines in Figure 5.3 are shown in Figure 5.4. Since the SO_2 cloud is in the lower stratosphere – most likely at around 12 km altitude – the comparison is done using the data set based on a stratospheric SO_2 plume (14 – 15 km).

The match between the location and magnitude of the SO_2 peak along and across the track (Figure 5.4, top row) is very good, especially if one takes into account that there has been some dynamical motion in the SO_2 cloud during the 40 minutes time difference. The maximum SO_2 values from SCIAMACHY are about 25 % higher compared to the GOME-2 columns in the along track comparison. For the along scan comparison the GOME-2 values are about 40 % higher in parts of the scan. It is likely that this is a result of the motion of the plume during the time span between the observations. Figure 5.3 shows that the lines for the comparison are right on the edge of an area within the plume with high SO_2 values. If the plume has moved slightly in the 40 minutes between the measurements, it is possible that the SCIAMACHY measurements are already in an area with lower SO_2 values. The resolution in the across-track direction of SCIAMACHY is higher than GOME-2's resolution, which means that the match along the scan (Figure 5.4, right column) will be less accurate than a match along a track.

The cloud cover fractions derived from both instruments (bottom row) match well, even for the SCIAMACHY nadir states north and south of the central one, where the along-track lines do not match completely. Note that the cloud data for SCIAMACHY are taken from the FRESCO+ data set (TEMIS website – www.temis.nl), whereas the GOME-2 cloud data come from the OCRA/ROCINN data (Loyola et al., 2007) available in the level-2 files.

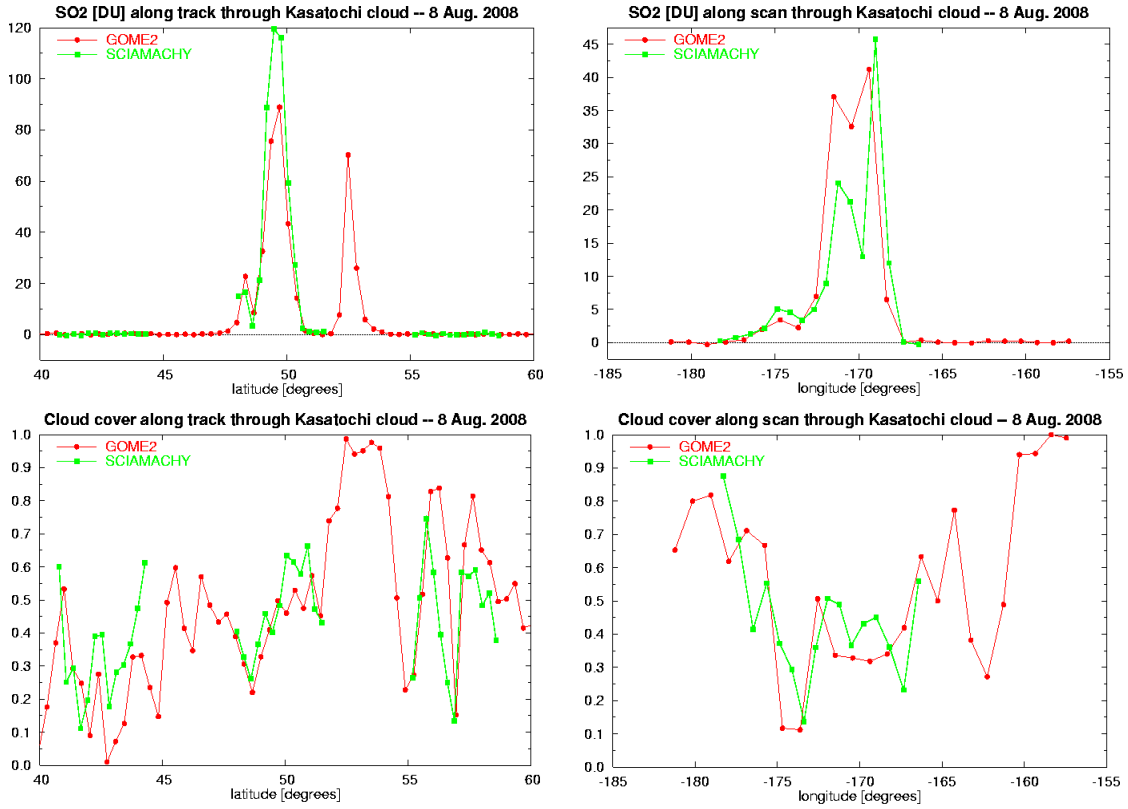

Figure 5.4: Comparison of the total SO_2 column (top row) from GOME-2 and SCIAMACHY, as well as of the cloud cover fraction (bottom row) for the along-track lines (left column) and along-scan lines (right column) as depicted in Figure 5.3.

Three days later, on 11 August, the SO_2 cloud lies off the coast of Alaska and another match is possible, as shown in Figure 5.5. The along-track match deviates about one ground pixel towards the end of the depicted range, but a comparison is still reasonable.

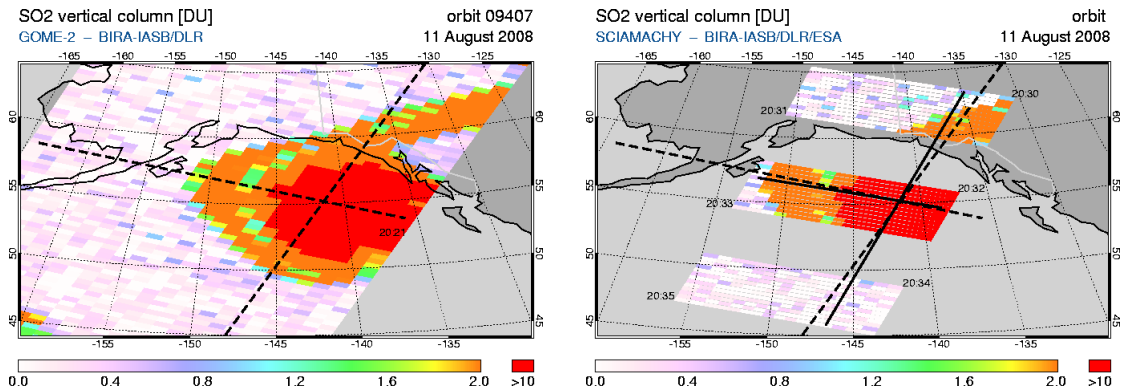

Figure 5.5: Along-track and along-scan lines in the GOME-2 (dashed) and SCIAMACHY (solid) orbit used for a direct pixel-to-pixel comparison of data on 11 August 2008

The results of the comparisons along the lines (Figure 5.5) are shown in Figure 5.6. The comparison of the SO_2 total column (Figure 5.6, top row) shows that both instruments capture the structure of the SO_2 cloud very well; the locations of the peak SO_2 values and the dimensions of the SO_2 cloud match nicely for both instruments. Differences can be found in the total SO_2 columns, SCIAMACHY gives total columns that are on the order of 20 DU higher. A similar difference is seen in the values three days earlier (Figure 5.4) in the along-track comparison (top, left), though less clear because the SO_2 cloud is smaller in size. The agreement in the cloud cover fraction (Figure 5.6, bottom row) shows that the difference in SO_2 columns is not related to cloud issues.

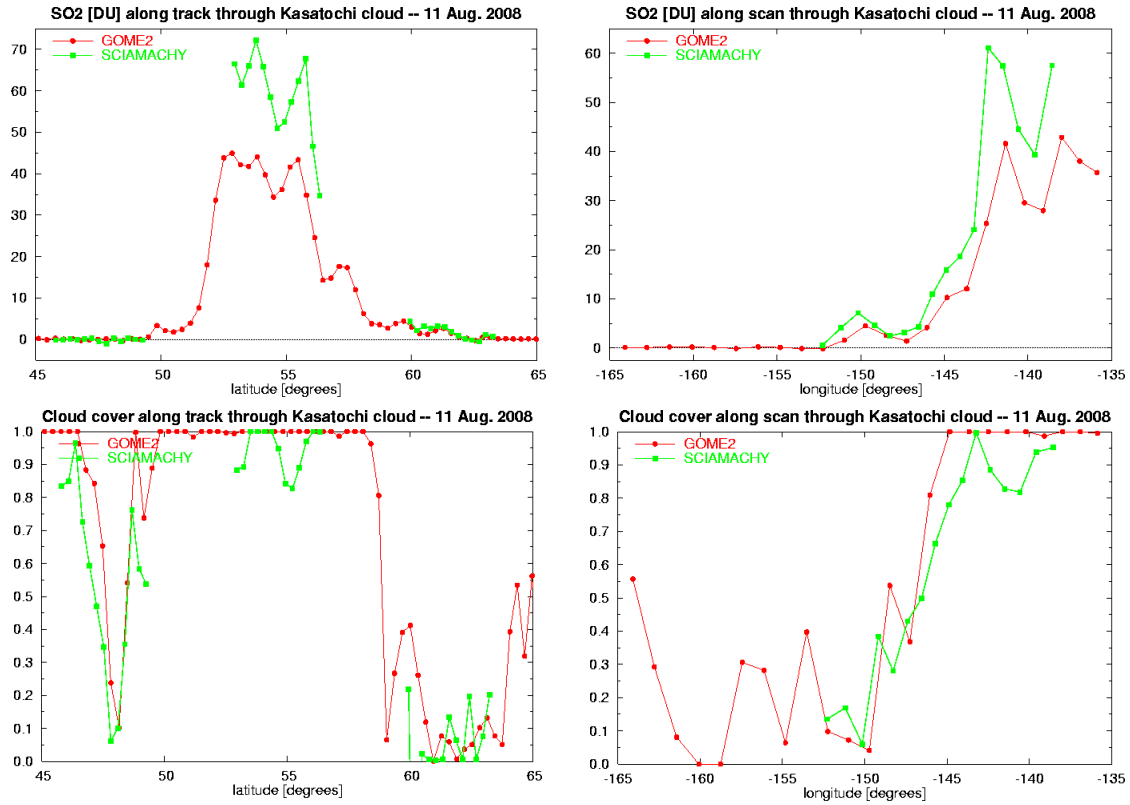

Figure 5.6: Comparison of the total SO_2 column (top row) from GOME-2 and SCIAMACHY, as well as the cloud cover fraction (bottom row) for the along-track lines (left column) and along-scan lines (right column) drawn in Figure 5.5.

Though dynamics in the SO_2 cloud result in a different SO_2 distribution for the moments the measurements are made, this cannot explain the large differences in most cases. The difference is primarily related to the retrieval of the SO_2 total column, as explained below.

For both instruments the SO_2 slant columns are retrieved using a DOAS approach. The total column of SO_2 is then determined from the slant column by division with an appropriate air-mass factor. Since the algorithm that is used to calculate the AMF (Chapter 3.4) is the same for both instruments, the main reason for the observed differences is the retrieval of the SO_2 slant columns.

One important difference between the SO_2 slant column retrieval from SCIAMACHY and GOME-2 is the use of different cross-sections at different temperatures. GOME-2 uses reconvolved SCIAMACHY FM cross-sections (Bogumil et al., 1999) at a temperature representative for the specific height, in this case a stratospheric

temperature for the 15 km retrieval, while for the SCIAMACHY retrieval a cross-section at a tropospheric temperature is used. This can result in up to 20% higher slant columns for SCIAMACHY and therefore explains large parts of the difference in total column SO_2. This also explains why low level SO_2 concentrations agree well, in this case a 20 % error due to a different cross-section temperature does not result in large absolute errors. Another issue that induces differences in the retrieved slant columns is the choice of reference spectra; for the GOME-2 retrieval a daily solar spectrum is used as reference, whereas the SCIAMACHY retrieval uses an earthshine spectrum as reference (selected from an equatorial region without SO_2 sources) (van Geffen et al., 2008).

5.2.3 Comparison of SO_2 plume in the mid to lower troposphere

The Kilauea volcano on Hawaii (19.42°N, 155.29°W; summit height: 1222 m) started a new period of eruptive activity in March 2008, with a large number of effusive eruptions. The SO_2 emitted by the volcano remains close to the volcano and is only visible for a day or two. This implies that the SO_2 is emitted at low altitudes, in the troposphere, where the lifetime of SO_2 is a few days. The total amounts of SO_2 emitted are not very large, with total columns typically between 5 and 15 DU. The series of Kilauea eruptions can therefore be used for comparing low-level SO_2 concentrations in the low and middle troposphere. Since the SO_2 cloud of the volcano is limited in size, the situation can also be used to compare background SO_2 concentrations.

17 May 2008 has been selected for the comparison, as a fairly large SO_2 eruption plume can be observed on this day. Figure 5.7 shows the GOME-2 and SCIAMACHY orbits that pass over the plume on this day. The orbits overlap completely and matching along-track and along-scan lines suitable for a comparison can be selected easily, because at this latitude the tracks of the instruments run parallel. Due to the ground pixel widths of 60 km for SCIAMACHY and 80 km for GOME-2, a match is found every three GOME-2 tracks. Therefore a set of four tracks and three scans is selected for the comparison on 17 May (Figure 5.7).

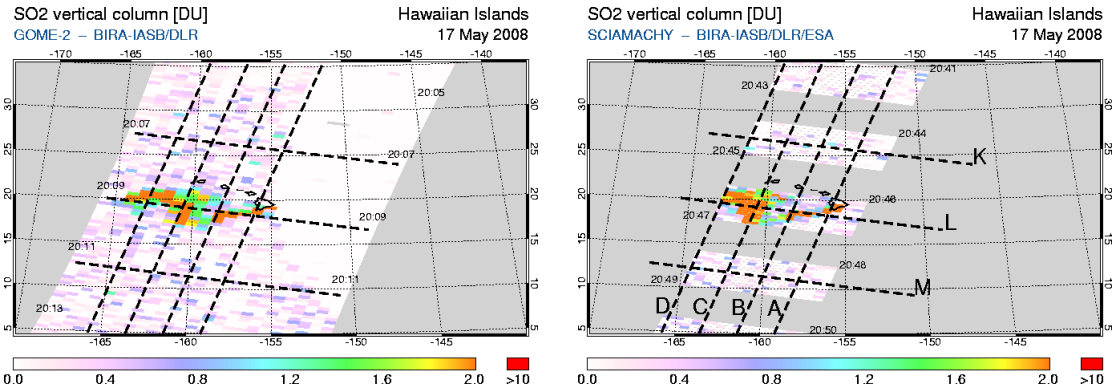

Figure 5.7: SO_2 distribution for GOME-2 orbit 8185 (left) and SCIAMACHY orbit 32490 (right), which passed over Hawaii on 17 May 2008. The dashed lines are used for along-track and along-scan comparisons, labeled with the letters in the right plot.

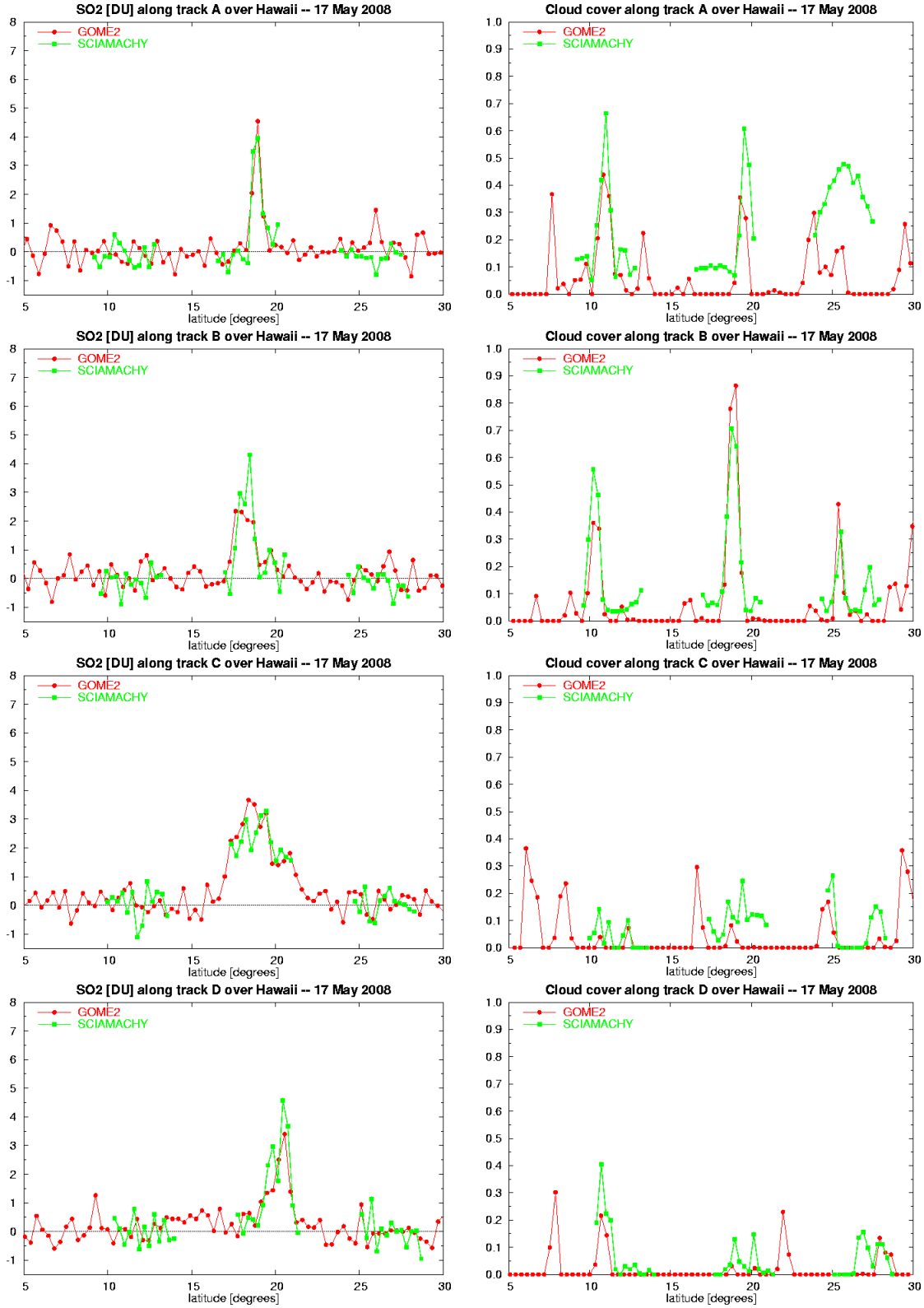

Figure 5.8: Comparison of the total SO_2 column (left column) and the cloud cover fraction (right column) from GOME-2 and SCIAMACHY for the along-track lines A – D (top to bottom) in Figure 5.7.

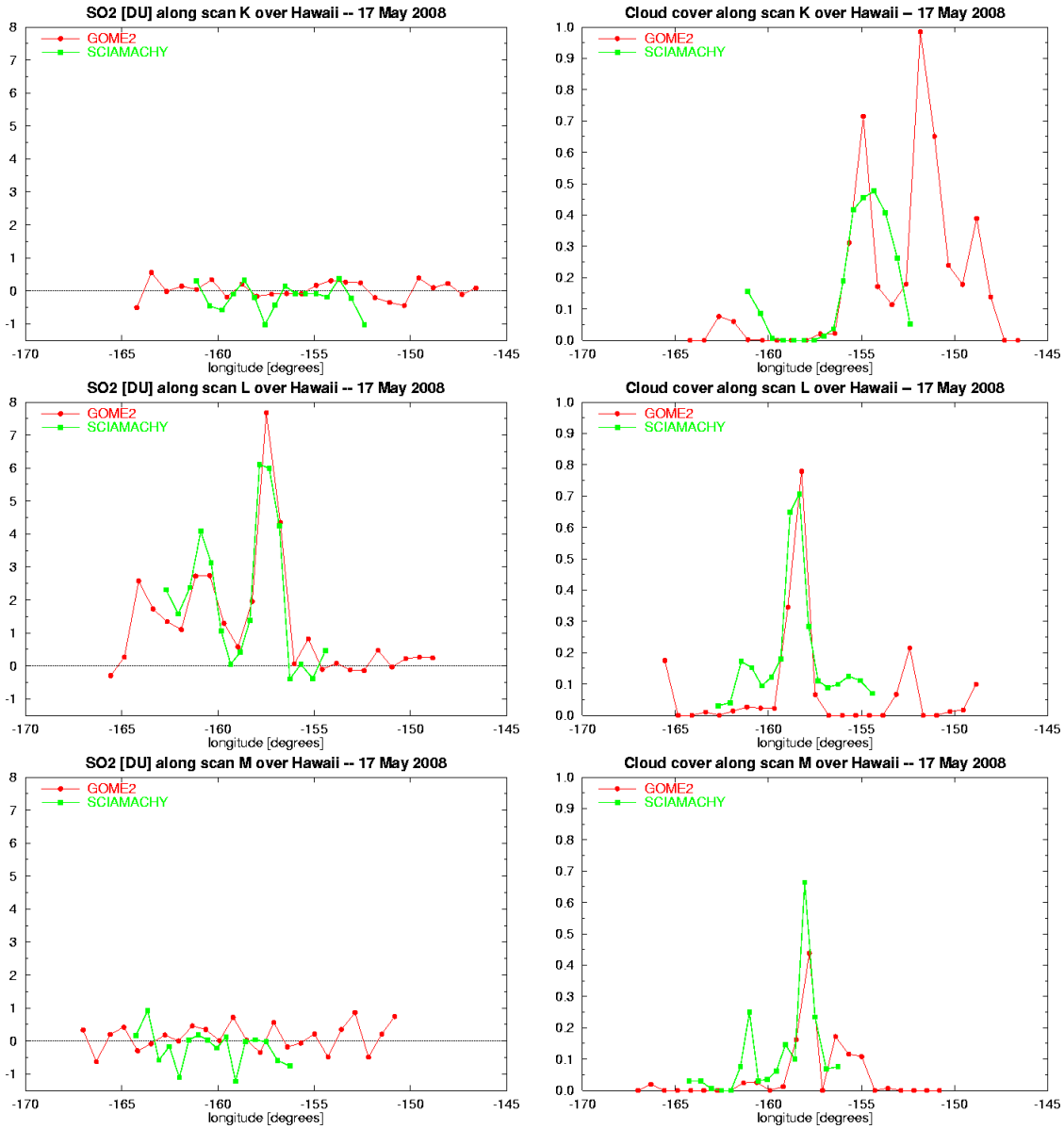

Figure 5.9: Comparison of the total SO_2 column (left column) and the cloud cover fraction (right column) from GOME-2 and SCIAMACHY for the along-scan lines K – M (top to bottom) in Figure 5.7.

Figure 5.8 shows the comparisons of the SO_2 total columns and cloud cover fractions along the four tracks A – D (Figure 5.7), while the comparisons along the three scans K – M are shown in Figure 5.9.

The correspondence between the SO_2 columns from GOME-2 and SCIAMACHY for these tracks and scans is very good. Especially for those cases where the cloud cover fraction is similar, the difference in total column is < 20 % (e.g. scan A). In the 40 minutes between the GOME-2 and the SCIAMACHY observations the cloudiness has changed somewhat, which can affect the results of the SO_2 retrieval, as the cloud cover fraction is an important parameter for the calculation of the AMF. In particular on the eastern side of the most northern of the three SCIAMACHY states (scan K) the cloud fraction for SCIAMACHY is considerably larger than the cloud fraction for GOME-2 (Figure 5.8, top-right panel).

The peak values of the SO_2 total columns correspond very well, keeping the different cloudiness in mind. This shows that the large differences in SO_2 peak values are

limited to very high SO_2 concentrations. The fact that the SO_2 cross-sections used are at different temperatures for the two instruments plays less of a role for tropospheric SO_2, as the temperature difference between the used cross-sections is small.

The comparison for background SO_2 (K and M) shows that for both instruments the total SO_2 columns are close to zero, as would be expected. The SCIAMACHY total columns are slightly lower compared to the GOME-2 total columns. They are negative in most cases and show higher negative values, whereas GOME-2 values are fairly evenly distributed around zero.

5.3 Comparison of GOME-2 SO_2 data with ground-based observations

In this section a comparison of GOME-2 SO_2 data with different ground-based instruments is presented. Comparisons have been carried out for Max-DOAS measurements of anthropogenic SO_2 pollution in Beijing and for measurements of volcanic SO_2. The validation of volcanic GOME-2 SO_2 data with ground-based instruments has been conducted for two eruptive scenarios. The GOME-2 SO_2 data are compared with FLYSPEC measurements from Kilauea, Hawaii, as an example of an effusive eruption releasing moderate SO_2 amounts at tropospheric levels. Additionally, a comparison has been done with Brewer instruments measuring the overpass of the Kasatochi eruptive cloud, as an example of an eruption that brought SO_2 to stratospheric altitudes.

5.3.1 Comparison with Max-DOAS measurements in Beijing, China

Close to the Olympic Stadium in Beijing, a Max-DOAS instrument has been placed by BIRA-IASB on the top of the roof of the Institute of Atmospheric Physics (IAP) in the framework of the AMFIC (Air Quality Monitoring and Forecast In China) project (www.amfic.de). This instrument has been measuring various trace gases, including SO_2, from mid-June 2008 to April 2009, focusing on air quality related compounds (Clémer et al., 2010).

Max-DOAS measurements
The Multi-axis DOAS (Max-DOAS) technique has been developed as a remote sensing tool to monitor tropospheric pollutants using the DOAS method (Heckel et al. 2005, Hönninger et al., 2004). Max-DOAS instruments are designed to observe the scattered sunlight at a range of different elevation angles from the zenith to the horizon. For observations of tropospheric SO_2 lower elevation angles are used, as the light path through the upper atmosphere is independent of viewing angle, whereas the light path in the lower atmosphere increases as the viewing direction approaches the horizon (Figure 5.10).

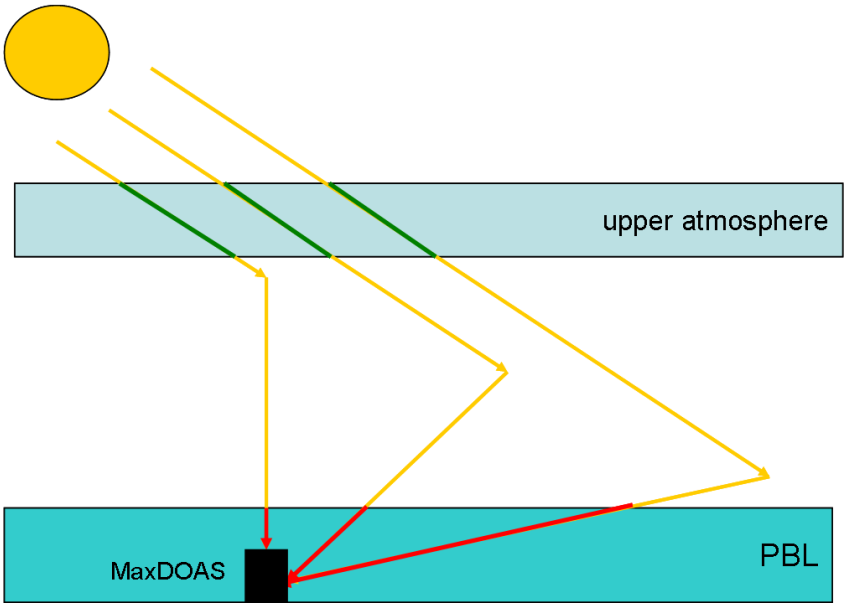

Figure 5.10: Schematic representation of Max-DOAS trace gas measurement in the planetary boundary layer (PBL)

If the last scattering point is above the SO_2 layer, the light path is determined only by geometry and a geometric AMF can be assumed. The tropospheric vertical column (V_{tropo}) is then calculated as:

$$V_{tropo} = \frac{S_{\alpha} - S_{zenith}}{\frac{1}{\sin(\alpha)} - 1} \tag{5.3}$$

where S_{α} is the slant column at the elevation angle α, and S_{zenith} is the measurement at zenith elevation (α=90°).

As anthropogenic pollution is generally assumed to be confined in the planetary boundary layer (PBL), the SO_2 total column density is determined from the measured slant column density – retrieved with the DOAS technique – using the geometrical approximation described above. The retrieval results of the measurements at 15º and 30º are compared, if they agree within 30%, the measurement is considered to be valid (Clémer et al., 2010).

Comparison of the SO_2 measurements

The SO_2 vertical columns of the Max-DOAS measurements at Beijing have been compared with GOME-2 observations of SO_2 pollution for the Beijing area. Figure 5.12 shows the comparison of the daily SO_2 observations. From the Max-DOAS instrument only measurements within 1 hour of the GOME-2 overpass have been taken into account and were averaged. As the pollution is very likely confined to the PBL, the GOME-2 SO_2 data for the lowest available plume height of 2.5 km has been used. The data was averaged over a 1.5° x 1.5° box (8 – 10 pixels) around Beijing (39.9°N, 116.4°E) to reduce the noise, which is high for the individual measurements at 2.5 km (Table 5.1). Averaging can improve the scatter but can also introduce errors due to averaging out inhomogenities within the SO_2 cloud. However, as Beijing is situated at the foot of a mountain chain and on the edge of the highly polluted area (Figure 5.11), the averaging box had to be chosen fairly small, as a larger averaging

area would significantly obstruct the results. Further, measurements with a cloud fraction > 0.2 were excluded from the comparison as for SO_2 in the PBL it is very likely that the clouds are above the SO_2 and will shield it from the view of the satellite.

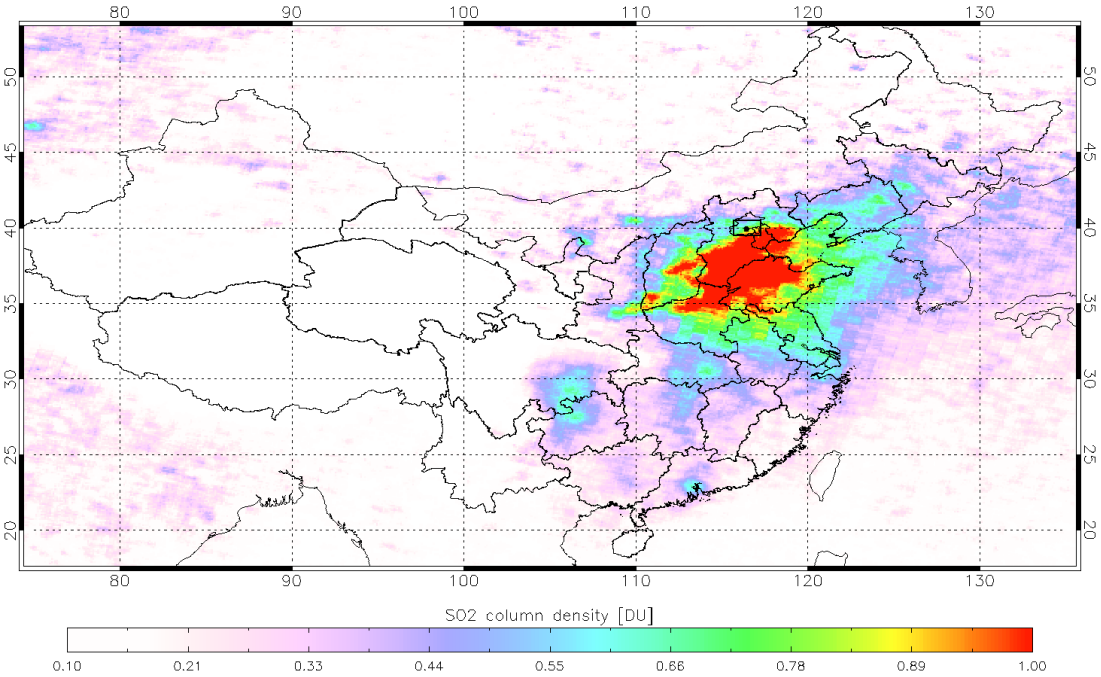

Figure 5.11: 3-year average (2007-2009) of SO_2 pollution in Eastern China. The box marks the area used for the comparison with the Max-DOAS SO_2 measurements in Beijing and the dot denotes the location of the Max-DOAS instrument.

The comparison of the daily SO_2 observations shows a qualitative agreement, both instruments capture the larger SO_2 values during the winter months, which are due to increased heating. When looking at the individual vertical SO_2 columns errors > 100 % can be found on many days (Figure 5.12). This is also shown by the correlation of the two instruments, which is 0.27. However, it should be kept in mind that comparing ground-based with satellite observations is always problematic. This is due to the fact that the Max-DOAS measurement is a point measurement, whereas the satellite averages over an area, which in the case of GOME-2 is 40 x 80 km. If the SO_2 pollution is homogeneous in the observed area, this is not problematic. However, the three year average of the SO_2 pollution (Figure 5.11) shows that Beijing is located in an area with a fairly high gradient in the SO_2 pollution, therefore errors due to an inhomogeneous SO_2 distribution are likely. A further important source of error is that the GOME-2 instrument has a limited sensitivity for SO_2 in the PBL.

To limit effects of random noise and inhomogeneous SO_2 distribution, the monthly averages of the Max-DOAS and GOME-2 observations have been compared (Figure 5.13). Doing so significantly improves the results of the comparison. Both instruments clearly show the annual variation of the SO_2 pollution in Beijing. The absolute errors are below 0.6 DU for all months, mainly the Max-DOAS SO_2 measurements are within 30 % of the GOME-2 values. Except for August 2008 the averaged GOME-2 values fall within the scatter of the daily Max-DOAS observations, denoted by the error bars. The correlation between the two instruments has improved significantly. The value of 0.79 indicates a good agreement between the Max-DOAS measurements and the GOME-2 observations.

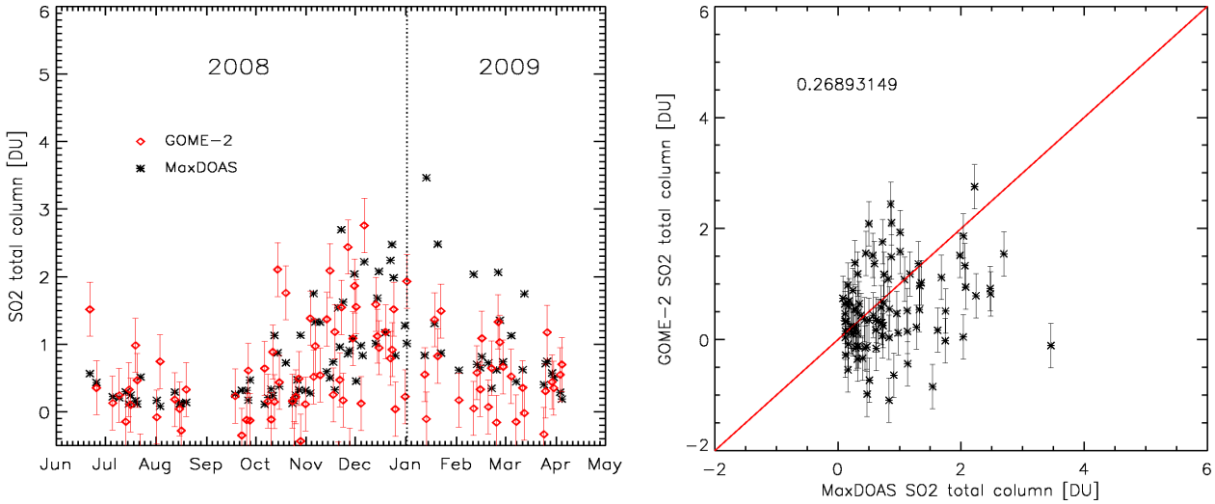

Figure 5.12: Comparison of daily Max-DOAS and GOME-2 SO_2 observations for Beijing (left). The scatter plot shows the correlation between the two observations (right).

Overall, the results of the comparison show that GOME-2 is able to detect annual changes in the SO_2 pollution over Beijing. For daily measurements both instruments show the enhanced SO_2 values during winter months, however the deviation in the individual values is large. Averaging over time improves the comparison significantly. The comparison shows that GOME-2 SO_2 is a valuable contribution for monitoring anthropogenic pollution.

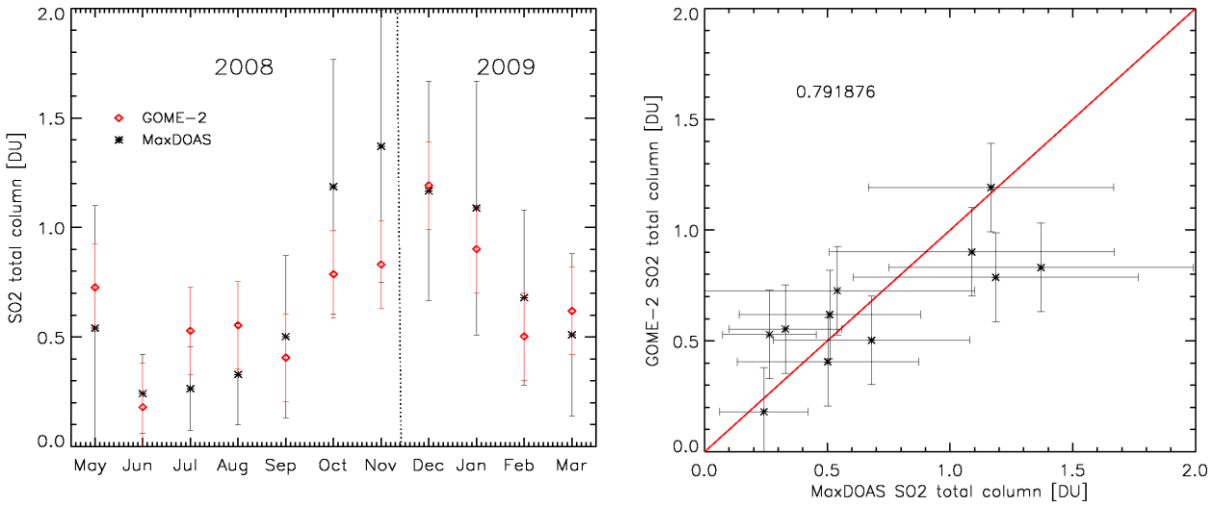

Figure 5.13: Comparison of monthly averages of Max-DOAS measurements of anthropogenic SO_2 pollution in Beijing with GOME-2 data (left). The scatter plot shows the correlation between the two observations (right).

5.3.2 Comparison with FLYSPEC measurements at Kilauea, Hawaii

The Hawaiian volcano observatory conducts regular SO_2 flux measurements at Kilauea volcano. The measurements are typically carried out at two different locations, the Kilauea summit and the Pu'u 'O'o crater, using a FLYSPEC instrument. The measurement results are made available through the daily volcano updates on the observatory's webpage (http://volcanoes.usgs.gov/hvo/activity/archive.php).

FLYSPEC measurements

The FLYSPEC instrument has been developed as a successor of the COSPEC (Chapter 2.4.1), its major advantage compared to the older COSPEC instruments is that it is small, lightweight and inexpensive (Horton et al., 2005). The instrument consists of an UV-spectrometer and a detector array (Figure 5.14). It has an optical resolution of 0.25 nm in the wavelength region from 177 nm – 330 nm. As with COSPEC, the instrument contains two SO_2 calibration cells of known concentration. It has a field of view of ~ 2.5°. When measuring SO_2 8 - 9 absorption peaks between 304 nm – 320 nm are analyzed. The FLYSPEC is extremely compact and lightweight with a size of only 89 mm x 64 mm x 34 mm and a weight of 200 g.
During the measurement a clear sky spectrum outside the SO_2 plume is recorded as reference. Additional reference spectra are obtained from the calibration cells. Calibration coefficients are derived from a least-squares quadratic fit of the absorbance peak to peak differences at each wavelength, as a function of the concentrations of the reference gas cells. The SO_2 concentration can be retrieved by applying these coefficients to the measurement spectra (Elias et al., 2006).

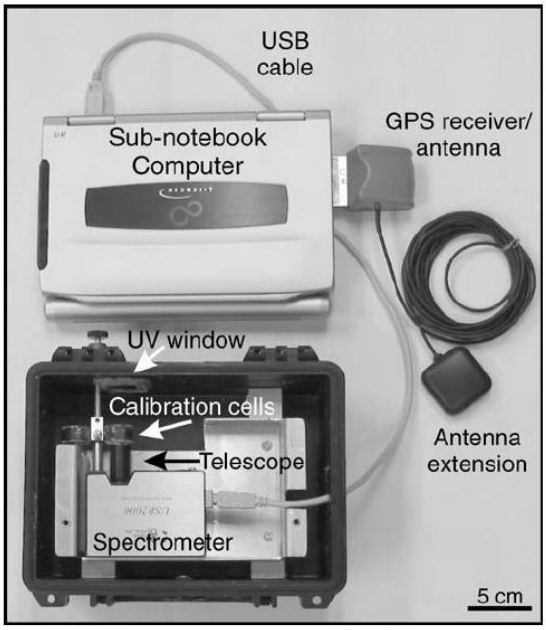

Figure 5.14: FLYSPEC components consisting of a miniature spectrometer, sub-notebook computer, and GPS. High and low calibration SO_2 gas cells are mounted above the spectrometer and telescope. The “telescope” is a fiber-optic collimating lens mounted directly to the spectrometer input aperture. The lens, in combination with the UV band-pass filter window mounted on the case, provides a field of view of approximately 2.5° (Horton et al., 2005).

Comparison of the SO_2 measurements

SO_2 fluxes from FLYSPEC measurements at Kilauea volcano, Hawaii, have been compared with SO_2 fluxes estimated from GOME-2 observations, from the beginning of the recent eruptive period in March 2008 to November 2008. The comparison has only been conducted for days where ground-based observations for both measurement locations (Kilauea summit and Pu’u ‘O’o crater) are available, as due to the large pixel size of GOME-2 it is not possible to distinguish the origin of the SO_2 such that GOME-2 will measure the combined emissions. Therefore the fluxes measured by FLYSPEC at both locations have been added to estimate the total SO_2 flux in t/day from Kilauea volcano.

For the estimation of the daily SO_2 flux from GOME-2 data, a simple method has been used. By taking into account the wind speed, it can be estimated how far the SO_2 has traveled from Kilauea within one day. According to that distance a latitude/ longitude box around the volcano is defined and within that box the total SO_2 amount is calculated. It is assumed that the SO_2 in the box has been emitted during the last day, which allows expressing the total SO_2 mass as a flux in t/day. For the calculations an average daily wind speed has been calculated. The wind direction is not taken into account, as Hawaii is in the trade wind region, the wind direction is fairly stable and from north-easterly directions on most days. Due to this stable wind direction, the north eastern corner of the box is fixed at latitude 19.92°N and longitude 155.77°W, which is 0.5° to the north and east of the volcano. Figure 5.15 shows examples of the boxes for different wind speeds.

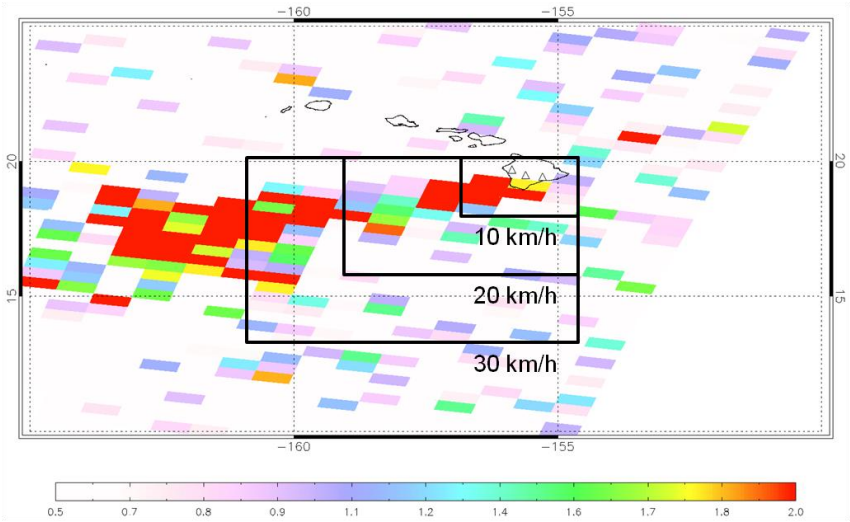

Figure 5.15: Latitude/ Longitude box for estimating the SO_2 flux according to the average wind speed

To calculate the total SO_2 mass within the area selected, a plume height of 2.5 km has been assumed, as Kilauea typically erupts effusively and has a summit height of 1222 m. Therefore the SO_2 will not rise to great altitudes. To exclude noise from the estimation of the total SO_2 mass, only measurements with SO_2 total column greater than twice the standard deviation (2σ) have been taken into account. With σ = 0.7 DU the cut-off value has been set to 1.5 DU. The standard deviation has been calculated for an SO_2 free reference area over the Pacific east of Hawaii (15°N-25°N, 120°W-140°W). The total SO_2 mass of a single pixel can then be calculated as:

$$M_{total,SO2} = V \cdot A_{pixel} \cdot \frac{m_{SO2}}{N_A} \tag{5.4}$$

where $M_{total,SO2}$ is the total SO_2 mass in kg, V is the SO_2 vertical column in molecules/cm^2, A_{Pixel} is the GOME-2 pixel size in cm^2, m_{SO2} is the molar mass of SO_2 (64 g/mol) and N_A is the Avogadro number (6.022x10^{23} molecules/mol). For a GOME-2 pixel size of 80 x 40 km a vertical column of 1 DU corresponds to a total SO_2 mass of 91.2 tons.

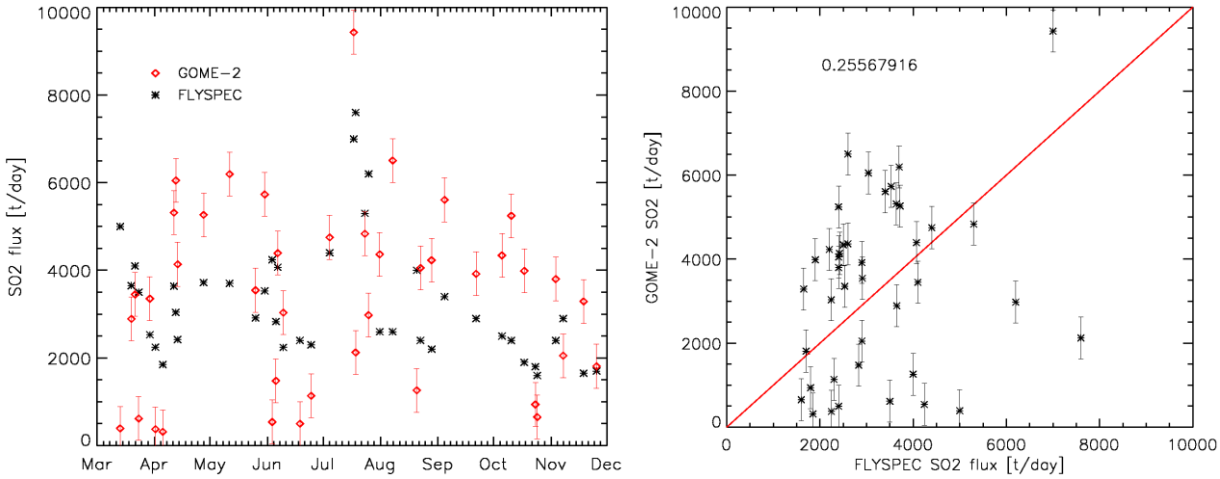

Figure 5.16: Comparison of daily SO_2 fluxes estimated from FLYSPEC and GOME-2 observations for Kilauea, Hawaii (left). The scatter plot shows the correlation between the two observations (right).

Figure 5.16 shows the comparison for the daily flux estimations at Kilauea volcano from March 2008 to November 2008. Both instruments capture the high SO_2 emissions in July 2008, with daily emissions of up to 8000 t/day. During this period the comparison yields good results with deviations between the two fluxes of typically < 30 %. However, it can also be seen that there are several days where the fluxes estimated from GOME-2 are much larger than those detected at the ground, especially during August and September, where the GOME-2 fluxes are always more than 100% higher. As explained below this can be due to the fact that the FLYSPEC measurements are not continuous, the emissions in t/day are inferred from shorter measurement time spans. If the SO_2 flux shows high variations over the last day, the FLYSPEC observations may not capture them correctly leading to deviations between the two measurements. Also the GOME-2 observation provides a snapshot of the SO_2 plume and can only give a rough estimate of the average fluxes during the last day. For the estimation of the SO_2 flux a constant plume height is assumed, while the correct plume height is not known and can vary in reality. Further, it cannot be ruled out, that SO_2 is emitted from another source than the two locations observed by the FLYSPEC measurements, these additional SO_2 emissions will be included in the GOME-2 observations. The underestimation on some days (e.g. 21/29 March and 23 October) can mainly be related to clouds, as these shield the SO_2 at lower altitudes from the view of the satellite. The correlation between the two observations is 0.25, for daily observations.

Apart from the daily observations the monthly averages of the estimated SO_2 fluxes have been compared. As for the comparison with the Max-DOAS observations in Beijing, looking at the monthly averages significantly improves the comparison. The averaging over one month in this case results not only in a decrease of random errors, but can also decrease some of the systematic errors. Examples are the assumption of the plume height, here a longer time span will reduce the error, if days where the assumed plume height was too low and days where the assumed plume height was too high are averaged. The same holds true for the issues due to the short measurement period of the FLYSPEC. Figure 5.17 shows that for most months the agreement between the fluxes estimated from the GOME-2 observations and those measured by the FLYSPEC instrument is good, they are mainly within 25 % of each other. Both instruments show the high emissions during the highly eruptive

period in July and the leveling off of the stronger eruptions towards October. Again for August and September higher GOME-2 SO_2 values can be seen, however for September only two FLYSPEC observations were available, therefore averaging does not have a big effect here. The correlation increases to 0.58 for the monthly averages, which is a good result considering that volcanic SO_2 fluxes are highly variable and that the comparison of ground-based and satellite observations is therefore difficult.

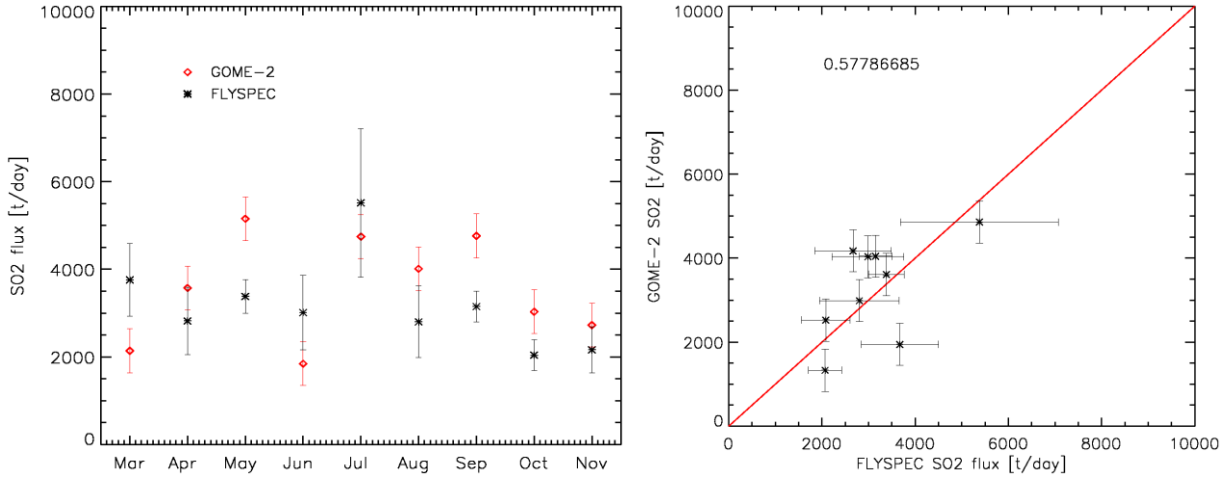

Figure 5.17: Comparison of monthly averages of FLYSPEC measurements of SO_2 fluxes at Kilauea, Hawaii with SO_2 fluxes estimated from GOME-2 data

To allow a more detailed comparison and an investigation of reasons for differences of the GOME-2 and FLYSPEC observations, a 2-day period from July 2008 has been selected with high SO_2 emissions and the distribution of the Kilauea SO_2 emissions has been simulated using the dispersion model FLEXPART (Stohl et al., 2005). FLEXPART is a Lagrangian particle dispersion model, which has been used for modeling long-range transport of volcanic clouds (Prata et al., 2007). The calculations are based on meteorological fields from the ECMWF model.
17 and 18 July have been selected for the simulation as the SO_2 emissions were high for these days and FLYSPEC measurements were available for two days in a row, allowing a continuous simulation for the two days, as the GOME-2 observation also shows SO_2 from the day before.
The FLEXPART model has been initialized using the FLYSPEC observations (17.07.2008: 7000 t/day, 18.07.2008: 7600 t/day). As no time for the FLYSPEC measurements is available, the SO_2 flux has been assumed to be constant over the day. The SO_2 was released at Kilauea volcano continuously at heights between the summit elevation and 5 km, as the correct plume height was unknown. The SO_2 distribution is calculated on a 0.5° x 0.5° grid every 30 minutes. Only dry and wet deposition processes have been taken into account in the simulation. Figure 5.18 shows for 18 July 2008 the FLEXPART simulation (right) and the GOME-2 observation regridded to 0.5° x 0.5° for easier comparison (left). It can be seen that the differences are quite large, especially at a greater distance from the volcano. Close to Kilauea the SO_2 plume shows a similar shape in the observations and in the simulation, also the total SO_2 amounts are of similar magnitude. These emissions are mainly from 18 July, for this day the comparison of the FLYSPEC SO_2 flux, 7600 t/day, and the SO_2 flux estimated from GOME-2, 8700 t/day, show a good agreement. The GOME-2 flux is ~ 15% higher than that from FLYSPEC, which is a

good result considering that the flux estimation from the GOME-2 observations is difficult and a very simple method for the flux estimation has been used.

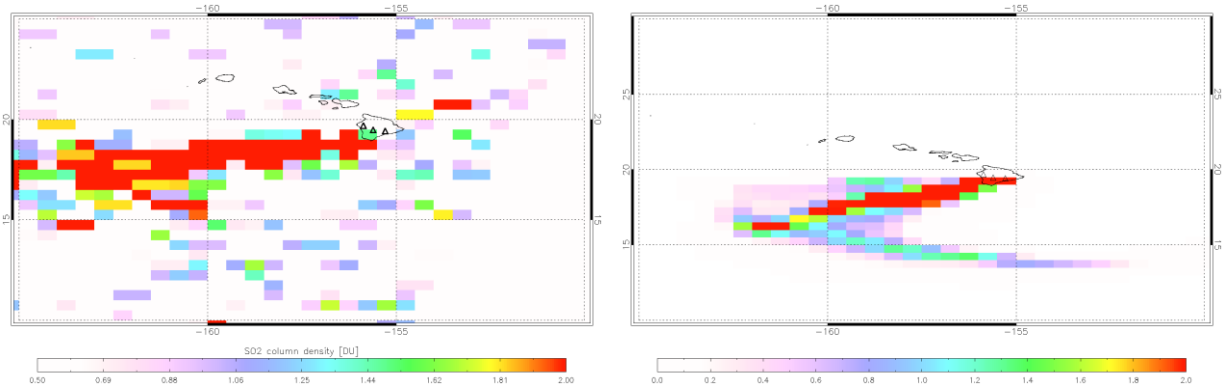

Figure 5.18: GOME-2 observation of SO_2 plume from Kilauea, Hawaii, on 18 July 2008, regridded to 0.5° x 0.5° (left) and FLEXPART simulation of Kilauea SO_2 emissions from 17 and 18 July 2008 (right).

Figure 5.19 shows the simulation for 18 July (left) and the GOME-2 observations (right) with the averaging region used on that day (wind speed: 12.25 km/h). The simulation shows, that this method to calculate the flux in this case should slightly underestimate the SO_2 flux, as the SO_2 in the simulation was already transported further. This is due to the fact that for calculating the averaging region an average wind speed that is measured at the volcano is used, therefore the wind speed at higher altitudes can be different. However, even though the averaging area was chosen too small, the SO_2 flux is overestimated compared to the FLYSPEC observations. The most likely reason for this is that the assumption of 2.5 km for the plume altitude is too low, estimating the flux with an assumed plume height of 6 km results in 5700 t/day, suggesting that the correct plume altitude might be in between. Typical plume heights at Kilauea are between 1 – 5 km. The issue concerning the correct assumption of the SO_2 altitude can also be seen in Figure 5.18. In the simulation of the volcanic plume a branch of SO_2 is visible drifting to the southeast, that cannot be observed in the GOME-2 measurements, which is due to the fact that the SO_2 was not emitted in the whole modeled altitude range.

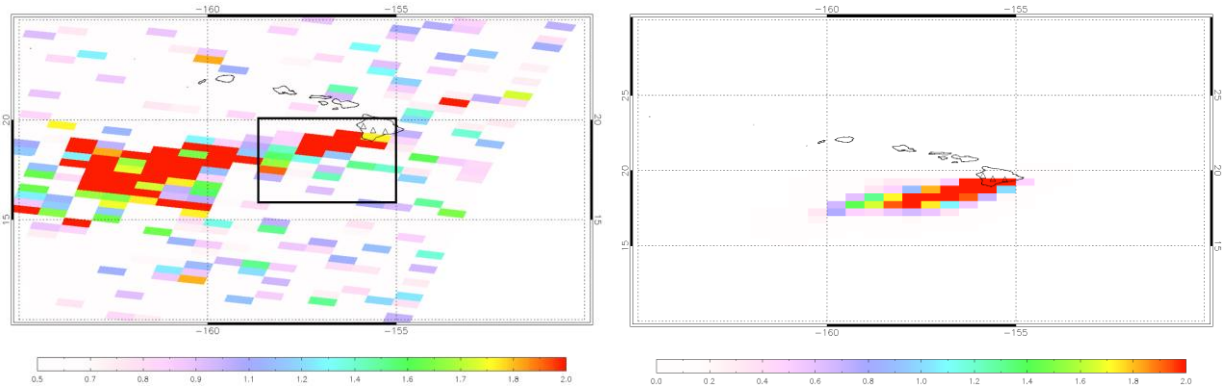

Figure 5.19: GOME-2 observation of SO_2 plume from Kilauea, Hawaii, on 18 July 2008, with averaging area used for flux estimation (left) and FLEXPART simulation of Kilauea SO_2 emissions from 18 July 2008 (right)

As can be seen in Figure 5.18 the SO_2 plume further away from the volcano is completely different for the simulation and the GOME-2 observation. The SO_2 amounts in the observation are much higher than in the simulation. Assuming that this SO_2 has been emitted earlier, this indicates that the SO_2 flux measured by the

FLYSPEC instrument on 17 July is too low. This is underlined by the fluxes estimated from GOME-2 observations for that day, they are around 11160 t/day, whereas the fluxes reported from the FLYSPEC observations are around 7000 t/day. The most likely explanation for the low FLYSPEC flux is that the SO_2 flux was much higher outside the FLYSPEC measurement period, as the two observations agree well on the next day, additional SO_2 sources are unlikely. As SO_2 has a lifetime of several days in the troposphere, a possible explanation for the high amounts of SO_2 far away from the volcano, that do not show up in the simulation at all, is that SO_2 from emitted on earlier days, where no FLYSPEC measurements were available, is still present in the atmosphere and measured by GOME-2.

5.3.3 Comparison with Brewer spectrometer measurements of the overpass of the Kasatochi eruption plume

Validation of satellite SO_2 measurements from explosive volcanic eruptions is difficult, as these events are rare and highly unpredictable. The distribution of the volcanic cloud depends on the atmospheric wind situation, making specific measurements of such events challenging. SO_2 clouds from explosive eruptions differ significantly from SO_2 released by anthropogenic activity or volcanic degassing, as they typically contain high SO_2 amounts and the SO_2 is brought to stratospheric heights. The eruption of Kasatochi in August 2008 produced an extensive SO_2 cloud that was distributed over the northern hemisphere the following weeks. The eruption cloud was detected by Brewer spectrometers in North America and Europe (Figure 5.20) providing one of the rare opportunities to compare GOME-2 SO_2 data from a stratospheric eruption plume with ground-based observations of the plume at various locations. Brewer spectrometer, that were originally designed and optimized to monitor ozone, are also capable of measuring SO_2 (Kerr, 1981) as described below.

Brewer measurements

Brewer spectrometers measure the intensity of light in the ultra violet wavelength region at five different wavelengths: λ_1=306.3 nm, λ_2=310.1 nm, λ_3=313.5 nm, λ_4=316.8 nm and λ_5=320.1 nm. After the determination of the ozone column from the measured solar intensity spectrum, the SO_2 total column can be determined as follows:

$$S + \Delta\beta m = S_0 - \Delta\alpha[O_3]\mu - \Delta\alpha^*[SO_2]\mu^* \quad (5.5)$$

with

$$S = \log I_1 - 4.2\log I_4 + 3.2\log I_5 \quad (5.6)$$

$$S_0 = \log I_{0,1} - 4.2\log I_{0,4} + 3.2\log I_{0,5} \quad (5.7)$$

$$\Delta\beta = \beta_1 - 4.2\beta_4 + 3.2\log\beta_5 \quad (5.8)$$

$$\Delta\alpha = \alpha_1 - 4.2\alpha_4 + 3.2\log\alpha_5 \quad (5.9)$$

$$\Delta\alpha^* = \alpha_1^* - 4.2\alpha_4^* + 3.2\log\alpha_5^* \quad (5.10)$$

where I_λ is the measured intensity at wavelength λ, $I_{0,\lambda}$ the measured reference intensity at wavelength λ, m denotes the air mass factor, O_3 and SO_2 are the column amounts of ozone and sulfur dioxide respectively, μ and μ^* are the enhancement of

the light path due to ozone and SO_2, respectively, and α_λ and β_λ are the ozone and SO_2 absorption coefficients at wavelength λ (Kerr et al., 1981).

Although newer methods have been developed for the retrieval of SO_2 from Brewer spectrometer observations (Kerr 2002, Kerr and Davis, 2007), the algorithm used operationally is still as described above, with some modifications (Fioletov et al., 1998). Sensitivity studies indicate an error in the derived total SO_2 column from 8 % for stratospheric SO_2 at 15 km height to 50 % for SO_2 in the lower troposphere at small solar zenith angles (Fioletov et al., 1998).

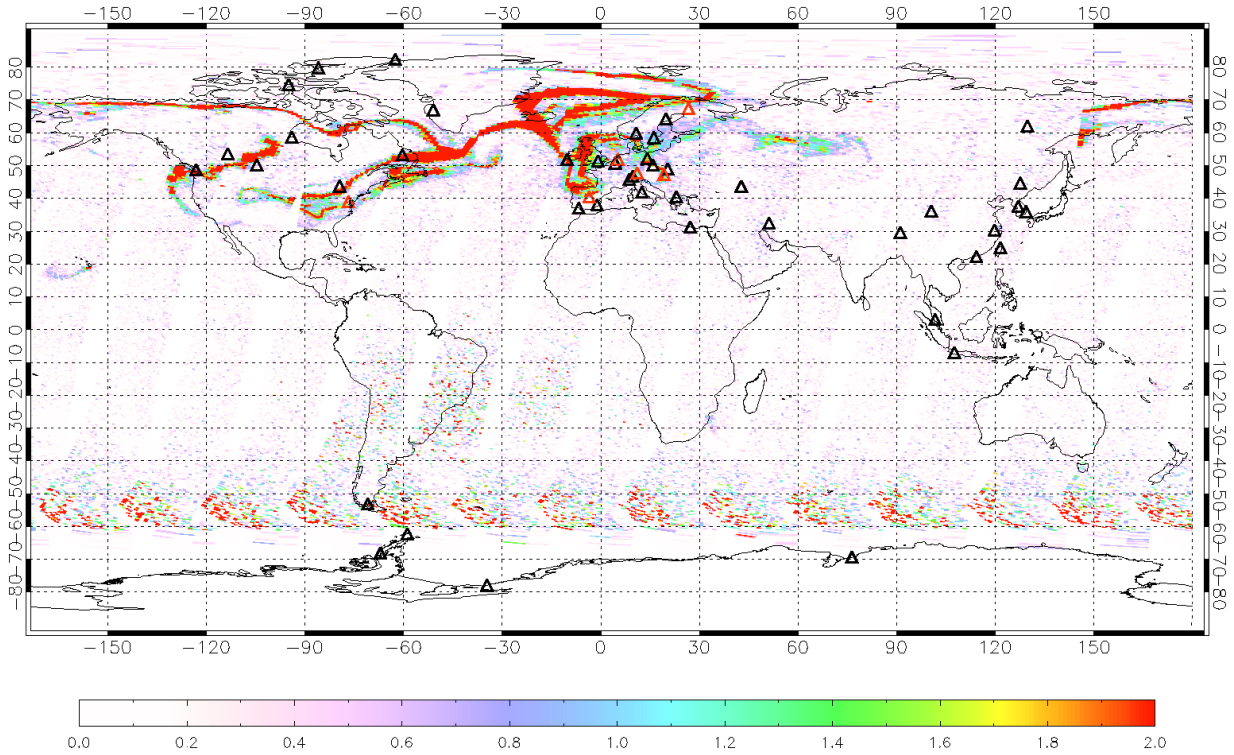

Figure 5.20: Kasatochi SO_2 eruption plume as seen by GOME-2 on 16 August 2008. The triangles mark the location of Brewer instruments. The instruments indicated in red were used for the comparison.

Comparison of SO_2 measurements

For the comparison with the GOME-2 SO_2 columns daily Brewer SO_2 data have been downloaded from the World Ozone and Ultraviolet Radiation Data Centre (WOUDC, www.woudc.org). Six Brewer stations, where data was available for the complete month of August and where the overpass of the eruption cloud was detected, were selected for a comparison with the GOME-2 SO_2 data: Budapest, Madrid, Hohenpeissenberg, De Bilt, Goddard and Sodankyla. The Brewer SO_2 data are provided by WOUDC as daily averages.
As the Kasatochi SO_2 plume reached stratospheric heights, GOME-2 SO_2 data with an assumed plume height of 15 km were used for the comparison. When the plume reached Europe on 14 August 2008, it had already been distributed into several rather small branches, therefore no regional averaging was used in the GOME-2 SO_2 data. The GOME-2 measurement closest to the location of the Brewer instrument has been selected for the comparisons. Important issues that can lead to differences, when comparing the two observations, are that GOME-2 measurements provide a snapshot from the time of overpass, whereas the Brewer observations are averaged

over the whole day. Further, the Brewer measurements are point measurements, while GOME-2 observations provide an averaged total column over the pixel size.

Budapest, Hungary (47.43°N, 19.18°E)

Figure 5.21 shows the daily SO_2 observations of the Budapest Brewer station and the GOME-2 instrument for August 2008. Both instruments show the overpass of the Kasatochi SO_2 cloud on 18 August. With 6 DU the GOME-2 observation shows approximately double the SO_2 amount of the Brewer measurement. Most likely this difference in total SO_2 column is due to the difference in time and location of the two measurements. As the Kasatochi SO_2 plume had been dispersed into smaller branches, when it reached Europe, high variations of the SO_2 amount with time and location can be expected, resulting in deviations of the total column amounts. For the days without volcanic SO_2, both instruments show a fairly large scatter of the SO_2 values between -1 DU and 2 DU. However, the overall correlation of the total columns is good with 0.65, when keeping in mind the difficulties that arise when comparing satellite and ground-based data.

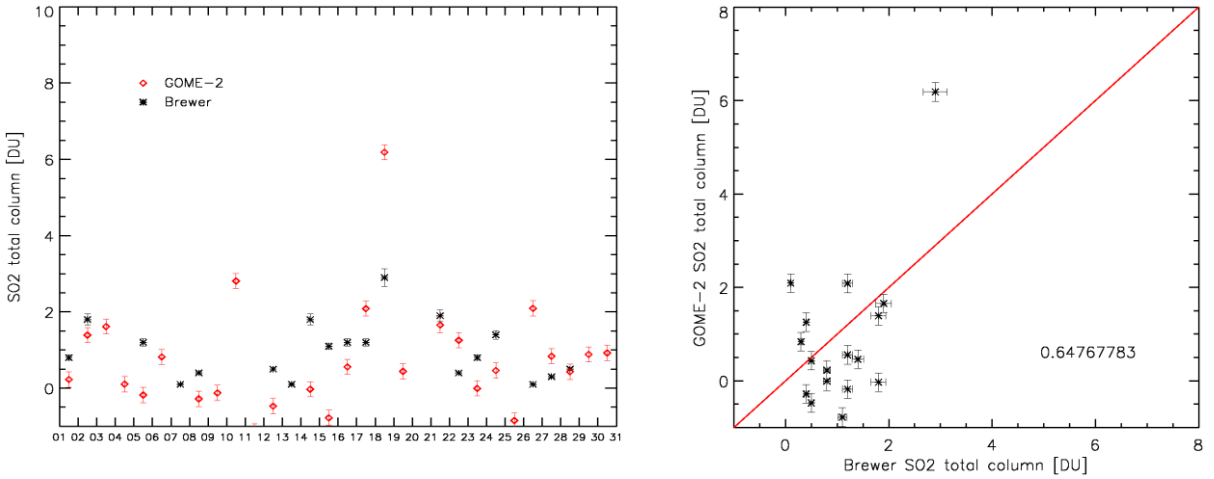

Figure 5.21: Comparison of daily Brewer and GOME-2 SO_2 observations for Budapest (left) for August 2008. The overpass of the Kasatochi eruption plume is clearly visible on the 18th.The scatter plot shows the correlation between the two observations (right).

Madrid, Spain (40.45°N, 3.55°W)

The comparison for the Brewer instrument located in Madrid is presented in Figure 5.22. The overpass of the Kasatochi eruption plume can be detected in both observations on 16 and 19 August. As has already been observed for the observations in Budapest the SO_2 amount measured by GOME-2 is much larger than for the Brewer instrument. The GOME-2 observations on the 16th show, that the Madrid Brewer was located exactly on the edge of the SO_2 plume. Due to the large GOME-2 pixel size, GOME-2 very likely has measured also the more central parts of the plume, where the SO_2 amounts were higher than towards the edges. On the 19th the SO_2 amounts that can be seen in the GOME-2 observations around Madrid are also high. Here the reason for the deviation in total column is probably the averaging over the day of the Brewer SO_2 values. If the SO_2 plume was not located over Madrid the whole day, the values measured by the Brewer instrument will be lower than those observed by GOME-2. For SO_2 free days, the GOME-2 observations show a similar scatter as for Budapest, whereas the Brewer values show less scatter, they are mainly within $\pm$ 0.5 DU of zero. The correlation of the two instruments is good and with 0.68 similar to that observed for Budapest.

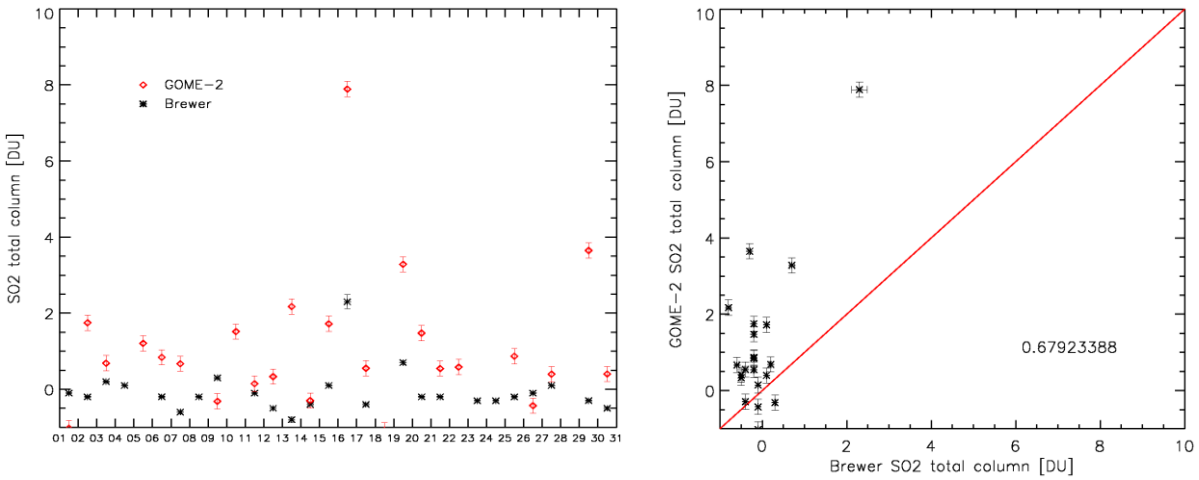

Figure 5.22: Comparison of daily Brewer and GOME-2 SO_2 observations for Madrid (left) for August 2008. The overpass of the Kasatochi eruption plume is clearly visible on the 16th and 19th.The scatter plot shows the correlation between the two observations (right).

Hohenpeissenberg, Germany (47.8°N, 11.02°E)

The GOME-2 SO_2 data in Figure 5.23 show that SO_2 from the Kasatochi eruption passed over the station at Hohenpeissenberg twice, unfortunately for the second overpass no Brewer data were available. For 17 August both instruments show the enhanced SO_2 values due to the eruption plume. Again the GOME-2 SO_2 is higher compared to the Brewer instrument. As explained above, this is most likely due to movement of the plume and daily averaging of the Brewer SO_2 data.

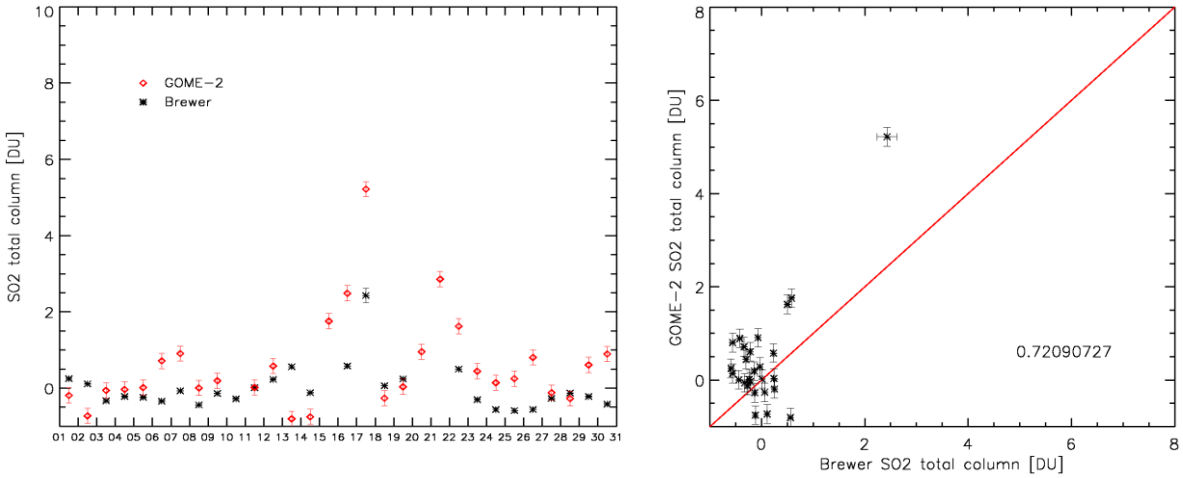

Figure 5.23: Comparison of daily Brewer and GOME-2 SO_2 observations for Hohenpeissenberg (left) for August 2008. The overpass of the Kasatochi eruption plume is clearly visible from the 15th to the 17th and on the 20th and 21st.The scatter plot shows the correlation between the two observations (right).

On 16 August the Brewer instrument detects only slightly enhanced SO_2 values (~ 0.5 DU), whereas GOME-2 clearly shows high SO_2 amounts from the volcanic plume. The effect of the movement of the SO_2 plume can be seen in the GOME-2 observations (Figure 5.24). Hohenpeissenberg is close to the area where two GOME-2 orbits overlap. While one observation shows the enhanced SO_2 values plotted in Figure 5.23, the earlier observation shows low SO_2 as suggested by the Brewer measurement. The scatter for days without volcanic SO_2 is for both instruments lower than observed for Madrid and Budapest, the correlation is with 0.72 also slightly better.

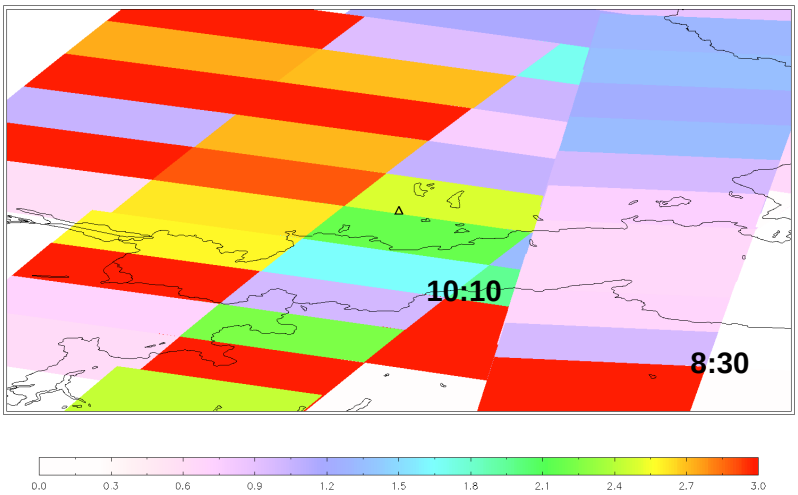

Figure 5.24: GOME-2 observation of Kasatochi SO_2 plume for 16 August. The movement of the SO_2 plume is clearly visible from the earlier observation (right orbit) to the later observation (left orbit). The approximate time of the GOME-2 measurements is given in UTC. The Brewer station at Hohenpeissenberg is depicted by the triangle.

De Bilt, Netherlands (52.0°N, 5.18°E)

The Brewer instrument in De Bilt detected the enhanced SO_2 values due to the overpass of the Kasatochi cloud on 16, 17 and 19 August and another overpass on 23 August (Figure 5.25). For the 16th and 23rd the measured SO_2 total columns match very well with those observed by GOME-2, they are within 5 % of the satellite observation. The enhanced SO_2 values on the 17th and 19th are not shown by the GOME-2 measurements. However, the GOME-2 observations show that the branch of the SO_2 plume close to De Bilt was very narrow on these days and during the time of GOME-2 observation De Bilt was located just beside the plume. It is very likely that the plume passed the station during the day, therefore the daily averages show the enhanced SO_2 values, while the GOME-2 observations in the morning did not detect any SO_2.
On the days without volcanic SO_2 the Brewer instrument shows a constant offset compared to the GOME-2 observations, while the GOME-2 values are scattered around zero, the Brewer measurements suggest values constantly around 1.5 to 2 DU. These values seem to be quite high as 2 DU SO_2 are typically only observed in highly polluted regions, e.g. China, and such high values should be visible also in the GOME-2 observations, as the comparisons with the Max-DOAS observations in Beijing have shown. The correlation of the two instruments is with 0.44 not as good as for the other Brewer instruments, however, this is to a large extent due to the offset between the two observations, as the observations on most days during the overpass show an excellent agreement.

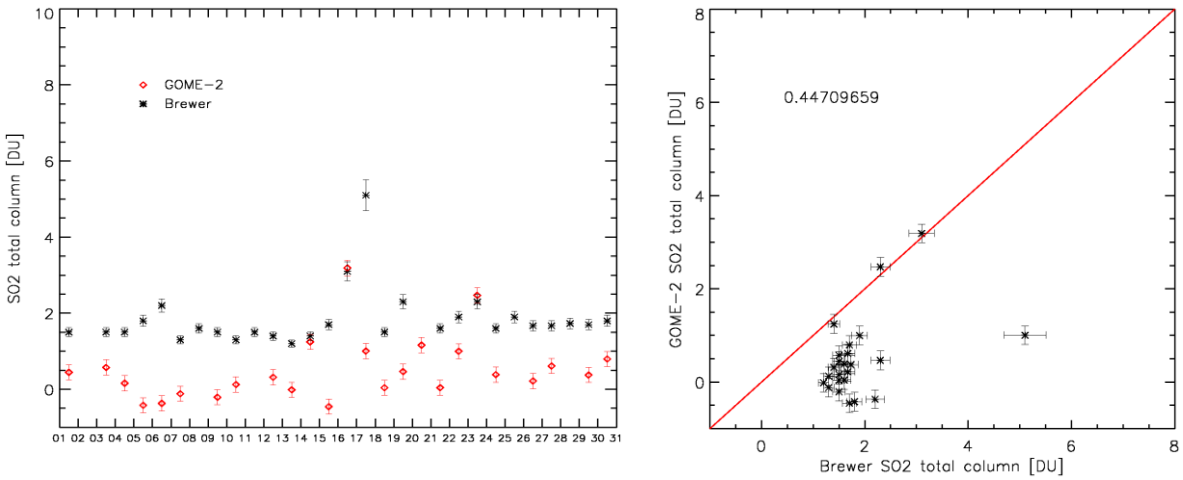

Figure 5.25: Comparison of daily Brewer and GOME-2 SO_2 observations for De Bilt (left) for August 2008. The overpass of the Kasatochi eruption plume is clearly visible from the 15th to the 19th and on the 23rd. The scatter plot shows the correlation between the two observations (right).

Sodankyla, Finland (67.37°N, 26.65°E)

Several branches of the SO_2 plume from the Kasatochi eruption passed the Brewer station at Sodankyla between 16 and 24 August (Figure 5.26). Both instruments show the enhanced SO_2 values very well, they are mainly within 20 % of each other, especially on the 22 August, both instruments detect the overpass of the Kasatochi eruption plume and show high SO_2 values around 13 DU. For the other days the SO_2 values measured by both instruments scatter around zero. The scatter of the GOME-2 measurements is higher as the station is relatively far north with larger solar zenith angles which results in a higher noise level. However, the correlation of the two measurements is with 0.85 very high showing an excellent agreement between the Brewer and GOME-2 observations for this station.

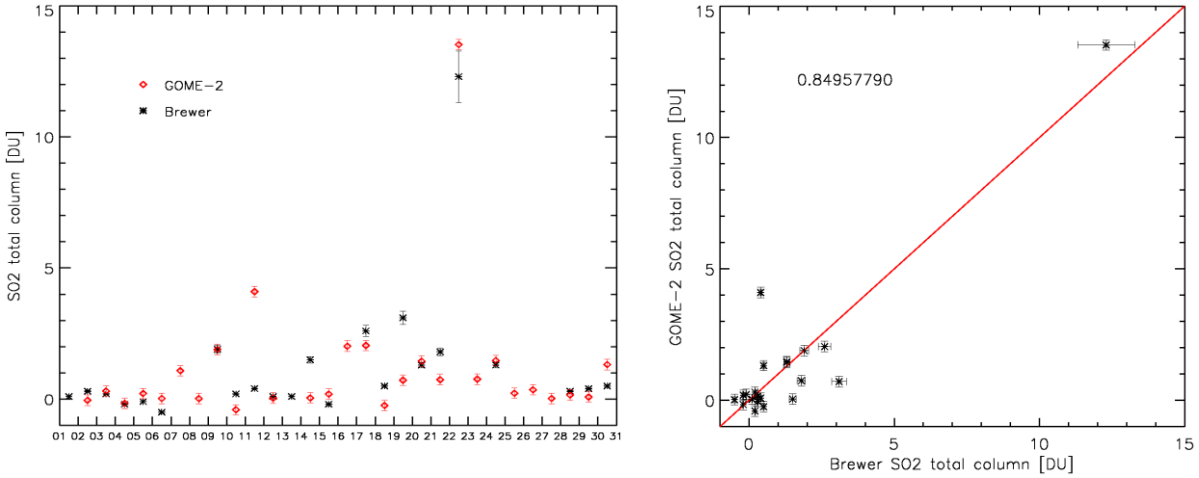

Figure 5.26: Comparison of daily Brewer and GOME-2 SO_2 observations for Sodankyla (left) for August 2008. The overpass of the Kasatochi eruption plume is clearly visible from the 16th to the 24th with very high SO_2 values on the 22nd. The scatter plot shows the correlation between the two observations (right).

Goddard, USA (38.99°N, 76.83°W)

Figure 5.27 shows the comparison of the SO_2 columns from the Brewer spectrometer at Goddard with the GOME-2 observations. The overpass of the Kasatochi eruption cloud is visible between 15 and 21 August. The differences between the two instruments are quite large for this station. On the first day of the overpass the

Brewer measurements detect an average SO_2 column of 5.5 DU, whereas the GOME-2 observations show no enhanced SO_2 values. On that day the Brewer station was located just beside the edge of the volcanic plume during the time of observation, therefore it is very likely that the daily average shows the overpass of the plume, which was not present at the time of the GOME-2 observation. On the next day the GOME-2 observation shows values of 6 DU compared to 3.3 DU in the Brewer measurement. Again, the Brewer is located on the edge of the plume at the time of the GOME-2 overpass, this time inside the plume. The Brewer average on that day very likely also includes measurements outside the area with the enhanced SO_2 values and is therefore lower than the SO_2 measured by GOME-2 inside the plume. For the other days the agreement is better, here both instruments detect the enhanced SO_2 values and the total columns are within a range of 35 %. As for De Bilt a continuous offset of the total column values can be observed for the days where no volcanic SO_2 is present. The Brewer total columns are mainly around 2 – 3 DU, while the GOME-2 values are from 0 – 1 DU. Again the SO_2 values suggested by the Brewer instrument seem very high, as the region is not highly polluted and no significant SO_2 can be observed in the GOME-2 monthly averages for this area. The correlation of the measurements is with 0.22 very low compared to the other stations, however, it is difficult to estimate the significance of the correlation as the quality of the Brewer measurements seems doubtful.

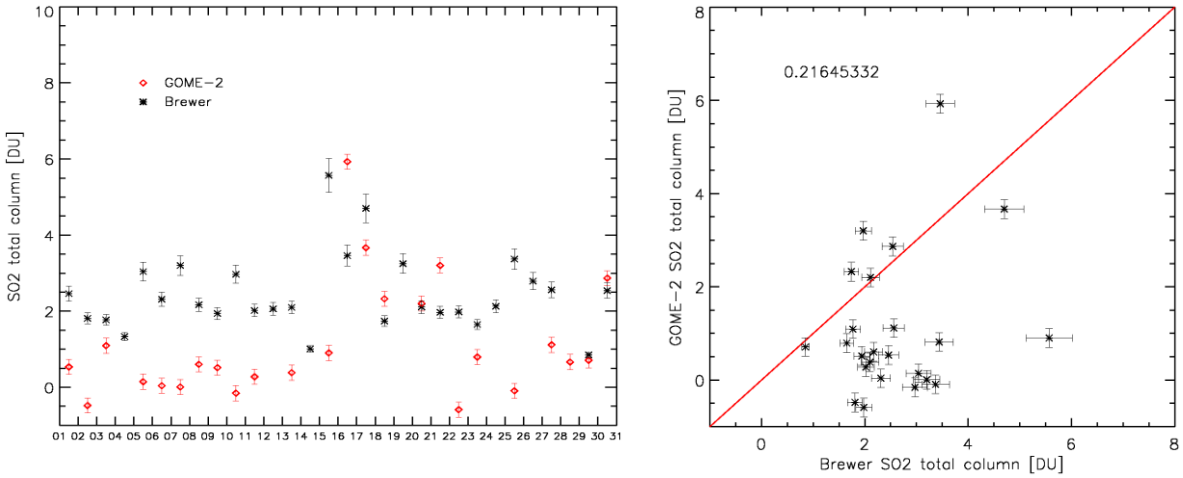

Figure 5.27: Comparison of daily Brewer and GOME-2 SO_2 observations for Goddard (left) for August 2008. The overpass of the Kasatochi eruption plume is clearly visible from the 15th to the 21st. The scatter plot shows the correlation between the two observations (right).

5.4 Conclusions

The comparisons with other measurements of atmospheric SO_2 show an overall good quality of the operational GOME-2 SO_2 data products. The comparison with SCIAMACHY SO_2 data for the eruptions of Kasatochi and Kilauea shows a good agreement between the two instruments with difference typically < 25 %. Differences in the total SO_2 columns for very high SO_2 amounts at stratospheric heights are due to the use of different settings for the SO_2 slant column retrieval and only occur in this specific situation.

Comparisons of GOME-2 SO_2 data with ground-based observations are difficult as ground-based instruments typically perform a point measurement, whereas the GOME-2 measurement averages over the pixel size (80 x 40 km²). Also the time difference between the observations can be problematic, especially if measuring highly variable volcanic SO_2 fluxes. Despite these differences a good agreement of GOME-2 SO_2 with ground-based observations could be shown. The best results were obtained for the comparison with Brewer observations of stratospheric SO_2 from the Kasatochi eruption, since the sensitivity of GOME-2 to SO_2 at high altitudes is very good. In this case, the comparison of daily SO_2 total columns yields good results with correlations up to 0.85. For SO_2 at lower altitudes the comparisons are more challenging also due to the reduced sensitivity of GOME-2 at these altitudes and the increased scatter. Here the daily observations of SO_2 in Beijing and at Kilauea do not agree well with the GOME-2 observations. The Max-DOAS observations of anthropogenic pollution at Beijing show a slightly better agreement with the GOME-2 measurements compared to the volcanic SO_2 flux measurements at Kilauea. This is due to the highly variable nature of volcanic SO_2 fluxes, making it difficult to compare the two observations that are both not continuous and because of the difficulty of estimating SO_2 fluxes from GOME-2 observations. However, if looking at the monthly averages, both comparisons yield good results. While the daily SO_2 data show only a reasonable qualitative agreement, the monthly averages also correspond well in terms of total SO_2 values with deviations mainly below 25 %.

Overall it has been shown that the operational GOME-2 SO_2 product is of good quality, especially for higher altitudes. For lower altitudes the GOME-2 SO_2 columns show a fairly large scatter, that continues to increase due to the instrument degradation. However, changes in the SO_2 emissions from anthropogenic pollution or volcanoes can be detected to a great extent and averaging improves the results significantly.

6. Near-real time estimation of volcanic SO_2 plume height

The correct determination of the volcanic plume height is a central issue for aviation safety, as well as for air quality and climate studies. For aviation safety information on the plume height is important to avoid flying through volcanic plumes. As the injection height also determines the further distribution of the volcanic cloud, it is an important input parameter for modeling and forecasting the future development of the plume. The altitude of the volcanic SO_2 also plays an important role in determining the climatic effects of an eruption, as sulfate aerosols forming from SO_2 can persist in the stratosphere for a long time and lower the global surface temperature (Pinatubo eruption, 1991) (McCormick et al, 1995).

Additionally, plume height information is required for the correct quantitative retrieval of the SO_2 total columns, as the DOAS methods and the direct fitting technique all use a priori assumptions on the vertical SO_2 distribution (Chapter 4). These profile assumptions are typically characterized through a central SO_2 plume height. If no additional plume height information is available at the time of the retrieval, errors are introduced due to differences between the assumed and the actual plume height.

Recently various techniques have been developed to retrieve the volcanic plume height from satellite observations. The inverse trajectory modeling uses a trajectory model to simulate the SO_2 transport for several assumed injection heights and matches the results with satellite observations to determine the most probable plume height (Eckhardt et al., 2008). A second approach is based on an extension of the Iterative Spectral Fitting (ISF) algorithm for the OMI instrument and can retrieve ozone column, SO_2 column and SO_2 altitude simultaneously (Yang et al., 2009) through a direct fitting technique. Both techniques have proven their ability to determine volcanic eruption heights, however, these techniques are computationally time consuming and especially for aviation safety the plume height information is required in near-real time (NRT). Therefore a new approach has been developed to estimate the plume height in NRT by matching GOME-2 measurement spectra with simulated GOME-2 spectra for various heights, which are stored in a look-up table (LUT).

6.1 Near-real time SO_2 plume height estimation

The height of a volcanic SO_2 plume determines the proportion of backscattered photons that pass the absorbing layer on their way to the satellite instrument. The higher the plume height the more photons are Rayleigh scattered below and therefore pass through the SO_2 plume resulting in more prominent SO_2 absorption structures in the measured radiances. If the layer is in the lower atmosphere more photons are scattered above. Therefore the measured radiances contain information about the SO_2 plume altitude besides the total column information.

The absorption depends on the total SO_2 amount as well as the plume height. The dependence is however caused by different processes, while a change in total column results in a different absorption optical thickness a change in plume height causes a variation in the number of photons that have passed the SO_2 plume. The total column and height weighting function and the corresponding differential

weighting functions show the responses of the TOA radiances (Figure 6.1). The weighting functions have a strong correlation as both clearly show the structure of the SO_2 absorption cross-section. However, there are differences in the response of TOA radiances to changes in the SO_2 total column and to changes in SO_2 plume height. Also the variation with the plume altitude is very different for the total column and height weighting function. The different structure of the weighting functions allows a retrieval of both total column and height information from the GOME-2 radiance measurements. The total column weighting functions are about one order of magnitude larger, indicating that the response to the total column is much stronger than to the SO_2 plume altitude. For the calculation of the weighting functions an SO_2 profile has been used, where the SO_2 is confined in a thin atmospheric layer, as this allows easy variation of the plume altitude. Tests have shown that the structure of the weighting functions is very similar to those for a Gaussian SO_2 profile, as is used for the simulation of the GOME-2 spectra.

For the estimation of the SO_2 plume height differential GOME-2 spectra are used to minimize the influence of albedo, clouds and aerosols, which are often present in volcanic plumes, as they show fairly broad extinction structures. The corresponding weighting functions are shown in Figure 6.1 (bottom).

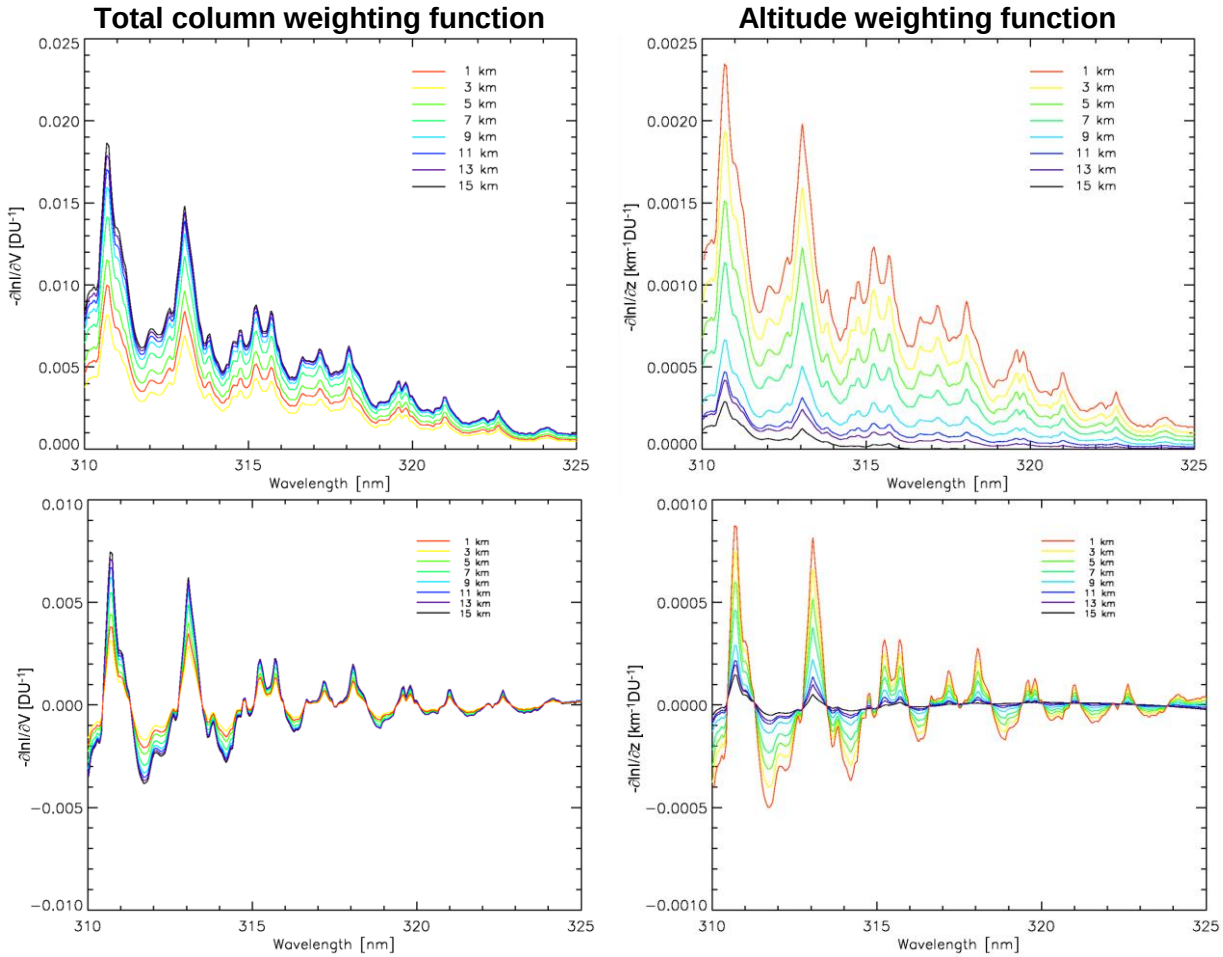

Figure 6.1: Total SO_2 column (top, left) and altitude weighting functions (top, right) and the corresponding differential weighting functions (bottom).

The plume height is estimated through a combination of the DOAS method to retrieve the total SO_2 column and matching of simulated GOME-2 spectra to retrieve the

plume height, as shown in Figure 6.2. The GOME-2 spectra are simulated with LIDORT-RRS (Spurr et al., 2008) for different assumed central plume heights z between 1 – 15 km. For modeling a Gaussian SO_2 profile is used (FWHM = 2.5 km) and the plume heights refer to the central height of the profile. Further input parameters for the simulation of the spectra are total ozone column and profile, satellite viewing geometry, surface albedo, cloud fraction and cloud top albedo. The ozone total column information is taken from the operational GOME-2 product, for profile information the TOMS version 7 column-classified ozone profile climatology (Wellemeyer et al., 1997) is used, the surface albedo is that used for the operational DOAS SO_2 retrieval (Chapter 3.4.3) and the cloud information is obtained from the OCRA and ROCINN algorithms (Loyola et al, 2007). For the simulations a wavelength range between 312 nm – 325 nm is used.

The first guess SO_2 vertical column $V^{(0)}$ is taken from the operational DOAS product with an assumed plume height of z_0 = 15 km. Then simulated spectra based on the first guess column are then matched through a least squares fit (F_{LSQ}) with the measurement.

$$R = \left(I_{\mathrm{mod}} - I_{meas}\right)^2 \tag{6.1}$$

where I_{mod} is the modeled GOME-2 spectrum and I_{meas} is the measured spectrum. The simulated spectrum, that shows the smallest difference R to the measured spectrum, is selected as the new plume height.

$$F_{LSQ}\left(V^{(n)}, z^{(n)}\right) \rightarrow z^{(n+1)} \tag{6.2}$$

If the retrieved plume height is not equal to the plume height assumed in the DOAS retrieval ($z^{(n+1)} \neq z^{(n)}$), the vertical column is recalculated using the DOAS method (F_{DOAS}) using the new plume height.

$$F_{DOAS}\left(V^{(n)}, z^{(n+1)}\right) \rightarrow V^{(n+1)} \tag{6.3}$$

To allow a NRT estimation of the plume height a look-up table approach is used with pre-calculated GOME-2 spectra. The simulated GOME-2 spectra are stored in the LUT according to total SO_2 column, SO_2 plume height, total ozone column, albedo, solar zenith angle, viewing angle and relative azimuth angle. The spectra for matching with the measurement are derived through interpolation in the LUT.

The iteration stops when the assumed and retrieved plume height converge. In a last step a polynomial is fitted through R to retrieve the final plume height, as the simulations are currently done with height steps of 2 km.

Figure 6.1 (right) shows that the altitude weighting functions in the used wavelength region are small for altitudes above 10 km. Other studies (Yang et al., 2009) have shown that the optimal region to retrieve plume heights between 10 km – 20 km is between 300 nm – 310 nm. However, below 312 nm the response of the instrument to radiance and irradiance decreases dramatically (EUMETSAT, 2011) resulting in a very limited data quality, which makes a correct retrieval impossible. For using lower wavelength regions, a combination of channel 1 and 2 would be necessary. Although

this is technically challenging, an extension of the plume height estimation to lower wavelength regions is planned for the future.

The effect of the small weighting functions for plume heights above 10 km can be compensated to some extent by choosing the starting height as 15 km. As for high plume altitudes this first guess is already very close to the actual plume height, the retrieval method still estimates the plume height correctly, when tested on simulated spectra (Section 6.2), while a lower starting height leads to errors when retrieving higher plume altitudes.

As the GOME-2 measurement provides an average over the pixel area (40 km x 80 km), the retrieved height is also an average height, often referred to as effective height, over the pixel area. This can cause uncertainties in the retrieval if the plume height shows large variations over the pixel area or especially if only part of the pixel area is covered by the SO_2 plume. Further uncertainties in the retrieved height can arise if the atmospheric SO_2 profile differs strongly from the Gaussian profile shape assumed in the simulations.

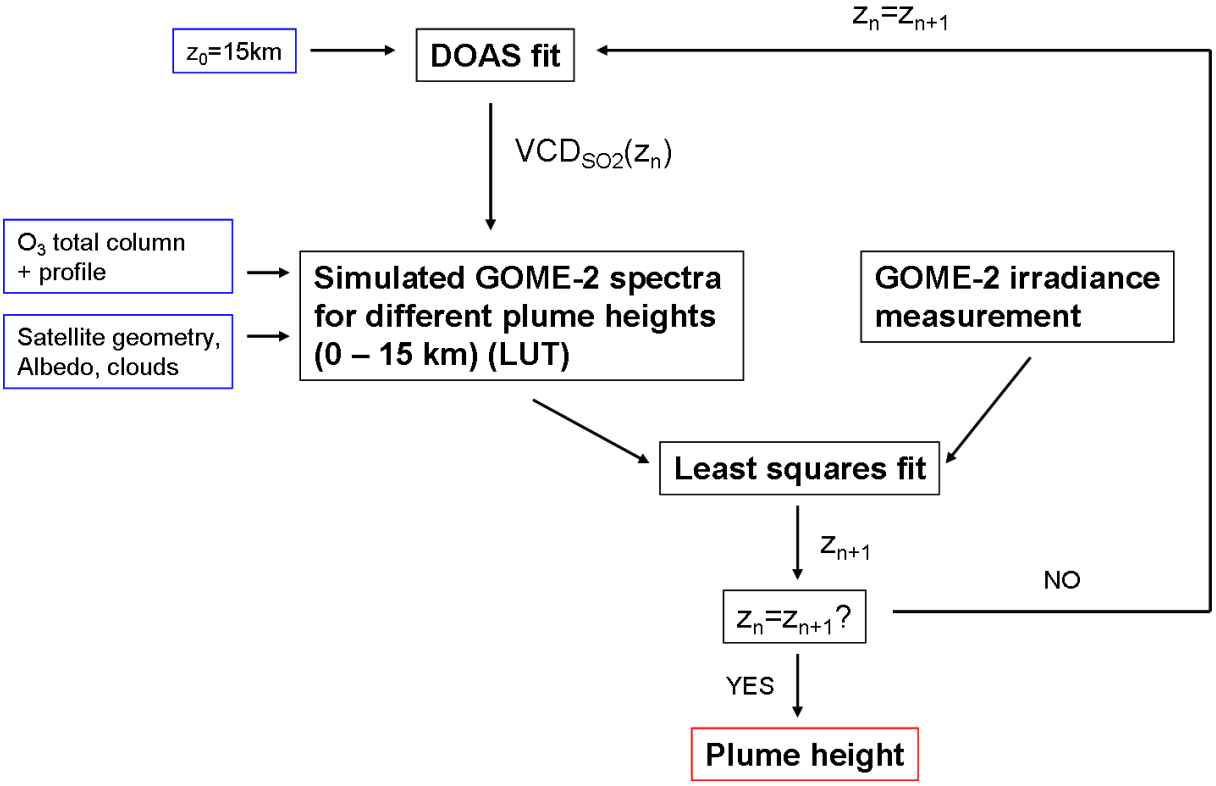

Figure 6.2: Schematic overview of the NRT plume height estimation algorithm

6.2 SO_2 plume height estimation using synthetic GOME-2 spectra

The height retrieval algorithm has been applied to synthetic GOME-2 spectra to evaluate its ability to retrieve the SO_2 plume height correctly. The tests have been conducted with synthetic measurement spectra for total SO_2 columns of 2 DU, 10 DU, 20 DU and 60 DU and plume heights of 1 km, 3 km, 5 km, 7 km, 9 km, 11 km, 13 km and 15 km. The initial guess for the total column $V^{(0)}$ has been determined using

the DOAS method with an assumed plume height of 15 km ($z^{(0)}$), hence taking into account the uncertainties of the DOAS retrieval. The tests were conducted for different ozone total columns and solar zenith angles. The results of the tests for the different total SO_2 columns are show in Table 6.1.

The approach yields good results, in most cases the plume height could be retrieved with an accuracy of 2 km or better. Despite the underestimation of higher SO_2 columns by the DOAS technique, the height estimation yields better results for medium to high total SO_2 column amounts. For a total column amount of 2 DU the retrieval overestimates the plume height by 2 km for simulated plume heights of 3 km and 5 km. For small solar zenith angles this overestimation can also be observed for a plume height of 7 km. For a total SO_2 column of 10 DU the plume height is overestimated for simulated plume heights of 1 km and 3 km and for low SZA also for 5 km, while for total column amounts over 20 DU the method retrieves the simulated plume height correctly. For plume heights above 7 km the retrieval results are very good in all situations. For plume heights in the lower troposphere and total columns up to 10 DU the height estimation yields better results for higher solar zenith angles, as in this case the light path through the atmosphere is longer and the Rayleigh scattering, which is mainly responsible for the spectral height information, has a higher effect. The method typically needs 3-4 iterations to retrieve lower tropospheric heights and 2-3 iterations for heights in the upper troposphere or lower stratosphere.

Overall the retrieval is working well for most situations, very low solar zenith angles can lead to an overestimation of lower tropospheric plume heights. This effect is more pronounced for low total SO_2 columns and cannot be observed for total SO_2 columns above 20 DU. The results indicate that the height estimation is less accurate for low total SO_2 amounts, but provides highly reliable results for SO_2 columns between 10 – 60 DU.

2 DU SO_2	**Retrieved plume height**				
Simulated	**O_3=325 DU**			**O3=175 DU**	**O3=525 DU**
plume height	**sza=30°**	**sza=55°**	**sza=70°**	**sza=55°**	**sza=55°**
1	1 (4)	1 (4)	1 (3)	1 (3)	3 (4)
3	5 (4)	5 (3)	5 (3)	5 (3)	5 (3)
5	7 (3)	7 (3)	7 (2)	7 (3)	7 (3)
7	9 (2)	7 (3)	7 (3)	7 (3)	7 (3)
9	11 (2)	9 (3)	9 (3)	9 (3)	9 (3)
11	11(2)	11 (2)	11 (2)	11 (2)	11 (2)
13	15 (1)	15 (1)	13 (2)	15 (1)	13 (2)
15	15 (1)	15 (1)	15 (1)	15 (1)	15 (1)

Table 6.1: Plume height retrieved for a total SO_2 column of 2 DU for different atmospheric settings. The value in the parentheses denotes the number of iterations necessary.

10 DU SO_2	Retrieved plume height				
Simulated	O_3=325 DU			O3=175 DU	O3=525 DU
plume height	sza=30°	sza=55°	sza=70°	sza=55°	sza=55°
1	3 (3)	3 (3)	3 (3)	1 (4)	3 (3)
3	5 (3)	5 (3)	3 (3)	3 (3)	5 (3)
5	7 (2)	5 (3)	5 (3)	5 (3)	7 (2)
7	7 (3)	7 (3)	7 (3)	7 (3)	7 (3)
9	9 (3)	9 (3)	9 (2)	9 (3)	9 (3)
11	11 (2)	11 (2)	11 (2)	11 (2)	11 (2)
13	13 (2)	13 (2)	13 (2)	13 (2)	13 (2)
15	15 (1)	15 (1)	15 (1)	15 (1)	15 (1)

Table 6.2: Plume height retrieved for a total SO_2 column of 10 DU for different atmospheric settings. The value in the parentheses denotes the number of iterations necessary.

20 DU SO_2	Retrieved plume height				
Simulated	O_3=325 DU			O3=175 DU	O3=525 DU
plume height	sza=30°	sza=55°	sza=70°	sza=55°	sza=55°
1	1 (3)	1 (3)	1 (3)	1 (3)	3 (3)
3	3 (3)	3 (3)	3 (3)	3 (3)	5 (3)
5	5 (3)	5 (3)	5 (3)	5 (3)	5 (3)
7	7 (3)	7 (3)	7 (3)	7 (3)	7 (3)
9	9 (3)	9 (3)	9 (2)	9 (2)	9 (3)
11	11 (2)	11 (2)	11 (2)	11 (2)	11 (2)
13	13 (2)	13 (2)	13 (2)	13 (2)	13 (2)
15	15 (1)	15 (1)	15 (1)	15 (1)	15 (1)

Table 6.3: Plume height retrieved for a total SO_2 column of 20 DU for different atmospheric settings. The value in the parentheses denotes the number of iterations necessary.

60 DU SO_2	Retrieved plume height				
Simulated	O_3=325 DU			O3=175 DU	O3=525 DU
plume height	sza=30°	sza=55°	sza=70°	sza=55°	sza=55°
1	1 (3)	1 (3)	1 (3)	1 (2)	1 (3)
3	3 (2)	3 (3)	3 (3)	3 (2)	3 (3)
5	5 (3)	5 (3)	5 (3)	5 (2)	5 (3)
7	7 (2)	7 (2)	7 (2)	7 (2)	7 (2)
9	9 (2)	9 (2)	9 (2)	9 (2)	9 (2)
11	11 (2)	11 (2)	11 (2)	11 (2)	11 (2)
13	13 (2)	13 (2)	13 (2)	13 (2)	13 (2)
15	15 (1)	15 (1)	15 (1)	15 (1)	15 (1)

Table 6.4: Plume height retrieved for a total SO_2 column of 60 DU for different atmospheric settings. The value in the parentheses denotes the number of iterations necessary.

6.3 Application of the NRT plume height estimation to GOME-2 observations of volcanic eruptions

The plume height estimation has been applied to GOME-2 measurement data of several volcanic eruption plumes. Three volcanic eruptions have been selected, where different altitudes of the SO_2 plume could be expected. First the retrieval was applied to SO_2 emissions of Kilauea, Hawaii, where due to the effusive nature of the eruption the plume altitudes are typically below 5 km. In addition the algorithm was applied to the eruption of Kasatochi, Alaska, which brought high amounts of SO_2 to stratospheric heights and to the eruption of Eyjafjallajökull, Iceland, that reached mid-tropospheric heights. The results were compared to those from other methods and sources, e.g. trajectory matching or LIDAR data.

6.3.1 Kilauea, Hawaii

As a first example the height of the SO_2 eruption plume of Kilauea volcano on 9 July 2008 has been analyzed. Since the beginning of a new highly eruptive phase in March 2008, Kilauea continuously emits SO_2 in an effusive eruption, typically reaching plume heights between the summit height (1222 m) and 5 km. As the tests with the simulated spectra have shown that low SO_2 total columns can lead to issues when retrieving low plume heights, the 9 July has been selected as the SO_2 amounts emitted were fairly high on that day, up to ~ 20 DU, while typical SO_2 total columns at Kilauea are below 5 DU. For the plume height estimation only measurements with a total column > 2 DU have been taken into account.

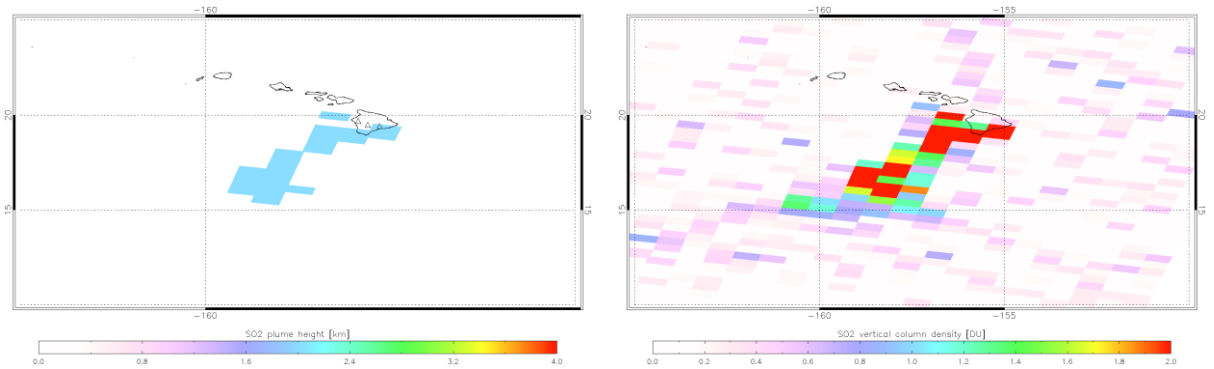

Figure 6.3: Estimated SO_2 plume height (left) and total SO_2 column (right) for the eruption plume of Kilauea, Hawaii, on 9 July 2008.

Figure 6.3 shows the results when applying the new height retrieval technique to the SO_2 plume at Kilauea volcano. The plume height is estimated to around 2 km, which is a typical plume height for Kilauea. The trajectory analysis with the FLEXTRA model for that day estimates the plume height to be between 1 km and 3 km, with the most likely plume height being 2 km (Figure 6.4). The results of the trajectory analysis match the plume heights retrieved directly from the GOME-2 measurements nicely indicating that the new plume height retrieval performs well for this eruption.

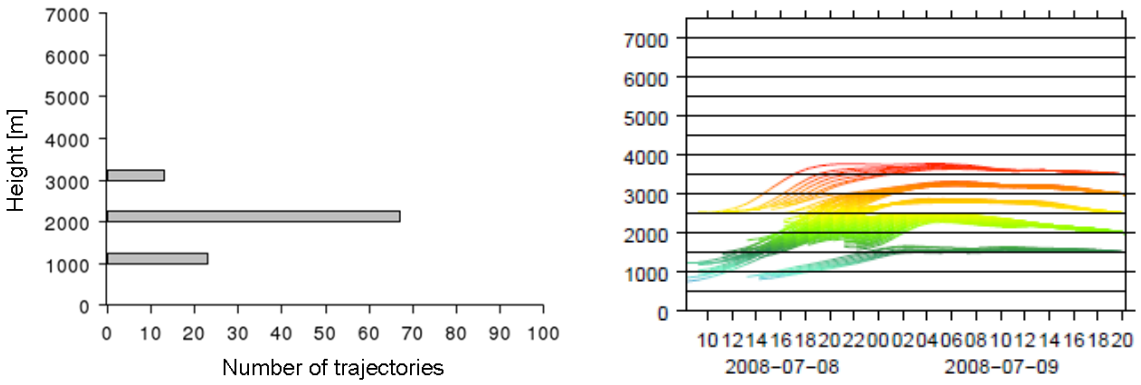

Figure 6.4: Plume height estimation from trajectory analysis using the FLEXTRA model for Kilauea volcano, 7 July 2008 (Seidenberger, 2009).

6.3.2 Kasatochi, Alaska

The Kasatochi eruption was selected as an example of a volcanic eruption that brought high amounts of SO_2 (up to 160 DU) to stratospheric heights. The eruption occurred on the evening of 7 August 2008 and was detected by GOME-2 the following day. For the analysis the first day after the eruption was selected and only measurements containing more than 5 DU SO_2 were used. The further distribution of the SO_2 cloud during the following weeks (Figure 7.1) showed that the SO_2 was brought into the stratosphere, where the SO_2 has a longer lifetime and can be distributed over long distances.

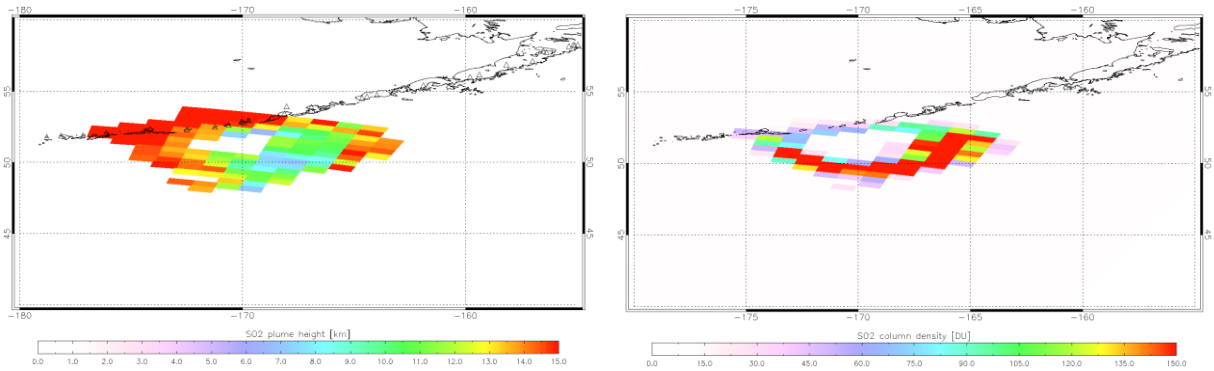

Figure 6.5: Estimated SO_2 plume height (left) and total SO_2 column (right) for the eruption plume of Kasatochi, Alaska, on 8 August 2008.

The NRT plume height retrieval estimates SO_2 plume heights between 7 km and 15 km for the Kasatochi eruption plume on the first day after the eruption (Figure 6.5), with a region of lower plume heights (7 - 11 km) mainly in the eastern part of the plume and higher plume heights (13 – 15 km) in the western part of the plume. Trajectory modeling with the FLEXTRA model for the Kasatochi eruption suggests SO_2 plume heights from 8 km – 14 km, with the most likely injection height being at 13 km and 14 km (Seidenberger, 2009). Kristiansen et al. (2010) determined a vertical SO_2 emission profile with two peaks at 13 km and 7 km (Figure 6.6) using the atmospheric transport model FLEXPART (Stohl et al., 2005). These results are very similar to those obtained by the NRT estimation, indicating a good performance of the retrieval.

The space based Cloud-Aerosols Lidar with Orthogonal Polarization (CALIOP) on board the CALIPSO platform also provides information on the height of volcanic plumes in the atmosphere. On the days following the eruption of Kasatochi volcano the CALIPSO data indicate the presence of volcanic aerosols between 5 km and 18 km (Westphal et al., 2008). These observations further support the results from the NRT plume height estimation, even though the volcanic SO_2 and ash can be at different altitudes in the atmosphere. An example of the CALIPSO observations is shown in Figure 6.7. On 11 August 2008 the CALIOP LIDAR detected an aerosol cloud that originated from the Kasatochi eruption. The aerosol cloud was at an altitude of ~ 13 km in the atmosphere.

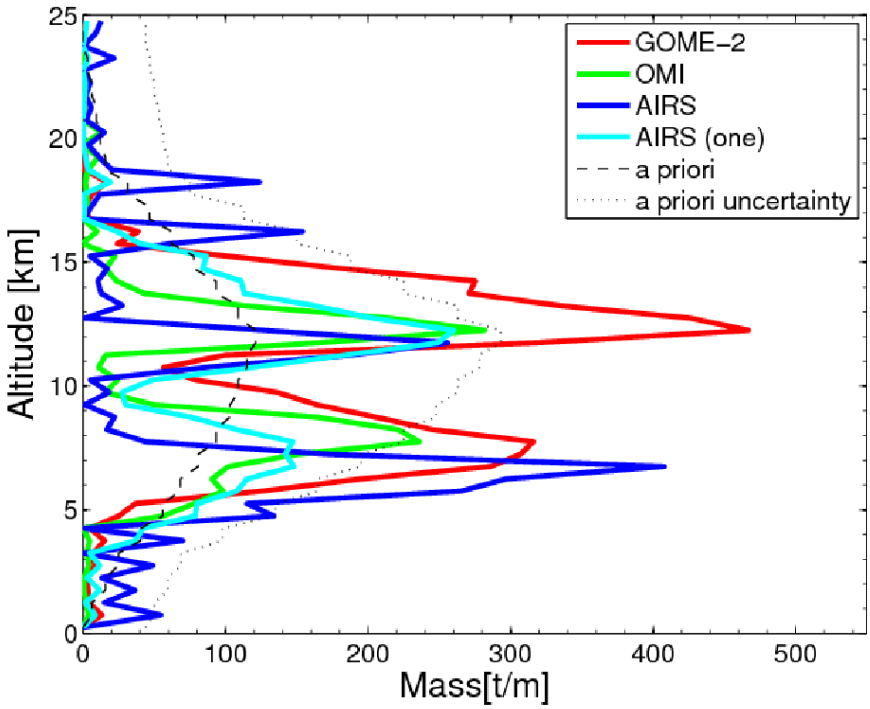

Figure 6.6: Vertical SO_2 emission profile of the Kasatochi eruption on 8 August 2008 determined using the FLEXPART model. (Adapted from Kristiansen et al., 2010)

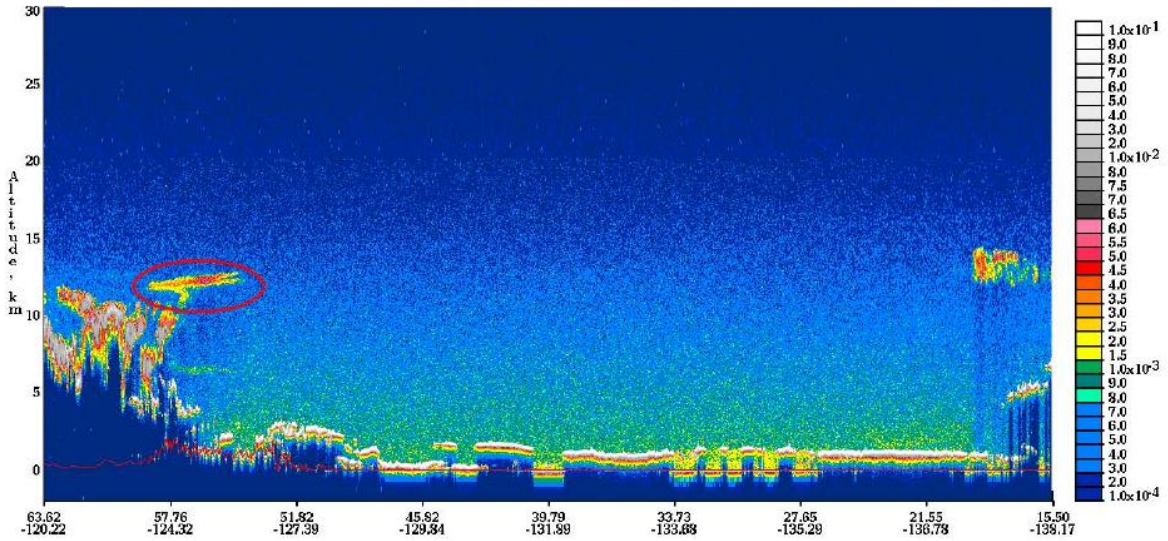

Figure 6.7: CALIOP observation on 11 August 2008, an aerosol cloud that could be related to the Kasatochi eruption was detected between 10 -13 km height (NASA, 2009).

6.3.3 Eyjafjallajökull, Iceland

As an example of an explosive eruption that emitted SO_2 at mid-tropospheric heights, the eruption of Eyjafjallajökull, Iceland, was selected. The eruption lasted from 14 April to 23 May 2010 and caused an unprecedented disruption of European air traffic. For analyzing the plume height 5 May has been selected, as the SO_2 emissions were fairly low during the eruptive period in April. As before, only measurements with a total column > 5 DU have been used in the retrieval.

Figure 6.8 shows that the retrieved heights are mainly between 8 km – 13 km, with lower heights between 3 km – 8 km in the eastern part of the plume. The plume height reported at the volcano that day was around 9 km and around 5 km the previous day. These reports agree quite well with the retrieved plume heights and could explain the lower SO_2 plume heights in the eastern part of the plume, as it is likely that the SO_2 in this part of the plume has already been emitted on the previous day. Trajectory analysis for 5 May shows SO_2 plume heights between 6 km – 13 km (C. Maerker, personal communication) indicating, as the reported plume heights, that the direct plume height retrieval produces reasonable results.

For the measurement closest to the volcano a plume height of 15 km is retrieved, which seems too high compared to the reported plume height and the trajectory matching. A possible explanation could be that the retrieval is obstructed by high amounts of volcanic ash, which are typically found close to the volcano. The effects of aerosol on the height retrieval should to some extent be compensated by the use of differential spectra, however high amounts of volcanic ash can lead to high optical thickness and therefore possibly influence the retrieval. A further difficulty for the analysis of the eruption plume of Eyjafjallajökull is the narrow character of the SO_2 plume. As explained above the plume height retrieval is problematic if only parts of the pixel area are covered by the SO_2 plume. However, for most parts of the plume the results of the NRT plume heights estimation seem to be reasonable.

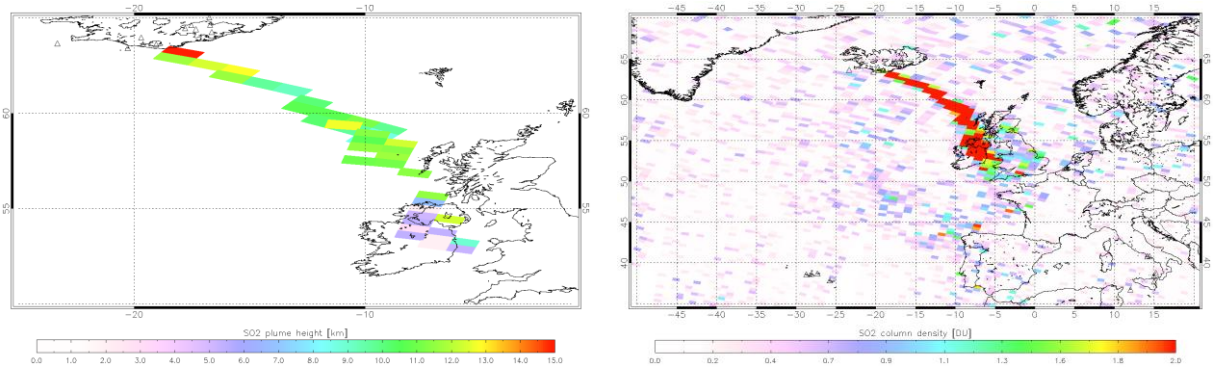

Figure 6.8: Estimated SO_2 plume height (left) and total SO_2 column (right) for the eruption plume of Eyjafjallajökull on 5 May 2010.

6.4 Conclusions

A new method to estimate the SO_2 plume height in NRT has been developed, that matches simulated GOME-2 radiances, which are stored in a look-up table, with GOME-2 measurement spectra. Tests using simulated GOME-2 spectra have shown that the developed NRT SO_2 plume height retrieval produces reliable results in most cases with an accuracy of 2 km and better. They also show that the plume height

estimation yields better results for higher total SO_2 columns, while for low total SO_2 columns the results for the lower plume heights are less accurate and the dependency on the solar zenith angle is stronger. The method has been applied to three different volcanic eruptions. It could be shown that the method is able to distinguish between the typically low plume heights observed at Kilauea and the stratospheric heights reached during the eruption of Kasatochi. Further the results of the NRT retrieval have been compared to plume heights obtained with other techniques, e.g. trajectory matching. The results of the new NRT plume height retrieval match those from other sources well, indicating that the new method produces reliable results.

However, several aspects need further investigation to obtain a more complete picture of the method's possibilities. The influence of clouds and aerosols on the height estimation has to be investigated in detail to understand how these parameters influence the retrieval results. Additionally the effect of the pixel area being only partly covered by the SO_2 plume has to be examined.

Further it is planned to improve the NRT height estimation by the use of GOME-2 channel 1 to extend the wavelength range used for the retrieval to wavelengths below 312 nm. As the weighting functions are larger in this wavelength region, especially for plume heights above 10 km, an improvement of the retrieval accuracy is expected. It is also planned to use a modification of the method. To avoid the errors that are introduced by uncertainties in the AMF an empirical approach is under development using synthetic SO_2 slant columns derived by performing a DOAS fit on the simulated GOME-2 spectra. This will allow matching the GOME-2 measurement spectrum with the simulated GOME-2 spectra according to the retrieved slant column instead of the vertical column, thus avoiding additional uncertainties being introduced by the AMF.

Overall, the new NRT SO_2 plume height estimation is a promising technique to obtain information about the volcanic plume height shortly after an eruption has occurred, which is especially valuable in terms of aviation safety.

7. Application of satellite SO_2 measurements in volcanic early warning services

Satellite based measurements of volcanic SO_2 are a valuable tool for early warning of volcanic hazards. In this chapter, the use of GOME-2 SO_2 measurements in the framework of two important applications related to early warning of volcanic hazard is discussed. The first application focuses on the threat volcanic eruption clouds pose to aviation. Satellite based observations provide valuable information for detecting and tracking eruption plumes and therefore minimize the risk of aircraft encounter with hazardous volcanic cloud (Carn et al., 2008, Prata, 2008). Although ash is the main hazard to aviation, SO_2 has proven to be an excellent tracer for volcanic eruption clouds, especially if ash detection techniques fail. SO_2 is always released during volcanic eruptions and is a robust marker for the onset of volcanic activity. Therefore satellite SO_2 observations are frequently being used in addition to ash measurements for aviation hazard mitigation.
In Section 7.1, the use of satellite SO_2 data in the Support to Aviation Control Service (SACS) is described which is part of the GMES Service Element for the Atmosphere (PROMOTE) (Van Geffen et al., 2007). The service has been developed to provide volcanic plume information to the Volcanic Ash Advisory Centers (VAACs), which are the official organizations to issue alerts to airlines and air traffic control organizations of the potential danger of volcanic eruption plumes. In the case of exceptional SO_2 concentrations, SACS sends notifications to the VAACs. Two examples, the Kasatochi eruption (Alaska, August 2008) and the Eyjafjallajökull eruption (Iceland, April – May 2009), that caused widespread disturbance to aviation operations, are discussed.
In the second part (Section 7.2), the focus is on the danger volcanoes pose to their immediate surroundings and the local population. In this context, the use of satellite SO_2 measurements of degassing volcanoes in early warning of volcanic activity is discussed. The application of GOME-2 passive degassing measurements within the Exupéry service is described, which is concerned with early warning of volcanic unrest (Hort and Zaksek, 2008). The main focus of Exupéry is on the development of a mobile volcanic fast response system (VFRS) that can be deployed on any volcano worldwide and will assist countries in case of a volcanic crisis.
For early warning services the near-real time (NRT) data processing and distribution is a crucial requirement. The operational GOME-2 SO_2 data is available within 2 hours after measurement (Chapter 3.2).

7.1 Aviation Hazard Mitigation

Volcanic eruptions can inject large quantities of volcanic ash and gases into the atmosphere. Depending on the strength of the eruption the height of the emissions can vary between the summit height of the volcano up to 20 km or higher (e.g. Pinatubo, Philippines, 1991). The ash emitted by volcanic eruptions is known to be the primary hazard to aviation in volcanic clouds. The ash can cause severe damages to aircraft from disrupting avionics and navigation systems, limiting the view of the pilots and severely scratching forward facing surfaces of aircraft to stalling engines as a result of ash melting in the aircraft's engines (Miller and Casadevall, 2000). Most dangerous are explosive magmatic eruptions where the thermal energy

allows the eruption plume to reach the cruising altitudes of jet aircraft. Effusive eruptions are less energetic but the eruption plumes can sometimes reach altitudes of 9 – 11 km where they become hazardous for aviation, e.g. eruption of Jebel al Tair, September, 2007 (Eckhardt et al., 2008) and Mount Etna, May, 2008. Atmospheric winds can transport the ash and gases rapidly over long distances; especially within the jet stream. Volcanic clouds occupying the jet stream are particularly hazardous as aircrafts use the same phenomenon to reduce their travel times and fuel consumption. Besides ash, volcanic eruption clouds contain large amounts of gases as these are the driving forces during explosive eruptions. Typically the dominant gases are water vapor, carbon dioxide and sulfur dioxide. Of these gases SO_2 is itself a hazard to aircraft as it reacts with water to form sulfuric acid (H_2SO_4), which is highly corrosive and may therefore damage the paint and windows of aircraft and can create sulfate deposits in the engines. The latter can block the cooling holes and lead to engine overheating (Bernard and Rose, 1990, Casadevall et al., 1996).

With approximately 60 eruptions per year and increasing volumes of jet aircraft traffic, more than 90 aircraft are known to have suffered severe damage after the encounter with volcanic ash clouds. In some cases, this resulted in the temporary loss of one or more engines during the flight. Since the threshold ash concentration that poses a threat to aircraft is currently unknown (Guffanti et al., 2005), the safest procedure for aircraft is to stay clear of volcanic clouds. Many airlines operate a “zero tolerance policy” regarding volcanic ash (Cantor, 1998). Onboard detection of volcanic ash clouds is not possible with aircraft radar since it cannot detect micron size particles. The use of onboard infrared sensors to detect volcanic ash is currently under investigation.

After the complete closure of the European airspace for several days due to the Eyjafjallajökull eruption in April 2010, new guidelines concerning volcanic ash have been introduced by the UK Civil Aviation Authority (CAA). Instead of completely avoiding volcanic ash, two threshold values based on the predicted ash concentrations have been established, a “No Fly Zone” (NFZ) including areas where the predicted ash concentrations are higher than 2×10^{-3} gm^{-3} and an “Enhanced Procedures Zone” (EPZ) with predicted ash concentrations of 2×10^{-4} gm^{-3} to 2×10^{-3} gm^{-3}. The EPZ is also referred to as “Time Limited Zone”, in this zone aircraft operations are allowed for a limited time and additional inspection of flight engines is recommended. The new tolerance levels are based on discussions with aircraft and engine manufacturers and airlines. The no-fly threshold level is well below the ash levels for two events with multiple engine flame-outs, which have been approximated to 2 gm^{-3}. The ash concentration that is currently considered tolerable is therefore three orders of magnitude lower. The new guidelines are currently only applied in European airspace, internationally the “zero tolerance” rules are still applied. The definition of global ash concentration thresholds together with options for improved detection of volcanic ash are planned to be completed in May 2011 (ICAO, 2010).

Of the main components of volcanic clouds, SO_2 is the most robust indicator for volcanic activity. Direct measurements of volcanic aerosol using IR sensors or the aerosol absorption index are also being used to track hazardous eruption clouds. However, these techniques can fail if for example the ash particles at higher altitudes are encased in ice or if the volcanic cloud is very dilute. Further it can be difficult to distinguish between volcanic aerosols and other types of aerosol, hence SO_2 is used as a marker for eruptive activity. GOME-2’s sensitivity to low SO_2 amounts and its almost daily global coverage make it possible to detect most volcanic eruptions regardless of magnitude. As described in Chapter 3.2, DLR provides GOME-2 SO_2

products in near-real time (within 2 hours after sensing) and a web based navigation tool (http://wdc.dlr.de/sensors/gome2) allows searching for events in user selected regions, time period and SO_2 amounts. The capability of the instrument to track volcanic SO_2 over long distances has been demonstrated for several recent eruptions, e.g. Jebel al Tair in 2007, Okmok and Kasatochi in 2008, which is discussed further in Section 7.1.2. Although the SO_2 and ash may separate into distinct clouds as the ash drops to lower altitudes due to gravity effects (Constantine et al., 2005, Schneider et al., 1998) and may be transported into different directions under conditions of vertical wind shear, the presence of SO_2 is a good indicator for volcanic eruption plumes and the presence of ash.

7.1.1 Support to Aviation Control Service

The Support to Aviation Control Service (SACS) has been designed as a service based on satellite measurements to provide volcanic plume information to the Volcanic Ash Advisory Centres (VAACs) (Van Geffen et al., 2007). The aim of SACS is the near-real time delivery of SO_2 and ash data related to volcanic eruptions derived from satellite measurement, and the tracking of volcanic plumes. The data will assist the VAACs in advising airlines on rerouting aircraft and flight cancellations. The main users are the VAACs in London and Toulouse covering Europe and Africa, but in principle the geographical coverage of the service is world-wide.
SACS uses SO_2 data derived from SCIAMACHY, GOME-2, OMI and IASI which allows multiple measurements a day, and rapid detection of volcanic SO_2 clouds. The SO_2 data and images are stored in a database, and are accessible to the VAACs and other users via the internet. The SO_2 is plotted in global maps with close-up maps for a total of 62 pre-defined geographical regions covering all active volcanoes.
Criteria for “exceptional SO_2 concentrations” were set up using archived SO_2 data together with a list of known volcanic eruptions. In case “exceptional SO_2 concentrations” are detected by the satellite instruments, the near-real time system will provide a notification via e-mail to the VAACs. The notification contains basic information regarding the detected event, start time and location of the observation and the peak SO_2 value observed. In addition, the user has access to images of the affected geographical regions with SO_2 concentrations, cloud cover fraction and information on the location of volcanoes via an internet link (http://sacs.aeronomie.be).

7.1.2 Eruption of the Kasatochi volcano

The eruption of the Kasatochi volcano on 7 August 2008 is a good example on how satellite measurements can provide valuable information on an eruption posing a danger to aviation, as in the region of the Aleutian Island chain the density of volcanoes is very high but most of these volcanoes are not regularly monitored. Three major eruptions emitted large amounts of volcanic ash and gas into the atmosphere that rose to a height of at least 10 km, an altitude where they are a major hazard to aircraft. Low levels of ash concentration made it difficult to use ash absorption features to track the cloud using satellite instruments. Therefore satellite SO_2 measurements were used to trace the eruption cloud. Due to the high altitude of the eruption plume, the SO_2 was located above the clouds.

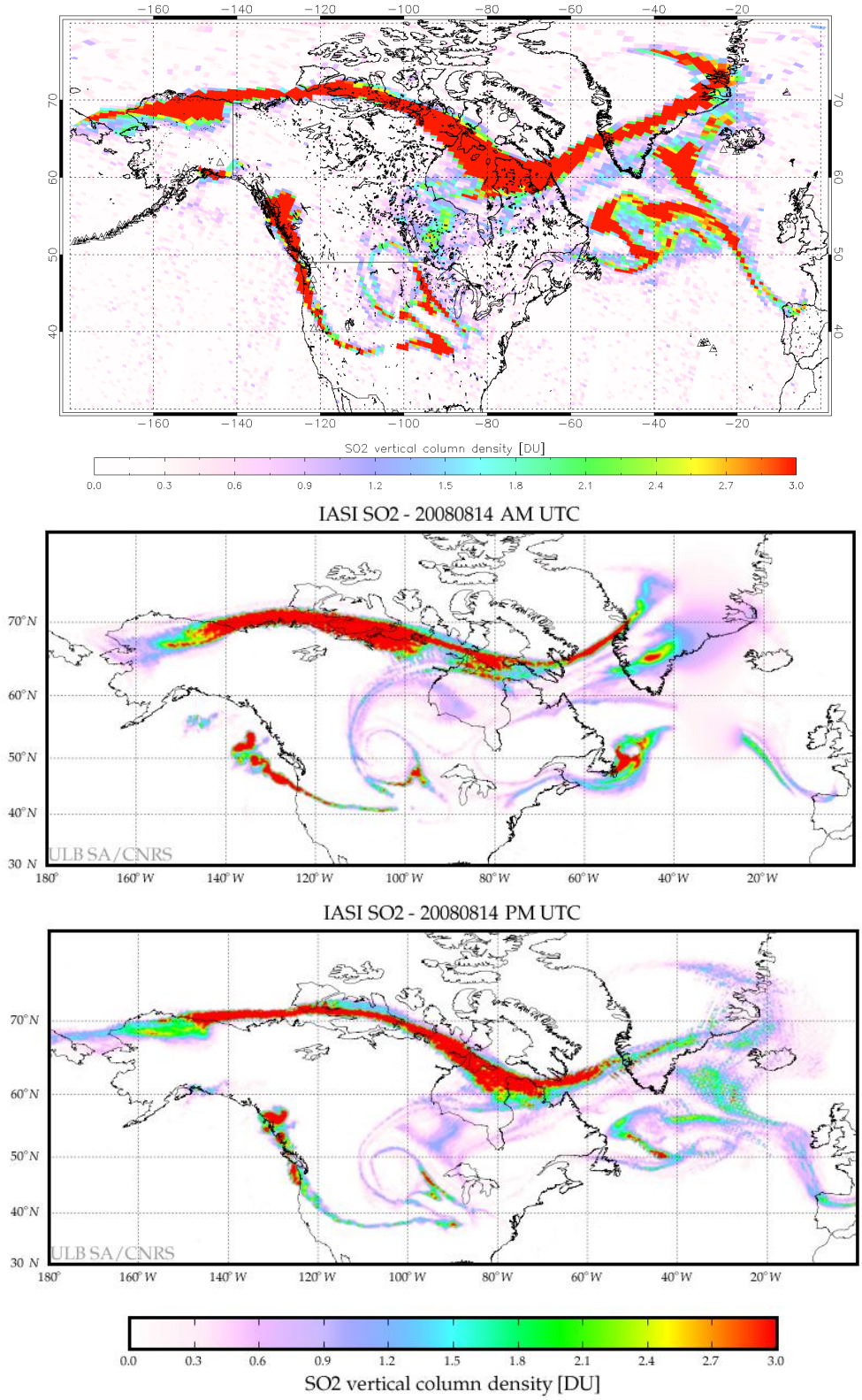

Figure 7.1: Volcanic SO_2 plume from the Kasatochi eruption (Aleutian Islands) as measured on 14 August 2008 by GOME-2 (top) and IASI, once in the morning (middle panel) and once in the evening (bottom panel). Kasatochi volcano erupted on 7 August 2008. The SO_2 cloud had been transported over North America and reached Europe one week after the eruption.

The SO_2 plume was first detected during the GOME-2 overpass on 8 August. GOME-2 measured maximum SO_2 column amounts of ~ 300 DU the first day after the eruption. An estimate from the GOME-2 data of the total erupted mass of SO_2 during

the Kasatochi eruption yields about 1.2 x 10^6 tons of SO_2.* The volcanic cloud was transported across North America intersecting some of the main air traffic routes in that region, as most intercontinental flights from the USA to Asia fly over Alaska. One week after the eruption the SO_2 cloud reached Spain on 14 August (Figure 7.1). For comparison the IASI SO_2 observations are shown as well (Rix et al., 2009). The SO_2 cloud could be tracked for several weeks as it was distributed all over the northern hemisphere, during this time it triggered multiple SACS alerts.
The eruption of the Kasatochi volcano caused 44 Alaska Airline flights to be cancelled between Anchorage and the US West Coast leaving about 6000 passengers stranded. Flights from other US airlines had to be cancelled or diverted as well. In addition several aircraft encounters with the volcanic cloud from the Kasatochi eruption were reported. Numerous pilots reported smelling sulfurous odors and a hazy, brown cloud at cruise altitudes as long as two weeks after the eruption. Flights had to be diverted around the cloud or their flight level had to be changed to fly above or below the volcanic cloud (Guffanti et al., 2008).

7.1.3 Eruption of the Eyjafjallajökull volcano

The eruption of Eyjafjallajökull volcano, southern Iceland, from 14 April to 23 May 2010 caused unprecedented and widespread disruption of European air traffic. The phreatomagmatic eruption produced high amounts of fine ash that were transported by the prevailing winds directly towards Europe.
Prior to this eruption only 3 minor eruptions occurred at Eyjafjallajökull during historical times, the last eruption taking place in 1821. Eyjafjallajökull volcano has shown signs of unrest for almost 20 years before the recent eruption including seismic swarms and crustal deformation. The eruption in spring 2010 was of similar magnitude as earlier events and started with a small flank eruption on 20 March which lasted until 12 April. On 14 April an eruption began from the summit of Eyjafjallajökull at 01:15 UTC. After the initial sub-glacial activity an eruption plume was seen around 6:00 UTC followed by large discharge of melt water. Eruptive activity picked up and a black ash rich volcanic plume was observed after 19:00 UTC. The following phreatomagmatic eruption ejected approximately several hundred tons of magma per second producing large quantities of very fine ash. This eruption phase lasted until 17 April and produced a 5 – 9 km high eruption column (Gudmundson et al., 2010). The prevailing winds carried the eruption plume to the south and southeast towards Europe, resulting in an uninterrupted closure of most of the northern European air space from 15 April to 21 April. The restrictions were only lifted through the introduction of new preliminary guidelines concerning the allowed concentration of volcanic ash (ICAO, 2010).
After April 17 the eruption changed from phreatomagmatic to magmatic, as external water was no longer involved. At the same time the eruptive intensity dropped by an order of a magnitude and the ash production was reduced. During this eruptive period which lasted until 4 May the magma discharge rate was between several tons per second and several tens of tons per second, the eruption column reached heights of 2 – 5 km. On 5 May the intensity of the eruption amplified again with increased ash production and eruption columns of 5 – 9 km height. This again led to a disruption of

* 1 DU corresponds to a total mass of approximately 91.2 tons of SO_2, for a GOME-2 pixel size of 40 km x 80 km as explained in Chapter 5.3.2

aviation in parts of Europe. The airspace was closed intermittently in parts of Europe, e.g. over Ireland and Scotland on 4 and 5 May, in Spain, northern Italy, Austria and southern Germany on 9 May and over Ireland and the UK on 16 and 17 May.

During the eruptive episode until 4 May only small amounts of sulfur dioxide were detected by GOME-2 and other satellite instruments, mainly close to the volcano (Figure 7.2). However during the eruptive activity following 4 May, large amounts of SO_2 were emitted into the atmosphere, and the volcanic gas plume could be traced by GOME-2 for several days. After the intensity of the eruption picked up again an SO_2 rich eruption plume was detected on 5 May that was distributed to the south-east and covered North-Ireland and parts of the UK (Figure 7.2). The following day the plume could be detected directly to the south of Iceland. On 7 and 8 May the GOME-2 observations show that part of the volcanic cloud was transported towards Spain. This led to the closure of the airspace over parts of southern and central Europe the following day. The observations agree very well with the modeled plume forecast of the London VAAC which the aviation warnings are based on (Figure 7.3) (UK MetOffice: www.metoffice.gov.uk/aviation/VAAC). The following days (9 – 12 May) the SO_2 plume can be observed south of Iceland over the Atlantic leaving Europe mainly unaffected, with only small parts of the plume touching Ireland on the 11 May and France on the 12 May. From 14 to 17 May GOME-2 SO_2 shows that, except for 15 May, the volcanic plume is again distributed towards northern Europe by the prevailing winds (Figure 7.2). During the airspace closure over Ireland and the UK on 16 and 17 May, GOME-2 observations show the volcanic SO_2 plume over the northern UK. SO_2 emissions from the Eyjafjallajökull eruption could be detected until the eruption ceased on 23 May.

Although the eruption of Eyjafjallajökull volcano can be considered fairly small (VEI = 2 – 3) it caused unprecedented problems not only in Europe. It left millions of travelers stranded and also effected the economy. The estimated economic loss due to the eruption is approximately 2.5 billion € in total (Gudmundson et al., 2010). Iceland has seen 8 eruptions of similar magnitude in the past 40 years (Hekla, 1971, 1980, 1991 and 2000, Gjalp 1996, Grimsvötn 1998 and 2004). In six of these cases the eruption plumes were dispersed towards the north and northeast leaving Europe unaffected. However, it is to be expected that a similar eruption will cause air traffic disruption again in large parts of Europe in the future.

The eruption of Eyjafjallajökull volcano has highlighted the importance for understanding and closely monitoring the world's active volcanoes. Although Icelandic volcanoes can be considered well monitored, NRT satellite data has proven to provide valuable information. Currently satellite data of volcanic ash and SO_2 are mainly used in validating model forecasts. In the future the planned assimilation of different satellite observations of volcanic ash and SO_2 into the dispersion models holds great potential to improve the volcanic plume forecasts and aviation warnings (Zehner, 2010).

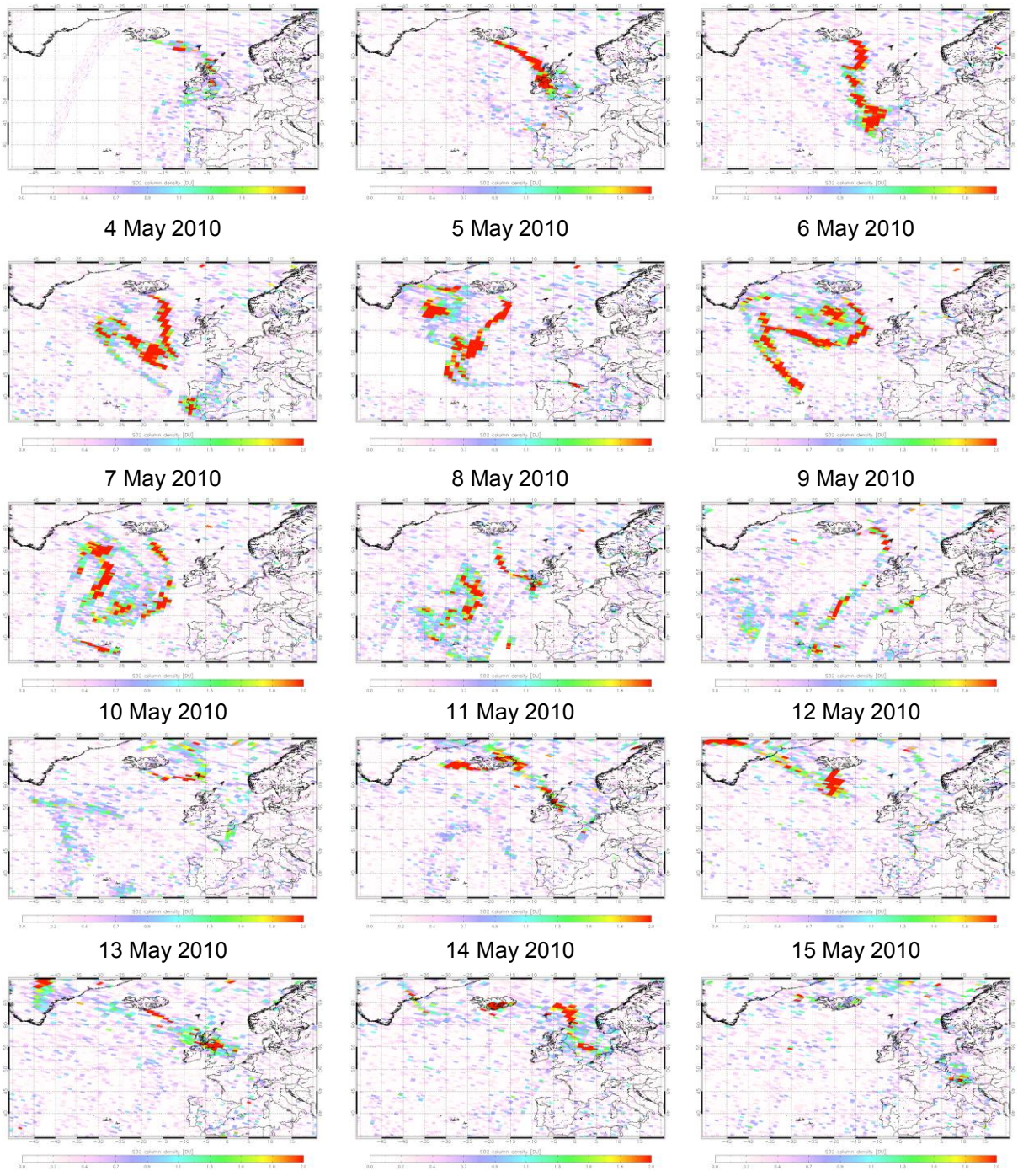

Figure 7.2: SO_2 emissions from Eyjafjallajökull eruption as seen by GOME-2 from 4 May to 18 May.

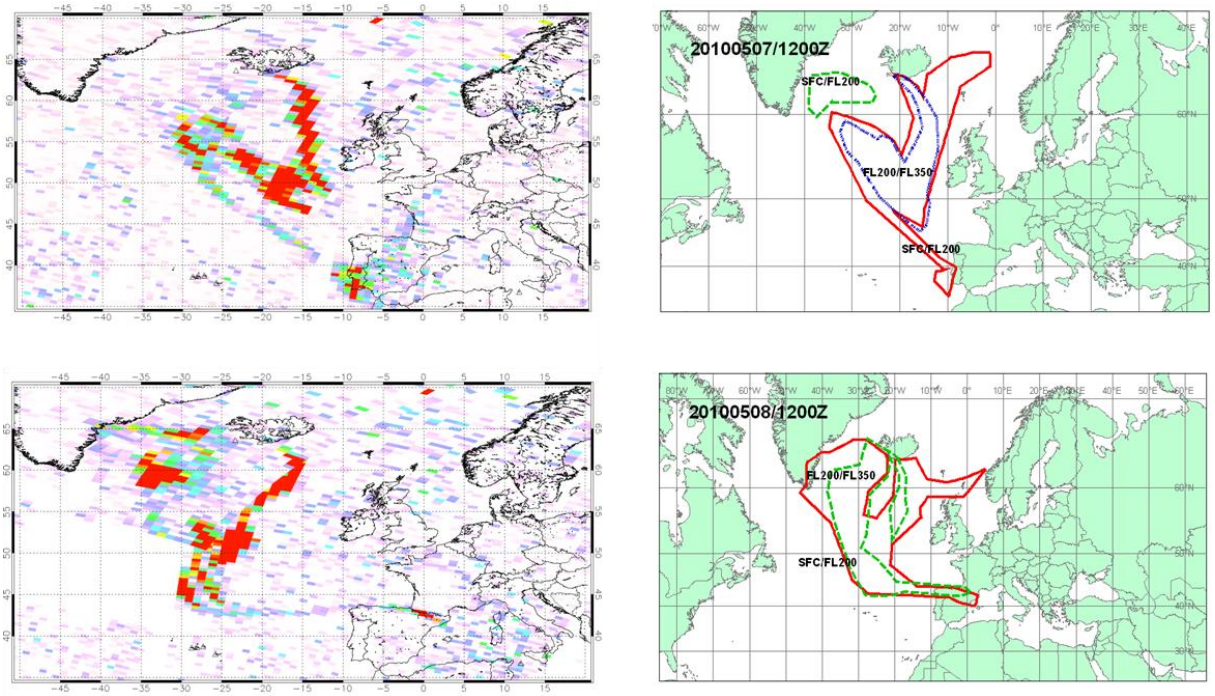

Figure 7.3: Volcanic SO_2 cloud from Eyjafjallajökull eruption as seen by GOME-2 on 7 May and 8 May (left). The GOME-2 observations agree well with the plume forecast of the UK MetOffice using the NAME dispersion model (right) (Jones et al., 2007).

7.2 Monitoring volcanic unrest

Most of the world's potentially active volcanoes are not monitored on a regular basis, of the ones known to have erupted in historic times less than twenty-five percent have basic monitoring and little more than 20 volcanoes have a well established monitoring network (Ewert and Miller, 1995). Furthermore many of the most explosive eruptions since 1800 have occurred at volcanoes that had not shown any activity for several thousand years (Simkin and Siebert, 1994). The danger associated with volcanoes is not restricted to eruptions, further volcanic hazards are earthquakes, dangerous gases (e.g. Lake Nyos, Cameroon) (Sigvaldason, 1989), flank movements and ground deformation, tsunamis (e.g. Stromboli, Italy) (Bonaccorso et al., 2003) landslides and climatic changes (e.g. eruption of Mount Pinatubo, Philippines, 1991) (McCormick et al., 1995). Monitoring and forecasting of volcanic activity in combination with early warning of volcanic risk is therefore of major importance.

7.2.1 Exupéry

The project Exupéry, as part of the German GEOTECHNOLOGIEN program, aims at developing a mobile volcano fast response system in order to support countries in case of a volcanic crisis if help is requested. The system is especially dedicated to supporting third world countries in dealing with volcanic risk. In the past response teams for volcanic crisis have proven to be very successful. The first rapid response system Volcano Disaster Assistance Program (VDAP) (Ewert and Miller, 1995) was successful in managing the crisis connected to the Pinatubo eruption (Philippines, 1991). Other successfully predicted eruptions include Mt. St. Helens, USA, in 1980 (Lipman and Mullineaux, 1981) and Merapi, Indonesia, in 2006.

The Exupéry system (www.exupery-vfrs.de) is designed for operating standalone or as a supplement to an existing monitoring network providing additional information on volcanic activity parameters that are not routinely observed (i.e. SO_2 measurements, thermal anomalies, deformation measurements). Using this additional information further insight into the volcanic processes is possible. Apart from traditional monitoring techniques like seismology, the system includes ground based observations of gas fluxes and surface deformation. One of the novelties of the system is the utilization of space-based observations, including monitoring of ground deformation, thermal anomalies and volcanic SO_2 emissions, the latter using GOME-2. The Exupéry system can be installed quickly due to intelligent cable free communication between the different stations and the data center, which is a major advantage. All acquired data are stored in a central data base together with data from an existing monitoring network. The data are then partially analyzed in near-real time and visualized via a GIS system. Activity parameters, such as automatically estimated alert levels, are derived from the data using various models and data evaluation is carried out including recommendations for crisis management. The whole system underwent a successful test phase on the Azores from April - August, 2009.
As Exupéry focuses on early warning of volcanic risk the ability of satellite instruments to detect volcanic degassing prior to an eruption is of great importance. Increasing activity at many volcanoes is indicated by increased gas fluxes at the surface. Rising high-temperature magma releases SO_2 and therefore increased SO_2 degassing can often be a precursor of a magmatic eruption. This connection between gas flux and eruption has been exploited in ground-based UV remote sensing measurements (Bruno et al., 2001). Detection of pre-eruptive passive degassing with satellite measurements is challenging as the emission plumes are typically of low altitude, because the emissions are non-eruptive and the concentrations of SO_2 will be relatively low. However, the newest satellite instruments, OMI and GOME-2, have proven their ability to detect passive degassing patterns for several volcanoes. For example it has been possible to relate daily measurement of passive SO_2 degassing at Ecuadorian volcanoes to eruptive activity at these volcanoes (Carn et al., 2008). In addition to the detection of the degassing patterns, one major task is to link the observed SO_2 patterns to the volcanic activity in combining them with measurements of other volcanic parameters. Within Exupéry, daily images of SO_2 are provided in near-real time for volcanic regions worldwide. The daily GOME-2 SO_2 data are being used to detect possible changes in volcanic degassing behavior prior to an eruption. Threshold levels for the SO_2 are determined to yield special SO_2 alerts in case of high SO_2 amounts, indicating exceptional SO_2 degassing levels. Furthermore additional information concerning location and maximum observed SO_2 value is supplied.

7.2.2 Monitoring volcanic degassing in Papua New Guinea/ Vanuatu

An example for the ability of the GOME-2 instrument to monitor changes in the degassing behavior of volcanoes is provided in Figure 7.4, where monthly averaged SO_2 maps for the geographical region of Papua New Guinea/ Vanuatu are shown. The three main degassing volcanoes in this area are clearly visible in the March 2008 image (Figure 7.4, top), from north to south they are Rabaul (1) (688 m), Bagana (2) (1750 m) and Ambrym (3) (1334 m). Given the low summit elevations of the considered volcanoes we assumed a plume height of 2.5 km for the analysis. Of these three volcanoes Rabaul shows the most frequent SO_2 emission and often the

highest SO_2 vertical column amounts, which are above 0.8 DU for most of the observed time period. However, the monthly averaged amounts of emitted SO_2 from this volcano are highly variable. From January to August 2008 Rabaul volcano emitted approximately 2.5 x 10^5 tons of sulfur dioxide. Rabaul can be considered the most active volcano in this region as the emission of the SO_2 gas is often accompanied by emission of ash plumes and explosions (Smithonian Institution, 2008). The other two volcanoes show a higher variability in the SO_2 emissions, with a total emitted amount of ~1.7 x 10^5 tons SO_2 for Bagana and ~ 1.9 x 10^5 tons for Ambrym. Ambrym volcano is one of the largest known point sources of SO_2. With SO_2 emissions normally being between 18 – 270 kg s^{-1} observed in ground-based measurements (Bani, 2009) and maximum emissions of up to 380 kg s^{-1} it is among the main volcanic contributors of SO_2 to the atmosphere, together with Nyiragongo (Democratic Republic of Congo) with mean emissions rates of 185 kg s^{-1} (Carn, 2004) and Popocatepetl (Mexico) with emission rates of 110 – 150 kg s^{-1} (Delgado-Granados et al, 2001). Mount Etna which is renowned as one of the major volcanic SO_2 sources emits < 30 kg s^{-1} (Burton et al, 2005) and can therefore be detected in GOME-2 SO_2 observations only irregularly. Estimating the daily emission rates from GOME-2 measurement, as explained in Chapter 5.3.2, suggest maximum emissions rates of 400 kg s^{-1} for Ambrym between 2007 and 2010.

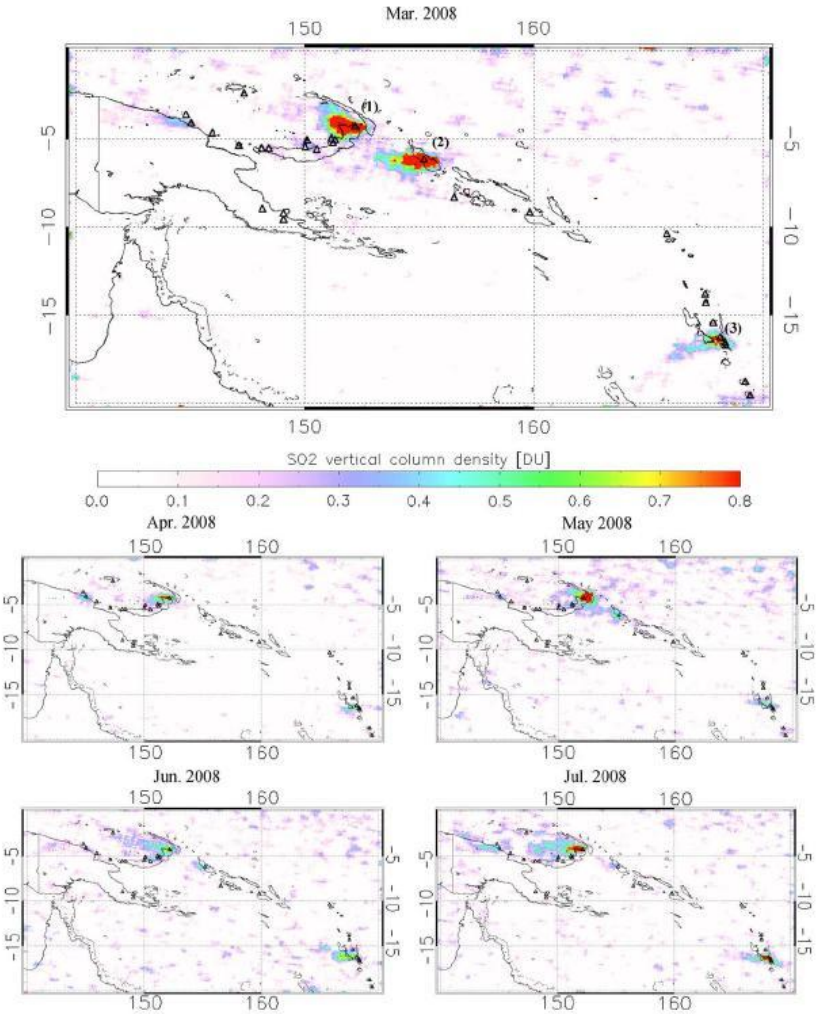

Figure 7.4: Monthly averaged SO_2 column amounts measured by GOME-2 from passively degassing volcanoes in the volcanic region Papua New Guinea/Vanuatu, March 2008–July 2008. The degassing volcanoes are Rabaul (1), Bagana (2), and Ambrym (3).

All three volcanoes are known to have erupted in historical times, with two recent major explosive eruptions at Rabaul in 1994 and 2006. These two eruptions led to evacuation of Rabaul town, damaged land and property and interfered with aviation. The 1994 eruption was also accompanied by lahars and pyroclastic flows and caused fatalities. Therefore it would be of great value to link the SO_2 emissions to the volcanic activity at these volcanoes, and use them as an additional precursor for the onset of future eruptions to reduce the threat to the local population.

7.2.3 Monitoring volcanic degassing at Nyiragongo, Democratic Republic of Congo

The 3469 m high Nyiragongo volcano (1.52°S, 29.25°E) is located in the Democratic Republic of the Congo on the western branch of the East African Rift System. It is one of Africa's most dangerous volcanoes as it is located only 18 km from the city of Goma (pop. 600,000) and its two historical eruptions have caused several fatalities. The crater contains one of the world's largest active lava lakes.
The first historical eruption of Nyiragongo occurred in 1977, when the crater walls fractured and the lava lake drained completely. Lava flows down the flanks reached speeds of up to 60 km h^{-1} destroying several villages and killing between 70 and 400 people (Durieux, 2003). During the second flank eruption in 2002 lava flows destroyed ~ 13% of Goma, including parts of the airport. The eruption killed 70-100 people and left 120,000 homeless. Since then several small eruptions have occurred that did not cause any damage (Smithonian Institution, 2002).

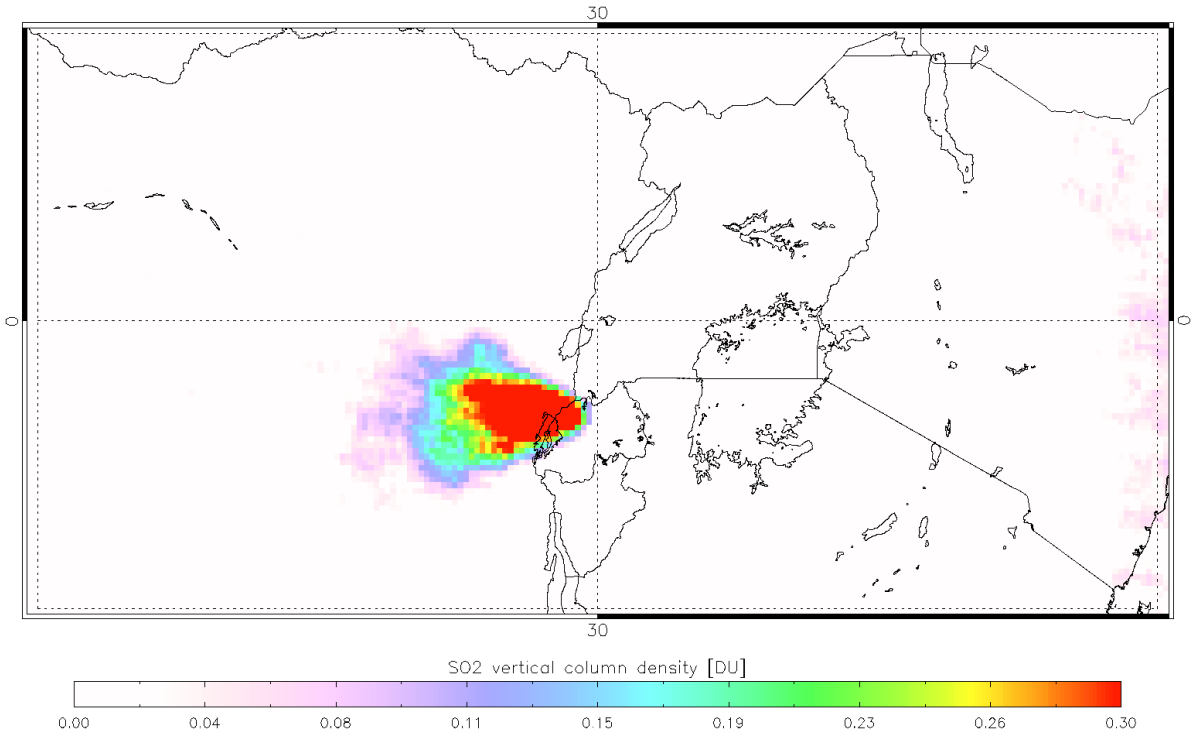

Figure 7.5: Average SO_2 emissions of Nyiragongo and Nyamuragira as detected by GOME-2 from 2007 – 2009.

Besides being a continuous threat to the population in the vicinity of the volcano, Nyiragongo is one of the main volcanic sources of SO_2 in the atmosphere. The volcano is continuously degassing fairly large amounts of SO_2 and can be detected as a major source of SO_2 on GOME-2 imagery (Figure 7.5). In the first place,

surveillance of the SO_2 emissions is important as the SO_2 itself poses a significant hazard to the surroundings by effecting human health and causing acidification of the soil (Baxter et al. 2004). Second the active lava lake still poses a major threat to the population of Goma. Satellite observations of this volcano are especially valuable as ground-based sensing has not been carried out regularly due to continuing political unrest in the region.

The estimated daily total SO_2 loadings from GOME-2 measurements in the volcanic region of Congo are displayed in Figure 7.6. Significant variations in the SO_2 emissions can be observed, which can provide some insight into the magma supply to the lava lake. Average SO_2 emissions from 2007 – 2009 were around 2300 tons per day. Before the minor eruption occurring at the beginning of September 2008 a distinct increase in SO_2 is observed followed by a sharp decrease before the eruptive event. For the second eruption occurring during the observation period in November 2007, a similar pattern can be observed, however the increase and decrease in measured total SO_2 amounts is not as pronounced. Increases in SO_2 usually indicate the supply of new magma into the system, that degasses during magma ascent due to the decreasing pressure, similar patterns have been observed in ground-based measurements, e.g. at Mount Pinatubo, where SO_2 emission measurements using COSPEC instruments provided an important contribution to forecasting the 1991 eruption (Daag et al., 1996). The patterns of increasing and decreasing emissions before the eruptions can be explained by the rise speed dependent model (RSD) for volcanic degassing (Parfitt and Wilson, 1995). If the magma speed is relatively low the gas bubbles are assumed to separate from the melt and rise through the magma, which is called open system degassing. If the speed of the magma is higher, e.g. before the onset of an eruption, the gas bubbles are thought to travel with the magma until it is erupted.
However, satellite SO_2 observations by itself are not a reliable tool to predict eruptive activity, as can be seen in the beginning of 2008 where a similar increase and decrease of SO_2 in observed that is not followed by an eruption. Also, in this particular case SO_2 emissions from Nyamuragira volcano which is located 13 km northwest of Nyiragongo could contribute to the estimated total SO_2 mass. Due to the large size of the GOME-2 pixels it is not possible to distinguish between these two emission sources. More information is needed to relate the observed degassing patterns to processes occurring inside the volcano and correctly predict the onset of volcanic eruptions, but the GOME-2 measurements show the potential to add valuable information for volcano observations and risk assessment.

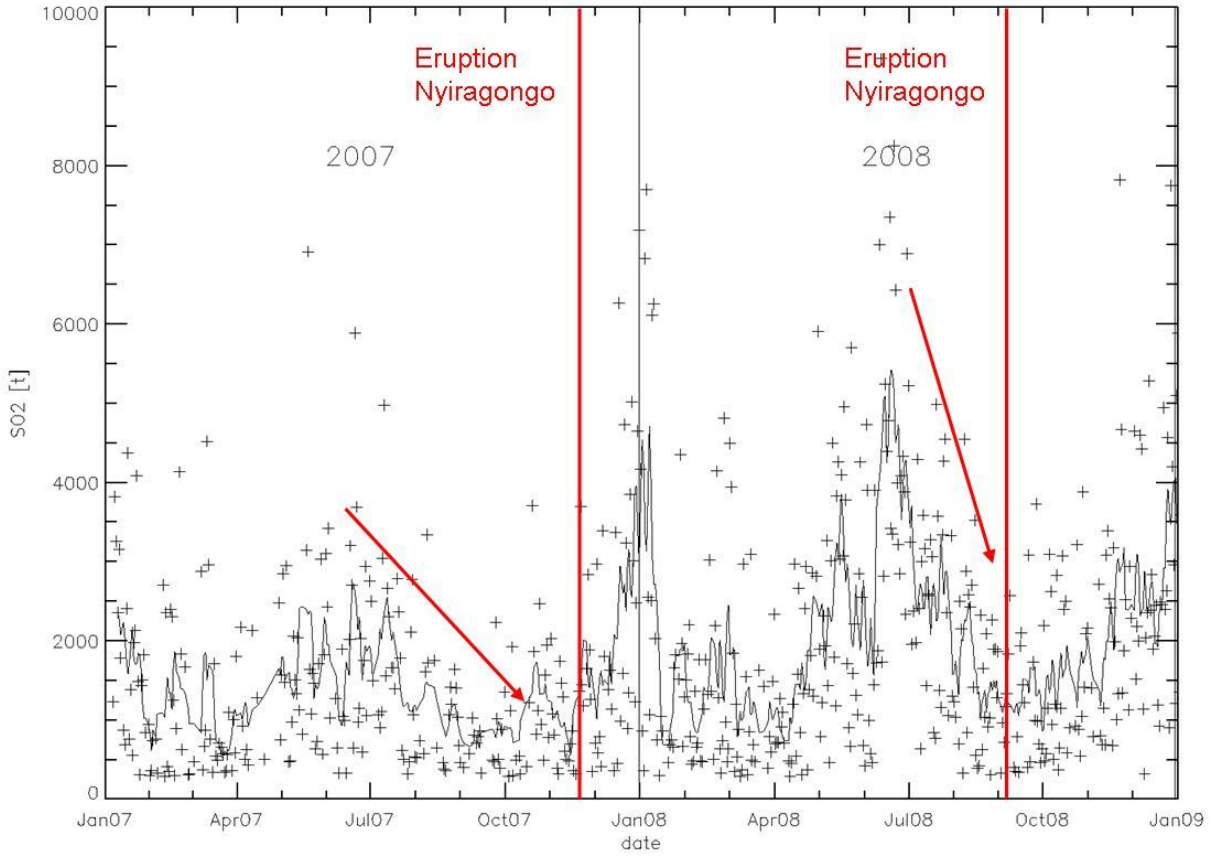

Figure 7.6: Total daily SO_2 from Nyragongo and Nyramuragira in tons as measured by GOME-2 for 2007 and 2008. The solid line denotes the 7-day moving average of the total SO_2 columns. Before the two eruptions of Nyragongo first a rise of total SO_2 followed by a distinct drop in SO_2 emissions is observed, as denoted by the red arrows.

7.3 Conclusions

The GOME-2 satellite measurements of volcanic SO_2 have proven to be a valuable tool for early warning of volcanic hazards. The NRT GOME-2 SO_2 columns are used within several services concerned with early warning of volcanic activity. One important application of the GOME-2 SO_2 data is aviation safety after volcanic eruptions. The use of the data in the Support to Aviation Control Service (SACS) has been described and the examples of the eruptions at Kasatochi and Eyjafjallajökull have shown that satellite detection of SO_2 allows tracking of the movements of volcanic eruption clouds. Further, GOME-2 SO_2 data is used within the mobile volcano fast response system Exupéry, which will assist, especially third world countries, in case of volcanic crisis. The ability of the GOME-2 instrument to detect passive degassing of volcanoes and changes in gas emissions provides valuable information for assessing the activity status of a volcano. Two examples of volcanic degassing in the volcanic regions of Papua New Guinea/ Vanuatu and Democratic Republic of Congo have been shown. At Nyiragongo volcano it was possible to relate the degassing patterns measured by GOME-2 to upcoming eruptions. These results show that satellite based SO_2 measurements can supply additional information for eruption forecasting.

8. Conclusions and perspectives

In this work the use of the GOME-2 satellite instrument for monitoring volcanic SO_2 emissions and the determination of the SO_2 plume height have been presented. The GOME-2 sensor on MetOp-A, launched in 2006, allows daily global observations of volcanic SO_2 emissions in near-real time, making the SO_2 product a valuable tool for early warning of volcanic hazards. The operational GOME-2 total column SO_2 product is provided by the German Aerospace Center (DLR) in the framework of EUMETSAT's Satellite Application Facility on Ozone and Atmospheric Chemistry Monitoring (O3M-SAF). For the operational GOME-2 SO_2 retrieval a DOAS method is used and the accuracy of the DOAS method, when retrieving volcanic SO_2, has been assessed. The results were compared with other retrieval methods, such as modified DOAS and direct fitting, providing detailed information on the strengths of the different retrieval techniques. The uncertainty in the plume height has been identified as a major error source in all retrieval techniques. Furthermore the plume height is important for aviation safety after volcanic eruptions. Therefore a method for retrieving the plume height in near-real time from GOME-2 observations has been developed.

In this thesis, first the adaptation of the SO_2 retrieval using the DOAS method to the GOME-2 measurements is addressed in Chapter 3. The settings for the slant column retrieval are discussed and the corrections, which are applied to the SO_2 slant columns to correct for equatorial offset, temperature dependence of the SO_2 cross-sections and ozone interference, are explained. The total SO_2 columns are then computed through the use of appropriate air mass factors, which are calculated with the radiative transfer model LIDORT. The air mass factor depends strongly on the SO_2 plume height, which is typically unknown at the time of measurement. Therefore the total columns are calculated for assumed plume heights of 2.5 km, 6 km and 15 km, representing typical volcanic eruption heights.

In Chapter 4 the potential of the standard DOAS method for retrieving volcanic SO_2 is assessed. The standard DOAS method assumes optically thin atmospheric conditions, which is not always fulfilled for the retrieval of SO_2, e.g. for large SO_2 amounts, which can result from explosive volcanic eruptions. Therefore the standard DOAS method has been applied to synthetic GOME-2 radiance spectra to evaluate the performance under different atmospheric conditions. Further the influence of the total ozone column and the Ring effect on the SO_2 retrieval has been examined. It has been shown that the standard DOAS method yields good results for total SO_2 columns < 20 DU. In this region the errors are dominated by ozone interference, but are typically < 1.5 DU. For high total SO_2 columns the use of standard DOAS leads to a significant underestimation of the total SO_2 column, with errors of up to 40 %. Here the wavelength dependence of the air mass factor was identified as the major error source.
For comparison a modified DOAS method and a direct fitting approach were applied to the synthetic GOME-2 spectra. The modified DOAS method fits a slant optical density instead of the slant column and therefore allows accounting for the wavelength dependence of the air mass factor. In the direct fitting approach a complete radiative transfer calculation is performed. It could be shown that the use of modified DOAS and direct fitting leads to a significant improvement in the retrieval of

high total SO_2 columns, with errors typically below 10 %. For low total columns the differences to the standard DOAS method where moderate, with errors < 1 DU.
All retrieval methods have been applied to GOME-2 measurements of the volcanic eruptions of Kilauea (July, 2008) and Kasatochi (August, 2008). The application of the different methods to the Kilauea eruption, with total columns < 20 DU, shows only small difference, as was expected from the simulations. For the Kasatochi eruption, with total columns > 100 DU, the differences between standard and modified DOAS (~ 15 %) were not as large as would be expected from the simulations (~ 40% - 60 %). Likely reasons are calibration errors in the GOME-2 irradiance data, uncertainties in the SO_2 cross-sections and high ash content of the volcanic plume, unknown SO_2 plume height and atmospheric temperature profile lead to additional uncertainties. Direct fitting retrieves much higher total SO_2 column (~ 100 %) values, compared to modified DOAS. The difference between the direct fitting and modified DOAS method, that can be only observed in the measurements, is probably related to volcanic ash, which is treated in a better way in direct fitting. Despite the limitations it was shown, that the standard DOAS method produces reliable results for low and moderate SO_2 columns and provides the major advantage of allowing near-real time processing of data, as the standard DOAS method is about one order of magnitude faster compared to direct fitting.

In Chapter 5 the GOME-2 SO_2 detection limit of has been estimated and a validation of the operational GOME-2 SO_2 data with ground-based observations is presented. The detection limit varies from ~ 0.4 DU for an SO_2 plume height of 15 km to ~ 1.2 DU for an SO_2 plume height of 2.5 km. The operational GOME-2 SO_2 data for the eruptions of Kilauea and Kasatochi have been compared with SO_2 observations from the SCIAMACHY satellite instrument on ENVISAT. The results show a good agreement between the two satellite instruments with differences typically below 25 %. Further the SO_2 data has been validated against ground-based measurements. Comparisons have been conducted with Brewer measurements in Europe and the U.S. of the overpass of the Kasatochi eruption cloud in August 2008. The comparison of daily observations of the Kasatochi eruption cloud, where the SO_2 was at stratospheric altitudes, yields good results. The correlation between the Brewer and GOME-2 daily SO_2 columns is between 0.65 and 0.85 for most of the stations. Further, comparisons with Max-DOAS observations of anthropogenic pollution in Beijing from June, 2008, to April, 2009, and FLYSPEC observations of volcanic SO_2 emissions at Kilauea from March to November, 2008, were carried out. The comparisons at Beijing and Kilauea for SO_2 in the lower troposphere show that comparing the daily values is difficult due to the high noise level and limited sensitivity of the satellite observations for lower atmospheric heights. The difference between the GOME-2 and the ground-based measurement is also a major reason for differences, as GOME-2 measures an average over the pixel area, while the ground based instruments perform a point measurement. At Kilauea the highly variable nature of volcanic SO_2 emissions contributes further to the differences, as the FLYSPEC observations are not continuous and GOME-2 provides only one observation per day. Monthly averaging reduces the noise and significantly improves the comparisons, with a correlation of 0.79 for the Beijing and 0.58 for the Hawaii observations.

As the determination of the SO_2 plume height is important for the correct retrieval of the SO_2 total column and plays an important role for aviation safety, in Chapter 6 a method to estimate the SO_2 plume height from GOME-2 measurements in near-real

time has been developed. The method estimates the plume height by matching GOME-2 measurement spectra with simulated GOME-2 spectra for various heights, that are stored in a look-up table. The application to synthetic GOME-2 spectra has shown that the method achieves accuracies better than 2 km. The near-real time plume height estimation has been applied to the GOME-2 observations of the eruptions of Kilauea, Kasatochi and Eyjafjallajökull. The method has proven to be able to distinguish between the low plume heights of the Kilauea eruption and the stratospheric plume heights of the Kasatochi eruption. Comparisons with plume height information from other sources, e.g. trajectory matching or reports from the observatory, show a good agreement, mainly within 2 km of the estimated plume heights.

In Chapter 7 it has been demonstrated that satellite measurements of volcanic SO_2 are a valuable tool for early warning of volcanic hazards. The near-real time GOME-2 SO_2 columns are used within several early warning services for volcanic activity. One important application of satellite SO_2 data is aviation safety after volcanic eruptions. The GOME-2 SO_2 data is used in the Support to Aviation Control Service (SACS), which has been developed to provide volcanic plume information to the Volcanic Ash Advisory Centers (VAACs). The eruptions of Kasatochi (August, 2008) and Eyjafjallajökull (April, 2010) are presented as examples of two volcanic eruptions that caused disruptions of air traffic. Further GOME-2 SO_2 data are used in the Exupéry system, that focuses on the development of a mobile volcanic fast response system (VFRS) that can be deployed on any volcano worldwide and will assist countries in case of a volcanic crisis. Examples of two volcanic regions, Papua New Guinea/ Vanuatu and Democratic Republic of Congo, were shown, where passive degassing of volcanoes and changes in gas emissions could be detected by GOME-2. At Nyiragongo volcano it was possible to relate the degassing patterns measured by GOME-2 in the period from 2007 – 2009 to upcoming eruptions.

Within this thesis the strengths and limitations of the standard DOAS method have been evaluated compared to modified DOAS and direct fitting and the errors were quantified. Further, a method has been developed, that allows NRT retrieval of SO_2 plume heights from GOME-2 measurements. However, open questions remain that need to be investigated further. It could not be clarified completely why the results when applying the standard and modified DOAS methods to the Kasatochi eruption differ significantly from what would be expected from the fits on synthetic spectra. The influence of volcanic ash, which is often present in volcanic plumes, on the different retrieval methods will be examined further. The aerosols can have a large effect on the air mass factor calculations for the DOAS retrievals. In this context the highly variable types of volcanic ash, concerning size and shape, should be taken into account. The same investigations are necessary for the plume height estimation. An improved calibration of the GOME-2 irradiance data and a correction for the instrument degradation would further improve the results.
It was shown that one of the major advantages of the standard DOAS method is the possibility of NRT processing. The fact that the DOAS method is about one order of magnitude faster compared to direct fitting is especially important in the view of upcoming satellite missions (Sentinel-5 precursor and Sentinel-4/ -5) that will provide a much better resolution in space and time and therefore ~ 50 times higher data rates than GOME-2. Therefore further improvements of the DOAS SO_2 retrieval are desired for high total SO_2 columns. A practical solution in the operational processing for the retrieval of high SO_2 total columns could be the use of a modified DOAS

method with a look-up table, which will improve measurements with total SO_2 column > 20 DU. Furthermore, the extension of the fitting window to lower wavelengths with stronger SO_2 absorption will result in a higher sensitivity for low SO_2 columns.
The extension to lower wavelength regions will also further improve the plume height retrieval, as the response to changes in the plume height is strong below 310 nm, especially for stratospheric heights. Even though the height retrieval already yields good results, further improvements seem possible by matching the measurement with the simulated spectra according to SO_2 slant column density instead of vertical column density, to avoid errors introduced by uncertainties in the AMF.

With the new GOME-2 instruments planned to be launched on MetOp-B and MetOp-C in 2012 and 2016, respectively, the time series of SO_2 observations will be continued at least until 2020. This is of major importance for early warning services as they rely on a continuous, long term data supply. Future satellite missions, like the upcoming Sentinel-4/-5 missions, offer new perspectives for monitoring volcanic SO_2 as they will provide a much higher temporal and spatial resolution. The Sentinel-5 precursor, which is planned to be launched in 2014, will include TROPOMI, a new UV-VIS-NIR-SWIR spectrometer, that will provide daily global coverage at a resolution of 7 km x 7 km. It will be followed by the Sentinel-5 mission on a MetOp Second Generation satellite in 2020. Additionally, Sentinel-4 on Meteosat Third Generation (MTG) will provide observations of Europe and North Africa every 60 minutes at a resolution of 8 km. It is expected to be launched in 2020. In combination with the new IR sensors onboard MTG and MetOp Second Generation, which provide the advantage of being able to detect SO_2 at nighttime, but are less sensitive to SO_2 in the lower troposphere than UV sensors, they will allow monitoring of volcanic emissions with an unprecedented resolution.
The high spatial and temporal resolution provides new opportunities for the use of satellite measurements of volcanic SO_2 for early warning purposes. Sentinel-5 and its precursor allow daily monitoring of volcanic emissions worldwide at a high spatial resolution, making it possible to detect small SO_2 amounts, e.g. from volcanic degassing, that are currently averaged out over the comparably large GOME-2 pixel. They will offer new possibilities in relating the observed SO_2 emissions to volcanological observations, e.g. seismicity measurements, and to eruptive cycles. Therefore they will be a valuable contribution for monitoring volcanic activity in remote locations and to detect changes in gas emissions, which is important information for early warning of eruptions. The high temporal resolution of Sentinel-4 allows monitoring the movements of volcanic plumes closely and will result in more accurate aviation warning. Further the high temporal and spatial resolution allows observations of degassing patterns of European and North African volcanoes. Changes in SO_2 emissions can be detected in near-real time, which will be valuable for early warning of volcanic activity and eruptions.

List of abbreviations

AIRS	Atmospheric Infrared Sounder
AMF	Air Mass Factor
AMFIC	Air Quality Monitoring and Forecast In China
BIRA	Belgian Institute for Space Aeronomy
CAA	Civil Aviation Authority
CALIOP	Cloud-Aerosols Lidar with Orthogonal Polarization
CCN	Cloud Condensation Nuclei
COSPEC	Correlation Spectrometer
DLR	German Aerospace Center (Deutsches Zentrum für Luft- und Raumfahrt)
DOAS	Differential Optical Absorption Spectroscopy
DU	Dobson Unit
ECMWF	European Centre for Medium-Range Weather Forecasts
ENVISAT	Environmental Satellite
EPS	EUMETSAT Polar System
EPZ	Enhanced Procedures Zone
ERS-2	Second European Remote-Sensing Satellite
EUMETSAT	European Organisation for the Exploitation of Meteorological Satellites
FTIR	Fourier Transform Infrared
FWHM	Full Width at Half Maximum
GDP	GOME Level-1-to-2 Data Processor
GODFIT	GOME Direct Fitting
GOME	Global Ozone Monitoring Experiment
IASI	Infrared Atmospheric Sounding Interferometer
IPA	Independent Pixel Approximation
IPCC	International Panel on Climate Change
IR	Infrared
ISF	Iterative Spectral Fitting
LER	Lambertian Equivalent Reflectivity
LIDAR	Light Detection and Ranging
LIDORT	Linearized Discrete Ordinate Radiative Transfer
LUT	Look-up Table
Max-DOAS	Multi-axis DOAS
MetOp	Meteorological Operational Satellite
MTG	Meteosat Third Generation
NFZ	No Fly Zone
NIR	Near Infrared
NRT	Near-real Time
O3M-SAF	Satellite Application Facility on Ozone and Atmospheric Chemistry Monitoring
OMI	Ozone Monitoring Instrument
PBL	Planetary Boundary Layer
PDU	Product Dissemination Units
PMD	Polarization Measurements Devices
RRS	Rotational Raman Scattering
RSD	Rise Speed Dependent model
RTE	Radiative Transfer Equation

SACS	Support to Aviation Control Service
SCIAMACHY	Scanning Imaging Spectrometer for Atmospheric Cartography
SCIA FM	SCIAMACHY Flight model
SWIR	Short Wave Infrared
SZA	Solar Zenith Angle
TES	Tropospheric Emission Spectrometer
TOA	Top of the Atmosphere
TOMS	Total Ozone Mapping Spectrometer
UPAS	Universal Processor for Atmospheric Spectrometers
UV	Ultraviolet
VAAC	Volcanic Ash Advisory Center
VDAP	Volcano Disaster Assistance Program
VEI	Volcanic Eruption Index
VFRS	Volcanic Fast Response System
VIS	Visible
WMO	World Meteorological Organization
WOUDC	World Ozone and Ultraviolet Radiation Data Centre

References

Aiuppa A., R. Moretti, C. Federico, G. Gaetano, S. Gurrieri, M. Liuzzo, P. Papale, H. Shinohara, M. Valenza (2007). Forecasting Etna eruptions by real-time observation of volcanic gas composition. Geology, Vol. 35, pp. 1115-1118.

Aliwell, S.R., M. Van Roozendael, P.V. Johnston, A. Richter, T. Wagner, D.W. Arlander, J.P. Burrows, D.J. Fish, R.L. Jones, K.K. Tornkvist, J.-C. Lambert, K. Pfeilsticker, and I. Pundt, (2002). Analysis for BrO in zenith-sky spectra; An intercomparison exercise for analysis improvement. J. Geophys. Res., Vol. 107, 4199, doi:10.1029/2001JD000329.

Andreae, M.O., C.D. Jones, P.M. Cox (2005). Strong present-day aerosol cooling implies a hot future. Nature, Vol. 435, pp. 1187-1190, doi:10.1038/nature03671

Andres, R.J. and A.D. Kasgnoc (1998). A time-averaged inventory of subaerial volcanic sulfur emissions. J. Geophys. Res., Vol. 103, pp. 25251–25261, doi:10.1029/98JD02091

Aumann, H.H., M.T. Chahine, C. Gautier, M.D. Goldberg, E. Kalnay, L.M. McMillin, H. Revercomb, P.W. Rosenkranz, W.L. Smith, D.H. Staelin, L.L. Strow, J. Susskind (2003). AIRS/AMSU/HSB on the Aqua mission: design, science objectives, data products, and processing systems. IEEE Trans. Geosci. Remote Sens., Vol. 41, No. 2, pp. 253- 264.

Badalamenti B., N. Bruno, T. Caltabiano, F. Di Gangi, S. Giammanco, G. Salerno (2004). Continuous soil CO_2 and discrete plume SO_2 measurements at Mt. Etna (Italy) during 1997-2000: a contribution to volcano monitoring. Bull. Volcanol., Vol. 66, pp. 80-89.

Bais, A.F., C.S. Zerefos, C. Meleti, , I.C. Ziomas, and K. Tourpali (1993). Spectral Measurements of Solar UVB Radiation and its Relations to Total Ozone, SO_2, and Clouds. J. Geophys. Res., Vol. 98(D3), pp. 5199–5204.

Bani P., C. Oppenheimer, V.I. Tsanev, S.A. Carn, S.J. Cronin, R. Crimp, J.A. Calkins, D. Charley, M. Lardy, T.R. Roberts (2009). Surge in sulphur and halogen degassing from Ambrym volcano, Vanuatu. Bul.l Volcanol., Vol. 71, pp. 1159 – 1168.

Baxter P., P. Allard, M. Halbwachs, J.-C. Komorowski, A. Woods, A. Ancia (2004). Human health and vulnerability in the Nyiragongo volcano eruption and humanitarian crisis at Goma, Democratic Republic of Congo. Acta Vulcanol., Vol. 14, pp. 109–114.

Berresheim H., P.H. Wine, D.D. Davis (1995). Sulfur in the Atmosphere. In: Singh HB (ed) Composition, Chemistry and Climate of the Atmosphere. Van Nostrand, Reinhold, New York, pp. 251-307.

Bernard A. and W.I. Rose (1990). The injection of sulfuric acid aerosols in the stratosphere by the El Chichon volcano and its related hazards to the international air traffic. Nat. Hazards, Vol. 3, pp. 59–67

Blitz M.A., K.J. Hughes, M.J. Pilling (2003). Determination of the High-Pressure Rate Coefficient and the Enthalpy of Reaction for OH + SO_2. Phys. Chem. A., Vol. 107, pp. 1971-1978.

Bluth G.J.S., S.D. Doiron, C.C. Schnetzler, A.J. Krueger, L.S. Walter (1992). Global tracking of the SO_2 clouds from the June 1991 Mount Pinatubo eruptions. Geophys. Res. Lett., Vol. 19, pp. 151-154.

Bobrowski, N., G. Hönninger, B. Galle, and U. Platt (2003). Detection of bromine monoxide in a volcanic plume. Nature, Vol. 432, pp. 273–276.

Bobrowski N. (2005). Volcanic Gas Studies by MAX-DOAS. PhD Thesis, University of Heidelberg.

Bobrowski, N., U. Platt (2007). SO_2/BrO ratios studied in five volcanic plumes. J. Volcanol. Geoth.

Res., Vol. 166, pp. 147–160.

Bogumil, K., J. Orphal, T. Homann, S. Voigt, P. Spietz, O. Fleischmann, A. Vogel, M. Hartmann, H. Bovensmann, J. Frerick, and J. Burrows (2003). Measurements of molecular absorption spectra with the SCIAMACHY Pre-Flight Model: instrument characterization and reference data for atmospheric remote-sensing in the 230-2380 nm region. Journal of Photochemistry and Photobiology A, Vol. 157, pp. 167-184.

Bonaccorso A., S. Calvari, G. Garfi, L. Lodato, and D. Patane (2003). Dynamics of the December 2002 flank failure and tsunami at Stromboli Volcano inferred by volcanological and geophysical observations. Geophys. Res. Lett., Vol. 30, doi: 10.1029/2003GL017702.

Bovensmann, H., J. P. Burrows, M. Buchwitz, J. Frerick, S. Noël, V. V. Rozanov, K. V. Chance, A. P. H. Goede (1999). SCIAMACHY – Mission objectives and measurement modes. J. Atmos. Sci., Vol. 56, pp. 127 – 150.

Bracher, A., L.N. Lamsal, M. Weber, K. Bramstedt, M. Coldewey-Egbers, J.P. Burrows (2005). Global satellite validation of SCIAMACHY O_3 columns with GOME WFDOAS. Atmos. Chem. Phys., Vol. 5, pp. 2357–2368, 2005.

Brasseur G. and C. Granier (1992). Aerosols, Chlorofluorocarbons, and Ozone Depletion. Science, Vol. 257, No. 5074, pp. 1239-1242, doi: 10.1126/science.257.5074.1239

Brasseur G.P., J.J. Orlando, G.S. Tyndall (1999). Atmospheric Chemistry and Global Change. Oxford University Press, New York

Brimblecombe, P. and M. Heymann (1998). TRAP-45—analysis of tropospheric air pollution problems and air pollution abatement strategies in Europe since 1945, A Subproject in EUROTRAC-2, International Scientific Secretariat, GSF-Forschungszentrum für Umwelt and Gesundheit GmbH, Munich

Bruno, N., T. Caltabiano, S. Giammanco, and R. Romano (2001). Degassing of SO_2 and CO_2 at Mount Etna (Sicily) as an indicator of pre-eruptive ascent and shallow emplacement of Magma. J. Volcanol. Geoth. Res., Vol. 110, 137–153.

Burrows, J.P., M. Weber, M. Buchwitz, V. Rozanov, A. Ladstätter-Weisenmayer, A. Richter, R. de Beek, R. Hoogen, K. Bramstedt, K.-U. Eichmann, M. Eisinger, D. Perner (1999) The Global Ozone Monitoring Experiment (GOME): Mission concepts and first scientific results. J. Atmos. Sci., Vol. 56, pp. 151 – 157.

Burton, M.R., M. Neri, D. Andronico, S. Branca, T. Caltabiano, S. Calvari, R.A. Corsaro, P. Del Carlo, G. Lanzafame, L. Lodata, L. Maraglia, G. Salerno, L. Spampinato (2005). Etna 2004 – 2005: An archetype for geodynamically-controlled effusive eruptions. Geophys. Res. Lett., Vol. 32, L09303, doi:10.1029/2005GL022527.

Callies, J., E. Corpaccioli, M. Eisinger, A. Hahne, A. Lefebvre (2000). GOME-2 – MetOp's Second Generation Sensor for Operational Ozone Monitoring. ESA Bulletin, No. 102.

Cantor, R. (1998). Complete avoidance of volcanic ash is only procedure that guarantees flight safety. ICAO Mag., Vol. 53, pp. 18–19.

Carn, S.A. (2003). Eruptive and passive degassing of sulphur dioxide at Nyiragongo Volcano (D. R. Congo): the 17th January 2002 eruption and its aftermath" Acta Vulcanol., Vol. 14(15), pp. 75-86

Carn, S. A., L. L. Strow, S. de Souza-Machado, Y. Edmonds, and S. Hannon (2005). Quantifying tropospheric volcanic emissions with AIRS: The 2002 eruption of Mt. Etna (Italy), Geophys. Res. Lett., Vol. 32, 02301.

Carn, S. A., A. J. Krueger, S. Arellano, N. A. Krotkov, and K. Yang (2008). Daily monitoring of Ecuadorian volcanic degassing from space. J. Volcanol. Geoth. Res., Vol: 176(1), pp. 141-150, doi: 10.1016/j.jvolgeores.2008.01.029.

Carn, S. A., A. J. Krueger, N. A. Krotkov, K. Yang, and K. Evans (2009). Tracking volcanic sulfur dioxide clouds for aviation hazard mitigation. Nat. Hazards, Vol. 51(2), pp. 325-343, doi:10.1007/s11096-008-9228-4.

Casadevall, T. J., P. J. Delos Reyes, and D. J. Schneider (1996). The 1991 Pinatubo eruptions and their effects on aircraft operations. In: Fire and Mud: Eruptions and Lahars of Mount Pinatubo, Phillipines, C. G. Newhall and R. S. Punongbayan, Eds. Seattle, WA: Univ. Washington Press, pp. 1071–1088.

Chance, K.V. and R.J.D. Spurr (1997). Ring effect studies: Rayleigh scattering, including molecular parameters for rotational Raman scattering, and the Fraunhofer spectrum. Applied Optics LP, Vol. 36, Issue 21, pp. 5224-5230, doi: 10.1364/AO.36.005224.

Chandrasekhar S. (1989). Selected papers, vol. 2. New York: University of Chicago Press.

Clarisse, L., P. F. Coheur, A. J. Prata, D. Hurtmans, A. Razavi, T. Phulpin, J. Hadji-Lazaro, C. Clerbaux (2008). Tracking and quantifying volcanic SO_2 with IASI, the September 2007 eruption at Jebel at Tair. Atmos. Chem. Phys., Vol. 8, pp. 7723 – 7743.

Clémer, K., M. Van Roozendael, C. Fayt, F. Hendrick, C. Hermans, G. Pinardi, R. Spurr, P. Wang, M. De Marière (2010). Multiple wavelength retrieval of tropospheric aerosol optical properties from MAXDOAS measurements in Beijing. Atmos. Meas. Tech., Vol. 3, pp. 863–878.

Clerbaux, C., P.-F. Coheur, L. Clarisse, J. Hadji-Lazaro, D. Hurtmans, S. Turquety, K. Bowman, H. Worden, S. A. Carn (2008). Measurements of SO_2 profiles in volcanic plumes from the NASA Tropospheric Emission Spectrometer (TES). Geophys. Res. Lett., Vol. 35, L22807, doi:10.1029/2008GL035566.

Clerbaux, C., A. Boynard, L. Clarisse, M. George, J. Hadji-Lazaro, H. Herbin, D. Hurtmans, M. Pommier, A. Razavi, S. Turquety, C. Wespes, P.-F. Coheur (2009). Monitoring of atmospheric composition using the thermal infrared IASI/MetOp sounder. Atmos. Chem. Phys. Discuss., Vol. 9, pp. 8307-8339.

Coldewey-Egbers, M., M. Weber, L.N. Lamsal, R. de Beek, M. Buchwitz, and J.P. Burrows (2005). Total ozone retrieval from GOME UV spectral data using the weighting function DOAS approach, Atmos. Chem. Phys., Vol. 5, pp. 1015–1025.

Constantine, E.K., G.J.S. Bluth, W.I. Rose (2000). TOMS and AVHRR observations of drifting volcanic clouds from the August 1991 eruption of Cerro Hudson. In Remote Sensing of Active Volcanism, Geophysical Monograph 116, P.J. Mouginis-Mark, J.A. Crisp, and J.H. Fink, Eds. Washington, DC: American Geophysical Union, pp. 45–64.

Daag, A.S., B.S. Tubianosa, C.G. Newhall, N.M. Tuñgol, D. Javier, M.T. Dolan, P.J. Delos Reyes, R.A. Arboleda, M.L. Martinez, T.M. Regalado (1996). Monitoring sulfur dioxide emission at Mount Pinatubo. In: Newhall, C.G., Punongbayan, R.S. (Eds.), Fire and Mud: Eruptions and Lahars of Mount Pinatubo, Philippines. Philippine Institute of Volcanology and Seismology, Quezon City. University of Washington Press, Seattle, WA, pp. 409–434.

Davies, J. (1970). Correlation Spectroscopy. Analytical Chemistry, Vol. 42, pp. 101–112.

Delbouille, L. (1993). Role of very-high-resolution FTS in recent determinations of the quantitative composition of the stratosphere. In 9th International Conference on Fourier Transform Spectroscopy, H.-L. Dai and S. J. Sibener, eds., Proc. SPIE 2089, pp. 32–37.

Delgado Granados, H., L. Cárdenas González, N. Piedad Sánchez (2001). Sulfur dioxide emissions from Popocatépetl volcano (Mexico): case study of a high-emission rate, passively degassing erupting volcano. J. Volcanol. Geoth. Res., Vol. 108, pp. 107-120.

Delmelle, P., J. Stix, P. Baxter, J. Garcia-Alavarez, J. Barquero (2002). Atmospheric dispersion, environmental effects and potential health hazard associated with the low altitude gas plume of Masaya volcano, Nicaragua. Bull. Volcanol., Vol. 64, pp. 423-434.

Dobson G.M.B. (1968). Forty years' research on atmospheric ozone at Oxford: A history. Appl. Optics, Vol. 7, p. 405.

Durieux, J. (2003). Nyiragongo: The January 10th, 1977, eruption. Acta Vulcanol., Vol. 15(1-2), pp. 145-147.

Eckhardt, S., A. J. Prata, P. Seibert, K. Stebel, A. Stohl (2008). Estimation of the vertical profile of sulfur dioxide injection into the atmosphere by a volcanic eruption using satellite column measurements and inverse trajectory modeling. Atmos. Chem. Phys. Discuss., Vol. 8, pp. 2761–3805.

Edmonds, M., C. Oppenheimer, D.M. Pyle, R.A. Herd (2003). SO_2 emissions from Soufrière Hills volcano and their relationship to conduit permeability, hydrothermal interaction and degassing regime. J. Volcanol. Geoth. Res., Vol. 124, pp. 22-43

Eisinger, M. and J.P. Burrows (1998). Tropospheric sulfur dioxide observed by the ERS-2 GOME instrument. Goephys. Res. Lett., Vol. 25, pp. 4177-4180.

Elias, T., A. J. Sutton, C. Oppenheimer, K. A. Horton, H. Garbeil, V. Tsanev, A. J. S. McGonigle, G. Williams-Jones (2006). Comparison of COSPEC and two miniature ultraviolet spectrometer systems for SO_2 measurements using scattered sunlight. Bull. Volcanol., Vol. 68, pp. 313–322, doi: 10.1007/s00445-005-0026-5.

EUMETSAT (2009). GOME-2 FM3 Long-Term In-Orbit Degradation – Status After 1st Throughput Test. Doc. No. EUM/OPS-EPS/TEN/08/0588, 7 December 2009.

EUMETSAT (2011). GOME-2 Product Guide. Doc. No..: EUM/OPS-EPS/MAN/07/0445, Issue: v3, 17 March 2011.

Ewert, J. W. and C. D. Miller (1995). The USGS/OFDA Volcano Disaster Assistance Program 1995. Available at: http://vulcan.wr.usgs.gov/Vdap/Publications/OFR95-553/OFR95-553.html

Fioletov, V. E., J. B. Kerr, and D. I. Wardle (1997). The relationship between total ozone and spectral UV irradiance from Brewer spectrophotometer observations and its use for derivation of total ozone from UV measurements. Geophys. Res. Lett., Vol. 24, No. 23, pp. 2997-3000, doi:10.1029/97GL53153.

Fioletov, V. E., E. Griffioen, J. B. Kerr, D.I. Wardle (1998). Influence of volcanic sulphur dioxide on spectral UV irradiance as measured by Brewer Spectrophotometers. Geophys. Res. Lett., Vol. 25, No.10, pp. 1665-1668.

Fischer, T.P., K. Roggensack, P.R. Kyle (2002). Open and almost shut case for explosive eruptions: Vent processes determined by SO_2 emission rates at Karymsky volcano, Kamchatka. Geology, Vol. 30, pp. 1059-1062.

Fish, D. and R. Jones (1995). Rotational Raman scattering and the Ring effect in zenith-sky spectra. Geophys. Res. Lett., Vol. 22, pp. 811-814.

Galle, B., M. Johansson, C. Rivera, Y. Zhang, M. Kihlman, C. Kern, T. Lehmann, U. Platt, S. Arellano, S. Hidalgo (2010). NOVAC - A global network for volcano gas monitoring: network layout and instrument description. J. Geophys. Res., Vol. 115, doi:10.1029/2009JD011823.

Galle, B., C. Oppenheimer, A. Geyer, A.J.S. McGonigle, M. Edmonds, L. Horrocks (2003). A miniaturized ultraviolet spectrometer for remote sensing of SO_2 fluxes: A new tool for volcano surveillance. J. Volcanol. Geoth. Res., Vol. 119, pp. 241-254.

Gao, C., L. Oman, A. Robock, G.L. Stenchikov (2007). Atmospheric volcanic loading derived from bipolar ice cores: Accounting for the spatial distribution of volcanic deposition. J. Geophys. Res., Vol. 112, D09109, doi:10.1029/2006JD007461.

Gasso, S. (2008). Satellite observations of the impact of weak volcanic activity on marine clouds. J. Geophys. Res., Vol: 113, D14S19

Gielen D. and C. Changhong (2001) The CO_2 emission reduction benefits of Chinese energy policies and environmental policies:: A case study for Shanghai, period 1995–2020, Ecological Economics, Vol. 39, No. 2, pp. 257-270

Graf, H.-F., I. Kirchner, A. Robock, I. Schult (1993). Pinatubo eruption winter climate effects: Model versus observations. Clim. Dyn., Vol. 9, pp. 81–93.

Graf, H.-F., J. Feichter, B. Langmann (1997). Volcanic sulfur emissions: estimates of source strength and its contribution to the global sulfate distribution. J. Geophys. Res., Vol. 102, pp. 10,727-10,738.

Grainger, J., and J. Ring (1962). Anomalous Fraunhofer Line Profiles. Nature, Vol. 193, p. 762.

Gudmundsson, M.T., R. Pedersen, K. Vogfjörd, B. Thorbjarnardottir, S. Jakobsdottir, M.J. Roberts (2010). Eruptions of Eyjafjallajökull Volcano, Iceland. Eos, Vol. 91, No. 21, pp. 190-191

Guffanti, M., J. W. Ewerts, G. M. Gallina, G. J. S. Bluth, G. L. Swanson (2005). Volcanic-ash hazard to aviation during the 2003–2004 eruptive activity of Anatahan volcano, Commonwealth of the Northern Mariana Islands. J. Volcanol. Geoth. Res., Vol. 146, pp. 241–255.

Guffanti, M., D. J. Schneider, J. W. Ewert, and S. Targosz (2008). Impact on aviation operations of volcanic gas and ash clouds from the 2008 eruptions of Okmok and Kasatochi, Alaska. Eos Trans. AGU, Vol. 89, No. 53, Fall Meet. Suppl., Abstract A53B-0277.

Gür, B., P. Spietz, J. Orphal and J. Burrows (2005). Absorption Spectra Measurements with the GOME-2 FMs using the IUP/IFE-UB´s Calibration Apparatus for Trace Gas Absorption Spectroscopy CATGAS. Final Report, IUP University of Bremen, Oct. 2005.

Gurevich, G.S. and A.J. Krueger (1997) Optimization of TOMS wavelength channels for ozone and sulfur dioxide retrievals. Geophys. Res. Lett., Vol. 24, No.17, pp. 2187 – 2190.

Harding, D. and J.M. Miller (1982). The influence on rain chemistry of the Hawaiian volcano Kilauea. J. Geophys. Res., Vol. 87, pp. 1225-1230

Heckel, A. , A. Richter, T. Tarsu, F. Wittrock, C. Hak, I. Pundt, W. Junkermann, J. P. Burrows (2005). MAX-DOAS measurements of formaldehyde in the Po-Valley. Atmos. Chem. Phys., Vol. 5, pp. 909–918.

Heinen T., S. Kiemle, B. Buckl, E. Mikusch D. Loyola (2009). The Geospatial Service Infrastructure for DLR's National Remote Sensing Data Library. IEEE Journal of Selected Topics in Applied Earth Observations and Remote Sensing, Vol. 2, pp. 260-269.

Herman, J.R. and E.A. Celarier (1997). Earth surface reflectivity climatology at 340 – 380 nm from TOMS data, J. Geophys. Res. Vol. 102, pp. 28,003-28,011.

Hofmann, D. J., and S. Solomon (1989). Ozone Destruction Through Heterogeneous Chemistry Following the Eruption of El Chichón. J. Geophys. Res., Vol. 94(D4), pp. 5029–5041, doi:10.1029/JD094iD04p05029.

Hönninger, G., C. von Friedeburg, U. Platt (2004). Multi Axis Differential Optical Absorption Spectroscopy (MAX-DOAS). Atmos. Chem. Phys., Vol. 4, pp. 231-254.

Hort, M. and K. Zaksek (2008). Exupéry: The mobile volcano fast response system. IEEE 2nd USEReSTWorkshop, Naples, Italy, Nov. 11–14.

Horton K.A., G. Williams-Jones, H. Garbeil, P. Mouginis-Mark, J.N. Porter, T. Elias, A.J. Sutton (2005). Real-time measurement of volcanic SO_2 emissions: validation of a new UV correlation spectrometer. Bull. Volcanol., Vol. 68, pp. 323 – 327

International Civil Aviation Organization (ICAO) (2010). Nature's Wrath, European civil aviation stakeholders keep safety paramount as Iceland's Eyjafjallajökull volcano blasts unprecedented volumes of ash into the skies over northern Europe", ICAO Journal, Vol. 65, No. 4.

IPCC (2001). Intergovernmental Panel on Climate Change (2001): Climate Change 2001 – Mitigation (29.04.2006). http://www.grida.no/climate/ipcc_tar/wg3/index.htm.

IPCC (2007). Intergovernmental panel on climate change: climate change 2007 - the physical science basis. http://www.ipcc.ch/ipccreports/ar4-wg1.htm

Joiner, J., P. Barthia, R. Cebula, E. Hilsenrath, R. McPeters, H. Park (1995). Rotational Raman scattering (Ring effect) in satellite backscatter ultraviolet measurements. Applied Optics, Vol. 34, pp. 4513-4525.

Jones, A., D. Johnson, M. Hort, B. Devendish (2007). The UK Met Office's Next-Generation Atmospheric Dispersion Model, NAME III. In: Air Pollution Modeling and Its Application XVII, edited by Borrego C, Norman AL, Springer

Kerr, J.B., C.T. McElroy, R.A. Olafson, (1981). Measurements of ozone with the Brewer spectrophotometer In: Proceedings of the Quadrennial International Ozone Symposium, edited by J. London, pp. 74–79, Natl. Cent. for Atmos. Res., Boulder, Colorado

Kerr, J. B. (2002). New methodology for deriving total ozone and other atmospheric variables from Brewer spectrophotometer direct sun spectra. J. Geophys. Res., Vol. 107, 4731, doi:10.1029/2001JD001227.

Kerr, J. B. and J. M. Davis (2007). New methodology applied to deriving total ozone and other atmospheric variables from global irradiance spectra. J. Geophys. Res., Vol. 112, D21301, doi:10.1029/2007JD008708.

Kerrick D.M. (2001). Present and past nonanthropogenic CO_2 degassing from the solid earth. Rev. Geophys., Vol. 39, pp. 565-585.

Kirchner, I., G. L. Stenchikov, H.-F. Graf, A. Robock, J. C.Antuna (1999). Climate model simulation of winter warming and summer cooling following the 1991 Mount Pinatubo volcanic eruption. J. Geophys. Res., Vol. 104, pp. 19,039 –19,055.

Khokhar, M.F., C. Frankenberg, M. Van Roozendael, S. Beirle, S. Kühl, A. Richter, U. Platt, T. Wagner (2005). Satellite observations of atmospheric SO_2 from volcanic eruptions during the time period of 1996 to 2002. Adv. Space Res., Vol. 36, pp. 879–887.

Koelmeijer R.B.A., J.F. de Haan, J.W. Hovenier, P. Stammes (2003). A database of spectral surface reflectivity in the range 335 – 772 nm derived from 5.5 years of GOME observations. J. Geophys. Res., Vol. 108(D2), 4070, doi:10.1029/2002JD002429.

Kravitz B. and A. Robock (2010). The Climate Effects of High Latitude Volcanic Eruptions: The Role of the Time of Year. J. Geophys. Res., submitted

Kravitz B., A. Robock, A. Bourassa (2010). Negligible climatic effects from the 2008 Okmok and Kasatochi volcanic eruptions. J. Geophys. Res., Vol. 115, No. 5, doi:D00L05, doi:10.1029/2009JD013525.

Kristiansen, N.I., A. Stohl, A.J. Prata, A. Richter, S. Eckhardt, P. Seibert,A. Hoffmann, C. Ritter, L. Bitar, T.J. Duck, K. Stebel (2010). Remote sensing and inverse transport modeling of the Kasatochi eruption sulfur dioxide cloud. J. Geophys. Res., Vol. 115, D00L16, doi:10.1029/2009JD013286.

Krotkov, M.A., B. McClure, R.R. Dickerson, S.A. Carn, C. Li, P.K. Bhartia, K. Yang, A.J. Krueger, Z. Li, P. Levelt, H. Chen, P. Wang, and D.R. Lu (2008). Validation of SO_2 retrievals from the Ozone Monitoring Instrument (OMI) over NE China. J. Geophys. Res., Vol. 113, D16S40, doi:10.1029/2007JD008818.

Krueger, A.J. (1983). Sighting of El Chichon sulfur dioxide clouds with the Nimbus 7 total ozone mapping spectrometer. Science, Vol. 220, pp. 1377 – 1379.

Krueger, A.J., L.S. Walter, C.C. Schnetzler, S.D. Doiron (1989). TOMS measurement of the sulfur dioxide emitted during the 1985 Nevado del Ruiz eruptions. J. Volcanol. Geoth. Res., Vol. 41, pp. 7 – 15.

Kurucz, R.L., I. Furenlid, J. Brault, and L. Testerman (1984). Solar flux atlas from 296 nm to 1300 nm. Natl. Sol. Obs. Atlas 1, 239 pp., Harvard Univ., Cambridge, Mass.

Lambert, J.-C., D.S. Balis, C. Fayt, P. Gerard, J.F. Gleason, J. Granville, G. Hansen, G. Labow, D. Loyola, V. Soebijanta, W. Thomas, J.H.G. van Geffen, R.F. van Oss, M. Van Roozendael, C. Zehner, and C.S. Zerefoset (2002). ERS-2 GOME GDP 3.0 Implementation and Delta Validation, Validation Report for GOME Level 1-to-2 Data Processor Upgrade to Version GDP 3.0. ERSE-DTEX-EOAD-TN-02-0006, ESA/ESRIN, Frascati, Italy.

Lautze N.C., A.J.L. Harris, J.E. Bailey, M. Ripepe, S. Calvari, J. Dehn, S.K. Rowland, K. Evans-Jones (2004). Pulsed lava effusion at Mount Etna during 2001. J. Volcanol. Geoth. Res., Vol. 137, pp. 231-246.

Lee, C., A. Richter , M. Weber , and J.P. Burrows (2008). SO_2 Retrieval from SCIAMACHY using the Weighting Function DOAS (WFDOAS) Technique: comparison with Standard DOAS retrieval. Atmos. Chem. Phys. Discuss., Vol. 8, pp. 10817–10839.

Levelt, P.F., G.H.J. van den Oord, M.R. Dobber, A, Malkki, H. Visser, J. de Vries, P. Stammes, J. Lundell, H. Saari (2006). The Ozone Monitoring Instrument," IEEE Trans. Geosci. Remote Sens., Vol. 44, No. 5, pp. 1093-1101.

Li, C., Q. Zhang, N. A. Krotkov, D. G. Streets, K. He, S.-C. Tsay, J. F. Gleason (2010). Recent large reduction in sulfur dioxide emissions from Chinese power plants observed by the Ozone Monitoring Instrument. Geophys. Res. Lett., Vol. 37, L08807, doi:10.1029/2010GL042594.

Lipman, P. W. and D. R. Mullineaux, Eds., (1981). The 1980 eruption of Mount St. Helens. US Geol. Surv. Prof. Pap., Vol. 1250, pp. 1–844.

Livschitz, Y. and D. Loyola (2003). Design Document for the GOME-2 Universal Processor for Atmospheric Spectrometers. SAF/O3M/DLR/DD/001, Issue 2.0, October 2003

Loyola, D., W. Thomas, Y. Livschitz, T. Ruppert, P. Albert, R. Hollmann (2007). Cloud properties derived from GOME/ERS-2 backscatter data for trace gas retrieval. IEEE Transactions on Geoscience and Remote Sensing, Vol. 45, No. 9, pp. 2747-2758.

Loyola, D., J. van Geffen, P. Valks, T. Erbertseder, M. Van Roozendael, W. Thomas, W. Zimmer, K. Wißkirchen (2008). Satellite-based detection of volcanic sulphur dioxide from recent eruptions in Central and South America. Advances in Geosciences, Vol. 14, pp. 35-40.

Loyola, D., W. Zimmer, S. Kiemle, P. Valks, T. Ruppert (2008). Product User Manual for GOME Total Columns of Ozone, Minor Trace Gases, and Cloud Properties, Doc. No: DLR/GOME/PUM/01, Iss./Rev.: 2/A, 17 November 2008, Available: http://wdc.dlr.de/sensors/gome2/

Malicet, J., D. Daumont, J. Charbonnier, C. Parisse, A. Chakir, J. Brion (1995). Ozone UV Spectroscopy. II. Absorption Cross-Sections and Temperature Dependence. J. Atmos. Chem., Vol. 21, pp. 263-273.

Malinconico, L.L. (1979). Fluctuations in SO_2 emission during recent eruptions of Etna. Nature, Vol. pp. 278, 43-45.

McCormick, P.M., L.W. Thomason, C.R. Trepte (1995). Atmospheric effects of the Mt. Pinatubo eruption. Nature, Vol. 373, pp. 399–404.

Meixner, F.X. and W.A. Jaeschke (1981). The Detection of Low Atmospheric SO_2 Concentrations with a Chemiluminescence Technique. Intern. J. Environ. Anal. Chem., Vol. 10, pp. 51-67.

Métrich, N., P. Allard, N. Spillaert, D. Andronico, M.R. Burton (2004). 2001 flank eruption of the alkali and volatile-rich primitive melt responsible for Mount Etna's evolution in the last three decades. Earth Planet Sc. Lett., Vol. 228, pp. 1-17.

Millan, M., S. Townsend, J. Davies (1969). Study of the Barringer refractor plate a correlation spectrometer as a remote sensing instrument. Utias rpt. 146, m.a.sc. thesis, University of Toronto, Toronto, Ontario, Canada. In: Morello N, (editor) “Volcanoes and History”,1998

Miller, T.P. and T.J. Casadevall (2000). Volcanic ash hazards to aviation. In: Encycl. Volcanoes, H. Sigurdson, Ed. San Diego, CA: Academic Press, pp. 915–930.

Munro, R., M. Eisinger, C. Anderson, J. Callies, E. Corpaccioli, R. Lang, A. Lefebvre, Y. Livschitz, A. Perez Albinana (2006). GOME-2 on METOP: From in-orbit verification to routine operations, in: Proceedings of EUMETSAT Meteorological Satellite Conference. Helsinki, Finland, 12-16 June.

NASA (2009). calypso.larc.nasa.gov/products/lidar/browse_images/show_calendar.php, National Aeronautics and Space Administration.

Newhall, C.G. and S. Self (1982). The volcanic explosivity index (VEI): an estimate of explosivity magnitude for historic volcanism. J. Geophys. Res., Vol. 87, pp. 1231-1238.

Nowlan, C.R., X. Liu, K. Chance, T.P. Kurosu, C. Lee, R.V. Martin (2010). SO_2 measurements from GOME-2: An optimal estimation approach. Proceeding of the ESA Living Planet Symposium 2010, Bergen, Norway

Okita, T. (1971). Detection of SO_2 and NO_2 gas in the atmosphere by Barringer spectrometer. JASCO, Tokyo, Rep. 8/7.

Olmos, R., J. Barrancos, C. Rivera, F. Barahona, D.L. López, B. Henriquez, A. Hernández, E. Benitez, P.A. Hernández, N.M. Pérez, B. Galle (2007). Anomalous Emissions of SO_2 During the Recent Eruption of Santa Ana Volcano, El Salvador, Central America. Pure Appl. Geophys., Vol. 164, pp. 2489-2506.

Parfitt, E.A. and L. Wilson (1995). Explosive volcanic eruptions. The transition between Hawaiian-style lava fountaining and Strombolian explosive activity. Geophys. J. Int., Vol. 121, pp. 226-232.

Pinardi, G., R. Campion, M. Van Roozendael, C. Fayt, J. van Geffen, B. Galle, S. Carn, P. Valks, M. Rix, S. Hildago, J. Bourquin, G. Garzon, S. Inguaggiato (2010) Comparison of volcanic SO_2 flux measurements from satellite and from the NOVAC network. Proceedings of the 2010 EUMETSAT Meteorological Satellite Conference, Cordoba, Spain

Pitari, G., E. Mancini, V. Rizi, D.T. Shindell (2002). Impact of future climate and emission changes on stratospheric aerosols and ozone. J. Atmos. Sci., Vol. 59, pp. 414-440, doi:10.1175/1520-0469.

Platt, U. (1994). Differential optical absorption spectroscopy (DOAS). In: Air Monitoring by Spectroscopic Techniques. Chem. Anal. Ser., Vol. 127, pp. 27-84, John Wiley, New York.

Platt, U., J. Stutz (2008). Differential Optical Absorption Spectroscopy: Principles and Applications (Physics of Earth and Space Environments). Springer-Verlag, Berlin Heidelberg

Prata, A.J., S.A. Carn, A. Stohl, J. Kerkmann (2007). Long range transport and fate of a stratospheric volcanic cloud from Soufriere Hills volcano, Montserrat. Atmos. Chem. Phys., Vol. 7, pp. 5093 – 5103.

Prata, J. (2008). Satellite detection of hazardous volcanic ash clouds and the risk to global air traffic. Nat. Hazards, doi:10.1007/s11096-008-9273-z.

Richter, A. (1997). Absorptionsspektroskopische Messungen stratosphärischer Spurengase über Bremen, 53° N. PhD Thesis, Universität Bremen

Ripepe M., A.J.L. Harris, R. Carniel (2002). Thermal, seismic and infrasonic evidences of variable degassing rates at Stromboli volcano. J. Volcanol. Geoth. Res., Vol. 118, pp. 285-297

Rix, M., P. Valks, N. Hao, J. van Geffen, C. Clerbaux, L. Clarisse, P.-F. Coheur, D. Loyola, T. Erbertseder, W. Zimmer, S. Emmadi (2009), Satellite Monitoring of Volcanic Sulfur Dioxide Emissions for Early Warning of Volcanic Hazards. IEEE Journal of Selected Topics in Applied Earth Observations and Remote Sensing, Vol. 2, No. 3, pp. 196-206.

Rix, M., P. Valks, N. Hao, D. Loyola, H. Schlager, H. Huntrieser, J. Flemming, U. Koehler, U. Schumann, A. Inness (2012). Volcanic SO_2, BrO and plume height estimations using GOME-2 measurements during the eruption of Eyjafjallajökull in May 2010. J. Geophys. Res., Vol. 117, doi:10.1029/2011JD016718

Robock, A., and J. Mao (1992). Winter warming from large volcanic eruptions. Geophys. Res. Lett., Vol. 19, pp. 2405–2408.

Robock, A. (2000). Volcanic eruptions and climate. Rev. Geophys., Vol. 38, pp. 191-219.

Robock, A., L. Oman, G. Stenchikov (2008). Regional climate responses to geoengineering with tropical and Arctic SO_2 injections. J. Geophys. Res., Vol. 113, D16101, doi:10.1029/2008JD010050.

Sanders, R.W., S. Solomon, J.P. Smith, L. Perliski, H.L. Miller, G.H. Mount, J.G. Keys, A.L. Schmeltekopf (1993). Visible and Near-Ultraviolet Spectroscopy at McMurdo Station Antarctica, 9. Obeservations of OClO from April to October 1991. J. Geophys. Res., Vol. 98, No. D4, pp. 7219–7228.

Schmincke, H.-U. (2004). Volcanism. Heidelberg: Springer Verlag.

Schneider, D.J., W.I. Rose, L.R. Coke, G.J.S. Bluth, I. Sprod, and A.J. Krueger (1998). Early evolution of a stratospheric volcanic eruption cloud as observed with TOMS and AVHRR. J. Geophys. Res., Vol. 104, pp. 4037–4050.

Schumann, U., B. Weinzierl, O. Reitebuch, H. Schlager, A. Minikin, C. Forster, R. Baumann, T. Sailer, K. Graf, H. Mannstein, C. Voigt, S. Rahm, R. Simmet, M. Scheibe, M. Lichtenstern, P. Stock, H. Ruba, D. Schauble, A. Tafferner, M. Rautenhaus, T. Gerz, H. Ziereis, M. Krautstrunk, C. Mallaun, J.-F. Gayet, K. Lieke, K. Kandler, M. Ebert, S. Weinbruch, A. Stohl, J. Gasteiger, H. Olafsson, and K. Sturm (2010). Airborne observations of the Eyjafjalla volcano ash cloud over Europe during air space closure in April and May 2010. Atmos. Chem. Phys. Discuss., Vol. 10, pp. 22,131–22,218, doi:10.5194/acpd-10-22131-2010

Seidenberger, K. (2009). Bestimmung der Charakteristik vulkanischer Emissionen mit Satelliten-basierten Messungen, Trajektorienensembles und Chemie-Transport-Modellierung. Diplomarbeit, Universität Augsburg

Seinfeld, J.H. and S.N. Pandis (2006). Atmospheric Chemistry and Physics: Air Pollution to Climate Change. John Wiley & Sons, New York

Siddans, R., B.G. Latter, B.J. Kerridge, J. Smeets, G. Otter, S. Slijkhuis (2006). Analysis of GOME-2, Slit function Measurements Final Report. EUMETSAT Contract No. EUM/CO/04/1298/RM.

Sigvaldason, G. E. (1989). International conference on Lake Nyos disaster, Yaounde, Cameroon 16–20 March, 1987: Conclusions and recommendations. J. Volcanol. Geoth. Res., Vol. 39, pp. 97–107.

Simkin, T. and L. Siebert (1994). Volcanoes of the World. 2nd ed. Tucson, AZ: Geoscience Press, 349

Sioris, C. and W. Evans (1999). Filling-in of Fraunhofer and gas-absorption lines as caused by rotational Raman scattering. Applied Optics, Vol. 38, pp. 2706-2713.

Smithonian Institution, Global Volcanism Program, SI/USGS Weekly Volcanic Activity Reports Available at: http://www.volcano.si.edu

Solomon, S. (1999). Stratospheric ozone depletion: A review of concepts and history. Rev. Geophys., Vol. 37, pp. 275–316.

Solomon, S., R.W. Portmann, R.R. Garcia, L.W. Thomason, L.R. Poole, M.P. McCormick (1996). The role of aerosol variations in anthropogenic ozone depletion at northern midlatitudes. J. Geophys. Res., Vol. 101, pp. 6713– 6727.

Spurr, R.J.D., T.P. Kurosu, K.V. Chance (2001). A linearized discrete ordinate radiative transfer model for atmospheric remote sensing retrieval. J. Quant. Spectrosc. Radiat. Transfer, Vol. 68, pp. 689 – 735.

Spurr, R. (2008). LIDORT and VLIDORT: Linearized pseudo-spherical scalar and vector discrete ordiate radiative transfer models for use in remote sensing retrieval problems. Light Scattering Reviews, Vol. 3, ed. A. Kokhanovsky, Springer.

Spurr R., J. de Haan, R. van Oss, A. Vasilkov (2008). Discrete-ordinate radiative transfer in a stratified medium with first-order rotational Raman scattering. Journ. Quant. Spectrosc. Rad. Transfer, Vol. 109, pp. 404–425.

Spurr, R., M. van Roozendael, D. Loyola, C. Lerot, J. van Geffen, J. van Gent, C. Fayt, J.-C. Lambert, B. Aberle, W. Zimmer, A. Doicu, S. Otto, D. Balis, M. Koukouli, C. Zehner (2009). GDP 5.0 Upgrade of the GOME Data Processor for Improved Total Ozone Columns. Algorithm Theoretical Basis Document, iss./rev. 1, Nov. 30

Stamnes, K., S.-C. Tsay, W. Wiscombe, K. Jayaweera (1988). Numerically stable algorithm for discrete ordinate method radiative transfer in multiple scattering and emitting layered media. Appl. Opt., Vol. 27, pp. 2502-2509.

Stevenson, D.S. ans S. Blake (1998). Modeling the dynamics and thermodynamics of volcanic degassing. Bull. Volcanol., Vol. 60, pp. 307-317.

Stoiber, R.E., L.L. Malinconico, S.N. Williams (1983). Use of the correlation spectrometer at volcanoes. In: Tazieff H, Sabroux, JC (ed) Forecasting volcanic events. Elsevier, Amsterdam, pp. 424-444

Stohl A., C. Foster, A. Frank, P. Seibert, G. Wotawa (2005). Technical note: The Lagrangian particle dispersion model FLEXPART version 6.2. Atmos. Chem. Phys., Vol. 5, pp. 2461 – 2474.

Stothers, R.B. (1996). Major optical depth perturbations to the stratosphere from volcanic eruptions: Pyrheliometric period, 1881–1960. J. Geophys. Res., Vol. 101, pp. 3901–3920, doi:10.1029/95JD03237.

Streets, D.G., N.Y. Tsaia, H. Akimotob K. Okac (2000). Sulfur dioxide emissions in Asia in the period 1985–1997. Atmospheric Environment, Vol. 34, No. 26, pp. 4413-4424.

Sutton, A.J., T. Elias, T.M. Gerlach, J.B. Stokes (2001). Implications for eruptive processes as indicated by sulfur dioxide emissions from Kilauea Volcano, Hawaii, 1979-1997. J. Volcanol. Geoth. Res., Vol. 108, pp. 283-302.

Sweeney, D., P.R. Kyle, C. Oppenheimer (2008). Sulfur dioxide emissions and degassing behavior of Erebus volcano, Antarctica. J. Volcanol. Geoth. Res., Vol. 117, pp. 725-733.

Textor, C., H. Graf, C. Timmreck, A. Robock (2004). Emissions from volcanoes. In: Emissions of Chemical Compounds and Aerosols in the Atmosphere, Kluwer, Dordrecht, The Netherlands, pp. 269–303.

Thomas, H.E., I.M. Watson , C. Kearney, S.A. Carn , S.J. Murray (2009). A multi-sensor comparison of sulphur dioxide emissions from the 2005 eruption of Sierra Negra volcano, Galápagos Islands. Remote Sensing of Environment, Vol. 113, pp. 1331–1342.

Thomas, W., T. Erbertseder, T. Ruppert, M. van Roozendael, J. Verdebout, D. Balis, C. Meleti, C. Zerefos (2005). On the Retrieval of Volcanic Sulfur Dioxide Emissions from GOME Backscatter Measurements. J. Atmos. Chem., Vol. 50, pp. 295-320.

USGS (1997). USGS/Cascades Volcano Observatory, Vancouver, Washington, http://vulcan.wr.usgs.gov/Glossary/PlateTectonics/Maps/map_plate_tectonics_world.html

U.S. Standard Atmosphere, 1976 (1976). U.S. Government Printing Office, Washington, D.C.

Valks, P., D. Loyola, N. Hao, M. Rix, S. Slijkhuis (2009). Algorithm Theoretical Basis Document for GOME-2 total Column Products of Ozone, NO_2, SO_2, BrO,H_2O, tropospheric NO_2 and Cloud Properties (GDP 4.3 for O3M-SAF OTO and NTO). DLR/GOME-2/ATBD/01, Iss./Rev.: 2/B, Oct. 30, [Online]. Available: http://wdc.dlr.de/sensors/gome2/

Van Geffen, J., M. Van Roozendael, W. Di Nicolantonio, L. Tampellini, P. Valks, T. Erbertseder, R. Van der A (2007). Monitoring of volcanic activity from satellite as part of GSE PROMOTE. Presented at the ENVISAT Symp., Montreux, 2007, Esa publication SP-636.

Van Geffen, J., M. Van Roozendael, M. Rix, P. Valks (2008). Initial validation of GOME-2 GDP 4.2 SO_2 total columns – ORR B. Validation Report, TN-IASB-GOME2-O3MSAF-SO2-01, issue 1

Van Roozendael, M. and C. Fayt (2001). WinDOAS 2.1. Software User Manuel.

Van Roozendael, M., V. Soebijanta, C. Fayt, J.-C. Lambert (2002). Investigation of DOAS Issues Affecting the Accuracy of the GDP Version 3.0 Total Ozone Product, in ERS-2 GOME GDP 3.0 Implementation and Delta Validation. Ed. J-C. Lambert, ERSE-DTEX-EOAD-TN-02-0006, ESA/ESRIN, Frascati, Italy, Chapt.6, pp. 97-129.

Vountas, M., V.V. Rozanov, J.P. Burrows (1998). Ring effect : Impact of rotational Raman scattering on radiative transfer in earth's atmosphere. J. Quant. Spectrosc. Rad. Transfer, Vol. 60, pp. 943-961.

Watson, I.M., C. Oppenheimer, B. Voight, P.W. Francis, A. Clarke, J. Stix, A. Miller, D.M. Pyle, M.R. Burton, S.R. Young, G. Norton, S. Loughlin, B. Darroux, MVO-Staff (2000). The relationship between degassing and ground deformation at Soufriere Hills Volcano, Montserrat. J. Volcanol. Geoth. Res., Vol. 98, pp. 117-126.

Weber, M., L.N. Lamsal, M. Coldewey-Egbers, K. Bramstedt, J.P. Burrows (2005). Pole-to-pole validation of GOME WFDOAS total ozone with groundbased data. Atmos. Chem. Phys., Vol. 5, pp.1341–1355.

Weisenstein, D.K., G.K. Yue, M.K.W. Ko, N.-D. Sze, J.M. Rodriguez, and C.J. Scott (1997). A two-dimensional model of sulfur species and aerosols. J. Geophys. Res., Vol. 102(D11), pp. 13,019–13,035, doi:10.1029/97JD00901.

Wellemeyer, C.G., S. Taylor, C. Seftor, R. McPeters P.Bhartia (1997). A correction for total ozone mapping spectrometer profile shape errors at high latitude. J. Geophys. Res., Vol. 102, pp. 9029 – 9038.

Wellemeyer, C.G., P.K. Bhartia, S.L. Taylor, W. Qin, C. Ahn (2004). A New Release of Data from the Total Ozone Monitoring Spectrometer (TOMS). SPARC Newsletter, Vol. 22, pp. 37-38, available at: www.aero.jussieu.fr/~sparc

Westphal, D.L., H. Chen, J.R. Campbell, K. Richardson, J.D. Doyle, and M.D. Fromm (2008). Numerical investigation and forecasting of the Kasatochi ash plume. Eos Trans. AGU, Vol. 89(53), Fall Meet. Suppl., Abstract A53B-0267.

Yang, K., N.A. Krotkov, A.J. Krueger, S.A. Carn, P.K. Bhartia, P.F. Levelt (2007). Retrieval of large volcanic SO_2 columns from the Aura Ozone Monitoring Instrument: Comparison and limitations. J. Geophys. Res., Vol. 112, doi:10.1029/2007JD008825

Yang, K., X. Liu, N.A. Krotkov, A.J. Krueger, S.A. Carn (2009). Estimating the altitude of volcanic sulfur dioxide plumes from space borne hyper-spectral UV measurements," Geophys. Res. Lett., Vol. 36, doi:10.1029/2009GL038025

Zehner, C. Ed . (2010). Monitoring Volcanic Ash from Space. Proceedings of the ESA-EUMETSAT workshop on the 14 April to 23 May eruption at Eyjafjöll volcano, South Iceland. Frascati, Italy, 26-27 May 2010" ESA-Publication STM-280. doi:105270/atmch-10-01

Zhang, D., Y. Maeda, M. Munemori (1985). Chemiluminescence Method for Direct Determination of Sulfur Dioxide in Ambient Air. Anal. Chem., Vol. 57, No. 13

Danksagung

Nachdem es nach jetzt knapp vier Jahren, in denen ich mich gelegentlich doch gefragt habe, wie ich eigentlich auf die Idee mit der Promotion gekommen bin, geschafft ist, wollte ich mich bei allen bedanken, die mich auf diesem Weg unterstützt haben.

Zuerst möchte ich mich bei meinem Doktorvater, Prof. Richard Bamler, sowie bei meinem zweiten Betreuer, Prof. Thomas Trautmann, für die Unterstützung und Motivation während der Arbeit, sowie dafür, dass sie mir die Möglichkeit gegeben haben, meine Ergebnisse auf diversen Konferenzen und Workshops zu präsentieren.

Ein besonders großes Dankeschön gilt meinem fachlichen Betreuer, Pieter Valks, für die wirklich ausgezeichnete Betreuung. Während des gesamten Verlaufs der Arbeit hatte er immer ein offenes Ohr für meine Probleme und hat sich immer die Zeit genommen Dinge zu besprechen und zu erklären. Außerdem hat er durch viele gute Ideen und gründliches Korrekturlesen dazu beigetragen, dass die Arbeit in der jetzigen Form entstanden ist.

In diesem Zusammenhang auch vielen Dank auch an die gesamte restliche Abteilung IMF-AP, die mich alle unterstützt haben und sich immer wieder die Zeit genommen haben mir bei Fragen oder Problemen zu helfen. Hier möchte ich mich besonders bei Diego Loyola für seine guten Ideen und Ratschläge bezüglich der SO2-Höhenbestimmung bedanken, bei Adrian Doicu für seine Hilfe bei den mathematischen Fragen und bei Walter Zimmer und Bernd Aberle für ihre Hilfe bei sämtlichen Computerproblemen.

Vielen andere haben auch zum Gelingen der Arbeit beigetragen haben, besonders möchte ich mich noch bedanken bei Jeroen van Gent (BIRA-IASB) für seine Unterstützung bezüglich des „direct fitting“, Jos van Geffen (BIRA-IASB) für die Zusammenarbeit beim Vergleich der Satellitendaten, Cordelia Maerker (DWD) für die Modellierung der Hawaii Daten und die gute Zusammenarbeit innerhalb des Eupery Projekts, Michel van Roozendael (BIRA-IASB) für die Bereitstellung der Max-DOAS Daten und bei MariLiza Koukouli (University of Thessaloniki) für die Bereitstellung der Brewer Daten. Vielen Dank auch an meinen Bruder Sören, der die ganze Arbeit, obwohl er sie ziemlich langweilig fand, auf Rechtschreibfehler Korrektur gelesen hat und sie hoffentlich alle gefunden hat.

Als letztes noch mal „Danke“ an Robert, der sich mein gelegentlich frustriertes und genervtes Gejammer über nicht funktionierende Computerprogramme, fehlende Daten, zu haltende Vorträge und all die anderen Probleme, die im Laufe einer Promotion auftreten, immer klaglos angehört hat und mich in diesen Situationen wieder aufgebaut und abgelenkt hat.